Satellite altimetry for land hydrology

– CryoSat-2 for inland water monitoring

Heidi Villadsen
PhD Thesis
March 2, 2016

DTU Space
National Space Institute

Satellite altimetry for land hydrology
– *CryoSat-2 for inland water monitoring*

Heidi Villadsen
National Space Institute
PhD Thesis, Kgs. Lyngby, March 2, 2016

http://www.space.dtu.dk

Dansk sammenfatning

Jordens hydrologiske kredsløb forventes at ændre sig i takt med klimaforandringerne, hvilket vil få fatale konsekvenser for store dele af verdens befolkning. På trods af det øgede fokus på jordens ferskvandsressourcer er antallet af målestationer langs floder og søer faldet drastisk.

Højdemålinger fra satellit bliver udført med et såkaldt radar altimeter, og gør det muligt at observere vandstanden i floder og søer uafhængigt af infrastruktur og politik. Satellitaltimetri er tidligere blevet brugt med stor succes over oceaner og inlandsis, hvorimod højdeestimaterne over floder og søer har været præget af en langt mindre præcision.

Her er det blevet undersøgt, hvordan højdemålinger fra satellitten CryoSat-2 bidrager til satellitaltimetri over floder og søer. CryoSat-2 benytter som den første satellitmission et "Synthetic Aperture Radar" (SAR) altimeter, der er i stand til at foretage observationer med en langt højere opløsning end traditionelle altimetre. Med SAR teknologien formår CryoSat-2 dermed at observere mindre søer og floder med en langt større præcision end tidligere missioner.

I denne afhandling er der udviklet metoder til at bestemme vandniveauer i floder og søer baseret på SAR ekkoer, samt metoder der kan benyttes til at udlede tidsserier, som opfanger de samme årstidssignaler som målestationer. Disse tidsserier bruges bl.a. af hydrologer til at kalibrere og validere hydrologiske modeller, der beskriver gennemstrømningen af vand i floder.

Metoderne udviklet i forbindelse med dette studie er en del af forberedelserne til Sentinel-3 missionen, og metoderne kan derfor anvendes, når data fra Sentinel-3 bliver tilgængelige i løbet af 2016.

Abstract

Fresh water availability is of increasing concern due to climate changes and a growing world population. At the same time, the number of in situ water gauges continues to decrease, making it difficult to monitor the state of rivers and lakes around the world. Satellite altimetry offers a way of monitoring surface water from space independent of infrastructure and political issues. This study aims to illustrate the potential of Synthetic Aperture Radar (SAR) altimetry for inland water monitoring using data from the CryoSat-2 mission, which has an unprecedented high along-track resolution due to its SAR altimeter.

The 369-day repeat period of CryoSat-2 is not ideal for river monitoring, and a method is developed to relocate observations to virtual stations. Results from the Brahmaputra and Ganges Rivers show that, when using this method, CryoSat-2 can capture the annual signals of the river similar to those from Envisat, although this was not expected from the CryoSat-2 mission. In Bangladesh and Thailand, Low Resolution Mode (LRM) and SAR mode data are used to detect flooding events. The inundated regions were detected as changes in height, peakiness, and backscatter coefficient.

Contamination of radar echoes from off-nadir specular targets, also called snagging, was found to be a significant problem over inland water when studying waveforms over the Brahmaputra River. Therefore, the Multiple Waveform Persistent Peak (MWaPP) retracker was developed during this work to reduce wrongly estimated heights. Studies showed that the biggest improvements were obtained in Lake Okeechobee, Florida, where the root-mean-square (RMS) error between satellite and in situ data decreased from 61.8 cm to 12.6 cm when compared to a traditional subwaveform retracker.

Furthermore, the benefits of using the physical SAMOSA3 model in combination with an empirical retracking method are investigated. The study reveals that combined methods give results similar to the chosen empirical method due to the high number of contaminated waveforms ($\sim$ 50% of all waveforms), for which SAMOSA3 is unable to provide reasonable height estimates. However, the study also shows that when the SAMOSA3 model is able to fit the altimetric waveforms, the SAMOSA3 model provides the best height estimates when compared to in situ data with RMS errors as low as 2.1 cm for Lake Okeechobee, albeit closely followed by the empirical retrackers with RMS errors of 2.4 cm.

Overall, the studies presented here show promising results for the new generation of SAR altimetry, which has a smaller measurement footprint compared to conventional altimeters, making it possible to derive stable height estimates for rivers and small lakes. The methods developed for CryoSat-2 SAR are fundamental for inland water applications of Sentinel-3, which has been launched in February 2016.

Preface

This thesis is submitted in fulfillment of the requirements for obtaining a PhD degree at DTU Space, National Space Institute, Technical University of Denmark. The research was carried out under supervision of Ole B. Andersen, Lars Stenseng, and Xiaoli Deng.

The PhD has been partially funded by the LOTUS (Land and Ocean Take-Up from Sentinel-3) EU 7th Framework project, and the objective of the study has therefore been to contribute to the preparations for Sentinel-3 by learning from CryoSat-2. Ideally, it would have been possible to test these findings on Sentinel-3 data, but unfortunately the mission launch was delayed until the very end of the PhD.

When undertaking a new project, the first thing to do is a litterature study. However, when this work began in 2013, the practical experience with SAR altimetry was still limited, and there were no publications on SAR altimetry for inland water purposes. For that reason, much of this project consisted of investigations of the potential of SAR altimetry over inland water, and as such, the project defined itself as challenges and opportunities were encountered. The work carried out during this PhD is presented chronologically in the dissertation, and in hindsight, some of the methods that were developed later in the PhD might have been beneficial for the earliest studies. In the end, I feel very hopeful about the future of satellite altimetry for land hydrology and the progress that has been made with SAR altimetry.

I would like to thank my amazing supervisors and colleagues at DTU Space with whom I have shared many great moments at the institute and while travelling for conferences and courses. I would also like to thank my external supervisor, Xiaoli Deng, for all her guidance, but more importantly for making me feel most welcome at the University of Newcastle, Australia, and for helping me in stressful times far away from my family.

I am grateful for my wonderful friends and family that have helped me through the tough times and with making my thesis understandable. Above all, I would like to thank my amazing fiancé for being ever so patient with me when I worked long nights or complained about deadlines.

In the end, I hope that the work I have done will be of use to future altimetry studies.

Heidi Villadsen
Lyngby, December 2015.

Acronyms

ACE2	Altimetry corrected elevations 2
AltiKa	Ka band altimeter (on board the SARAL mission)
DEM	Digital Elevation Model
DORIS	Doppler Orbitography and Radiopositioning Integrated by Satellite
ESA	European Space Agency
ERS	European Remote Sensing
GLWD	Global Lake and Wetland Database
GPS	Global Positioning System
KaRIn	Ka-band Radar Interferometer (on board the SWOT mission)
LEP	Leading Edge Point
LOTUS	Land and Ocean Take-Up from Sentinel-3
LRM	Low Resolution Mode
MOD44W	The MODIS 250 m land-water mask
MSS	Mean Square Slope
MWaPP	Multiple Waveform Persistent Peak Retracker
NGVD	National Geodetic Vertical Datum
NPPR	Narrow Primary Peak Retracker
NWIS	National Water Information System
OCOG	Off-Centre of Gravity
PP	Pulse Peakiness
PRF	Pulse Repetition Frequency
RA-2	Radar Altimeter 2 (on board the Envisat mission)
RMS	Root mean square
SAMOSA	SAR Altimetry MOde Studies and Applications
SAR	Synthetic Aperture Radar
SARAL	Satellite with ARgos and ALtiKa
SARIn	Synthetic Aperture Radar Interferometer
SIRAL	Synthetic Aperture Interferometric Radar Altimeter (on board the CryoSat-2 mission)
SRAL	Sentinel-3 Ku/C Radar Altimeter
SRTM	Shuttle Radar Topography Mission
SWH	Significant Wave Height
SWOT	Surface Water Ocean Topography
VS	Virtual Station

List of Figures

List of Tables

Contents

Chapter 1

Introduction

1.1 Motivation

All forms of life on Earth depend on fresh water. Humans depend on it directly as drinking water and for sanitation purposes, but it is also necessary for agriculture, the energy sector, and for transportation. The need for readily accessible and clean fresh water is especially vital in developing countries, where other alternatives are not available. In many areas of the world the strain on freshwater resources is becoming significantly more critical as the demand increases due to population growth and urbanization, and as climate changes affect the dynamics of lakes and rivers.

Therefore, monitoring the state of our freshwater resources is of great importance. Being able to identify the general behaviour and detect any changes in river and lake hydrology is useful for water resources management and flood detection as well as for climate change detection. Unfortunately, areas that are most sensitive to changes in land hydrology are also areas without the necessary infrastructure to maintain monitoring stations. As such, a significant decrease in the number of operating in situ stations has been witnessed over the past few decades and in situ data are often sparse (*Brakenridge et al.*, 2012).

Observation of river and lake levels from space therefore provides a way of monitoring our water resources independent of borders and infrastructure, which motivates the development of accurate satellite altimetry of land hydrology.

1.2 Previous studies

Initially, satellite altimetry was developed for the purpose of sea level determination (see e.g. *Chelton et al.* (2001)). Now, satellite altimetry has also been recognized as a useful source of information in other areas of the world, such as over the major ice-sheets, and most recently over lakes and rivers.

Satellite altimetry has been used for monitoring purposes of inland waters for more than 20 years. Some studies have focused on lakes (*Birkett*, 1994; *Cretaux and Birkett*, 2006; *Schwatke et al.*, 2015a; *Song et al.*, 2014), while others have focused on rivers (*Berry et al.*, 2005; *Birkett*, 1998; *da Silva et al.*, 2010; *Jarihani et al.*, 2013; *Koblinsky et al.*, 1993; *Maillard et al.*, 2015; *Schwatke et al.*, 2015a), or wetlands (*Zakharova et al.*, 2014). Table 1.1 holds a selection of relevant papers over lakes and rivers, and lists the key results with regards to retracking method and obtained RMS (root mean square) error compared to in situ gauge data. As seen from studies such as *Birkett* (1995); *Nielsen et al.* (2015a); *Schwatke et al.* (2015a), water levels obtained from altimetry over large lakes agree very well with in situ data with RMSEs down to 3-5 centimetres. Over rivers the results vary much more due to several factors such as signal contamination caused by topography or varying surface types within the measurement footprint, distance between virtual stations (VS) and river gauges, quality of in situ data. Of these error sources, *Maillard et al.* (2015) found that the surface type of the land surrounding the river was the most important factor for obtaining time series with low RMS errors over rivers. More specifically, they found the lowest RMS errors in areas of the river where the surrounding land was covered by dense vegetation, as this provided a good contrast between river and land returns in the signals retrieved by the altimeter.

There are already several studies on the use of CryoSat-2 data for inland studies, such as *Tourian et al.* (2015), who investigated the desiccation of Lake Urmia in Iran using CryoSat-2 Low Resolution Mode (LRM) data. *Nielsen et al.* (2015a) showed that it is possible to obtain very reliable lake levels from high resolution CryoSat-2 Synthetic Aperture Radar (SAR) data, for which lake levels were estimated for three small (8-40km^2) lakes in Denmark, obtaining an along-track precision of only 2-3 centimetres. In a study by *Kleinherenbrink et al.* (2015), lake level changes of several lakes on Tian Shan and the Tibetan Plateau were estimated using CryoSat-2 SAR Interferometric (SARIn) data. So far, there are no published studies on CryoSat-2's potential regarding monitoring of river levels aside from *Villadsen et al.* (2015a).

By now, satellite altimetry for land hydrology is accepted as an important source of global inland water heights with a unique monitoring capability (*Berry*, 2006), and its benefits in near real-time and long-term applications have been demonstrated in several studies with purposes such as discharge modelling and flood warning (*Biancamaria et al.*, 2011; *Michailovsky et al.*, 2013; *Neal et al.*, 2009). Satellite altimetry offers a solution to the difficulties that arise when local governments

classify their hydrological measurements and thereby prevent transboundary river management and flood forecasting.

Multiple projects already provide historical inland water levels from altimetry through web databases, such as the ESA River&Lake project (`http://earth.esa.int/riverandlake`, *Berry et al.* (2005)), the Global Reservoir and Lake Monitor (`http://www.pecad.fas.usda.gov/cropexplorer/global_reservoir/`, *Birkett et al.* (2011)), the HYDROWEB database (`http://www.LEGOS.obs-mip.fr/soa/hydrologie/HYDROWEB`, *Crétaux et al.* (2011)), and the Database for Hydrological Time Series of Inland Waters (DAHITI) database (*Schwatke et al.* (2015c), `http://dahiti.dgfi.tum.de/en`). Of these four databases, DAHITI is the only one that provides heights from CryoSat-2 data. At DTU Space at the Technical University of Denmark a new data product has therefore been developed that provides water level time series from CryoSat-2 for a number of lakes around the world (*Nielsen et al.* (2015b), `http://altwater.dtu.space/`).

Table 1.1: Overview of a selection of papers on inland water altimetry relevant to the current study. Key results are identified by code: (1) Used retrackers (2) RMSE from comparison with in situ gauges. For some of the earlier studies the used retracker was not stated in the manuscipt, which is here marked as "Not listed". Studies without comparison with in situ gauges at virtual stations (VS) have been left out. (*Villadsen et al.*, 2015b)

Study	**Mission(s)**	**Study area**	**Key results** 1: Retrackers 2: Obtained RMS errors
Koblinsky et al. (1993)	Geosat (1986-1989)	Four locations on the Amazon River.	1. Not listed. 2. 20-120 cm.
Birkett (1995)	TOPEX/Poseidon (T/P)	Lake Ontario (18960 km^2), Lake Michigan (58000 km^2), and Lake Superior (82100 km^2).	1. T/P GDR data. 2. 3-5 cm.
Birkett (1998)	T/P	One location on the Paraguay River and several on the Amazon River.	1. Not listed. 2. Paraguay River: 10.7-13.5 cm. Amazon River: 19-75 cm.
Birkinshaw et al. (2010)	Envisat and ERS-2	Mekong River (widths $\geq$0.4 km)	1. Not listed. 2. Envisat: 44-65 cm. ERS-2: 46-76 cm
da Silva et al. (2010)	Envisat and ERS-2	Five VS in The Negro River and Madeira River (widths of 0.2 - 1.7 km). 20 VS in the Amazon basin.	1. Ice-1 and Ice-2. 2. Negro/Madeira Rivers: $\sim$34 cm (Envisat) and $\sim$108 cm (ERS-2). Amazon River: $\sim$48 cm (Envisat) and $\sim$79 cm (ERS-2).
Jarihani et al. (2013)	Jason-2, Envisat, T/P, GFO, and Jason-1	Lake Eildon, Australia (138 km^2) and Lake Argyle, Australia (1000 km^2)	1. Ice-1/Ice-3 (Jason-2), Ice-1/Ice-2 (Envisat), Ocean retracker (T/P, GFO, Jason-1) 2. Lake Eildon: 28 cm/32 cm (Jason-2). Lake Argyle: 42 cm/138 cm (Envisat), 150 cm (T/P), 89 cm (GFO), 112 cm (Jason-1)

Continued on next page

Table 1.1 – *Continued from previous page*

Study	Mission(s)	Study area	Key results
Michailovsky et al. (2012)	Envisat	20 VS in the Zambezi River, Africa.	1. Not listed. 2. ∼58 cm (24-106 cm) when adjusting the obtained amplitude from altimetry.
Yi et al. (2013)	Jason-1 and Envisat	Lake Baikal, Siberia (31722 km^2)	1. Envisat: Ice-1 and a 50% Threshold Retracker (TR) Jason-1: Ice-1 and ocean (MLE4 type). 2. Envisat: 9.5 cm (Ice-1) and 12.1 cm (TR). Jason-1: 10.7cm (ocean) and 9.7 cm (TR).
Schwatke et al. (2015a)	Envisat and SARAL	The Great Lakes: Lake Superior (82100 km^2), Lake Huron (59570 km^2), Lake Michigan (58000 km^2), Lake Eerie (25744 km^2), Lake Ontario (18960 km^2). 9 VS in the Amazon.	1. Ice-1 and Brown retrackers. 2. Lakes: ∼4.27 (2.92-5.34) cm for Envisat and ∼ 3.83 (2.42-5.04) cm for SARAL. Amazon: ∼32.3 (8.3-58.8) cm for Envisat, ∼17.5 (7.8-31.8) cm for SARAL.
Nielsen et al. (2015a)	CryoSat-2 SAR and Envisat	In situ and altimetry data compared for two lakes: Vänern (Sweden, 5650 km^2) and Lake Okeechobee (Florida, 1900km^2).	1. Ice-1 (Envisat) and NPPR (CryoSat-2). CryoSat-2 SAR data were retracked using several empirical retrackers. The NPPR method proved to be the most stable of them all. 2. Lake Vänern: 5 cm (CryoSat-2) and 9 cm (Envisat). Lake Okeechobee: 8 cm (CryoSat-2) and 4 cm (Envisat).
Maillard et al. (2015)	Envisat and SARAL	São Francisco River, Brazil. Satellite altimetry and in situ gauges were compared for 16 locations.	1. Ice-1. 2. Envisat: ∼66.8 (15.7-163.3) cm. SARAL: ∼46.9(2.2-134 cm).

1.3 Objective of this work

This thesis aims at developing methods for CryoSat-2 SAR data to improve river and lake levels obtained from altimetry. The study is a part of the LOTUS (Land and Ocean Take-Up for Sentinel-3) project. Part of the objective of the LOTUS project has been to develop new methodologies, data processing, and applications of the SAR mode data to be retrieved by Sentinel-3 over inland water. The original plan for this PhD was to develop methodologies for inland water level estimation using CryoSat-2 data obtained from the SIRAL altimeter, and then use these methods for Sentinel-3 data when they became available. However, the launch of Sentinel-3 has been postponed several times, which has made it possible to conduct a more elaborate study on the possibilities of CryoSat-2. CryoSat-2 marks the birth of a new generation of satellite altimeters, as it carries the first spaceborne delay/Doppler altimeter, which brings the along-track width of the measurement footprint down to 300 m compared to the conventional 5-10 km. Another peculiarity of the CryoSat-2 mission is the orbit repeat period of 369 days with 30 day subcycles. The charac-

teristics of the CryoSat-2 mission give rise to an entirely new set of challenges and opportunities, some of which are investigated in this thesis. Sentinel-3 was successfully launched on February 16th, 2016, from Plesetsk, Russia.

1.4 Thesis outline

Firstly, an introduction to satellite altimetry is given in Chapter 2, which is followed by a brief presentation in Chapter 3 of a number of retracking methods that are used in this thesis, while CryoSat-2 as well as other satellite missions and various datasets that have been used for the different studies undertaken during the PhD are presented in Chapter 4. Chapters 5 to 7 present different studies carried out during the PhD study, and, finally, Chapter 8 provides a brief summary of the findings and conclusions of the presented studies, as well as an outlook. Papers related to the PhD are included in the Appendix.

Chapter 2

Satellite altimetry

This chapter provides the reader with a short introduction to altimetry. Section 2.1 briefly describes the basic concept of satellite radar altimetry and gives a summary of some of the corrections that need to be applied to obtain an accurate height measurement. Different types of radar altimeters are described in Section 2.2, and the signals recorded by the altimeters are explained in Section 2.3.

2.1 Basic concept of satellite altimetry

Satellite altimetry is a technique to obtain surface heights, which are derived by estimating the distance between the altimeter and the surface below, also called the *range*. The radar altimeter measures the range by transmitting microwave pulses that are bounced back at the surface and received again by the altimeter. The time it takes the pulse to travel from the altimeter down to Earth and back again reveals the travelled distance, since the pulse travels with the speed of light. If the transit time is measured with great precision, the range from the satellite to the surface below can be measured with a precision of a few centimetres. Since the precise height of the satellite with respect to the ellipsoid, also called the *altitude*, is known from the Global Positioning System (GPS), the position of the surface below the satellite can be derived from the range. A sketch of the general concept is shown in Figure 2.1.

From the sketch it is seen, that the surface height, h, as referenced to the geoid can be written as follows:

$$h = H - r - n, \tag{2.1}$$

where H is the altitude of the satellite above the reference ellipsoid, r is the range from the satellite to the sensed surface below, and n is the height of the geoid rela-

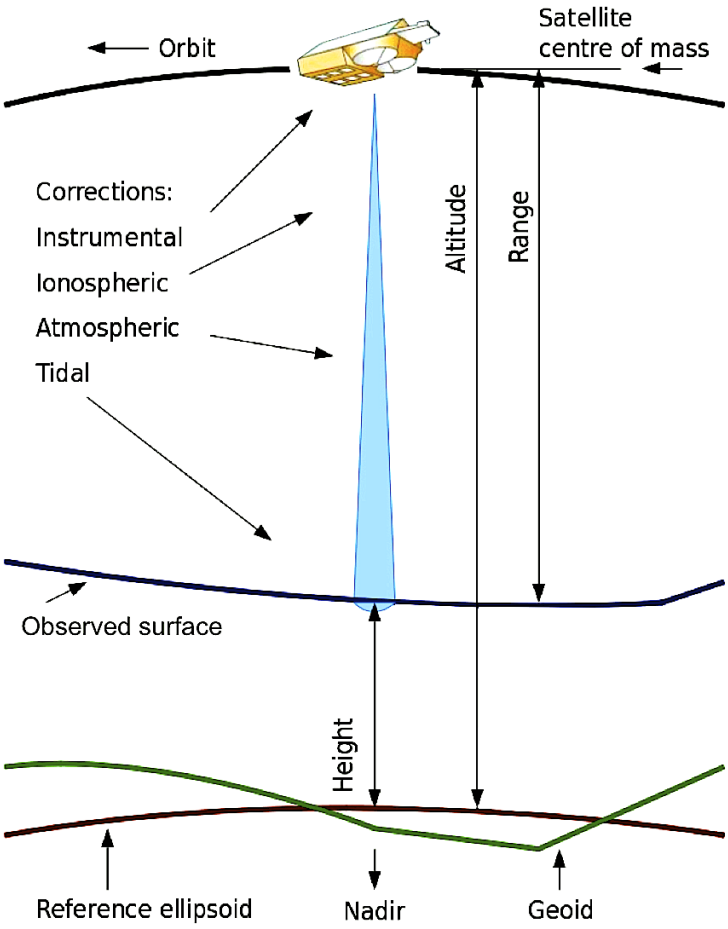

Figure 2.1: The concept of satellite altimetry. (Adapted from The CryoSat Product Handbook (*Bouzinac*, 2013).)

tive to the ellipsoid. The range is primarily derived from the two-way travel time, t, and the speed of light, c, as $\hat{r} = ct/2$, which seems deceptively simple. However, to increase the precision of the height measurement it is necessary to apply various geophysical corrections and a retracking correction. The range can then be described as follows:

$$r = \hat{r} + r_c + \sum r_g, \tag{2.2}$$

where r_c denotes the retracking correction, and $\sum r_g$ is the sum of all geophysical corrections. The retracking correction is an adjustment of the range given by the on-board tracking system, which can be several metres off. The retracking correc-

Correction	Range of correction
Dry troposphere	1.7 to 2.5 m
Wet troposphere	0 to 50 cm
Ionosphere	6 to 12 cm
Ocean loading tide	-2 to +2 cm
Solid Earth tide	-30 to +30 cm
Geocentric polar tide	-2 to 2 cm

Table 2.1: Magnitudes of the different geophysical corrections applied for inland water altimetry as listed in The CryoSat Product Handbook (*Bouzinac*, 2013).

tion depends on the shape of the return signal (called a waveform), which is described in Section 2.3, and several retracking methods are presented in Chapter 3. The total geophysical correction consists of both atmospheric corrections as well as tidal corrections. The atmospheric corrections are needed to compensate for the time delay of the pulse as it travels through the Earth's atmosphere, and the tidal corrections remove various effects of local tides caused by the Moon and the Sun. These corrections can add up to several metres and need to be taken into account. The various atmospheric and tidal corrections that are applied over inland water are briefly described in Sections 2.1.1 and 2.1.2, respectively. Of course, direct ocean tide corrections and the dynamic atmosphere correction are not applied, since lakes and rivers are closed systems (*Fernandes et al.*, 2014; *Raney and Phalippou*, 2011).

2.1.1 Atmospheric corrections

The largest correction applied to altimetry data is the *dry tropospheric correction*, which is corrects for the pulse delay caused by non-polar gases such as nitrogen and oxygen. The correction is usually of a magnitude of around 2.3 m and is obtained from meteorological models. The *wet tropospheric correction* compensates for the delay caused by polar gases such as water vapour. The wet tropospheric correction is usually between 0 and 50 cm and varies with the season. It is determined from radiometer measurements over ocean and from meteorological models over land (*Desportes et al.*, 2007).

The *ionospheric correction* accounts for the path delay caused by the free electron content in the atmosphere and mostly depends on the solar activity, meaning that it varies a lot from day to night, from season to season, and depends on the solar cycle. The ionospheric correction can be modelled, determined from dual frequency measurements, and using Doppler Orbitography and Radiopositioning Integrated by Satellite (DORIS) measurements.

In general, the atmospheric corrections over land are associated with many er-

rors, as the corrections were originally conceived for oceanographic purposes. Corrections provided from atmospheric models will be erroneous if they are provided at sea level, and when radiometers or other on-board instruments are used the obtained correction will often be contaminated by land signals except for in central parts of lakes. More about atmospheric corrections over inland water can be found in *Fernandes et al.* (2014).

2.1.2 Tidal corrections

Corrections that account for tidal effects are applied to make the range measurements appear as if they were obtained over the tide-free mean sea surface. Correcting for the *ocean loading tide* removes the effect of deformation of the Earth's crust due to the weight of overlying tides. This correction ranges from -2 to +2 cm. Another tidal correction, the *solid earth tide* correction, removes the effect of the deformation of the Earth due to lunisolar gravitation. The solid earth tide effect ranges from -30 to +30 cm. The *geocentric polar tide correction* removes the distortion of the Earth's crust due to variations in the centrifugal force as the Earth's rotational axis moves its geographic location. This correction is usually of a size between -2 and +2 cm. The ranges given here are those listed for ocean. Over land the applied corrections are much smaller.

2.2 Types of radar altimeters

In order to understand the shape of the encountered waveforms and estimate the retracking correction, one has to know how these waveforms are obtained by the altimeter. Today, there exist two different forms of altimeters - the conventional Low Resolution Mode (LRM) altimeter, and the delay/Doppler altimeter, also known as a Synthetic Aperture Radar (SAR) altimeter. The basic principle described in Section 2.1 is the same, but the way the altimeter handles the pulses depends on the mode. In addition, two SAR altimeters can be combined to obtain the SAR Interferometric mode (SARIn). The following sections will briefly describe the main concepts of each of these three modes. The waveform shapes are discussed in Section 2.3, and various retracking methods are presented in Chapter 3.

2.2.1 Low Resolution Mode (LRM)

LRM altimetry refers to the conventional pulse-limited altimetry as used by the Envisat satellite (see Section 4.1.2). LRM mode is most useful over smooth surfaces such as open ocean, since the extent of the footprint makes echoes retrieved over topographic surfaces or areas with different surface types hard to interpret, and it

can be difficult to estimate the surface elevation directly below the satellite, which is also called the *nadir* point. Some illustrations of the measurement footprints from conventional altimetry can be seen in Figure 2.2. According to *Chelton et al.* (2001), the diameter of the pulse-limited circular altimeter footprint from a pulse-limited altimeter is described as:

$$D_{PL} = 2\sqrt{2cH\tau} \quad , \quad \tau = \sqrt{\rho^2 + \frac{H_s^2}{c^2}\ln(2)}, \tag{2.3}$$

where c is the speed of light, H is the satellite altitude, and τ describes the effect of the pulse length, ρ, and the significant wave height (SWH), H_s. For an SWH of 0, the equation reduces to $D_{PL} = 2\sqrt{2cH\rho}$.

The pulse repetition frequency (PRF) of the altimeter is constrained by several factors. Of course, a high PRF would maximize the number of observations, but effective averaging requires statistical independence, which puts an upper bound on the PRF. The maximum PRF has been shown to be:

$$f^{max} = \frac{2V}{\lambda}\frac{D_{PL}}{r}, \tag{2.4}$$

where V is the spacecraft velocity and λ is the radar wavelength (*Raney and Phalippou*, 2011).

2.2.2 Synthetic Aperture Radar (SAR)

SAR altimetry was first introduced as delay/Doppler altimetry by *Raney* (1998), as a way of obtaining a smaller altimeter footprint by utilizing the effects of Doppler shift. As the satellite moves the altimeter emits bursts of pulses which are reflected at the surface and received by the altimeter. Depending on where the signal hits the surface it will have no or a high Doppler shift by the time it is received by the altimeter. By detecting the Doppler frequency the along-track origin of the reflected echo can be determined and the footprint can be divided into along-track bands. The information stored from these multiple antenna positions is then combined using several signal processing techniques (described below), and the strips laid down by successive bursts are superimposed on each other and averaged to reduce noise, making it possible to obtain waveforms retrieved from a surface area with a much smaller along-track width compared to conventional altimetry with circular altimeter footprints. As such, the SAR altimeter is pulse-limited in the across-track direction, and Doppler-limited in the along-track direction. An illustration of the Doppler beams in SAR mode altimetry is shown in Figure 2.3.

The shape of the altimeter footprints from both LRM and SAR altimeters are shown in Figure 2.2. When the studies in this thesis were completed, the only op-

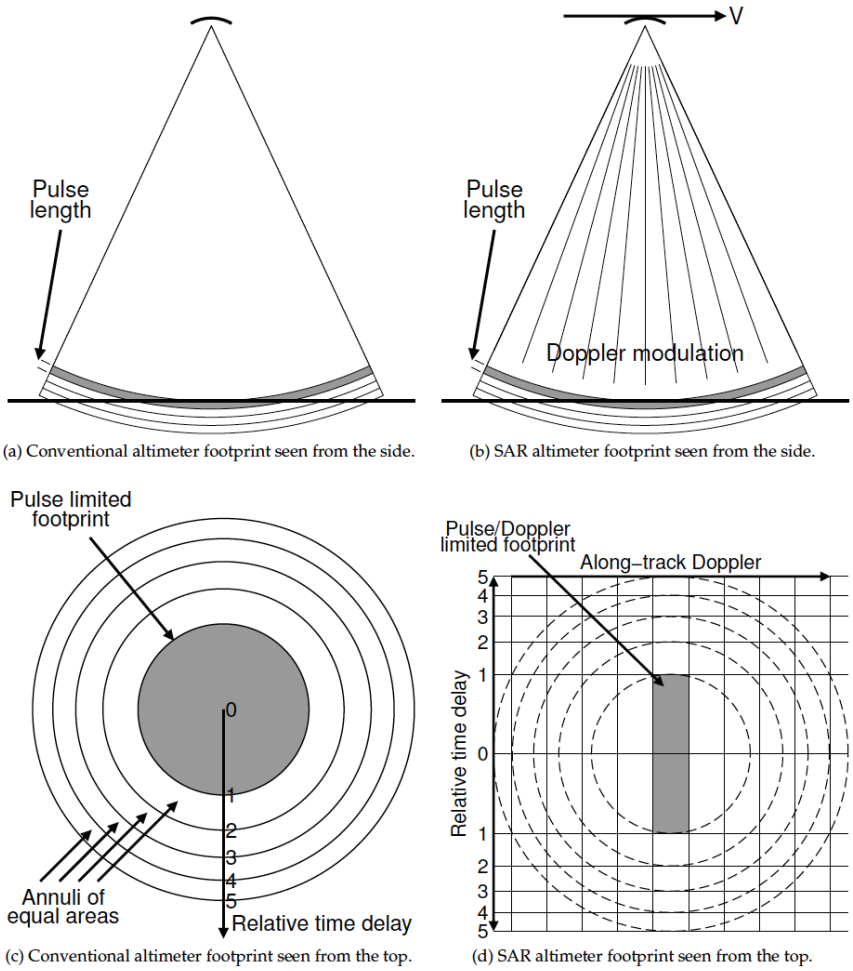

Figure 2.2: Illustrations of the different altimeter footprints of conventional LRM altimetry and Delay/Doppler SAR altimetry shown as a vertical cross-section and a top-down view. (*Raney*, 1998)

erating satellite with a SAR mode altimeter was CryoSat-2, but Sentinel-3 has been launched in February 2016, carrying an altimeter that operates in SAR mode globally, whereas CryoSat-2 only offers SAR mode data in certain regions. More about these satellite missions can be found in Chapter 4.

Delay/Doppler altimetry requires a few extra steps in order to arrive at the multi-looked waveform that characterizes this type of altimeter. These steps have been described below as according to *Dinardo, S.* (2013). For delay/Doppler altimetry, most of the signal processing is performed on the ground as opposed to conventional altimetry where the processing is carried out on board the satellite.

Step 1. As the satellite overflies the surface, the altimeter footprint is divided

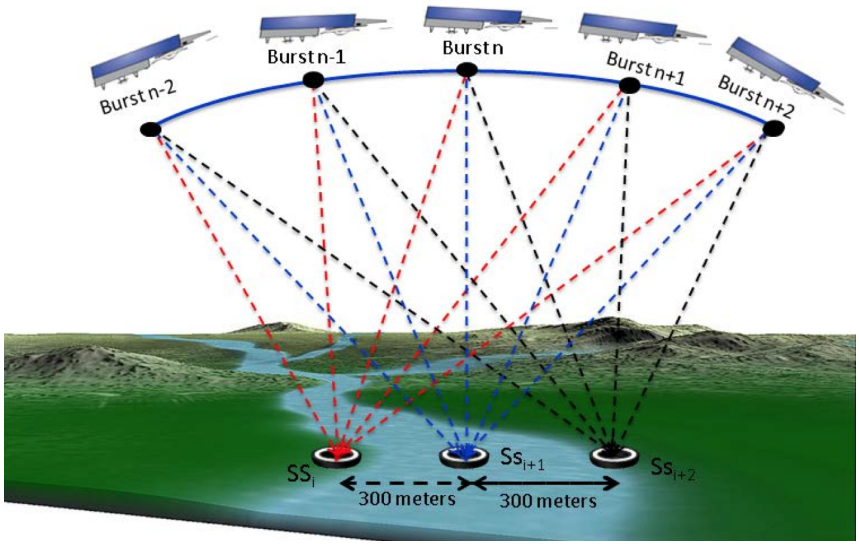

Figure 2.3: Illustration of Doppler beams in SAR mode. (*Dinardo, S.*, 2013)

into N_D ground cells in the along-track direction, which are referred to as Doppler cells. The Doppler cells have a width of approximately 300 m in the along-track direction.

Step 2. The altimeter sends out N_D pulses in bursts that are transmitted at a very high PRF (∼20 kHz). The beams can either be steered approximately or exactly to the Doppler cell locations on the surface depending on the need for precision. For approximate beam steering all Doppler beams are steered by the same angle in each burst, and only the central Doppler beam will have a footprint that coincides exactly with its corresponding Doppler cell from Step 1. However, in areas of highly variable topography the angularly equispaced beams might cause unvenly spaced projections on the ground. Exact beam steering adjusts the angles of each beams so each Doppler beam footprint will be perfectly co-located with its Doppler cell for all bursts and the Doppler cells will be equispaced.

Step 3. All the altimeter looks covering the same Doppler cell are gathered in a stack. These looks illuminate the same Doppler cells at different look angles from different burst center positions (see Figure 2.3). To align the ranges of the different beams in the stack, a slant range correction is applied to compensate for slant range migration (each beam observes the Doppler cell with a different radial distance), a tracker range correction is applied to compensate for changes in the range of the on-board tracker between each Doppler beam, and a Doppler range correction

is applied to compensate for range differences caused by the Doppler shift.

As opposed to conventional LRM altimetry where the waveforms are range compressed on board, in delay/Doppler altimetry the Doppler beams in the stack are range compressed on ground using a Fast Fourier Transform.

Step 4. The final stage involves incoherent summation in the along-track direction of the waveforms obtained in Step 3 to obtain the final multi-looking waveform. The effect of the summation of waveforms is a higher signal to noise ratio compared to LRM waveforms.

The Doppler processing used in SAR altimetry is described in more detail in *Wingham et al.* (2006) and *Dinardo, S.* (2013).

The signal processing of SAR altimetry requires a higher PRF as each ground cell must be illuminated a sufficient number of times, compared to conventional altimeters, where there only exists an upper bound for the PRF. The minimum PRF, f_{min}, for a SAR altimeter can be calculated using the Nyquist sampling theorem and is described by:

$$f_{min} = \frac{2\Delta X_{Dop} V}{r\lambda} \tag{2.5}$$

where r is the range, λ is the wavelength of the emitted pulse, V is the platform speed relative to the ground, and ΔX_{Dop} is the along-track size of the Doppler ground cells, which can be described as:

$$\Delta X_{Dop} = \frac{f_{PRF}\lambda r}{2VN_B} \tag{2.6}$$

where f_{PRF} is the PRF in Hz, and N_B is the number of pulses per burst (*Raney*, 2012). In the across-track direction the width of the footprint is described by Equation (2.3).

2.2.3 SARIn

In SARIn mode the altimeter activates a second antenna to receive the radar echo with two antennas simultaneously in order to determine the arrival angle. When the echo comes from a point that is located off-nadir there will be a difference in the travelled distance of the radar wave, which will be measured. The angle between the baseline joining the antennas and the echo direction can then be estimated using simple geometry.

So far, CryoSat-2 is the only satellite altimetry mission that is able to operate in SARIn mode. However, with the launch of SWOT (Surface Water Ocean Topography) embarking a Ka-band Radar Interferometer (KaRIn) the entire planet will be covered by SARIn altimetry as KaRIn contains two Ka-band SAR antennae. Unlike the altimeter carried by CryoSat-2, the KaRIn altimeter will point slightly off-nadir in the cross-track direction (*eoPortal*, 2015).

2.3 Waveforms and the retracking correction

The echo received by the altimeter is recorded in the *range window*. The power echo is called a *waveform*, and the shape of the waveform depends on the altimeter and the underlying surface. The retracking correction mentioned in Equation 2.2 can be determined from the waveform and greatly improves the height estimate, since the default range given by the altimeter can be off by several metres as it is just range corresponding to the centre of the range window.

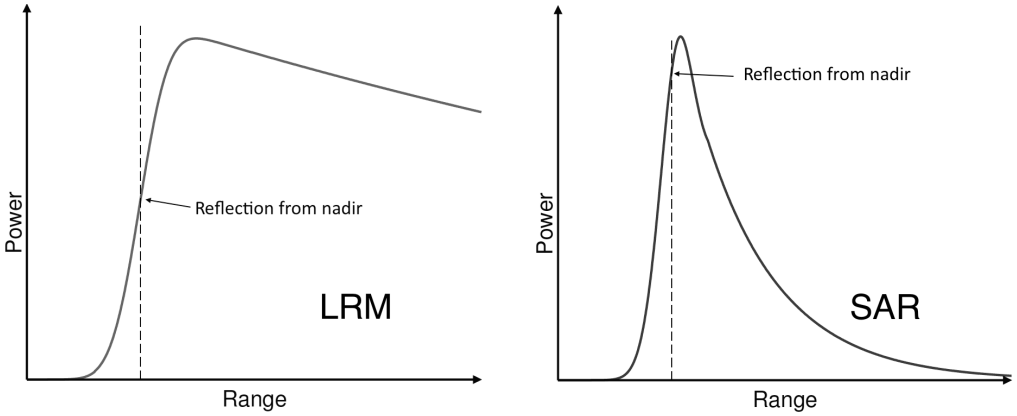

Figure 2.4: Idealized waveforms as retrieved by conventional (LRM) and delay/Doppler (SAR) altimeters. (*Stenseng*, 2011)

Waveforms retrieved over open ocean have a very recognizable shape, and waveforms with this particular shape are therefore mostly referred to as "ocean-like". The ocean-like waveform features a steep rise called the "leading edge" up to a maximum value, which is followed by the "trailing edge". The leading edge corresponds to the reflections coming from the time when the pulse first hits the surface, while the trailing edge consists of reflections coming from annuli situated further away from nadir (*Brown*, 1977). Idealized ocean waveforms for LRM as well as SAR type altimeters are shown in Figure 2.4, where it is seen that both the leading and trailing edges of the SAR waveform are much steeper than those of the LRM waveform. The dashed lines correspond to the points of reflection from the surface at nadir in these idealized cases.

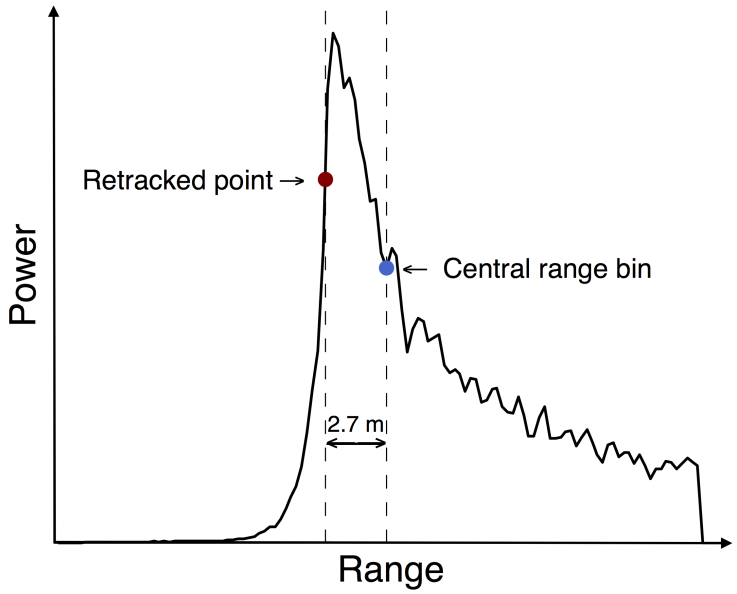

Figure 2.5: Example of SAR mode CryoSat-2 waveform showing the central range bin and the retracking point.

An accurate height estimate is obtained by *retracking* the waveform - i.e. by finding the point on the waveform that corresponds to the reflection from nadir, which can be difficult when dealing with complex waveforms. An example of a waveform obtained by CryoSat-2 is shown in Figure 2.5. The retracking correction, r_c, is then determined as the range difference between the nominal range bin and the bin found from retracking. The difference between the assumed height and that obtained from retracking is 2.7 m in the shown example. Several retracking methods are described in Chapter 3. However, heights are not the only valuable information that can be obtained from the power echoes, and some other parameters are described in the following section.

2.3.1 Parameters derived from waveform shape

Several parameters can be determined from the echo shape, and they all tell us something about the surface sensed below. A selection of these parameters are described below.

Backscattering
The backscatter, also called sigma naught (σ_0), is derived from the power of the received waveforms and can provide valuable information about the wind speed and the dynamics of the surface properties depending on the sensed surface. The backscatter has long been known to depend on wind speed (*Quartly et al.*, 1996)

and it has since been demonstrated, that the backscatter coefficient also follows soil moisture, vegetation, and sea ice properties (*Frappart et al.*, 2015). The backscatter coefficient is given in dB and generally ranges between 0 and 100.

Peakiness
The pulse peakiness is a measure of how "peaky" the echo is - i.e. how concentrated the reflected power is within the range window. It is defined as the ratio between the maximum power and the sum of all the received power. The pulse peakiness was first defined by *Laxon* (1994) for the use of sea ice mapping. For a waveform, P, with N bins, the pulse peakiness, PP, is given as:

$$PP = \frac{max(P)}{\sum_{i=1}^{N} P_i}, \tag{2.7}$$

where P_i is the power of the ith bin in the waveform, and N is the total number of bins. The peakiness defined here therefore ranges between 0 and 1. A high peakiness is obtained for very narrow waveforms, which are often retrieved over extremely smooth surfaces such as sea ice leads or small lakes. The types of surfaces that cause high peakiness values are often referred to as specular.

Significant wave height (SWH)
Another very useful parameter that can be extracted from the waveform shape is the SWH. The waves that are present on the sea surface at the time of reflection affect the waveform shape. The leading edge of the waveform is stretched out due to wave crests on the surface, causing earlier return signals than those from nadir. SWH can therefore be estimated from the slope of the leading edge.

SAR beam behaviour parameters
For SAR type waveforms additional parameters can be estimated from the stack of multilook waveforms for which the SAR waveform was obtained. To obtain these parameters, an average of each waveform in the stack is calculated, which results in one value for each look. These values are then plotted as a function of incidence angle and fitted with a Gaussian function.

Two examples of the power distribution in such stacks are shown in Figure 2.6 for a rough (left) and a smooth (right) surface. As the simulated stacks show, the power distribution is more spread out for the rough surface, which is caused by stronger reflections at high incidence angles.

The standard deviation, the skewness, and the kurtosis of a stack can be found by fitting it with a Gaussian (*Wingham et al.*, 2006). As an example, a specular surface such as shown in Figure 2.6 would result in a lower standard deviation than a rough surface. More information on the beam behaviour parameters can be found in *Wingham et al.* (2006) and the CryoSat Product Handbook (*Bouzinac*, 2013).

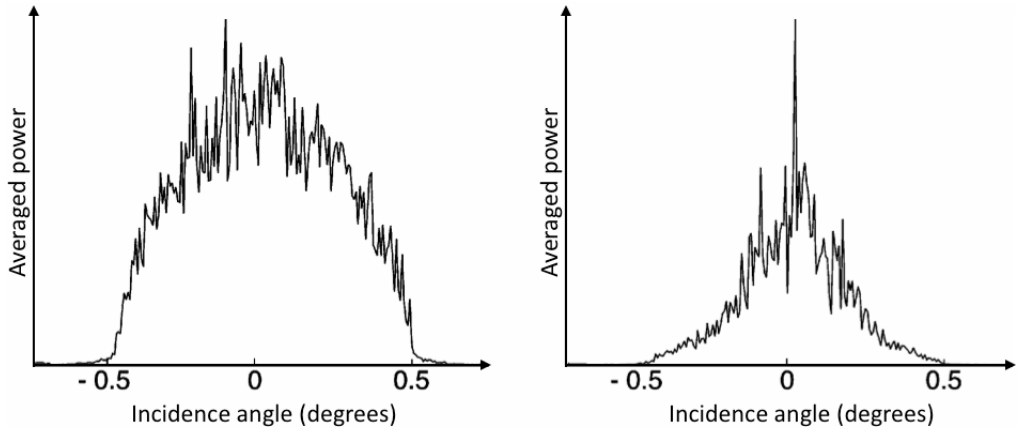

Figure 2.6: Simulated variation of averaged power in SAR mode over (left) a uniformly rough, spherical surface (such as ocean or a large lake), and (right) a surface with a highly specular object at nadir (such as a small lake). (Adapted from *Wingham et al.* (2006).)

2.4 Snagging

One of the biggest issues with satelitte altimetry over non-homogenous surfaces such as land and inland water is off-ranging, also called hooking or snagging (*Armitage and Davidson*, 2014; *Fetterer et al.*, 2013). Snagging and hooking occurs when the on-board tracking system is dominated by specular surfaces that are located off-nadir and lead to incorrect height estimates. Here, "hooking" will refer to the effect of waveform contamination due to bright targets in front of or behind the nadir position, while snagging will refer to bright targets to the side.

Hooking occurs when a bright target leads to a parabolic profile in the waveforms as the satellite flies over the specular surface. The parabolic shape appears because the radar pulse propagates with a circular wavefront, and the target enters and leaves the altimeter footprint (*Gomez-Enri et al.*, 2010; *Quartly*, 2010). The hyperbolas caused by the hooking effect are only visible in LRM, where the large, circular footprint allows for off-ranging in both the along- and across-track directions. The hooking effect can be corrected for by fitting curves to the along-track hyperbolas, even over rivers (*da Silva et al.*, 2010; *Maillard et al.*, 2015; *Schwatke et al.*, 2015a).

For SAR altimetry hooking issues are negligible due to the smaller measurement footprint, which is achieved by the Doppler processing and has an along-track size of $\sim$300 m. Only across-track snagging will cause these range errors, and as such, there are no hyperbolic curves that can be identified, fitted, and subsequently removed. Figure 2.7 shows an example of how snagging occurs in SAR altimetry for a ground track located on Lake Vänern in Sweden. As seen, the nearby shore, which is parallel to the ground track, causes a lot of jumps in the height profile with height

estimates that are 10 m lower than the surrounding lake level. The positive effect of the higher across-track resolution on snagging occurances in SAR altimetry was also shown in *Thibaut et al.* (2014), where they investigated coastal waveforms. In general, the SAR altimeter waveforms will be much more affected by land signals if the track lies parrallel to the coastline compared to a perpendicular target angle due to the dimensions of the altimeter footprint.

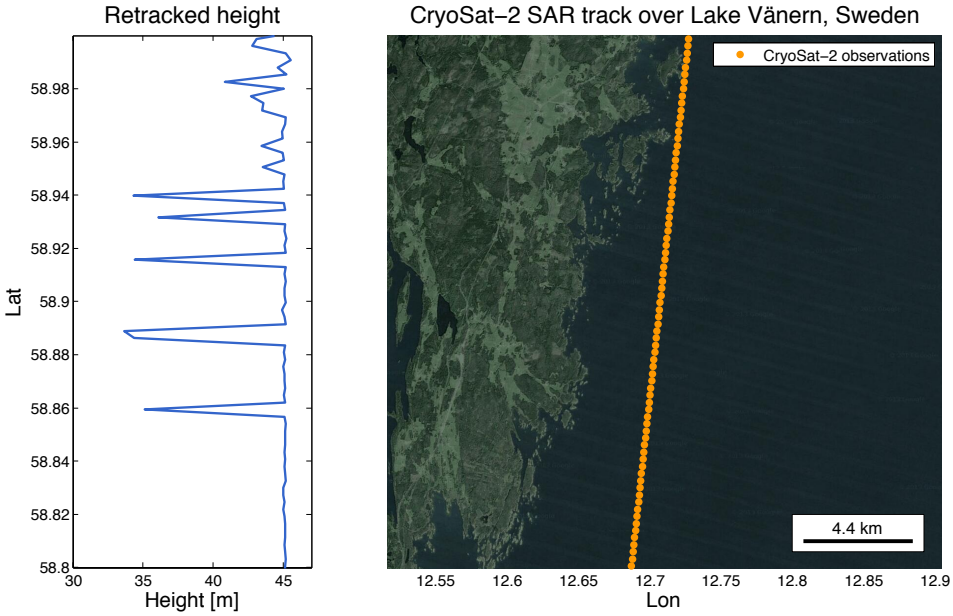

Figure 2.7: Track location and retracked heights obtained from a descending CryoSat-2 SAR track crossing Lake Vänern in Sweden on October 31st, 2011.

2.4.1 Correcting for snagging effects with SARIn data

SARIn is unique as it offers a solution to the before mentioned snagging problem, since it becomes possible to pinpoint the origin of the received echo. By knowing the origin of the reflection it is possible to correct for the range error. This correction was described by *Armitage and Davidson* (2014), where the goal was to correct for the elevation error that occurred during off-ranging over sea ice, as leads were dominating the received power echoes. The range correction that needs to be applied due to off-nadir ranging is estimated by using the phase difference between the two antennas. This is done by estimating the across-track angle between a highly reflective target, such as a small inland water body, at M and the nadir point at S. An illustration of the problem is shown in Figure 2.8.

The phase difference, ϕ, between the two echoes can be described as follows:

$$\theta \simeq \frac{\phi}{k_0 B}, \tag{2.8}$$

where k_0 is the carrier wavenumber, B is the interferometer baseline length (the distance between the two antennas). As the satellite platform is rarely parallel to the surface, the baseline roll angle, χ, is subtracted from the obtained angle, θ, to derive the angle, ρ, between the local vertical and the direction of the bright target.

$$\rho = \theta - \chi \tag{2.9}$$

The across-track distance, d, to the lead can then be determined as:

$$d = r_m \sin(\rho) \simeq r_m \rho, \tag{2.10}$$

where r_m is the measured range from the satellite to the bright target. The range error caused by the off-nadir ranging is given by:

$$dh_\rho \simeq \eta r_m \frac{\rho^2}{2}. \tag{2.11}$$

The total range error, dh, can therefore be described by:

$$dh = dh_\rho - dh_\alpha \simeq \frac{\eta r_m}{2} \rho^2, \tag{2.12}$$

and the corrected range, r, is obtained by subtracting the corresponding range error, dh_ρ:

$$r = r_m - dh \simeq r_m - \frac{\eta r_m}{2} (\rho^2 - 2\rho\alpha), \tag{2.13}$$

where η is a geometric factor used to correct for the curvature of the Earth. The effect of an across-track surface slope can be estimated in a similar manner, but this has not been done for the studies presented in this thesis.

The capabilities of SARIn altimetry allows us to see the actual origin of the retracked reflection. Figure 2.9 shows the corrected position of the retracked SARIn echoes above a tributary of the Brahmaputra River. The corrected coordinates reveal how the altimeter tracks the specular reflections caused by a small river. In SAR mode the obtained range would mistakenly be assumed to be the range between the satellite and nadir, when in fact the range could be a measure of the distance to a completely different location more than 10 km off-nadir.

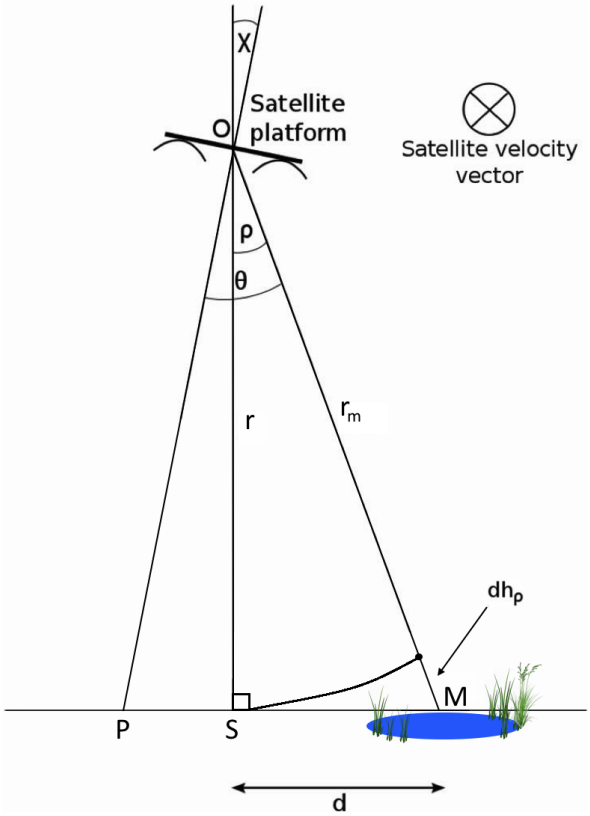

Figure 2.8: Geometry of the SARIn range correction. (Adapted from *Armitage and Davidson* (2014).)

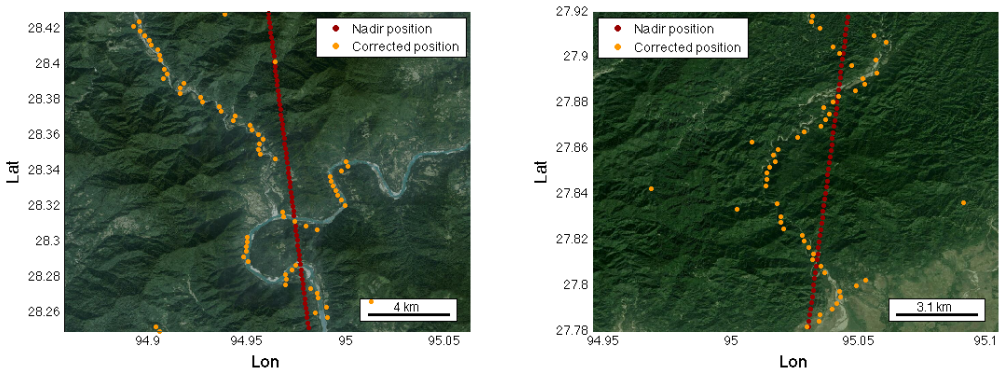

Figure 2.9: Examples of SARIn tracks over some tributaries of the Brahmaputra River before and after the applied range correction.

Chapter 3

Retracking methods

When determining the surface height at nadir, the final range estimate is achieved by adding a retracking correction, which is the difference between the nominal range bin and the retracked point on the waveform. To estimate the retracking point on the waveform, two types of retrackers can be used: physical and empirical.

This chapter briefly describes a number of such retrackers. Some of these are used in this thesis, and some are described as they are part of the derivation of the implemented retrackers.

3.1 Physical retrackers

Physical retrackers are based on analytical formulations, or models. Over open ocean, physical retrackers provide valuable information about not only range, but also SWH and wind speed, and they are often preferred due to their high accuracy and precision. Examples of downfalls of the physical retrackers include long computation times and an inability to fit waveforms that deviate from the modelled return signal. Up until the launch of CryoSat-2, physical retrackers only existed for ocean-like waveforms. Now, a number of models are available for sea ice covered regions where more specular waveforms are obtained (*Jain*, 2015; *Kurtz et al.*, 2014).

3.1.1 Brown

The Brown model (*Brown*, 1977) describes the signal received by a conventional altimeter, assuming that the underlying surface is open ocean, i.e. without any signals coming from other surface types such as land or sea ice. The Brown model describes the detected waveform, $W(t)$, as a convolution of three terms:

$$W(t) = P_{FS} * q_s(t) * s_r(t) \tag{3.1}$$

where $P_{FS}(t)$ is the average flat surface impulse response, $q_s(t)$ is related to the surface elevation probability density of the scattering points, and $s_r(t)$ is the radar system point-target response. The three terms are described in detail in *Brown* (1977) and *Hayne* (1980). The Brown model is fitted to the observed waveforms using Maximum Likelihood Estimators (MLE), which lead to the retrackers MLE3 and MLE4 (*Thibaut et al.*, 2010). MLE3 estimates the three parameters range, significant wave height, and power, whereas the MLE4 algorithm estimates four parameters (the three previous ones and the slope of the waveform trailing edge).

3.1.2 SAMOSA3

With the introduction of delay/Doppler altimeters, the Brown model was no longer applicable due to the smaller along-track width of the measurement footprint, and a new model had to be described. This gave rise to the SAMOSA (SAR Altimetry Mode Studies and Applications) project, which was initiated in 2007. The objective of the SAMOSA project was to investigate the improvements offered by SAR mode altimetry over ocean, coastal and inland water areas, and to develop practical implementation of new theoretical models for the SAR echo waveforms. The project consortium consisted of several international teams from SatOC (Satellite OCeanographic Consultants Ltd, UK), DMU (De Montfort University, UK), Starlab (ES), NOCS (National Oceanography Centre, UK), and DTU (Technical University of Denmark, DK).

The SAMOSA model is based on the Brown model but takes into account the effects of the multi-looking capabilities used in SAR mode. Within the project, three theoretical models were described. The first model, SAMOSA1, assumed Gaussian ocean wave statistics and a circular antenna pattern, and included the effect of Earth curvature and antenna mispointing in the along-track direction only. In the second model, SAMOSA2, non-Gaussian ocean wave statistics were included, as well as Earth curvature and a better representation of mispointing effects both along- and across-track. The model also included radial velocity effects and an elliptical antenna pattern. As a consequence of the changes made to obtain SAMOSA2, the model became semi-analytical. For efficiency purposes some expressions were therefore truncated to arrive at the fully-analytical physically-based SAMOSA3 model, which only includes Gaussian ocean wave statistics. In this thesis, the SAMOSA3 model as presented in *Dinardo et al.* (2013) will be used, since this is the version of the model that has been selected for the operational processing chain of the Sentinel-3 mission. In addition to *Dinardo et al.* (2013), information on the general concepts of the SAMOSA model as well as details about the previous and current versions can be found in *Martin-Puig et al.* (2008a), *Martin-Puig et al.* (2008b)

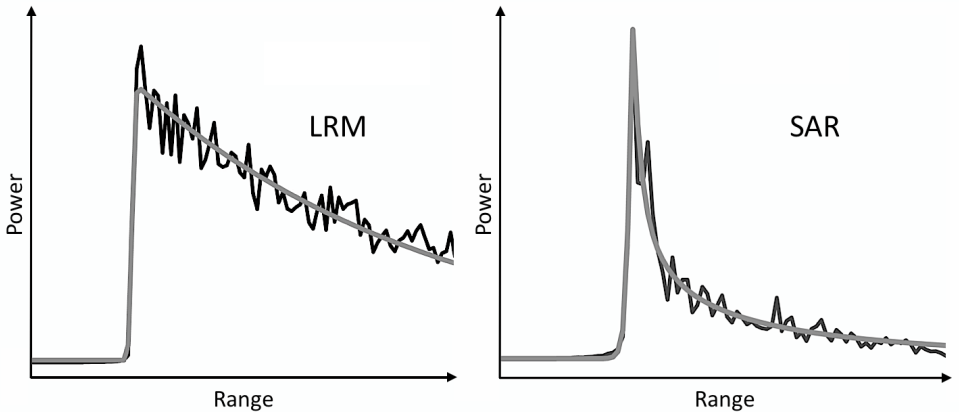

Figure 3.1: Typical ocean type waveforms from conventional altimetry (left) and SAR mode altimetry (right) along with Brown and SAMOSA model fits, respectively. (Adapted from *Gommenginger et al.* (2013).)

and *Ray et al.* (2015).

The approach used to define the theoretical SAMOSA models was similar to that of *Brown* (1977) and *Hayne* (1980). A comparison of a conventional LRM and a SAR waveforms as well as the Brown and SAMOSA3 model fits are shown in Figure 3.1.

SAMOSA3 consists of a single-look model and a multi-look model, which are used to estimate the retracking position (and thereby the surface height), SWH, the mean-square slope, and the amplitude corresponding to a SAR waveform. The single-look model is the base of the SAMOSA3 model and computes a series of waveforms for different look angles. The single-look waveforms are created using the theoretical model for a given set of geophysical input parameters and a specified input Doppler frequency. All the single-look waveforms are then stacked and averaged to obtain the final multi-looked SAR waveform. The mathematics of the respective models are described in the following. For easy reference, the constants, parameters, and variables used to describe the waveform models are listed in Table 3.1.

3.1.2.1 Single-look model

The analytical expression of the SAMOSA3 single-look model is given by:

$$W_{k,l} = P_u \sqrt{(g_l)} \Gamma_{k,l}(0) e^{-\frac{1}{4}(g_l k)^1/2} \begin{cases} \sqrt{-g_l k} K_{\frac{1}{4}}(\frac{1}{4}(g_l k)^2), & \text{if } g_l k < 0 \\ \frac{\pi}{\sqrt{2}} \sqrt{g_l k} \left(I_{-\frac{1}{4}}(\frac{1}{4}(g_l k)^2) + I_{\frac{1}{4}}(\frac{1}{4}(g_l k)^2) \right), & \text{if } g_l k > 0 \end{cases} \tag{3.2}$$

where k is the range bin number relative to the retracking point, l is the Doppler

frequency index, P_u is a variable that accounts for all multiplicative factors, g_l and $\Gamma_{k,l}$ are defined below, and I and K are modified Bessel functions of the first and second kind, respectively.

Here, g_l is defined as:

$$g_l = \frac{1}{\sqrt{\alpha_p^2 + 4\alpha_p^2 \left(\frac{L_x}{L_y}\right)^4 l^2 + \left(\frac{H_s}{4L_z}\right)^2}} \tag{3.3}$$

where α_p is a factor resulting from the mathematical approximation of the point target response of the Delay/Doppler altimeter, and H_s is the SWH. α_p is well-described in literature and for this implementation $\alpha_p = 0.513$ as given in *Amarouche et al.* (2004) is used. L_x, L_y, and L_z are calculated from the system parameters:

$$L_x = \frac{cH}{2Vf_cT_b} \quad , \quad L_y = \sqrt{\frac{cH}{\alpha B_r}} \quad , \quad L_z = \frac{c}{2B_r} \tag{3.4}$$

where c is the speed of light, H is the satellite altitude, V is spacecraft velocity, f_c is the central frequency, T_b is the burst length, α is the Earth curvature effect, and B_r is the received bandwidth. L_x and L_y are the along-track and across-track resolutions on the ground, respectively, and L_z is the range resolution.

Γ is also calculated from the system parameters:

$$\Gamma_{k,l}(0) = exp\left(-\alpha_y\gamma_p^2 - \alpha_x(x_l - x_p)^2 - \frac{x_l^2 v}{H^2} - \left(\alpha_y + \frac{v}{H^2}\right) y_k^2\right) \cosh(2\alpha_y y_p y_k) \tag{3.5}$$

where x_p and y_p are respectively the along- and across-track location of the centre of the beam on the surface. Γ_0 is then determined by using the relationships defined below, where MSS refers to the mean square slope, which is a fitted parameter within the SAMOSA3 model.

$$x_l = L_x l \quad , \quad y_k = \begin{cases} L_y\sqrt{k} & \text{if } k > 0 \\ 0 & \text{otherwise} \end{cases} \quad , \quad x_p = H\theta_{\text{pitch}} \quad , \quad y_p = -H\theta_{\text{roll}} \tag{3.6}$$

$$\alpha_x = sh_x \frac{8ln(2)}{H^2\theta_x^2} \quad , \quad \alpha_y = sh_y \frac{8ln(2)}{H^2\theta_y^2} \quad , \quad v = \frac{1}{\text{MSS}} \tag{3.7}$$

3.1.2.2 Multi-look model

The multi-look model takes the sum over all the effective single-look modelled waveforms for the current ground cell location. First, the Doppler frequency for each angle, ϕ, in the beam stack is calculated using:

$$f_{Dop}(n) = \frac{2V_s}{\lambda_0}\cos(\phi(n)) \quad \text{for } 1 \leq n \leq N_{eff}, \tag{3.8}$$

and the adimensional Doppler frequency index l is calculated as:

$$l = \frac{f_{Dop}(n)}{PRF/N_B}. \tag{3.9}$$

Finally, the modelled multi-looked waveform to which the observed waveform is fitted is given as the sum of the single-look waveforms from all effective look angles:

$$W_{ML}(k) = \sum_{n=1}^{N_{\text{eff}}} W_{k,l}(k,l). \tag{3.10}$$

3.1.2.3 SAMOSA3 adaptation for specular waveforms

A version adapted for specular waveforms has also been used (see *Jain et al.* (2014) and *Jain* (2015) for details). This adaptation was originally developed for lead type waveforms, but since waveforms received over leads resemble those of calm inland water, the modified version has been included in this thesis. In the adapted mode, the significant wave height is set to zero, and the leading and trailing edges are able to fit the narrow shape of a specular waveform. Figure 3.2 shows the ability of the standard SAMOSA3 ocean model (reffered to as SAMOSA-O from now on), and of the adapted lead mode (referred to as SAMOSA-L). The figure clearly shows how the model within the SAMOSA-L retracker is able to fit both the ocean-like and specular waveforms.

3.2 Empirical retrackers

An empirical retracker can be used without making any assumptions about the surface below the satellite. In comparison to physical retrackers it is therefore possible to obtain a height estimate without time-consuming algorithms, and independently of the surface type. Unfortunately, empirical retrackers are not as accurate, and they

Symbol	Explanation	Units
c	Speed of light	[m/s]
a	Equatorial radius	[m]
b	Polar radius	[m]
f_c	Central frequency	[Hz]
B_r	Received bandwidth	[Hz]
θ_x	Along-track 3dB beamwidth	[rad]
θ_y	Across-track 3dB beamwidth	[rad]
θ_{pitch}	Pitch angle	[rad]
θ_{roll}	Roll angle	[rad]
h_{rate}	Spacecraft altitude rate	[m/s]
θ_{plat}	Ground cell latitude	[rad]
α	Earth curvature effect, $\alpha = 1 + H/R_e$	-
H	Satellite altitude	[m]
R_e	Earth radius	[m]
v	Inverse of MSS, $v = 1/MSS$	[rad^{-2}]

Table 3.1: Constants, parameters, and variables related to the SAMOSA3 model.

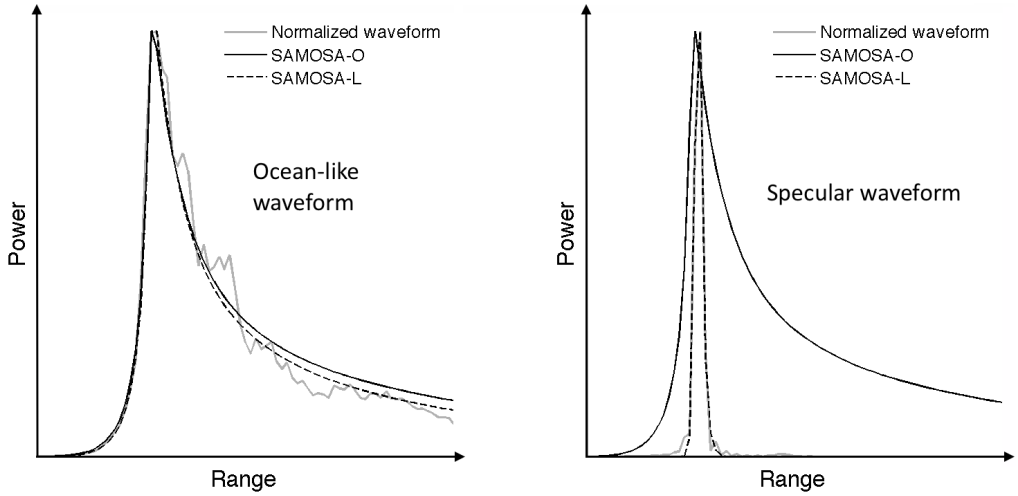

Figure 3.2: Comparison of fits obtained from the standard version of the SAMOSA3 model, SAMOSA-O, and the version adapted for specular waveforms, SAMOSA-L, for an ocean-like waveform (left) and a specular waveform (right).

do not provide direct estimates of other physical parameters such as SWH. This section briefly describes the empirical retrackers used in this thesis, which are all based on the waveform statistics.

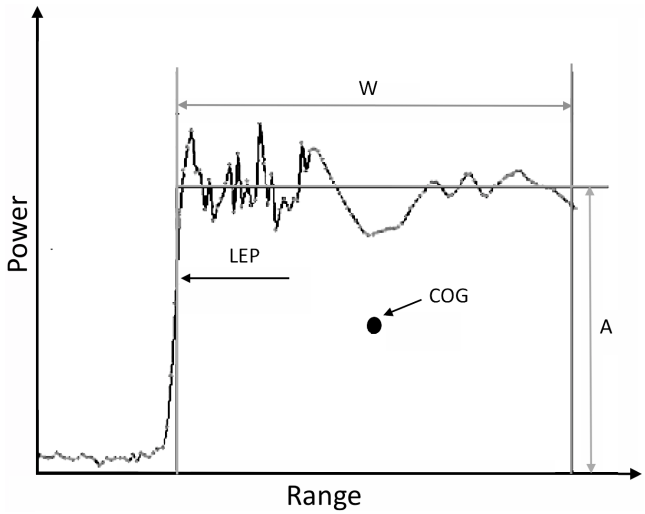

Figure 3.3: Illustration of the different parameters estimated by the OCOG retracker for an LRM waveform. (Adapted from *Gommenginger et al.* (2011), originally presented by *Wingham et al.* (1986).)

3.2.1 Offset centre of gravity retracker (OCOG)

The algorithm for the offset centre of gravity (OCOG) retracker was developed by *Wingham et al.* (1986). It is a completely statistical approach that does not assume any functional form of the retrieved echo as compared to the physical retrackers described above. The retracker finds the centre of gravity (COG), amplitude (A), and width (W) of the waveform before estimating the leading edge point (LEP), i.e. the retracking point.

$$A = \sqrt{\frac{\sum_{i=5}^{N-5} P_i^4(t)}{\sum_{i=5}^{N-5} P_i^2(t)}}, \tag{3.11}$$

$$W = \frac{(\sum_{i=5}^{N-5} P_i^2(t))^2}{\sum_{i=5}^{N-5} P_i^4(t)} \tag{3.12}$$

$$COG = \frac{\sum_{i=5}^{N-5} i P_i^2(t)}{\sum_{i=5}^{N-5} P_i^2(t)} \tag{3.13}$$

In the equations above, P_i is the waveform power, and N is the total number of samples in the waveform. Finally, the LEP is given by:

$$LEP = COG - \frac{W}{2} \tag{3.14}$$

The benefits of the OCOG retracker is that it is easy to implement, provides stable results, and that it only depends on the statistics of the waveforms. This retracker forms the basis for the algorithm behind the ICE-1 retracker used for the Envisat RA-2 altimeter introduced later in Section 4.1.2.

3.2.2 Threshold Retracker

Davis (1995, 1997) developed the threshold retracker to improve the range estimate compared to the results obtained with the method described above. The threshold retracker uses the amplitude estimated by the OCOG method in Equation 3.11 to compute a threshold value. The threshold choice depends on the underlying surface and the altimeter mode. Waveforms obtained over surfaces such as ocean and ice-sheets, have a trailing edge that decays slower than for surface scattering surfaces such as sea ice and inland water. The suggested thresholds for LRM waveforms are 10-20% for waveforms dominated by volume scattering, and 50% for those dominated by surface scattering. For SAR waveforms these thresholds should be higher, and *Stenseng* (2011) suggest using 80% for ice leads, a surface type that leads to radar echoes similar to those obtained over smaller lakes and rivers.

The threshold retracker consists of a few steps. First, the thermal noise, P_N is calculated as the mean power of the first five bins:

$$P_N = \frac{1}{5}\sum_{i=1}^{5} P(i) \tag{3.15}$$

Then the threshold level is computed, using the desired threshold level, q (e.g. 50%):

$$T_h = P_N + q(A - P_N) \tag{3.16}$$

The decimal range bin where the waveform exceeds the threshold power level is then determined using linear interpolation between bins k and $k-1$, where the waveform power level is slightly higher and slightly lower than T_h, respectively. The retracking point, G_r is determined as:

$$G_r = k - 1 + \frac{T_h - P_{k-1}}{P_k - P_{k-1}} \tag{3.17}$$

where P_k is the received power in the kth bin. G_r is then used to calculate the retracking correction.

3.2.3 Improved Threshold Retracker

For complex waveforms with several leading edges it is necessary to determine the subwaveform that corresponds to the reflection from nadir. The method presented here does so without using external information, and is very similar to the empirical retracker used throughout this thesis. This will be explained in greater detail in Section 3.2.4.

Subwaveforms are determined by locating leading edges and trailing edges based on only the statistics within the waveform itself as presented in *Bao et al.* (2009); *Lee et al.* (2008). A leading edge is detected if the power increase between two gates is higher than a threshold value ϵ_1, and the corresponding trailing edge is marked as the bin when the power difference between two gates is smaller than the threshold value ϵ_2. The values of ϵ_1 and ϵ_2 are determined by following the steps described below.

First, the power difference between neighbouring bins, d_1^i, and the mean power difference between every other bin, d_2^i, are calculated:

$$d_1^i = P_{i+1} - P_i \tag{3.18}$$

$$d_2^i = \frac{1}{2}(P_{i+2} - P_i) \tag{3.19}$$

The threshold values for the leading and trailing edges are then defined as $\epsilon_1 = 0.2S$ and $\epsilon_2 = 0.2S_1$, where S is the standard deviation of all power differences for a bin separation of 1, given by:

$$S = \sqrt{\frac{(N-2)\sum_{i=1}^{N-2}(d_2^i)^2 - \left(\sum_{i=1}^{N-2} d_2^i\right)^2}{(N-2)(N-3)}} \tag{3.20}$$

where N is the number of bins in the waveform. Similarly, S_1 is the standard deviation of all power differences for neighbouring bins:

$$S_1 = \sqrt{\frac{(N-1)\sum_{i=1}^{N-1}(d_1^i)^2 - \left(\sum_{i=1}^{N-1} d_1^i\right)^2}{(N-1)(N-2)}} \tag{3.21}$$

Using the method described above, several leading edges can be detected in the waveform depending on its complexity. Choosing the subwaveform that corresponds to the reflection from nadir can be done in several ways. Some require external information, while others do not. When the subwaveform of interest has been selected, the retracking point is determined from the OCOG amplitude, A, in the same way as for the threshold retracker using Eqs. 3.15 to 3.17, but this time the amplitude is calculated only for the subwaveform.

3.2.4 The narrow primary peak (NPPR) retracker

The retracking algorithm chosen for this study is almost identical to the improved threshold retracker presented in the previous section. The different steps in the retracking routine are:

1. Bins 1:5 and N-5:N are set to zero.
2. Thermal noise is defined as the average power in bins 6:15 and is removed from the waveform.
3. Negative values are set to zero.
4. The leading and trailing edge points, k_l and k_t, are detected using the improved threshold retracking method, where $\epsilon_1 = 0.4S$ and $\epsilon_2 = 0.1S_1$. An additional requirement is that the detected LEP is at least 25% of the maximim value of the waveform.
5. The subwaveform belonging to the primary peak is defined as the power echo within the range $k_l - 2 : k_t + 2$. A couple of bins have to be added on each side of the waveform due to the specular characteristics of the SAR altimeter waveforms (see *Jain et al.* (2015)) as well as the nature of the waveforms over inland water.
6. The OCOG amplitude is calculated for the subwaveform, and the threshold is set to 31.3% for LRM and 80% for SAR and SARIn waveforms. The 80% threshold was chosen due to previous studies such as *Stenseng* (2011), and the LRM threshold percentage was chosen based on an early study of Lake Onega, Russia, where the altimeter switches from LRM to SAR mode. This allowed for a comparison of the estimated water levels, and the chosen threshold of 31.3% ensured a smooth transition and thereby a stable water level.
7. Finally, the algorithm finds the decimal range bin where the waveform exceeds the threshold using linear interpolation between the two adjacent bins.

3.3 The Multiple Waveform Persistent Peak (MWaPP) retracker

This section describes the MWaPP method, which has been developed as a part of this PhD study and submitted for publication in Journal of Hydrology (Villadsen et al., 2015b).

Bright targets are one of the biggest challenges for inland water altimetry, especially in conventional altimetry, where snagging occurs due to highly reflective surfaces far away from nadir in both the across- and along-track directions. So far, no retracking methods have been developed with the purpose of obtaining more stable water levels over lakes and rivers. For this reason, the following section will mention some previous studies done over coastal zones, as coastal altimetry and inland water altimetry have much in common.

In the coastal zone, there has long been a need for another approach to handle complex waveforms, and several methods have been developed to minimize the effect of snagging in the coastal zone in order to obtain a more stable sea surface height estimate closer to the coast. Some of the methods proposed for coastal altimetry follow an iterative approach, where each waveform is first retracked individually followed by an assumption that the sea surface height or SWH should be fairly constant along the track. This is what was done by *Sandwell and Smith* (2005), who applied a two-pass iterative approach to ERS-1 data assuming that the sea surface roughness varies smoothly along the track to retrieve stable sea surface heights for gravity field recovery. A similar two-pass approach was presented in *Passaro et al.* (2014), where the ALES retracker uses SWH estimates from the first iteration to define subwaveforms that are subsequently retracked using the Brown model. Another option is to retrack multiple waveforms at once, such as done in *Maus et al.* (1998), where they aligned a sequence of waveforms simultaneously and assumed that geophysical variables (SWH, wind speed) are constant, and that the variation in sea surface height undulations can be described by a polynomial with 41 unknowns. This successfully improved the along-track resolution of the ocean-geoid from 41 km to 31 km. *Thibaut et al.* (2014) improved height estimates in coastal regions by reducing the analysis window when retracking CryoSat-2 SAR waveforms. This reduction excluded most of the contamination from land signals and allowed for obtaining a better height estimate. In conventional altimetry, snagging occurrences have also been mapped by identifying hyperbolic patterns in successive waveforms, as the bright target enters and leaves the antenna footprint (*Powell et al.*, 1993; *Quartly*, 1998; *Tournadre et al.*, 2008).

All the methods mentioned above were developed for waveforms retrieved over ocean with conventional altimeters, whereas this study focuses on SAR altimetry over inland water, which changes the rules immensely. Therefore, the approach presented in this chapter is very simple and does not involve hyperbola detection or any assumptions about geophysical parameters such as SWH and wind speed,

as these methods are no longer applicable or appropriate. The proposed algorithm was kept simple in order to avoid making too many assumptions about the water body. The only assumption that is made, is that neighbouring observations should give approximately the same height estimations over the water surface, as this can be assumed to be constant over small distances. The MWaPP retracker looks at adjacent waveforms in order to determine the best subwaveform for retracking. In this way it is possible to identify persistent peaks, which are expected to represent the underlying water body of interest. Looking at neighbouring waveforms can help alleviate snagging issues, where a waveform is dominated by reflections from points off-nadir. The method presented here does not average waveforms, but simply tries to determine the bins in the waveform where the reflection from the water surface at nadir is most likely found. The proposed retracking method consists of the following steps:

Step 1. For each waveform the heights corresponding to all 128 bins are determined according to Equation 2.1. This yields $N_w \times N$ height estimates, where N_w is the number of waveforms in the track and N is the number of bins in each waveform. Thus, a height is estimated for each k=1:128 and p=1:N_w for CryoSat-2 SAR mode waveforms.

$$h^{all}(p,k) = H(p) - \hat{r}(p) + w_b(k_0 - k) - \sum r_g(p) - n(p), \tag{3.22}$$

where H is the satellite altitude, $\hat{r}$ is the range to the nominal range bin, w_b is the bin width (0.2342 m for CryoSat-2 SAR mode waveforms), k_0 is the nominal range bin number, $\sum r_g$ is the sum of the applied geophysical corrections, and n is the geoid correction.

Step 2. The surface height span of all waveforms for each track (within the water body) is determined as min(h^{all}):max(h^{all}) and the waveforms are oversampled to 1 cm height intervals using linear interpolation to derive the interpolated waveforms W_p^{int}. This allows for aligning the waveforms with respect to the obtained surface height instead of bin number.

Step 3. For each W_p^{int}, the sum of the current and the four nearest waveforms is calculated. Since the height of the water body at nadir should be the same for all observations, a summation of waveforms is not dominated by off-nadir echoes and can be used to determine the subwaveform, which holds the nadir reflection.

$$W_p^{sum} = \sum_{\max(p-2,1)}^{\min(p+2,N_w)} W_p^{int} \tag{3.23}$$

Step 4. For each of these summed waveforms, W_p^{sum}, the first peak that exceeds 20% of the maximum power is flagged. This is assumed to represent the water level common to all five waveforms.

Step 5. For each original waveform the peak closest to the flagged peak from the previous step is found, and a subwaveform consisting of the three previous and following bins around this peak is extracted.

Step 6. The OCOG amplitude (see Section 3.2.1) is then calculated for the extracted subwaveform, which consists of N bins of which all but 7 are zero. The point where the subwaveform exceeds 80% of the amplitude is marked as the retracking point.

To increase the computational efficiency for large water bodies or mountainous areas, the algorithm should be rewritten so the height estimation and interpolation steps are done in batches instead of interpolating over all heights covered by the entire track crossing the lake/river. However, as the study areas used for this thesis were of a modest size and without too much topography this was concluded to be unnecessary.

To illustrate the benefits of the MWaPP retracker, some intermediate results for an ascending track crossing Lake Okeechobee in Florida December 29th, 2010, are shown in Figure 3.4.

The map in Figure 3.4(a) shows the location of a specific waveform and highlights the adjacent waveforms, which are located within 2 km of the coast. As seen from the retracked heights in Figure 3.4(b), the standard NPPR retracker fails to determine the leading edge of the nadir reflection and instead retracks the echo coming from an off-nadir bright target located near the coast. By using the MWaPP algorithm, the obtained water level is much more stable. Figure 3.4(c) shows how the leading edges of the lake surface reflection are not aligned when the waveforms are referenced to bin number. But when oversampled waveforms are referenced to surface height, as shown in Figure 3.4(d), a persistent leading edge appears around a height of 4-5 m and the correct subwaveform can be extracted.

A more thorough study of the MWaPP method is presented in Chapter 6.

3.4 Switching between retrackers

For some studies it might be advantageous to combine retrackers, as not all retrackers are appropriate for all waveforms. When this is done, one has to decide when to use which retracker, and how to deal with the bias that is introduced due to different offsets of the retracking methods.

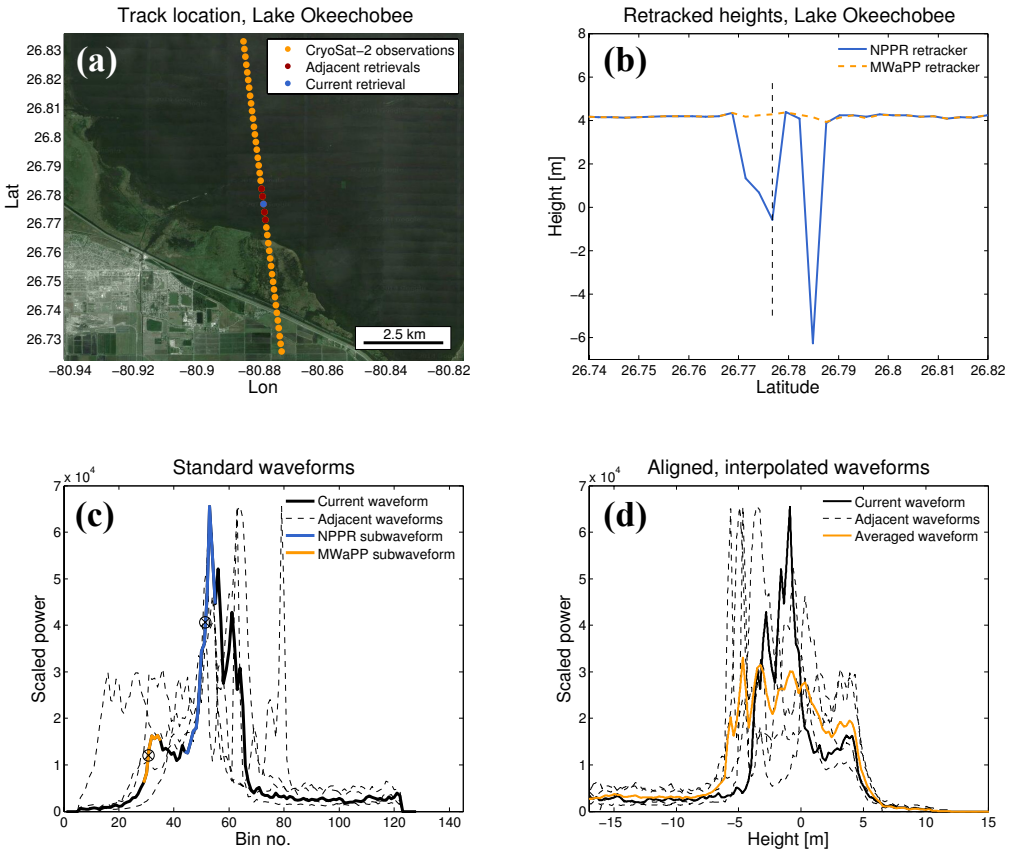

Figure 3.4: Illustration of the MWaPP method and the results for an ascending track over Lake Okeechobee in Florida, December 29th, 2010. **(a)** Part of the track with the current observation (blue) and its adjacent points (red) highlighted, **(b)** the retracked heights obtained from both the NPPR retracker (blue) and the proposed MWaPP retracker (yellow), **(c)** the current (solid) and the four adjacent (dashed) waveforms along with the subwaveforms and retracking points obtained with the NPPR retracker (blue) and the proposed MWaPP retracker (yellow), and **(d)** the aligned and oversampled current (solid), adjacent (dashed), and averaged waveforms (yellow).

Assigning a retracker to each waveform is most easily done using classification, which can be based on the waveform shape, or on various parameters related to the waveform, such as peakiness or backscatter.

Regarding the bias between retrackers, most of the retrackers presented in this chapter are of the empirical kind where the user has to define a threshold level. Of course, the true absolute water level can only be obtained by choosing the perfect threshold, which is not practically possible, as it will depend on the characteristics of the underlying surface and antenna aperture. As a result, all of the retrackers presented above will have different offsets. To obtain a smooth transition between

retrackers one has to minimize the introduced bias, which can be done in several ways.

Chapter 7 deals with the combination of the physical SAMOSA3 model and empirical retrackers and will go into the issues mentioned above in more detail.

Chapter 4

Datasets

This chapter briefly describes the datasets mentioned in this thesis – both altimetric datasets, water masks, and digital elevation models (DEMs). The chapter is meant to serve as a reference for the coming chapters, where the datasets are used for different studies.

4.1 Altimetric datasets

The initial objective of the thesis was to prepare for the Sentinel-3 mission using CryoSat-2 data, *and* to implement these methods once data from Sentinel-3 became available. However, since the Sentinel-3 mission was postponed multiple times during this PhD study and was finally launched in February 2016, it has only been possible to study the SAR data acquired by CryoSat-2. As such, CryoSat-2 will take up most space in this chapter, followed by missions that have been used for comparisons, finally, a brief overview of the Sentinel-3 mission will be given. A comparison of various specifications is included in Table 4.1 and a comparison of the ground tracks for the different missions can be found in Figure 4.1.

4.1.1 CryoSat-2

CryoSat-2 was launched by the European Space Agency (ESA) on the 8*th* of April 2010 to monitor variations in the cryosphere, i.e. the marine ice cover and continental ice sheets. The primary objective of the mission is to test the prediction that Arctic sea ice is thinning due to global warming and to determine to which extent the Antarctic and Greenland ice sheets are contributing to global sea level rise. As these are the only objectives of the mission, the selection of the satellite orbit and

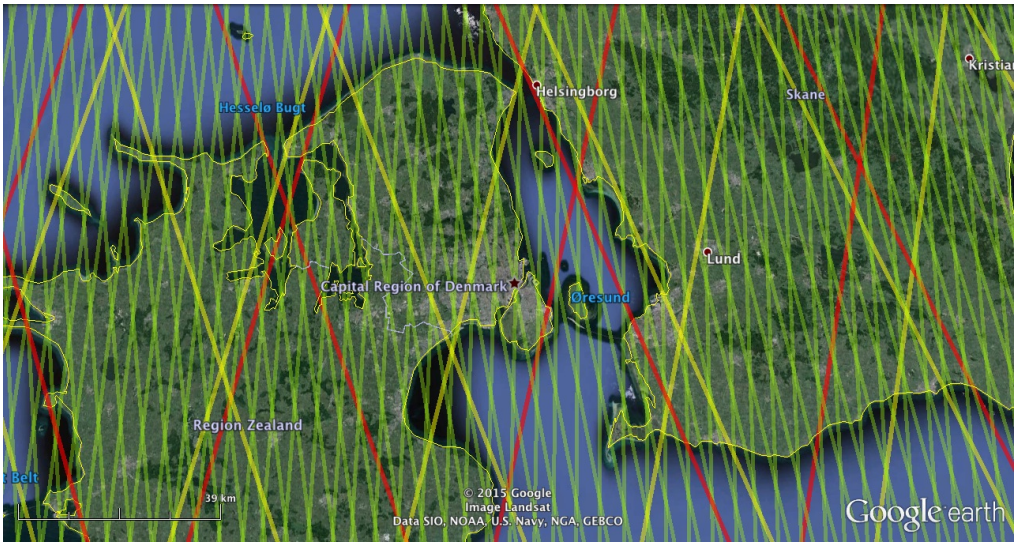

Figure 4.1: Comparison of ground tracks over Denmark/Sweden for CryoSat-2 (green), Envisat and SARAL/AltiKa (yellow), and Sentinel-3 (red).

basic characteristics were based entirely on their scientific requirements. Therefore, the CryoSat-2 orbit has an unusually high inclination of 92°, allowing it to measure at latitudes as high as 88° N/S. The orbit has a repeat period of 369 days with underlying subcycles of 30 days to increase the spatial coverage. The drifting, polar CryoSat-2 orbit is therefore very different from previous satellite missions. To determine position of the satellite as accurately as possible, CryoSat-2 carries both a DORIS radio receiver and a small laser retroreflector, and the orientation of the baseline is measured with three star trackers.

CryoSat-2's primary payload is the SAR/Interferometric Radar Altimeter (SIRAL), which operates at Ku-band at 13.575 GHz, with a pulse bandwidth of 320 Mhz, and has an antenna footprint with a diameter of 15 km. SIRAL is a state of the art altimeter with the ability to operate in three different measurement modes depending on a geographical mode mask (*Wingham et al.*, 2006). The mode mask determines when and where the different altimeter modes are employed by the altimeter, and the current version is shown in Figure 4.2. The mode mask divides the Earth's surface into zones, which are to be measured in either LRM, SAR or SARIn mode. The geographical mode mask can be updated on request, and it also changes monthly to account for seasonal changes in sea-ice extent. The location accuracy of a mode switch on a satellite track is 30 km, and the break in data continuity between switches of measurement modes is 700 m (*Wingham et al.*, 2006). A brief description of the different modes of SIRAL and where they are used is described in the following:

Mission specifications				
	CryoSat-2 (SIRAL)	**Envisat (RA-2)**	**SARAL/AltiKa**	**Sentinel-3 (SRAL)**
Mission length	April 2010 -	March 2002 - April 2012	February 2013	February 2016
Frequency	13.575 GHz (Ku)	13.575 GHz (Ku)	35.75 GHz (Ka)	13.575 GHz (Ku)
Bandwidth	320 MHz	320 MHz	520 MHz	320 MHz
Footprint radius	7.7 km	7.6 km	5.7 km	7.1 km
Footprint area	185.1 km^2 (4.9 km^2 for SAR)	181.4 km^2	100.8 km^2	5 km^2
Altitude	717 km	790 km	800 km	815 km
Inclination	92°	98.4°	98.55°	98.5°
Latitudinal limit	88°	81.5°	81.5°	81.5°
Repeat period	369 (30) days	35 days	35 days	27 days

Table 4.1: Satellite and altimeter specifications for different missions. Altimeter footprint dimensions were found in *Thibaut et al.* (2012) and *Andersen et al.* (2014).

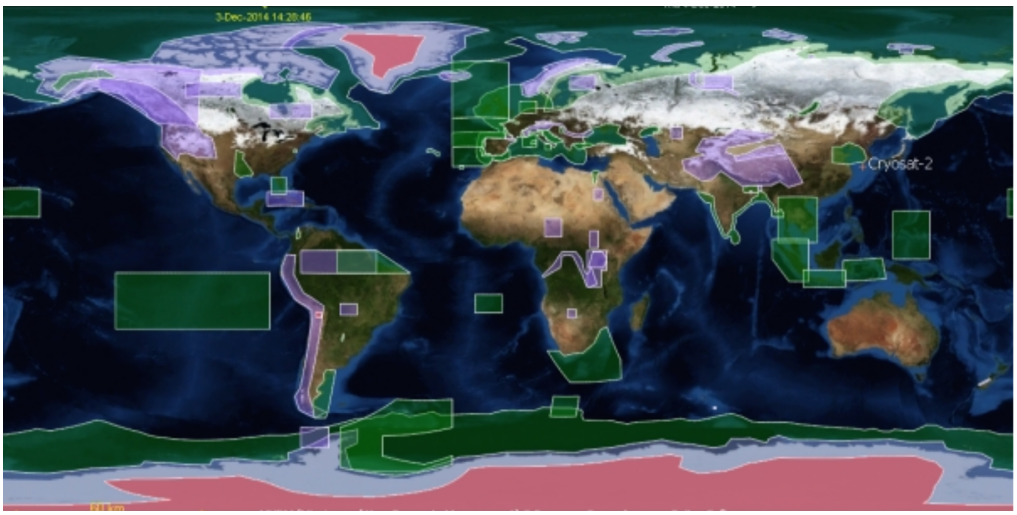

Figure 4.2: CryoSat-2 geographical mode mask v. 3.6. SAR and SARIn mode regions are marked with green and purple polygons, respectively.

LRM: Over the oceans and ice sheet interiors, CryoSat-2 operates like a conventional radar altimeter in low resolution mode. The LRM waveforms are averaged over the entire antenna footprint, they have 128 range bins with a sample size of 0.4684 m. In LRM mode, the altimeter has a PRF of around 2 kHz.

SAR: Over sea ice and coastal areas, coherently transmitted echoes are combined via SAR processing to reduce the along-track surface footprint so that CryoSat-2 can map varying surface types more satisfactory using the along-track resolution of $\sim$ 300 m. The SAR capabilities of CryoSat-2 ensure an altimeter footprint area far smaller than for conventional altimetry. SAR waveforms from CryoSat-2 have 128 range bins with a width of 0.2342 m. In SAR mode, the altimeter has a PRF of approximately 18 kHz.

SARIn: The most advanced mode of SIRAL is used in areas with high surface slopes, and is as such used mostly over mountainous regions and the margins of the ice sheets. When in SARIn mode, the altimeter has an extended sampling window (120 m compared to 30 m for SAR), which decreases the chances of the altimeter losing lock. The SARIn waveforms have 512 bins with the same range bin width as SAR, and the along-track resolution is also $\sim$ 300 m. However, the cost of using two antennas is a degraded accuracy due to a lowered burst mode PRF.

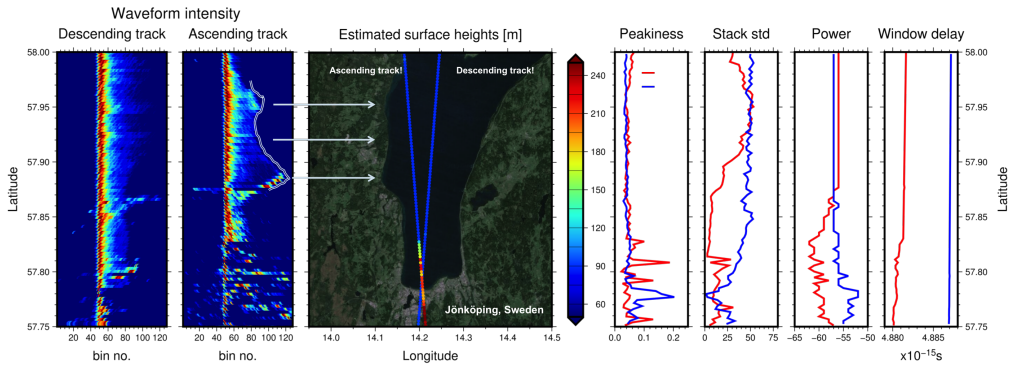

Figure 4.3: Comparison of heights obtained for an ascending and a descending track crossing Lake Vättern in Sweden. The difference between the ascending and descending track heights reveal how the altimeter sometimes loses lock of the surface over topographic areas.

The SIRAL altimeter was designed for smooth ice sheets, not varying topography. Therefore, it has been seen that the altimeter sometimes "loses lock" of the surface. When this happens the altimeter does not receive the reflection from the

surface, because the timings of the reception window and the return of reflected signal do not match. An example of how the altimeter fails to track the surface is shown in Figure 4.3, where both an ascending and a descending track over Lake Vättern in Sweden are shown. The tracks shown here are in LRM mode, where the explored range window is around 60 m, but the example is comparable to what would happen in SAR mode, where the range window spans 30 m. The southern boundary of the lake near Jönköping is characterized by steep topography, and when the satellite crosses the lake during ascending flight, the surface elevation changes too quickly for the altimeter to see it within its 30 m range window. The altimeter therefore overestimates the height of the lake for several kilometres. The opposite thing happens when the satellite approaches Jönköping during descending flight, and the surface elevation of the city of Jönköping is underestimated. For this reason, the range window of the SIRAL altimeter has been increased to 120 m when operating in SARIn mode, as this mode is intended for regions with topographic challenges.

It is worth noticing how the pulse transmission occurs depending on altimeter mode, and the different chronograms of SIRAL are shown in Figure 4.4. While in LRM, the altimeter works in open-burst mode with a PRF of only 2 kHz, where the transmitted and received pulses are interleaved. The open-burst mode is used on all conventional missions, where the upper bound on PRF is defined by Equation 2.4. In SAR mode, however, where there is a constraint on the *lower* bound of the PRF, the altimeter works in a closed-burst mode where the transmission of a bursts of 64 pulses takes 3.5 ms. The interval between each burst is 11.8 ms, allowing time for transmission and successive reception, which means that the altimeter is only gathering information about the ground 30% of the time. 70% of the time, the altimeter therefore misses an opportunity to make measurements. Effectively, this means that the precision of SAR waveforms is not as high as it could be, as they are averaged over fewer looks than possible. *Raney* (2012) showed that it would be possible to achieve SAR measurements in open-burst/interleaved mode with a PRF of around 9 kHz, which will be done with the launch of Jason-CS/Sentinel-6. More about the CryoSat-2 burst modes can be found in *Raney* (2012) and *Gommenginger et al.* (2013).

The CryoSat-2 data used in this thesis are from the Baseline-B Level 1B (L1B) and Level 2 (L2) ESA products and were retracked using the NPPR method described in Section 3.2.4 unless otherwise stated.

4.1.2 Envisat

The Envisat mission was launched on March 1st, 2002, by ESA. Its main objective was to continue the altimetric observations that started with the ERS-1 satellite in 1991. Envisat remained on its nominal orbit until October 2010, and provided data

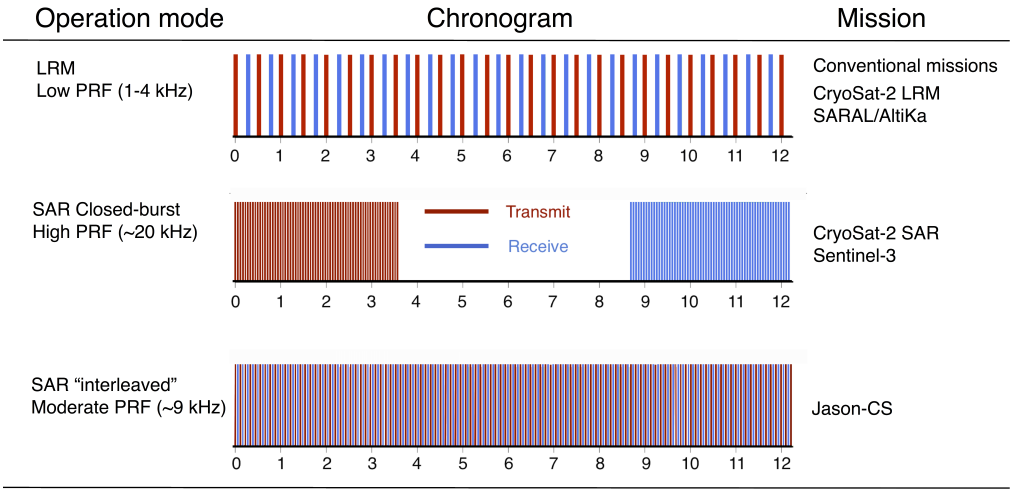

Figure 4.4: Burst modes for various missions.

until all communication with the satellite was lost in April 2012.

The science objectives of Envisat included contributing to the study of changes on interannual to decadal time scales of global and regional sea level and of dynamic ocean circulation patterns.

Envisat carried the conventional radar altimeter, RA-2. RA-2 was a nadir-pointing Ku-band altimeter operating at 13.575 GHz and provided continuous LRM data between 81.5° N/S in a 35-day repeat period until October 2010. In November 2010 the so-called "Envisat extension orbit" was implemented, which introduced a minor drift in the orbit and a new repeat cycle of 30 days. More information about the Envisat mission can be found in the *ENVISAT RA2/MWR Product Handbook (2007)*.

The Envisat data used for this study have been processed using the ICE-1 retracker. The ICE-1 retracker has previously been found to be the Envisat retracker that compares best to in situ measurements over inland water (*Cheng et al.*, 2009; *da Silva et al.*, 2010; *Frappart et al.*, 2006). Previous studies using Envisat data over large rivers have shown that the altimetric data is a powerful tool for obtaining river levels for hydrological purposes (*da Silva et al.*, 2010; *Frappart et al.*, 2006; *Michailovsky et al.*, 2012; *Papa et al.*, 2010). For this reason, when in situ data are not available for comparison, Envisat time series will be used instead.

4.1.3 SARAL/AltiKa

SARAL/AltiKa (Satellite for ARgos and ALtiKa) is a new collaboration between CNES (Centre National d'Études Spatiales/French Space Agency) and ISRO (In-

dian Space Research Organization), and the satellite was launched on February 25th, 2013. SARAL/AltiKa is a follow-on mission to the Envisat mission and uses the same sun-synchronous orbit with an average altitude of 790 km, an inclination of 98.54 degrees, and a repeat cycle of 35 days. AltiKa is the first altimeter to operate at Ka-band (35.75 GHz), and the altimeter is expected to provide inland water measurements significantly better than previous conventional Ku-band altimeters, as the Ka-band footprint is much smaller (about 11 km in diameter compared to 15 km for Envisat), and because the along-track sampling takes place at 40 Hz, which is twice that of Envisat and Jason-2. Using Ka-band the altimeter is rarely influenced by ionospheric effects but susceptible to disturbance caused by atmospheric water. Furthermore, the higher bandwidth of SARAL/AltiKa supports a smaller range resolution compared to Envisat and CryoSat-2 LRM. More information about the mission can be found in the *SARAL/AltiKa Products Handbook 2013*.

4.1.4 Sentinel-3

Sentinel-3 is an ESA mission and part of the Copernicus programme, which responds to the requirements for operational and near-real-time monitoring of ocean, land and ice surfaces over a period of 20 years. The mission is a constellation of two seperate satellites launched at different times separated by 180°. The first satellite, Sentinel-3A, was launched on February 16th, 2016, and the second satellite, Sentinel-3B, will be launched in the beginning of 2017. With the launch of Sentinel-3B, the repeat cycle will be the same but the SRAL coverage will be increased.

The primary purpose of Sentinel-3 is to provide ocean data for continuity of the ERS and Envisat missions, but Sentinel-3 will also provide data for land applications. The orbit is quite similar to that of Envisat and SARAL/AltiKa with similar altitude, inclination, and an orbital cycle of 27 days.

Sentinel-3 carries the SRAL (SAR Altimeter) instrument, which comprises one nadir-looking antenna, that operates in Ku-band (13.575 GHz). The altimeter can operate in both LRM and SAR mode, however, it has been decided that Sentinel-3 will stay in SAR mode everywhere due to the favourable along-track resolution of 300 m. The SRAL design includes two different tracking modes: a closed-loop mode, where the range window is determined from the previous measurements, or the open-loop mode, where the position of the range window is based on a priori knowledge of terrain altitude derived from a DEM. More information about the Sentinel-3 mission can be found in the *Sentinel-3 User Handbook (2015)*.

4.2 Water masks

This section describes the water masks used for the studies presented in this thesis. Firstly, the challenges of using water masks over rivers will be briefly addressed.

Water masks can be very inaccurate over rivers, where the requirements on resolution is high. In addition, using static water masks can introduce a lot of confusion, since channel patterns change with time due to erosion, sediment transport, and changes in water volume. When dealing with highly alluvial rivers, masking out signals using a static mask can introduce a lot of unnecessary outliers, and on the other hand wrongly remove observations retrieved over the actual water surface. To illustrate the challenges of static water masks, Figure 4.5 shows a part of the Brahmaputra River near Tezpur in Bangladesh as seen from Landsat 8. The false colour composites consist of spectral bands 2 (blue), 5 (NIR), and 7 (SWIR 2), and show the river at low water stages (November 17th-25th, 2014) and high water stages (September 6th-14th, 2013). As seen, the river pattern has changed dramatically from September 2013 to November 2014, and using a static water mask will undeniably introduce some errors.

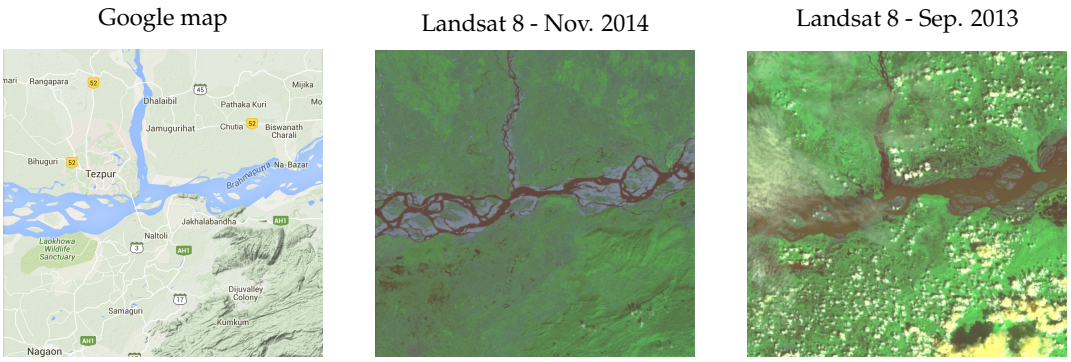

Figure 4.5: Illustration of the river pattern variability of the Brahmaputra River near Tezpur in Bangladesh. The figure includes a google map (left), a false colour composite from Landsat 8 during low flow season (middle), and during high flow season (right).

Due to the challenges of using static water masks, the ability to identify inland waters directly from waveform shape would be very beneficial for inland water altimetry. With the introduction of SAR, a smaller waveform footprint sparked new hope for the possibility of classifying inland water waveforms, which was therefore investigated for this study. However, finding common characteristics for return signals from inland water bodies has proven to be very challenging, since the characteristics of a water body are not always the same, and a classification method that works in one region might not work in another. As such, it was chosen to rely

on two different water masks for the work presented here. The two water masks are introduced below. Alternatively, dynamic masks can be created using monthly images from satellite imagery, but this was found to be outside the scope of this study.

4.2.1 MOD44w mask

This MODIS (Moderate Resolution Imaging Spectroradiometer) land-water mask is an improvement of the previous MODIS Nadir Bidirectional Reflectance Distribution Function (BRDF)-Adjusted Reflectance (NBAR) and MODIS land cover-based global land-water mask (*Salomon et al.*, 2004). The binary grid mask has a resolution of 250 m, and was interpolated onto the locations of the altimetric observations, resulting in a fraction between 0 and 100%. In the studies presented here, only observations which are classified as $\geq$99% inland water by the MODIS mask will be used.

4.2.2 GLWD mask

The water masks GLWD-1 and GLWD-2 are products from the Global Lakes and Wetlands Database (*Lehner and Doll*, 2004). The masks were derived from a variety of existing maps, data, and information by the World Wildlife Fund (WWF) and the Center for Environmental Systems Research, University of Kassel, Germany. The product is available on global scale (1:1 to 1:3 million resolution), and can be downloaded as a shapefile from the WWF website (`https://www.worldwildlife.org/pages/global-lakes-and-wetlands-database`). The Level 1 product consists of the 3067 largest lakes and the 654 largest reservoirs worldwide. Level 2 comprises permanent water bodies with surfaces areas down to 0.1 km^2, excluding the water bodies contained in GLWD-1.

4.3 Digital elevation models

4.3.1 SRTM DEM

The Shuttle Radar Topography Mission (SRTM) obtained elevation data on a near-global scale to generate the most complete high-resolution digital topographic database of Earth. SRTM consisted of a specially modified radar system carried by the Space Shuttle Endeavour during an 11-day mission in February of 2000. The SRTM payload included two antennas 60 m apart that were used to obtain SARIn data (*Nikolakopoulos et al.*, 2006).The project was directed by the National Geospatial-Intelligence Agency (NGA), NASA, the Italian Space Agency (ASI) and the German

Aerospace Center (DLR), and the result was three outputs in different resolutions. The available resolutions are: 1 km, 90 m, and 30 m (initially only over the US, but now available globally). The vertical accuracy of this dataset is said to be up to $\pm$16 m.

4.3.2 ACE2 DEM

The ACE2 Dataset has been created by merging the SRTM dataset with satellite radar altimetry between $\pm 60^{\circ}$ N/S. Over the areas lying outside the SRTMs latitude limits other sources have been used such as data from the The Global Land One-km Base Elevation (GLOBE) Project and the original ACE DEM, together with altimetry data from ERS-1 and Envisat. The ACE2 dataset is available at resolutions of 3″, 9″, 30″ and 5′, and can be downloaded from `http://tethys.eaprs.cse.dmu.ac.uk/ACE2`. For the study presented later, the 3" dataset was used, which has a resolution of around 100 m.

4.4 Gauge data

Gauge stations are usually set up by hydrologists or environmental scientists in rivers and lakes to provide hydrometric measurements such as water level, discharge, and water quality. Water levels from in situ gauges are necessary for validation of the altimetric data sets. Unfortunately, the number of gauges has decreased dramatically the last couple of decades (*Brakenridge et al.*, 2012; *Tourian*, 2013). Of course, it should be remembered, that the lack of gauges is the main reason for the increased interest in the potential of satellite altimetry for land hydrology.

This thesis focuses on SAR data, which further limits the amount of available in situ water levels, as SIRAL only operates in SAR mode over certain areas (see Figure 4.2). The studies presented in this dissertation include gauge data from Lake Vänern in Sweden, Lake Okeechobee in Florida, and a stretch of the Amazon River near Óbidos in Brazil. The data were obtained from the Swedish Meteorological and Hydrological Institute (SMHI, `http://www.smhi.se/klimatdata/hydrologi/`), the National Water Information System (NWIS, `http://waterdata.usgs.gov/nwis`), and through The Observation Service SO HYBAM website (`http://www.ore-hybam.org`), respectively.

Chapter 5

Study I: Inland water monitoring in remote and ungauged waters

This chapter includes two studies: 1) A study of time series derived from CryoSat-2 data in the Ganges-Brahmaputra River basin, which is based on the work published in Villadsen et al. (2015a) (see appendix A.2), and 2) a brief study on the ability of CryoSat-2 data to capture flooding events that occurred in Bangladesh in 2014 and in Thailand in 2011.

All studies in this chapter are done in remote areas, where obtaining in situ data from river gauges is very difficult, since they are treated as confidential by the local governments. Of course, evaluating CryoSat-2 without in situ data is not ideal, but these study regions were requested by the hydrologists participating in the LOTUS project.

5.1 River time series from CryoSat-2 in the Ganges–Brahmaputra River basin

The most important product of inland water altimetry is the time series from which it is possible to monitor the state of inland water bodies. A key concern for the CryoSat-2 orbit has been its long repeat period of 369 days, which is usually undesirable for river monitoring, as there will only be one observation every 369 days, making it impossible to capture seasonal signals at traditional virtual stations. However, by utilizing the high spatial coverage and the sub-cycle period of 30 days it might be possible to gain some information about the annual signals.

In this study time series are constructed at several virtual stations along the Ganges and Brahmaputra Rivers by relocating CryoSat-2 observations down- or upstream. The annual signals of time series obtained from CryoSat-2 are compared with those obtained from the Envisat and SARAL/AltiKa mission, which have tra-

ditional repeat periods of 35 days.

The work presented here is very similar to what was published in *Villadsen et al.* (2015a), with the exception of the added comparison with SARAL/AltiKa data in the Brahmaputra River. As mentioned in 4.1.3 the antenna footprint of SARAL/AltiKa is smaller compared to those of CryoSat-2 and Envisat due to the Ka-band altimeter. SARAL/AltiKa is therefore expected to provide increased water level stability over inland water compared to Envisat.

5.1.1 The Ganges-Brahmaputra River basin

The Ganges and Brahmaputra rivers were chosen as study regions following a request from the hydrologists in the LOTUS project, and due to the decent size of the river basin, which makes it a good base for conducting an initial validation of CryoSat-2 altimetry data. Choosing this river basin also has the benefit that the area is covered by all three CryoSat-2 SIRAL modes (LRM, SAR and SARIn; see Section 4.1.1) making an intercomparison possible.

Together, the Ganges and Brahmaputra rivers constitute one of the largest river basins in the world, and is home to around 600 million people across five Asian countries: India, Bangladesh, Nepal, China and Bhutan, which makes exchange of river gauge information complicated. The drainage basin includes some of the highest mountains in the world, the Himalayas, and is plagued by floods and droughts as well as sedimentation in the rivers and flood plains due to erosion of the steep topography surrounding the river (*Babel and Wahid*, 2011). The high rate of erosion and subsequent deposition of sediments in the river basin leads to constant changes in channel pattern and shifting of bank lines (*Sarkar*, 2012). The Ganges-Brahmaputra delta is one of the most densely populated areas in the world, and the people living here depend heavily on the state of the rivers and their tributaries. 89% of the extracted water is used for agricultural purposes, corresponding to an annual demand of around 230 billion m^3 (*Babel and Wahid*, 2011). The strong seasonal signal caused by the summer monsoon and the melting of glaciers in the Himalayas gives rise to flooding from June to October, which is followed by a much drier period in the winter months.

5.1.2 Handling of the altimetry data

Since the launch of CryoSat-2 in July 2010 the mode mask has changed over the river basins. The previous as well as the current mode masks can be seen in Figure 5.1. The current mode mask was implemented in October 2012 and introduced a region where the altimeter operates in SAR mode instead of LRM mode along the coast of Bangladesh.

All data was taken from the ESA baseline-b L1b 20 Hz data product and locations were taken directly from the L2 product processed by ESA without further corrections.

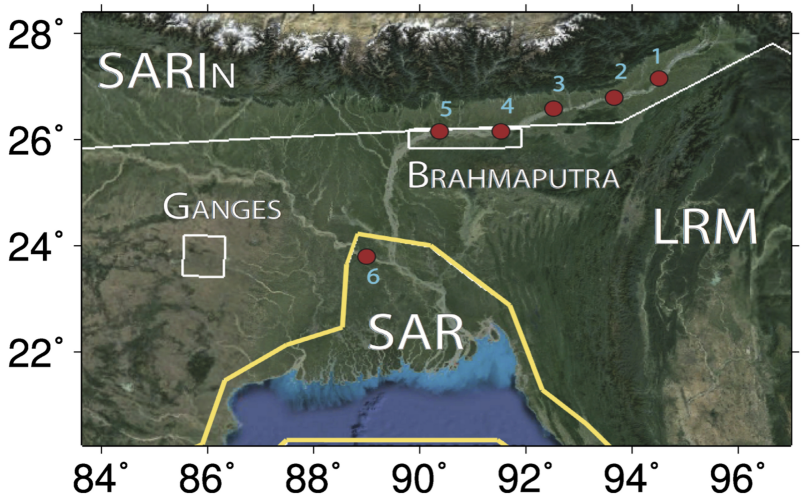

Figure 5.1: Original CryoSat-2 mode mask (white polygons) and the SAR mask which was implemented in October 2012 (yellow). Red markers indicate the locations of the virtual stations (VS1-VS6).

CryoSat-2 data were retracked using the NPPR retracker described in Section 3.2.4 with thresholds of 31.3% and 80% for LRM and SAR/SARIn waveforms, respectively, and the range and location of SARIn data were corrected as described in Section 2.4.1. Envisat and SARAL/AltiKa data had been retracked using the ICE-1 retracker, which has been found to be the most appropriate choice for Envisat over inland water, as mentioned in Section 4.1.2.

After the surface elevations were estimated, the heights measured over the Brahmaputra and Ganges rivers were extracted using the MOD44W mask described in Section 4.2.1.

The extracted 20 Hz height estimations for CryoSat-2 retrievals from the launch of the satellite in April 2010 to August 2014 are shown in Figure 5.2 relative to the geoid (EGM08). As seen, the mask captures the Ganges and Brahmaputra river basins very well south of the Himalayas. On the Tibetan plateau, no-data regions in the digital elevation model (DEM) derived from the Shuttle Radar Topography Mission (SRTM, *Farr et al.* (2007)) in the mountainous regions cause discontinuities in the MODIS mask, but river heights can still be retrieved. The discontinuities in the northern part of the Brahmaputra River can be ignored as the focus here is on the parts of the rivers south of the mountain range. The corresponding map of Envisat heights is also shown in Figure 5.2.

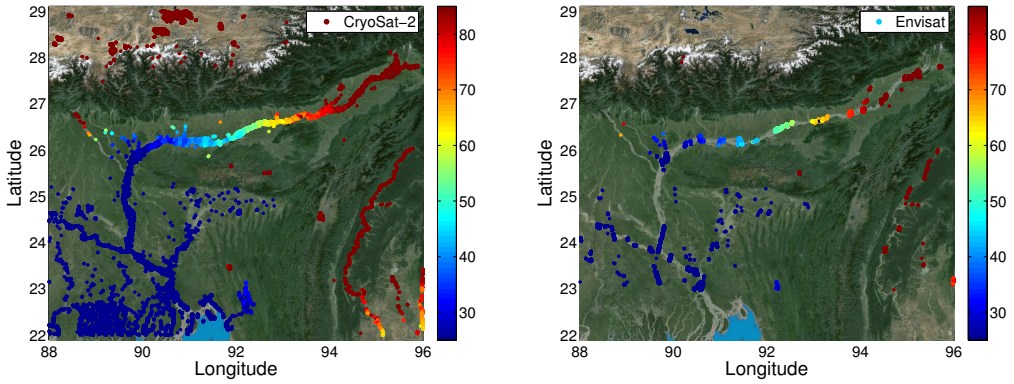

Figure 5.2: Retracked CryoSat-2 heights over the Ganges-Brahmaputra River basin from July 2010 to August 2014 for all modes (left) and Envisat heights from January 2003 to March 2012 (right).

For each river crossing, 20 Hz height estimates beyond two standard deviations of the mean were excluded to remove outliers. If less than a certain number of observations remained (six for Brahmaputra, three for Ganges) within the river crossing the track was discarded. Even after removing the worst outliers, the height estimates within each track still displayed high variation, which most likely was caused by the inability of MOD44w to accurately mask the highly dynamic and complex river channel pattern. Therefore, only the lowest three heights observations for each crossing were used to derive a mean for the time series. Including only the lowest height estimates, it is assumed that these will be those with the highest chance of being non-contaminated river retrievals. This might be untrue due to snagging issues, but none the less, this method proved to be more stable than taking the mean of all observations for each crossing.

Once a mean was derived for all crossings for both Envisat and CryoSat-2, their along river positions were determined using river centrelines derived from the SRTM DEM and provided by the LOTUS project partners at DTU Environment. To find the along-river distance for each mean, the centreline point closest to the mean position of the three observations used to derive the mean was found. In this way, the retracked heights can be represented with respect to along river distance instead of latitude/longitude. For both of the river stretches presented in this study, the along river distance was referenced to the most western point of the individual river stretch, which was defined to have an along river distance of 0.

5.1.3 Deriving time series

The special orbit of CryoSat-2 does not allow for a traditional comparison of time series due to the long repeat period. However, by taking advantage of the spatial

coverage of the sub-cycle ground track and spatially relocating the observations to a series of virtual stations (VS) time series with temporal resolutions comparable to those of Envisat and SARAL/AltiKa can be obtained. The locations of these stations were chosen arbitrarily at 90.5, 91.5, 92.5, 93.5 and 94.5°E (VS5-VS1) for the Brahmaputra and 89.3°E (VS6) for the Ganges river. In this way, river observations between 90 and 91°E will be relocated to 90.5°E, points from 91 to 92°E to 91.5°E, and so forth. To get as many observations from a satellite as possible it is preferred that the river flows in a zonal direction although this is not necessary.

The short mission overlap between Envisat and CryoSat-2 (and between CryoSat-2 and SARAL/AltiKa) introduces another challenge. As the overlapping period between the two missions is too short for a thorough analysis and has a bias towards winter data, which are more prone inaccurate height estimates caused by contaminated waveforms during low water stages, consequently, our study compares mean annual signals estimated for all available data and not only the overlapping period. The temporal and spatial distribution of CryoSat-2 data retrieved over the Brahmaputra River is seen in Figures 5.3 and 5.4.

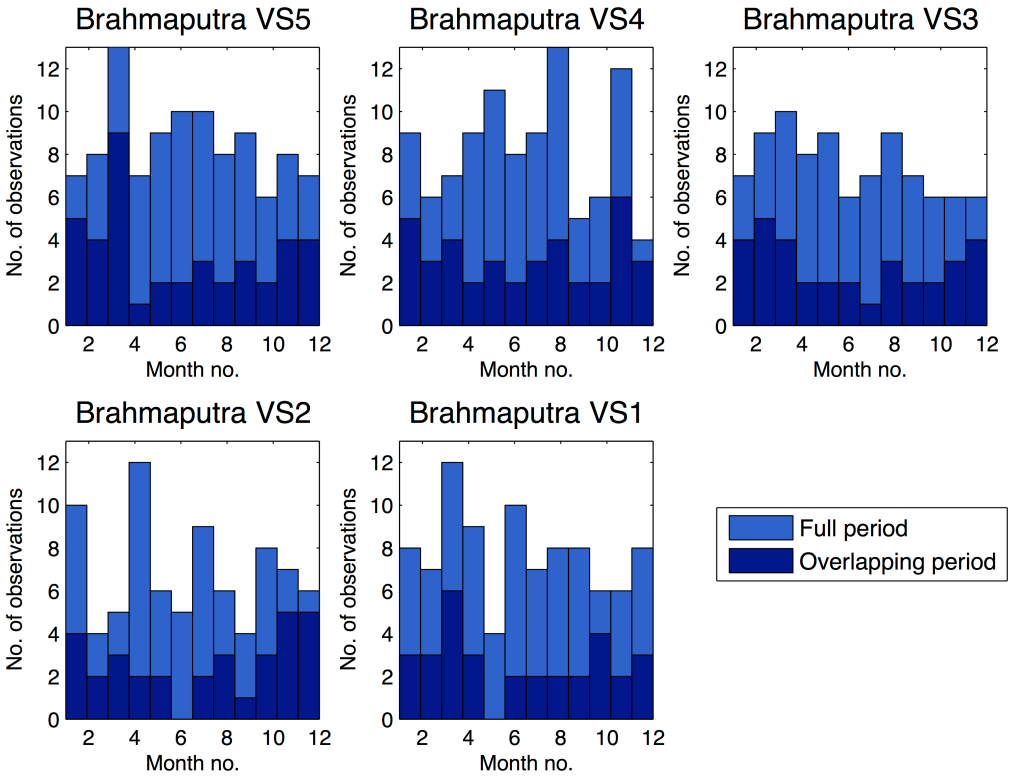

Figure 5.3: Histograms showing the temporal distribution of observations at the virtual stations in the Brahmaputra River basin.

The time series derivation in this study consists of several steps, once the data

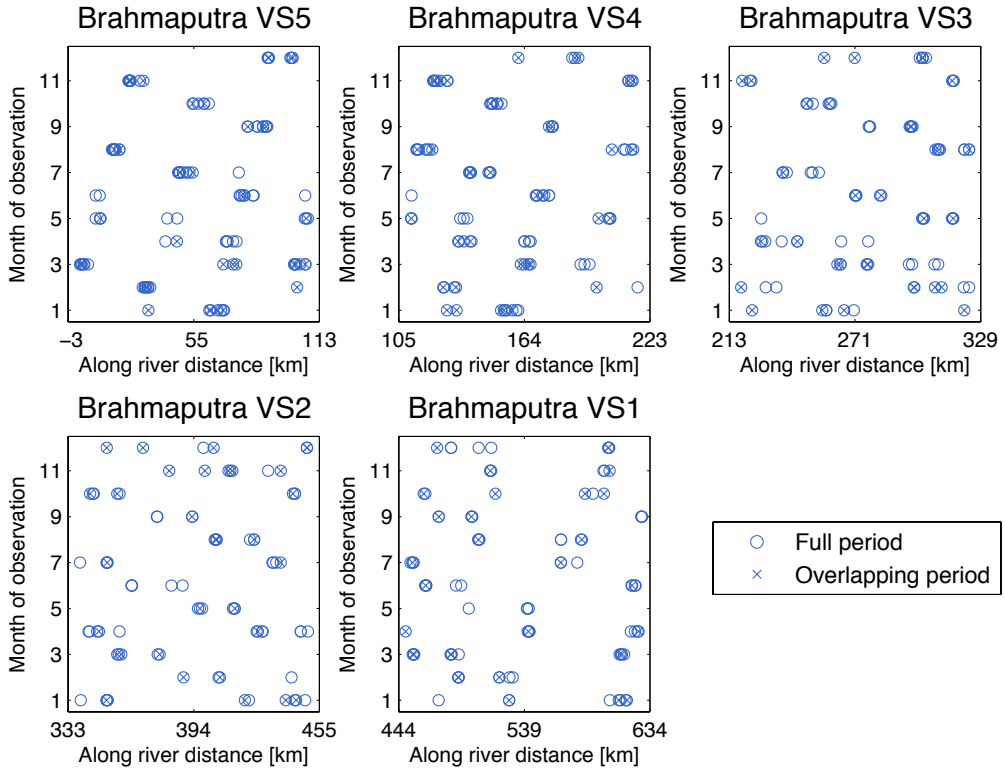

Figure 5.4: Scatter plots showing the temporal and spatial distribution of observations at the virtual stations in the Brahmaputra River basin.

have been masked, outliers removed, means for all crossings are derived, and the positions of the virtual stations are chosen:

1. The retracked heights (means) are used to determine along-river height profiles for the Ganges and Brahmaputra Rivers. The heights profiles are derived as linear and cubic fits of the CryoSat-2 observations (see Section 5.1.3.1).

2. Adding the height difference (according to the height profile) between the point of observation and the VS, the observation can be spatially relocated along the river centerline (see Section 5.1.3.2).

3. Once all observations have been relocated to their respective VS, information about the seasonality of the rivers is extracted by fitting a simple model to the obtained time series. The model consists of a combination of a linear trend and the sum of a cosine and sine wave (see Section 5.1.3.3).

5.1.3.1 Height profiles of the rivers

In order to apply the slope correction to be described in Section 5.1.3.2, a height profile along the river is necessary. The height profiles are obtained by fitting a linear (Ganges) or a cubic function (Brahamaputra) to the heights as a function of along river distance. By fitting simple functions to the retrieved CryoSat-2 heights over the rivers, it is ensured that an uneven temporal distribution of the observations does not affect the height model used for the slope correction. Unfortunately, these functions will not be able to describe local topography, which introduces some errors in the relocation.

Similarly, the mean height profiles used here do not account for varying river slopes caused by portions of the river reacting differently to high flow and low flow seasons.

Ganges River
The heights retrieved over the Ganges River are shown in Figure 5.5 as a function of along river distance starting from 89.1°E going downriver. Fitting the retracked heights in this river segment with a linear function the following model was obtained:

$$H = -0.024x + 7.1 \text{ m} \tag{5.1}$$

where x is the along river distance in km.

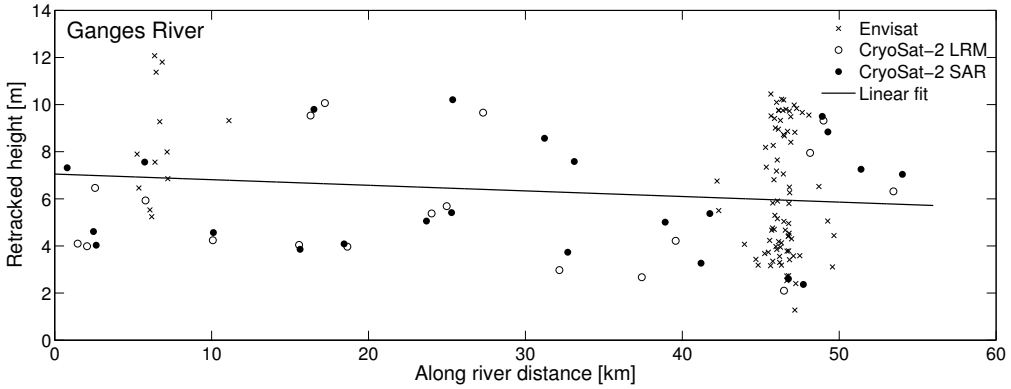

Figure 5.5: Retracked heights in metres above EGM08 for CryoSat-2 and Envisat as a function of along river distance and the corresponding linear fit used for the slope correction for VS6 (see location in Figure 5.1.)

Brahmaputra River
The heights retrieved over the Brahmaputra River are shown in Figure 5.6 as a function of along river distance starting from 90°E going eastward. Fitting the CryoSat-2 data with a cubic function the following height model is obtained:

$$H = -3.121 \cdot 10^{-8}x^3 + 7.242^{-5}x^2 + 0.08999x + 26.08 \text{ m} \quad (5.2)$$

where x is the along river distance in km.

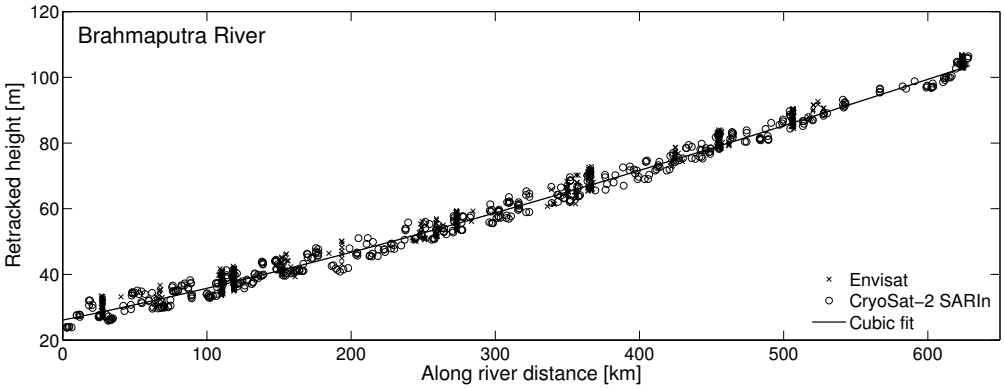

Figure 5.6: Retracked heights in metres above EGM08 for CryoSat-2 SARIn and Envisat as a function of along river distance and the corresponding linear fit used for the slope correction for VS1-VS5 (see locations in Figure 5.1.)

It was attempted to use the digital elevation model from SRTM (see Section 4.3.1) and ACE2 (see Section 4.3.2) to relocate the observations to the chosen virtual stations. However, this introduced much more noise, and so this approach was abandoned. The relatively high noise of the SRTM dataset compared to that of CryoSat-2 is illustrated in Figure 5.7, which shows the height measurements (before outlier removal) from CryoSat-2, Envisat, and SARAL/AltiKa over the Brahmaputra River alongside the heights as given by the SRTM and ACE2 DEMs in the same locations as the CryoSat-2 data. From the figure it is seen that CryoSat-2 and Envisat provide very stable height estimates compared to the other datasets. In general, the SARAL/AltiKa heights appear to be of a similar quality except for some very obvious clusters of outliers around 90.4°E and 91.7°E.

5.1.3.2 Relocation of observations

Once the height profiles were estimated, the observations were relocated segment-wise to their corresponding virtual stations using slope correction based on the height profiles. The distance between the observation and the VS to which the observation is relocated was determined from the along river distance derived from the river centreline. Using a river centreline, the mean height along the river was estimated from CryoSat-2 data and observations were moved by adding the height difference between the point of observation and the location of the virtual station. By doing this, it is possible to estimate time series at chosen virtual stations for both

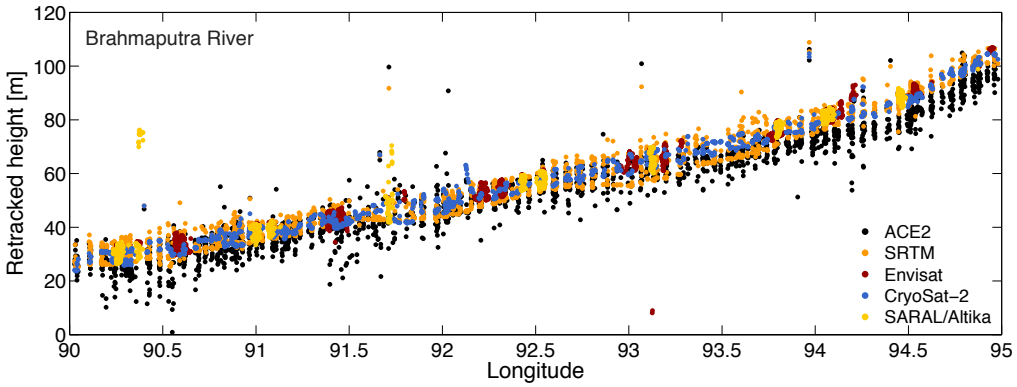

Figure 5.7: Comparison of altimetric heights in the Brahmaputra river with heights from SRTM and ACE2.

CryoSat-2 and Envisat. Naturally, the relocation is larger for CryoSat-2 than for Envisat, as seen in Figures 5.6 and 5.5.
A sketch of the slope correction is given in Figure 5.8 and the corresponding equations are as follows in equation (5.3).

$$\begin{aligned} h_{new} &= h_{obs} + H_D \\ &= h_{obs} + (H_{VS} - H_{OBS}) \end{aligned} \tag{5.3}$$

In the equation above h_{obs} is the instantaneous measurement from the altimeter, H_D is the difference between the mean heights at the point of observation (H_{OBS}) and the corresponding virtual station (H_{VS}). After the height difference has been calculated, the absolute height, h_{new}, at the virtual station is calculated by simply adding the difference to the original retracked height, h_{obs}.

5.1.3.3 Estimation of annual phase and amplitude

A model was fitted to the obtained time series in order to derive their annual phases and amplitudes. The model includes an offset, A, a trend, B, and a linear combination of a cosine and sine wave with amplitudes C and D, respectively.

$$f(t) = A + Bt + C\cos(t') + D\sin(t') \tag{5.4}$$

where t is the time in decimal years relative to January 1st 2012 and $t' = 2\pi t$. E.g. January 1st 2011 would correspond to $t = -1$ and July 1st 2012 would correspond to $t = 0.5$. The model was fitted to the data using multiple linear regression, where

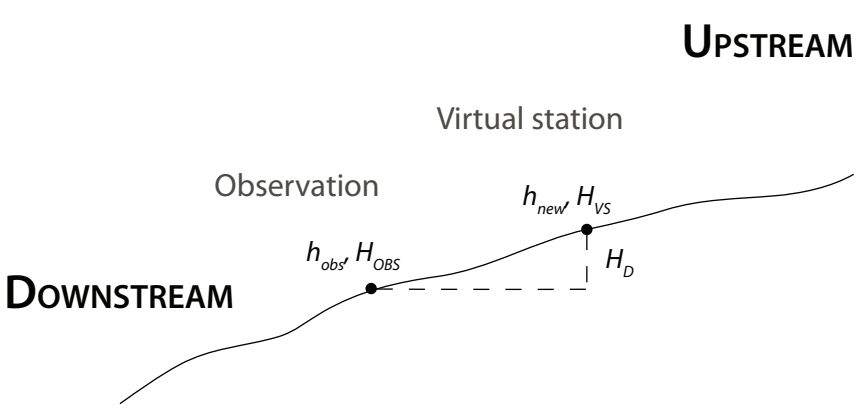

Figure 5.8: Sketch of slope correction applied for relocation of observations. In this study the river slopes were given as simple functions obtained from fitting the retracked data with linear or cubic polynomia.

it is assumed that the retracked heights, $Y = (h_1, h_2, ..., h_n)^T$, can be described as a function of time:

$$Y(t) = X(t) \cdot \beta + \epsilon \tag{5.5}$$

where X is the design matrix describing the model:

$$X = \begin{pmatrix} 1 & t_1 & cos(t'_1) & sin(t'_1) \\ 1 & t_2 & cos(t'_2) & sin(t'_2) \\ \vdots & \vdots & \vdots & \vdots \\ 1 & t_n & cos(t'_n) & sin(t'_n) \end{pmatrix} \tag{5.6}$$

and β is a vector holding the coefficients A, B, C and D: $\beta = (A, B, C, D)^T$.

Here, the phases will be given in decimal months, where all months have been assumed to be equally long.

The amplitude, a, is derived from the amplitudes of the cosine and sine waves:

$$a = \sqrt{C^2 + D^2} \tag{5.7}$$

The resulting phase of the cosine and sine waves can be found by using the atan2 function and converting from degrees to months:

$$p_d = \frac{180}{\pi}\text{arctan2}(D,C) \tag{5.8}$$

$$p_m = \frac{12}{360}p_d + 1 \tag{5.9}$$

The amplitude, a, in equation (5.7) is given in metres and the phase, p_m, in equation (5.9) is given in decimal months. If the phase in equation (5.8) is negative, 360 degrees must be added before converting the phase to decimal months.

Error estimation Once the coefficients in equation (5.4) were determined, their corresponding standard errors could be computed according to equation (5.10), which gives the standard error matrix, S, in which the standard errors of the estimated coefficients (s_A,s_B,s_C and s_D) are found in the diagonal.

$$S = \sqrt{\frac{\sum_i^n (r_i^2)}{n-m-1}(X^T X)^{-1}} \tag{5.10}$$

where n, is the number of data points in the time series, r_i is the residual for the ith data point, m is the number of estimated coefficients (i.e. four in this case) and X is the design matrix introduced earlier. The standard errors on phase, δp_m, and amplitude, δa, were then determined from standard error propagation as given by Equation (3.47) in *Taylor* (1997).

$$\delta p_m = \frac{6}{\pi}\frac{\sqrt{C^2 s_C^2 + D^2 s_D^2}}{C^2 + D^2} \tag{5.11}$$

$$\delta a = \sqrt{\frac{C^2 s_C^2 + D^2 s_D^2}{C^2 + D^2}} \tag{5.12}$$

5.1.4 Evaluation of CryoSat-2 river height retrievals

The observations obtained from the CryoSat-2 and Envisat missions over the Ganges and Brahmaputra are compared in this section to see how well they agree on annual time scale. Time series as well as estimated phases and amplitudes obtained according to the method described in Section 5.1.3 are compared.

5.1.4.1 CryoSat-2 LRM and SAR over the Ganges River

The observations used for constructing the time series at virtual station no. 6, i.e. VS6 (see Figure 5.1), from Envisat and CryoSat-2 can be seen in Figure 5.9. The

figure shows how the observations from CryoSat-2 are more spread out in the zonal direction compared to the repeat orbit observations from Envisat and that the river level decreases towards the east as the river approaches the Bay of Bengal.

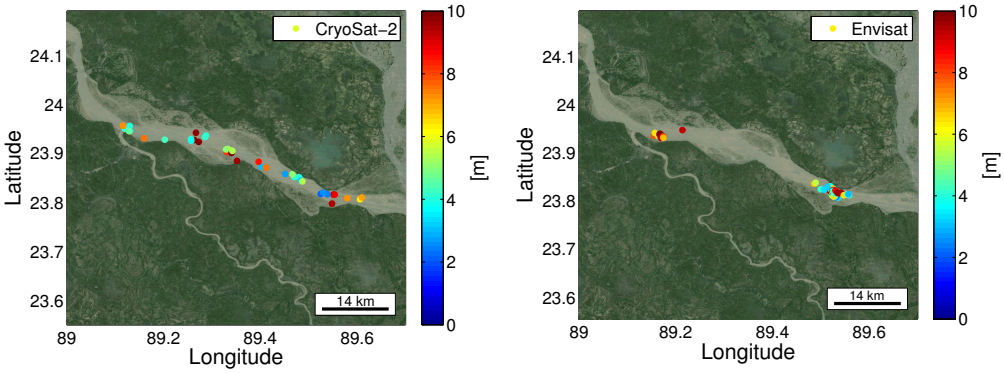

Figure 5.9: Retracked heights in metres above EGM08 for CryoSat-2 LRM/SAR (left) and Envisat (right) from April 2010 to March 2012 in a portion of the Ganges River.

Correcting for the slope and referencing all the observations to VS6 at 89.3°E time series obtained for both missions are shown in Figure 5.10. There is a small offset ($\sim$1 m) between the Envisat and CryoSat-2 data, which was not investigated for temporal or spatial variation. The offset is caused by a range bias between the two missions, as well as the different retracking methods and geophysical corrections, and errors introduced to the CryoSat-2 dataset when relocating the observations. The offset has been removed in all time series presented here without further study.

From the estimated river level time series it is evident that both satellites capture the annual signal nicely. Estimated phases for the time series were found to be 9.06$\pm$0.08 and 8.83$\pm$0.06 for CryoSat-2 and Envisat, respectively, which corresponds to a peak flow in the river around the end of August to early September. The annual phases agree reasonably well. It is especially worth noticing that the CryoSat-2 LRM phases, which are the only data for this VS that coincides with the Envisat data, are identical. Any discrepancies in the other phase estimates could be due to the crude assumptions made throughout the post processing, i.e. the static water mask, the assumed linearity of the river slope, and the fit of the simple time series model. Differences in the temporal sampling of the two altimeters could also contribute to the difference between the captured phases. And of course, the timing of high and low flows might have changed slightly. The amplitude of the CryoSat-2 data was found to lie between 3.36$\pm$0.22 m and 3.56$\pm$0.15 m, which is in good agreement with the estimated phase for the Envisat data of 3.63$\pm$0.11 m.

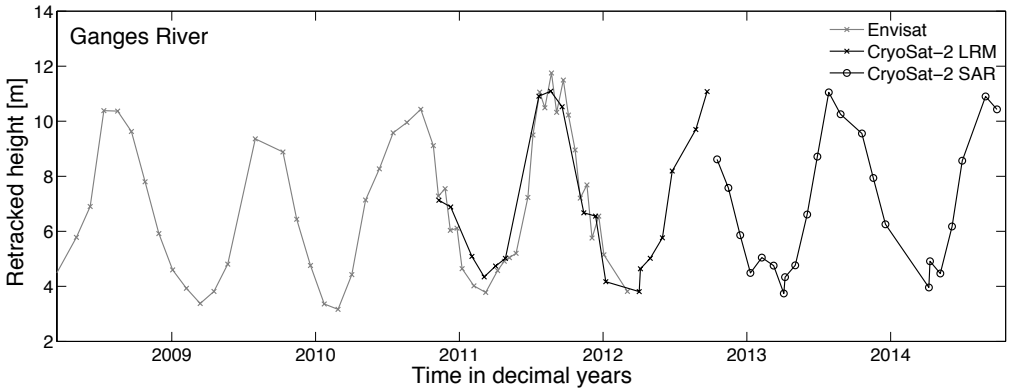

Figure 5.10: Ganges River time series showing estimated river levels for Envisat, and CryoSat-2 LRM and SAR for VS6 (see location in Figure 5.1.).

Data set	Period	Phase, p_m	Amplitude, a	n
CryoSat LRM	07/2010-10/2012	8.83±0.16	3.50±0.29	19
CryoSat SAR	10/2012-08/2014	9.10±0.13	3.36±0.22	23
LRM+SAR	07/2010-08/2014	9.06±0.08	3.56±0.15	42
Envisat	01/2003-03/2012	8.83±0.06	3.63±0.11	92

Table 5.1: Comparison of amplitudes and phases as derived from CryoSat-2 and Envisat data over the Ganges River. Phases are given in decimal months and amplitudes in metres.

5.1.4.2 CryoSat-2 SARIn over the Brahmaputra River

Another stretch of river in the river basin that is used for the comparison is the Brahmaputra River from 90°E to 95°E. In this portion of the river time series were constructed for VS1-5, and in addition to the work published in *Villadsen et al.* (2015a) the corresponding results obtained from SARAL/AltiKa data have been included. The retracked heights included from the different missions can be seen in Figure 5.11.

The time series obtained for VS1-5 within the SARIn mask of CryoSat-2 (see Figure 5.1) of Brahmaputra are shown in Figure 5.12. From the time series it is obvious that the late Envisat orbit provides time series that are less smooth compared to the previous exact repeat orbit of Envisat. This is most likely due to 1) the assumption that the elevation along the river can be described by a cubic function and 2) variations in the riverbanks, which determines how different parts of the river react to a higher or lower inflow of water. This effect is not included here as it would require a high number of rating curves, which are unavailable, and at last 3) local tributaries can affect the local river level, which would also introduce errors when the observations are relocated from one location to another. However, the time series

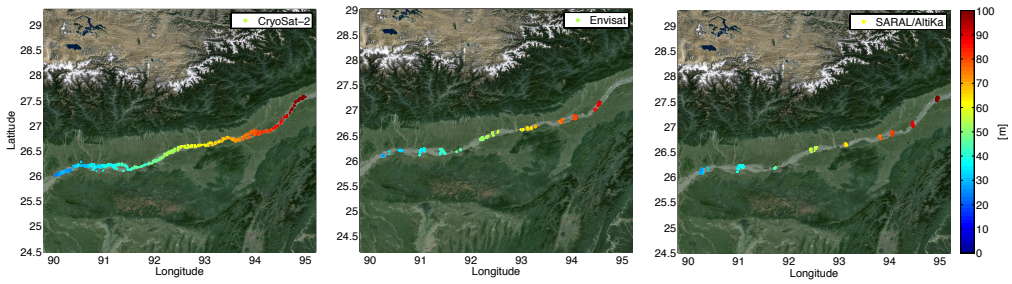

Figure 5.11: Retracked heights in metres above EGM08 for CryoSat-2 SARIn (left), Envisat (middle) from April 2010 to August 2014, and SARAL/AltiKa (right) from March 2013 to August 2014 in the Brahmaputra River.

still appear with the same seasonal patterns despite these fluctuations.

Figure 5.13 shows three examples of how well the time series model fit the time series obtained in the Brahmaputra River. All Envisat time series show almost equally good time series, as seen in the top curve for VS5. The middle curve for VS3 shows the most noisy of the CryoSat-2 data in the Brahmaputra, and the bottom curve shows one of the better fits for CryoSat-2, here for VS4. In general, all time series follow the time series model very well.

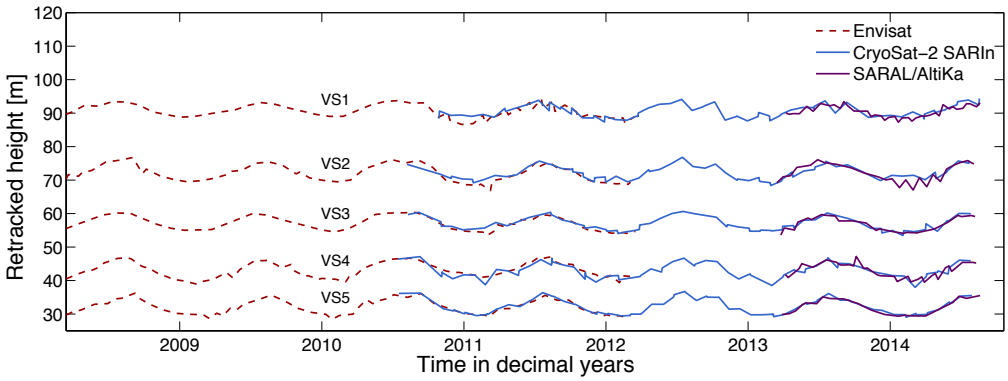

Figure 5.12: Brahmaputra River time series showing estimated river levels for Envisat, CryoSat-2 SARIn, and SARAL/AltiKa data.

Figure 5.14 shows the detailed estimated fitted amplitudes and phases for CryoSat-2 SARIn (blue), Envisat (red), and SARAL/AltiKa (yellow). The largest difference in amplitude between CryoSat-2 and Envisat is $\sim$ 30 cm and the corresponding mean difference of all five stations is $\sim$10 cm. The phase of the annual variation captured by CryoSat-2 and Envisat in each segment of the river has a mean difference of 2.7 days, which is surprisingly good considering the nature of the orbits. As seen, the SARAL/AltiKa signals deviate slightly from the rest, which could be due to the low number of observations caused by the short time period included in the study, or the sawtooth behavior seen in Figure 5.12. However, the

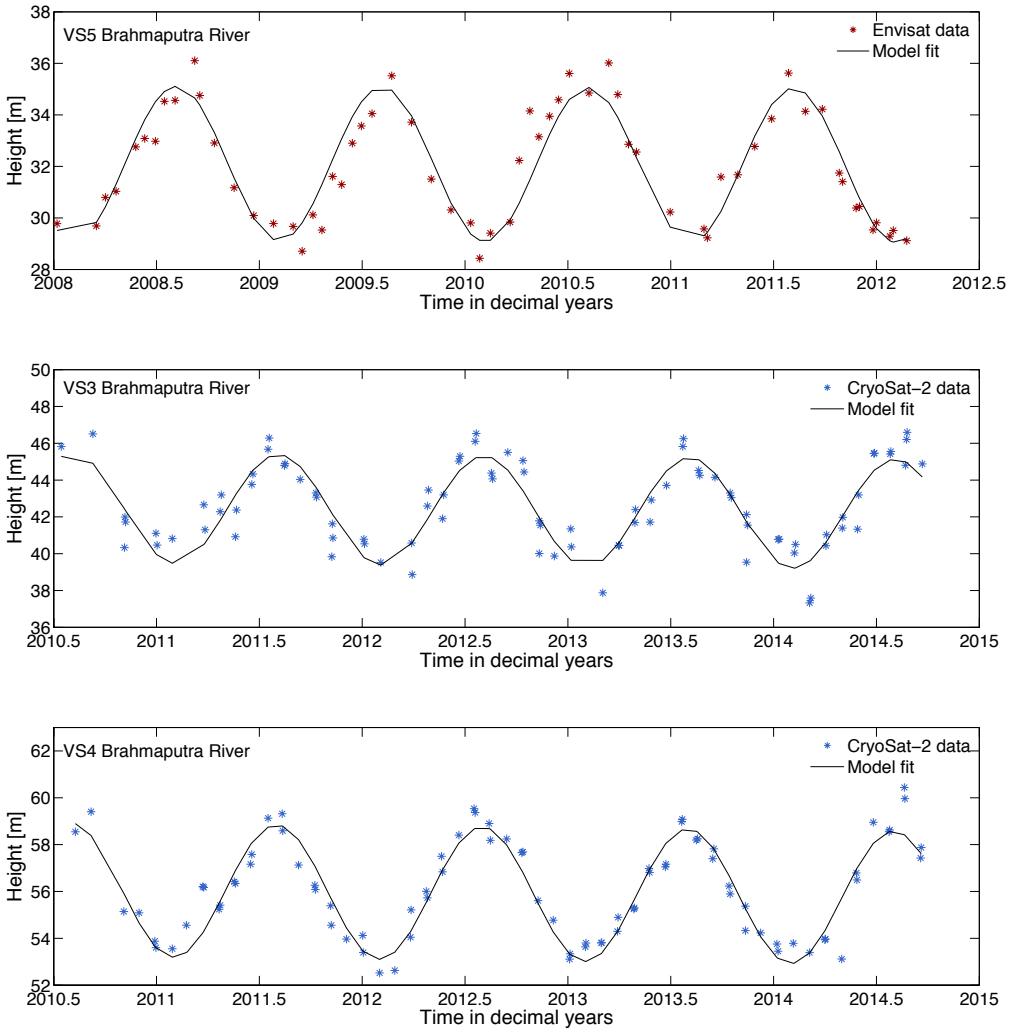

Figure 5.13: Examples of the estimated model fits compared to the data in the Brahmaputra River. Top) Model fit for Envisat data at VS5 middle) model fit for CryoSat-2 data at VS3, and bottom) model fit for CryoSat-2 data at VS4.

SARAL/AltiKa data still agrees well with the two other missions.

The time series fitting has its limitations, as the temporal distribution of the points affects the fit of the model. All phases and amplitudes with their corresponding uncertainties can be seen in Tables 5.2 and 5.3. It should be noted, that the standard errors estimated from equation (5.10) mainly depend on the number of observations.

As an additional experiment the analysis in the Brahmaputra River was done using pseudo-SAR data, also known as degraded SARIn. Here, no off-nadir correction was applied for the SARIn data, instead the nadir location as given in the

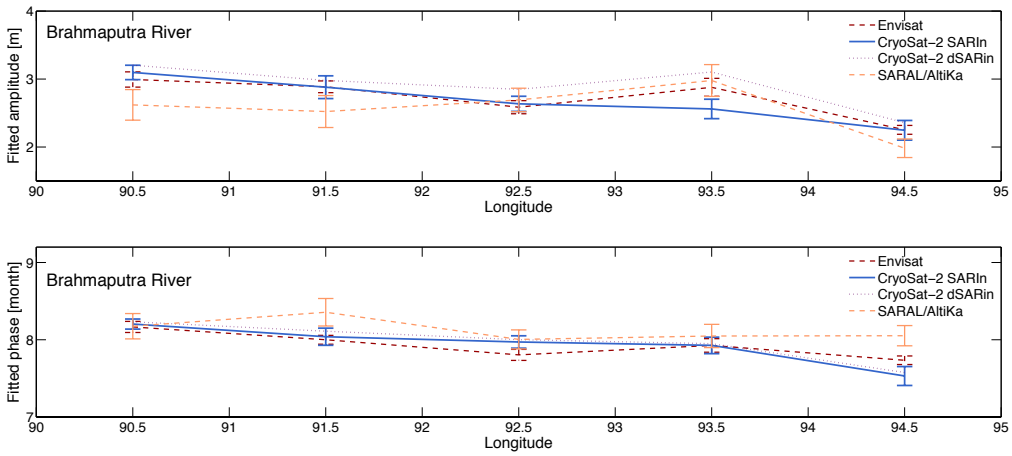

Figure 5.14: Fitted phases and amplitudes for time series obtained from CryoSat-2 SARIn and degraded SARIn (dSARIn), Envisat, and SARAL/AltiKa data in the Brahmaputra River.

VS no.	Longitude	Mode	p_m, CS-2	p_m, Envisat	p_m, AltiKa	n, CS2/Envisat/AltiKa
1	94.5°E	SARIn	7.53±0.12	7.73±0.06	8.05 ±0.13	91/183/43
2	93.5°E	SARIn	7.93±0.11	7.93±0.09	8.05 ±0.15	82/97/25
3	92.5°E	SARIn	7.97±0.08	7.80±0.07	8.00 ±0.12	89/90/25
4	91.5°E	SARIn	8.04±0.11	8.00±0.06	8.36 ±0.18	96/145/32
5	90.5°E	SARIn	8.20±0.07	8.17±0.07	8.18 ±0.16	102/94/20

Table 5.2: Comparison of phases, p_m, for CryoSat-2 (CS-2) SARIn from launch to August 2014, Envisat data from launch to March 2012, SARAL/Altika data from March 2013 to August 2014. Phases are given in decimal months.

CryoSat L1b product was used. Annual phases and amplitudes for the pseudo-SAR time series are shown in Figure 5.14 as purple dotted lines. Although the phase for degraded SARIn looks more similar to the Envisat phase at VS2 at 93.5°E, the overall mean difference is 3.34 days, which is higher than for the range-corrected SARIn data. The mean difference of the amplitudes is 18 cm, which is also higher than for the SARIn data.

5.1.5 Summary

Annual signals were determined for CryoSat-2, Envisat, and SARAL/AltiKa data over the Brahmaputra River and for CryoSat-2 and Envisat data over the Ganges River. The annual signals were studied by relocating the observations to a series of virtual stations in the Ganges-Brahmaputra River basin due to the orbital pattern of CryoSat-2. The results showed that CryoSat-2 and Envisat captured comparable

VS no.	Longitude	Mode	a, CS-2	a, Envisat	a, AltiKa	n, CS2/Envisat/AltiKa
1	94.5°E	SARIn	2.25±0.14 m	2.25±0.07 m	1.98±0.14 m	91/183/43
2	93.5°E	SARIn	2.56±0.14 m	2.89±0.13 m	2.98±0.23 m	82/97/25
3	92.5°E	SARIn	2.63±0.11 m	2.59±0.10 m	2.69±0.17 m	89/90/25
4	91.5°E	SARIn	2.88±0.17 m	2.89±0.09 m	2.52±0.24 m	96/145/32
5	90.5°E	SARIn	3.10±0.11 m	2.99±0.11 m	2.62±0.23 m	102/94/20

Table 5.3: Comparison of amplitudes, a, for CryoSat-2 (CS-2) SARIn from launch to August 2014, Envisat data from launch to March 2012, SARAL data from March 2013 to August 2014.

annual signals even though CryoSat-2 is in a drifting orbit with a repeat period of more than a year and Envisat is in a near-repeat orbit. Fitting a set of harmonic functions to the river level time series revealed a peak flow in late July and late August for Brahmaputra and Ganges, respectively, with differences between Envisat and CryoSat-2 of just a couple of days. The amplitudes of the flow in the rivers also showed encouraging results, with a difference of 10 cm or less between CryoSat-2 and Envisat for all virtual stations in both Ganges and Brahmaputra except for the virtual station at 93.5°E in the Brahmaputra River. The phase and amplitudes derived from the SARAL/AltiKa data seem to be affected by the short time period included in the study - a better agreement might be obtainable by including recent observations.

The method presented in this study makes it possible to perform river level monitoring using not only CryoSat-2, but also Sentinel-3 data, when these become available in the future, due to the similarities of the altimeters. With this it is possible to continue the river level time series retrieved from satellite radar altimetry and to keep providing hydrologists with valuable information needed for fresh water monitoring which is important for millions of people.

The study presented here highlights the need for a better mask for extracting the observations retrieved over rivers. A dynamic, or at least a high-resolution mask, could be obtained with the use of satellite imagery, which would allow for less data editing.

Furthermore, the mean along-river heights used for relocating the observations in this study are simplified due to lack of a satisfactory digital elevation model and/or rating curves along the river. More information about the nature of the rivers would be very beneficial - e.g. in the form of rating curves, which links the discharge and water level, since it is assumed in this study that an elevation change at one location of the river would have been the same at another location at the same time.

Another error source in this study involves the time lag of flow in the river,

which could cause errors spanning from minutes to days depending on the distance between the observation and the chosen virtual station. Accounting for this is not trivial, and in this study it is assumed that the corresponding error is negligible since the segments that are used are no longer than ∼100 km.

One of the most crucial parts of constructing these time series lies within the way the waveforms are being retracked. Retracking waveforms from inland water is challenging due to the highly varying topography within the radar footprint. More effort should be put into developing a retracker specifically for retracking inland water waveforms in order to ensure that the height estimations are, in fact, from the desired lake or river surface and not from the surrounding topography. Chapter 6 will propose a method that takes adjacent waveforms into account in order to avoid as much snagging as possible.

5.2 Flood detection from CryoSat-2

Moving the focus away from the Ganges-Brahmaputra Rivers, this section studies two separate flood events to investigate the ability of CryoSat-2 to detect changes caused by inundation of land. The data used here are L1b 20Hz LRM and SAR waveforms retracked with the NPPR method presented in Section 3.2.4, the ESA L2 backscatter coefficients, and a waveform peakiness obtained from Equation (2.7).

The study focuses on two major flood events:

- The recent flood event in Bangladesh in August 2014. Here, the flooding is detected both as an elevation change, and as a change in waveform characteristics compared to the same overpasses in 2011 and 2013.
- The prolonged flood event in Thailand in 2011. The southward flood progression that occurred during the Fall is detected by looking simply at changes in the retracked surface height compared to corresponding tracks in 2013.

5.2.1 Flood in Bangladesh (August 2014)

In August 2014, continuous rainfall and onrush of upstream waters in north and northeastern Bangladesh caused severe flash floods around the Upper Meghna. The Upper Meghna is a comparatively small river, but acts as a distributary of the Brahmaputra, formed inside Bangladesh by the joining of several rivers from the mountainous regions of India. Several low-lying and densely populated areas were totally inundated, forcing the local population to relocate. By the end, almost half a million people were left homeless due to the flood (*Al-Mahmood*, 2014).

Figure 5.15: Photograph of the 2011 flood near Bangkok, Thailand (*Defense Video & Imagery Distribution System - Navy Visual News Service*, 2011).

Figure 5.16 shows the location of the CryoSat-2 LRM track that covered the inundated region on August 26th 2014. The observed backscatter and peakiness as well as the estimated surface elevations from this track are compared with the corresponding observations from 2011 and 2013. The observations from 2012 are excluded, as the track was located further away than the tracks from 2011 and 2013 and therefore not found suitable for direct comparison. The tracks from 2011 and 2013 are not shown in Figure 5.16 as they coincided completely with the track in 2014.

The flooding was detected by CryoSat-2 as changes in surface heights (Figure 5.17), peakiness (Figure 5.18), and in backscatter (Figure 5.19) along the satellite track crossing the border between the Sylhet and Sunamganj Districts in August 2011, 2013, and 2014.

As seen in Figure 5.17, the surface height estimates during the flood show much less variation compared to the same tracks in 2011 and 2013. This is expected, since an inundation will mask small topographic changes. The flooded regions appear to be covered in around 1 m of water, or even several metres in valley regions, which is surely enough to disrupt the lives of locals and destroy houses and crops.

The peakiness values given in Figure 5.18 are noticably higher during the flood, which is caused by the shallow water covering the region acting like a mirror sur-

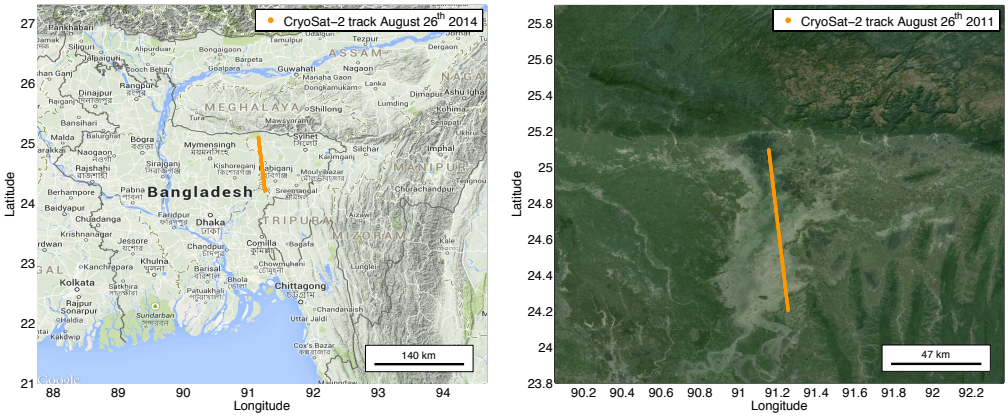

Figure 5.16: Location of CryoSat-2 track crossing inundated region in Bangladesh on August 26th, 2014.

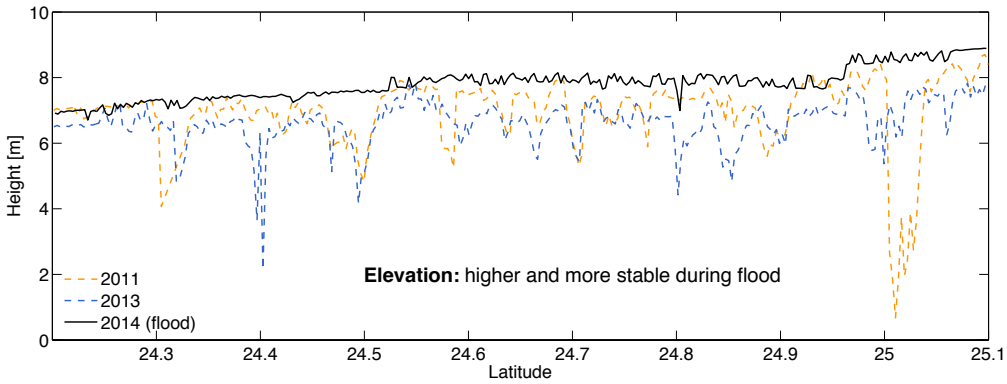

Figure 5.17: Estimated surface elevations of the three tracks crossing the part of Bangladesh that was flooded in 2014.

face, whereas the values in 2011 and 2013 are more or less the same. In the same way, a higher backscatter is witnessed in Figure 5.19 in 2014 compared to 2011 and 2013.

5.2.2 Flood in Thailand (2011)

In Autumn 2011, major parts of Thailand were affected by severe flooding of the Chao Phraya River Basin. The Chao Phraya River flows southward from the northern mountains of Thailand and ends in the Gulf of Thailand. The flooding in 2011 was caused by accumulation of rainfall from March to October, further enhanced by five tropical storms that affected Thailand from July through October. Although the flood was not the highest in history, its duration was the longest ever recorded as it lasted 158 days (*Promchote et al.*, 2015). The flooding started in the north as a result

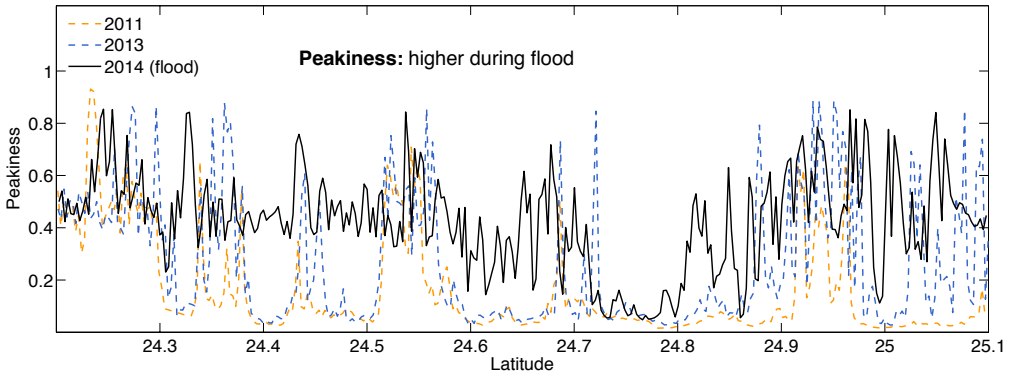

Figure 5.18: Estimated waveform peakiness of the three tracks crossing the part of Bangladesh that was flooded in 2014.

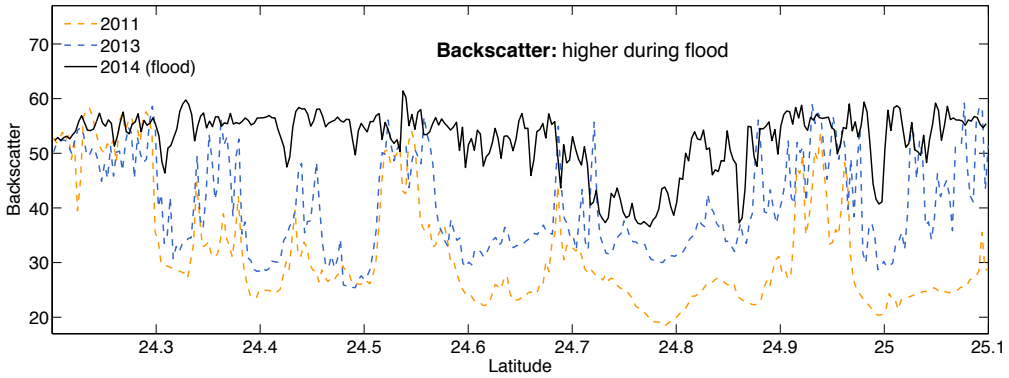

Figure 5.19: Estimated backscatter coefficients for the three tracks crossing the part of Bangladesh that was flooded in 2014.

of heavy rainfall and migrated southwards in the Mekong and Chao Phraya River basins where it was combined with high tides that hit the Gulf of Thailand in the months of October and November (*Wongsa*, 2014). In October the flooding reached the city of Bangkok. By the end, most of Thailand was flooded, and approximately 13.6 million people were affected (*Promchote et al.*, 2015). The

Here, the progression of the flood during the Autumn period as seen from three CryoSat-2 SAR tracks is shown. Figure 5.20 shows the location of the tracks that are compared to track the extent of the flood, as well as a false colour composite from MODIS showing the extent of the flood on October 19th, 2011. To see the changes in surface elevations caused by the flood, three tracks in August, October, and November from 2011 and 2013 are compared. Tracks from 2013 were chosen, as these were located within 100 m of the 2011 tracks. In 2012, the tracks were displaced around 2 km compared to 2011.

For tracks crossing the flooded region in the months of August, October, and

November the retracked heights in 2011 and in 2013 are shown. The height profiles are compared with the flood extent maps shown in Figure 5.21 and 5.22. Figure 5.22 shows the extent of the flood in August and November 2011, whereas Figure 5.21 show the maximum flood extent together with the SRTM DEM and the location of the three (six, counting both years) tracks compared in this study.

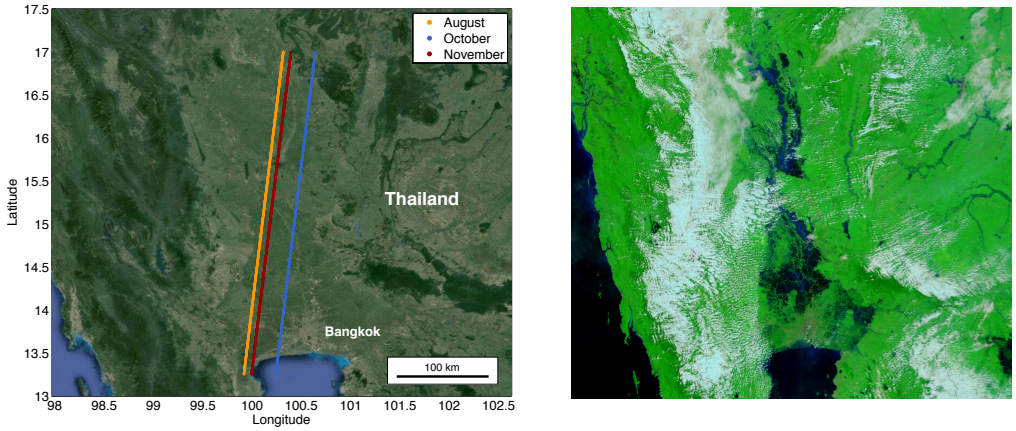

Figure 5.20: Location of CryoSat-2 SAR tracks to be compared in the Chao Phraya River basin (right), as well as a false-colour satellite image showing the extent of the flooding on October 19th, 2011. Water appears as dark blue. (*MODIS Rapid Response Team*, 2011)

Figure 5.23 shows the estimated surface elevations for August 2011 where the flood had not yet reached the southern part of Thailand (see Figure 5.22). The height profile clearly shows an increase in surface heights in the northern part of the track, which is accompanied by a decrease in height variability. As shown in Figures 5.21 and 5.22, the inundation in the north is quite scattered across the region, probably due to local topography. To have partially coinciding height profiles as seen in Figure 5.23 around 16-16.2°N is therefore not unexpected.

In Figure 5.24, the heights retrieved from the track crossing the flooded region in October shows how the flood has reached the southern parts of Thailand. However, the track from October is shifted towards the east, and as a result, the northern part of the height profile does not cover any inundation (see Figure 5.21), which is also seen from the similarity of the two profiles from 2011 and 2013.

The track from November flies over the flooded provinces in the north as well as in the south. The retracked heights for this track are shown in Figure 5.25. As CryoSat-2 passes over the Chao Phraya River basin in November, it is possible to see the inundation in both the southern and northern regions.

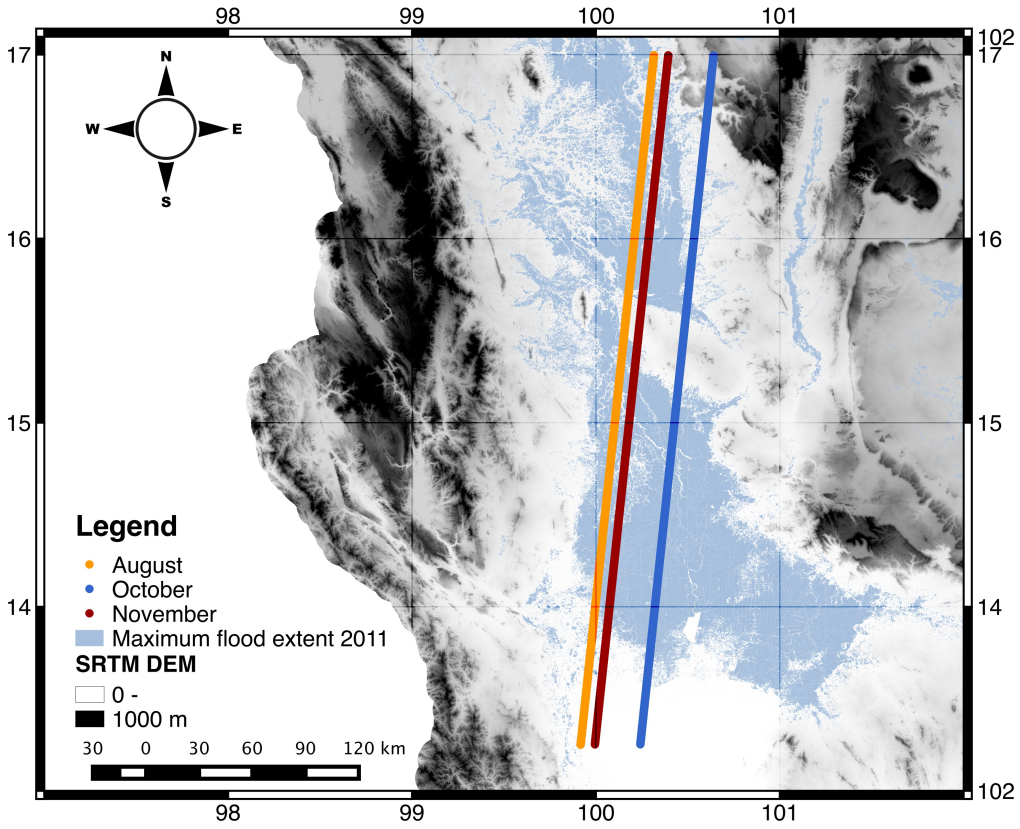

Figure 5.21: Map of track locations of flood crossings in Thailand 2011 along with the maximum flood extent and the SRTM DEM.

5.3 Summary of the chapter

This chapter dealt with the posibilities of CryoSat-2 to detect temporal changes in surface hydrology. The first study focused on river level monitoring, which is slightly more difficult for CryoSat-2 as its orbit is geodetic and was designed for fine spatial sampling of (relatively) slow-changing ice sheets. By relocating the observations to virtual stations it was possible to derive time series with annual signals comparable to those from time series obtained with Envisat. Over the Ganges and Brahmaputra Rivers river levels with annual phases and amplitudes for both LRM, SAR, and SARIn data that were comparable to those of Envisat were derived. Some of the biggest challenges with this study was: 1) the river mask, since the channel pattern changes frequently, 2) complicated waveforms and retracking of these, and 3) the relocation technique which simplifies the river profile from CryoSat-2 altimetry data as the digital elevation models available for this area were found unsuited for the purpose.

The second study looked into two floods in Thailand 2011 and Bangladesh in

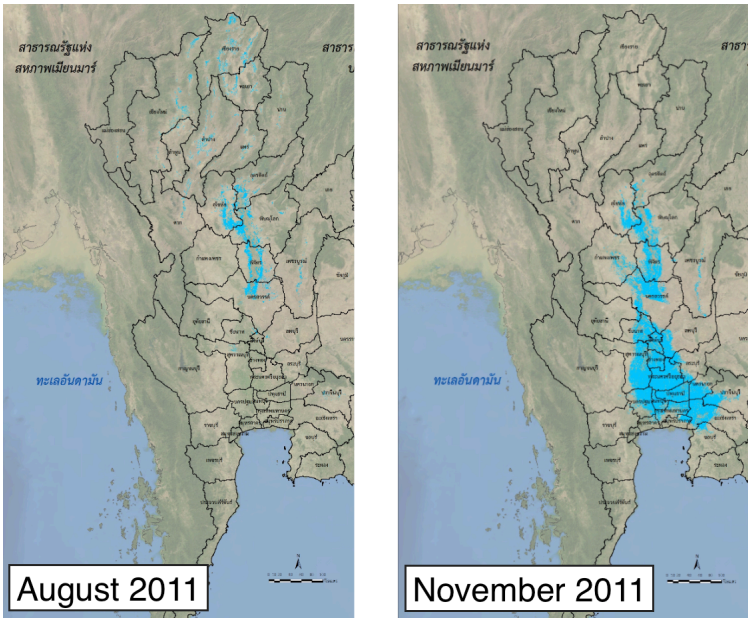

Figure 5.22: Extent of inundation (blue) in August (left) and November 2011 (right). (Adapted from *GISTDA* (2015).)

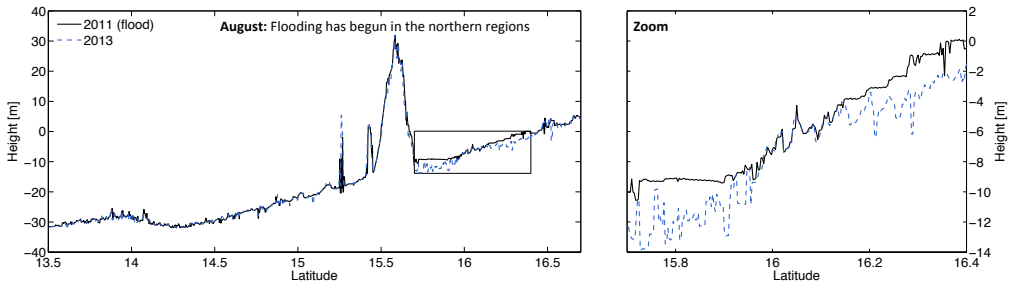

Figure 5.23: Estimated surface elevation in the Chao Phraya River basin in August 2011 and 2013.

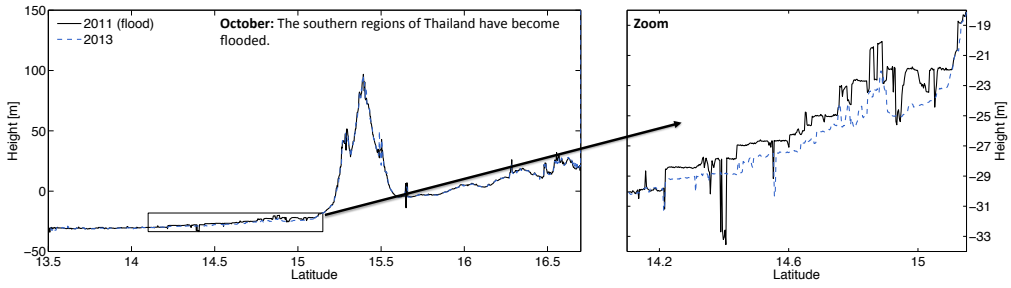

Figure 5.24: Estimated surface elevation in the Chao Phraya River basin in October 2011 and 2013.

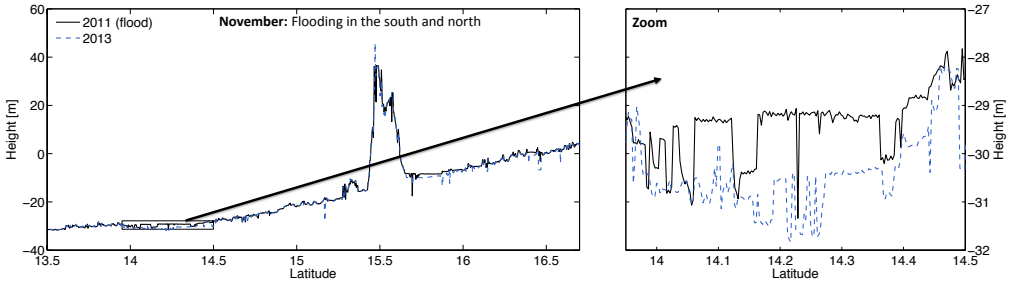

Figure 5.25: Estimated surface elevation in the Chao Phraya River basin in November 2011 and 2013.

2014. The results showed that it was possible to see the floods both as increased surface elevations of a couple of metres, and as an increase the waveform parameters peakiness and backscatter. In the future, it would be interesting to compare satellite imagery with our findings from CryoSat-2 in more detail, to investigate to which extent the CryoSat-2 data is able to see the inundated regions.

All in all, this study shows that it is possible to utilize the geodetic orbit of CryoSat-2 to exstract knowledge about temporal and spatial changes about river flows and flood events. Of course, the amount of available information from CryoSat-2 depends on the duration and extent of the event, but it is clear that the CryoSat-2 orbit offers some very interesting possibilities compared to missions that have been used for hydrological purposes up until now.

Chapter 6

Study II: Remedying snagging – results from the MWaPP Retracker

The method investigated in this chapter was designed entirely by the author, and has been described in the manuscript submitted for Journal of Hydrology (see Appendix A.2). The algorithms behind the MWaPP retracker were defined in Section 3.3, and this chapter contains a comparison between the new method and the NPPR retracker that has previously been shown to provide the most stable water levels for inland water (Jain, 2015; Nielsen et al., 2015a). All CryoSat-2 20 Hz L1b SAR data processing was carried out by the author.

6.1 Introduction

Altimetric waveforms over inland water show extreme variation due to the different surfaces within the satellite footprint. One of the often encountered problems with radar altimetry is snagging (see Section 2.4). Snagging is especially a problem when the ground track is located close to the shore of the water body.

From the time series study previously presented in Chapter 5, it was found necessary to develop an empirical retracking method for SAR altimetry that avoids snagging as much as possible. This resulted in the MWaPP retracker, which was previously described in Section 3.3, and for which some results will be presented in this chapter and the next.

6.2 Study areas

This section briefly describes the chosen study areas and the obtained in situ data. The choice of study regions was limited by the availability of SAR data from

CryoSat-2, the size of the water body, and the availability of in situ data. Unfortunately, the Ganges-Brahamputra River basin is mostly covered with SARIn, and there were found no in situ data overlapping with the CryoSat-2 mission. In this chapter, it was therefore necessary to choose new study regions to allow for a more thorough evaluation of the MWaPP retracker.

6.2.1 Lake Vänern

Lake Vänern is the largest lake in Sweden and in the European Union with an area of 5,650 km^2 (*Seppälä*, 2005). The average depth of the lake is 27 m with a maximum depth of 106 m. Gauge data for Lake Vänern are available from the Swedish Meteorological and Hydrological Institute (SMHI, `http://www.smhi.se/klimatdata/hydrologi/`) and are referenced to the Swedish height system Riket höjdsystem 1900 (RH 00). Lake Vänern along with the available CryoSat-2 data and the location of the gauge station can be seen in Figure 6.1.

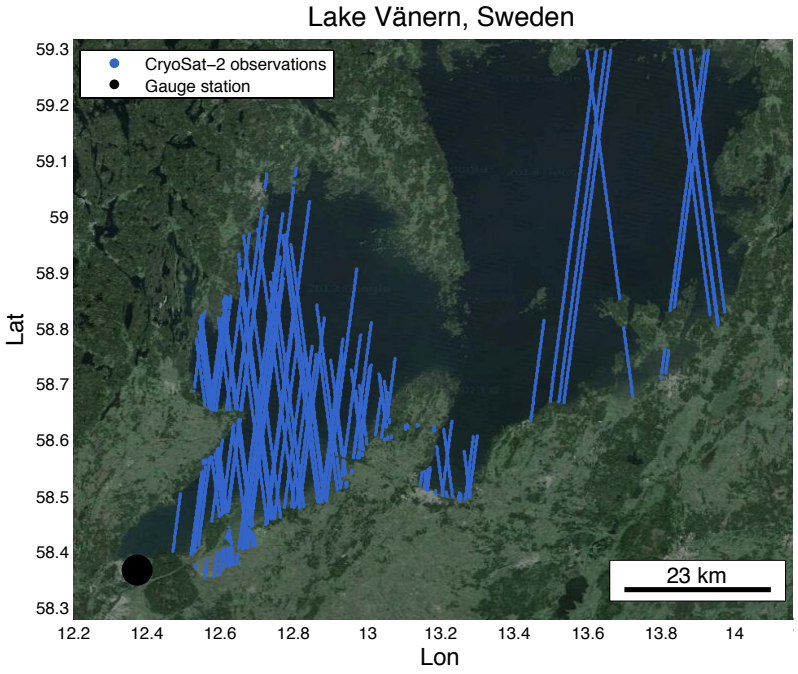

Figure 6.1: Available CryoSat-2 observations in Lake Vänern and the location of the gauge station.

6.2.2 Lake Okeechobee

Lake Okeechobee is the largest freshwater lake in Florida with an area of 1900 km^2 and has an average depth of around 3 m. in situ data from Okeechobee were obtained from the National Water Information System (NWIS, `http://waterdata.usgs.gov/nwis`), and are relative to National Geodetic Vertical Datum of 1929 (NGVD 29). Lake Okeechobee along with the available CryoSat-2 data can be seen in Figure 6.2. In situ data are an average of multiple gauge stations for which the locations are not unknown.

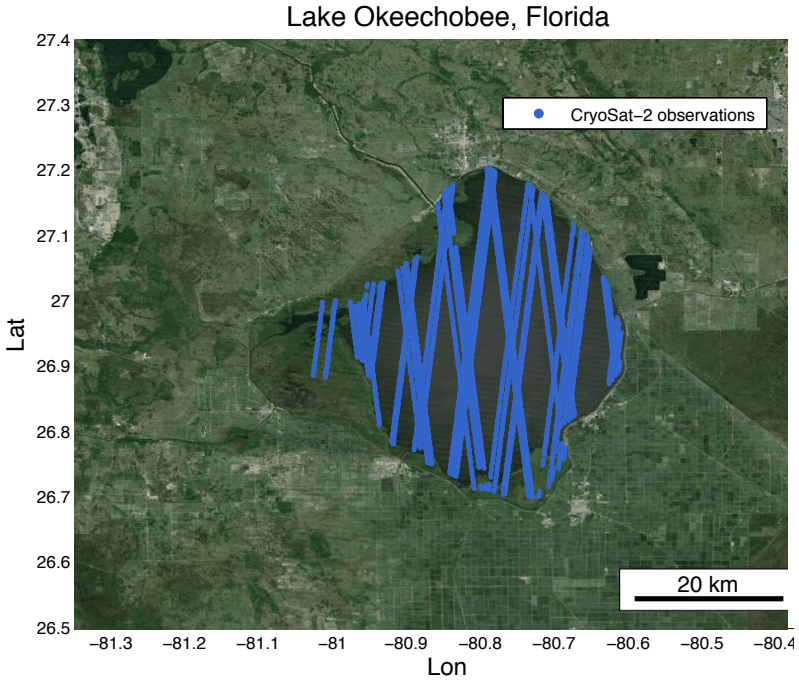

Figure 6.2: Available CryoSat-2 observations in Lake Okeechobee. Gauge stations are spread out along the lake.

6.2.3 Amazon River near Óbidos

The Amazon River is the largest river in the world with respect to discharge and has a dry season width of several kilometres – sometimes as much as 48 km in the wet season. The properties and width of the Amazon River provides a good testing ground for the method developed in this study, since most types of waveforms will be present here. Daily water levels were obtained through the The Observation Service SO HYBAM website (*Cochonneau et al.* (2006), `http://www.ore-hybam.org`). The chosen stretch of the Amazon River along with the available CryoSat-2 data and the location of the gauge station can be seen in Figure 6.3.

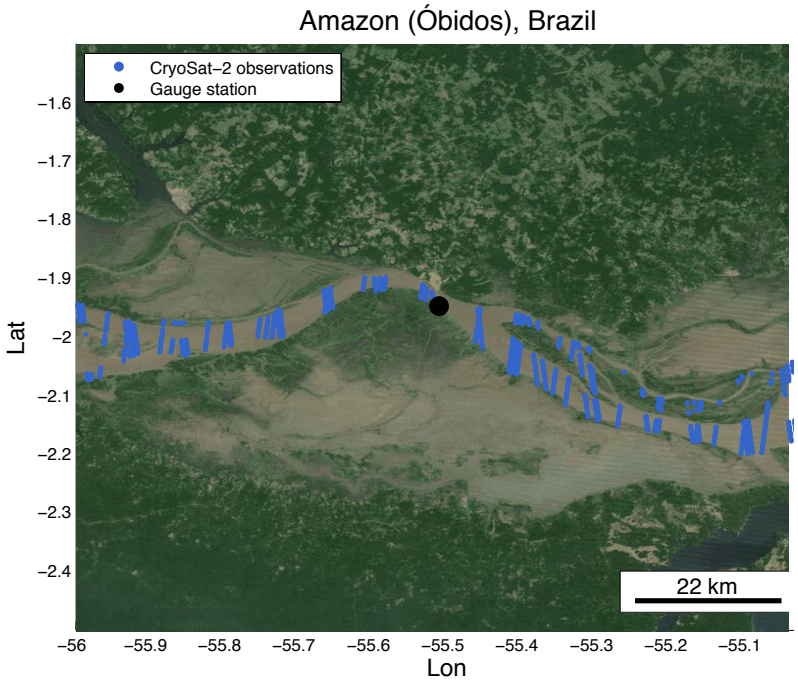

Figure 6.3: Available CryoSat-2 observations in the Amazon River near Obidós, Brazil, along with the location of the gauge station.

6.3 Methods

The MWaPP method is evaluated by comparing the standard deviation of the mean obtained from MWaPP and NPPR, respectively, for the three study regions. In adition, time series along with their RMS errors will be presented. The RMS errors are calculated after removing the offset between the altimetric and the in situ time series. This bias is caused by different height datums and a bias in the retracking correction for the various retrackers.

The standard deviation of the mean is a measure of the mean range precision of all overpasses crossing the water body. The standard deviation, s, is defined as:

$$s = \left(\frac{1}{n-1} \sum_{i=1}^{n} (x_i - \bar{x})^2 \right)^{\frac{1}{2}} \tag{6.1}$$

For each retracking method, a standard deviation is calculated for each overpass before taking the mean of all standard deviations. These mean values are used to compare the range precisions of the different retracking methods.

Once the time series are derived using the mean value of each overpass, the RMS

error is calculated for each retracking method (rm) by comparing the retracked water levels, l_{rm}, compared to in situ (is) water levels, l_{is}. The RMS error is calculated as defined below in Eq.(6.2), where N is the total number of retracked mean water levels available for that particular retracking method. The offset between the in situ and retracked water levels is removed by deriving l_{is}^{corr}, which allows for a more fair comparison as only the relative changes in water level are of interest and not the ability of a retracker to estimate the absolute water level.

$$RMS_{rm} = \sqrt{\left(\frac{\sum(l_{rm} - l_{is}^{corr})}{N}\right)^2} \quad , \quad l_{is}^{corr} = l_{is} + \overline{l_{rm} - l_{is}} \tag{6.2}$$

6.4 Results

Figure 6.4 shows an example of how the MWaPP algorithm works for a track crossing the Amazon River in Brazil on May 9th 2013. The heights retrieved by the MWaPP retracker provide a stable water level, whereas the heights obtained from NPPR are subjected to severe snagging. This allows for keeping four height estimates that would otherwise have to be discarded as outliers. The snagging occurs in the middle of the river, causing a decrease in height estimates of around 8-m, which could be due to contamination from the shore or shallow water on land. An overestimation in the range (underestimation of height) of 8 m corresponds to a distance of around 3.5 km to a bright target assuming that the surface slope is negligible.

Figure 6.5 shows an example for a track crossing Lake Harris in Florida, where the NPPR method overestimates the height of the lake with about 5 m for the last observation above the lake. The MWaPP retracker ignores the earlier peak responsible for the overestimated height and instead finds the peak that corresponds to the lake level at nadir.

Looking at the observed waveforms in Figures 6.4 and 6.5 it is worth noticing that the waveforms received over rivers and lakes do not always have a higher peakiness than the waveforms observed over land. As seen, the waveforms retrieved over land have a much more specular power return, which is probably due to flooded areas that are very shallow and calm compared to the river.

Figure 6.6 shows the retracked heights for the two empirical retrackers for a descending track crossing Lake Vänern in Sweden in October 2011. The track is located just a few kilometres from the shore and is subjected to severe snagging, which is seen in both the height estimates of the NPPR retracker and the jumping window delay. Due to the summation of waveforms the MWaPP retracker is able to determine the correct retracking positions despite the dominating off-nadir bright targets. Usually the range window will be timed so the strongest part of the echo

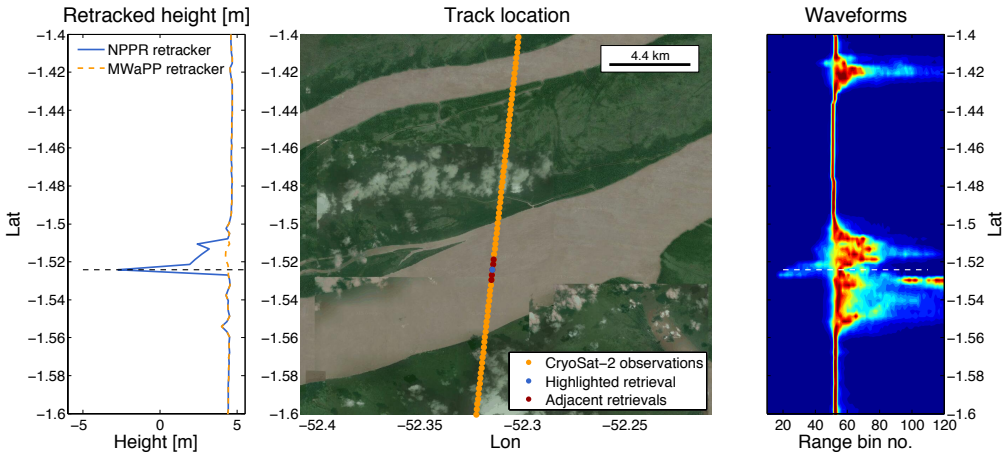

Figure 6.4: Comparison of retracked heights from the NPPR and the MWaPP retracker for a track crossing the Amazon River on May 9th, 2013, along with the track location and the observed waveforms.

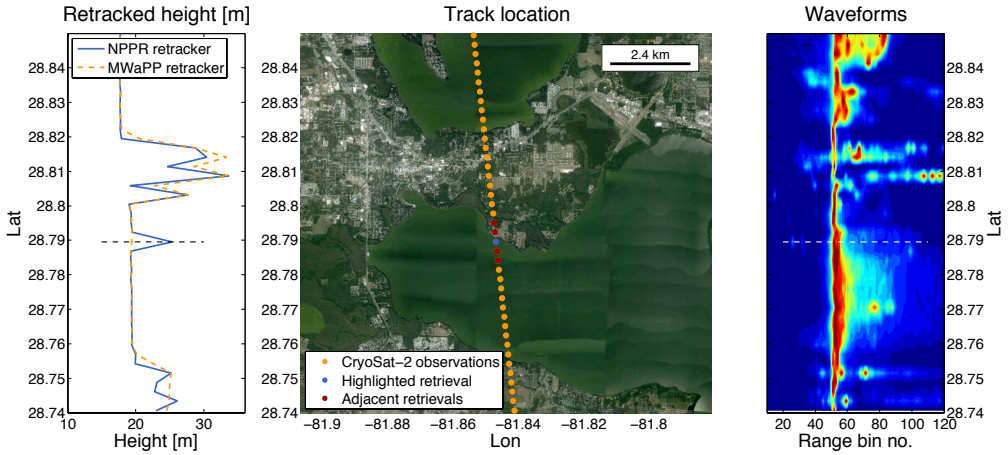

Figure 6.5: Comparison of retracked heights from the NPPR and the MWaPP retracker for a track crossing Lake Harris and Lake Griffin in Florida, US, on June 25th, 2013, along with the track location and the observed waveforms.

will be located around bin 50. However, due to severe snagging from specular targets off-nadir, the actual reflection from nadir is received much sooner in the range window. In this case, some of the correct retracking points where found to be located around bins 6-20 and with a power much lower than the maximum power. For example, the corrected retracking point for the observation around 58.89°N was estimated as bin 5.75 with a power of only 16.7% of the maximum power in the waveform.

A comparison between the NPPR, MWaPP and the ESA L2 heights over the

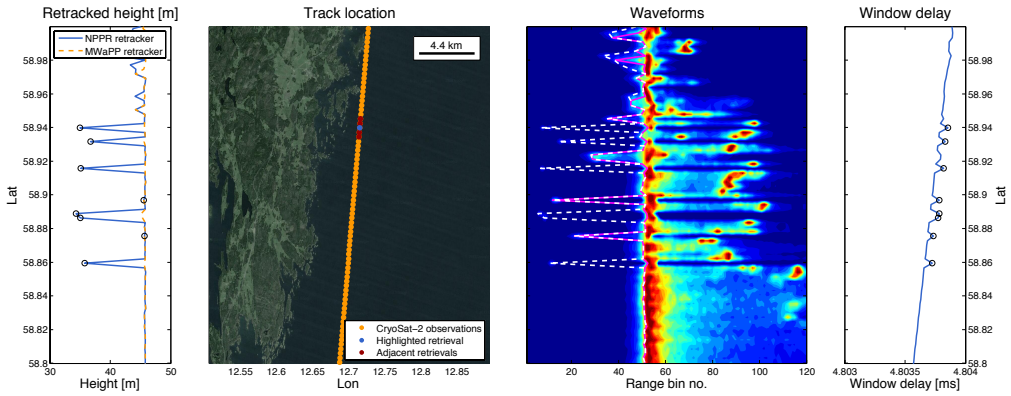

Figure 6.6: Comparison of retracked heights from the NPPR and the MWaPP retracker for a track crossing Lake Vänern on October 31st, 2011, along with the track location, the observed waveforms, and the window delay.

Retracking method	Lake Vänern (∼100)	Lake Okeechobee (∼98)	Amazon River (∼16)
NPPR	15.32 cm	39.23 cm	29.91 cm
MWaPP	9.11 cm	13.35 cm	29.00 cm
ESA L2	53.86 cm	78.82 cm	81.62 cm

Table 6.1: Mean track standard deviations for the different methods for all available tracks over the three study regions. The average number of data points per crossover is shown in parenthesis.

three study areas can be seen in Table 6.1, which contains the mean standard deviation of all track means. Before calculating these values, the data was masked using the GLWD mask presented in Section 4.2.2 and a simple outlier removal method was applied: all height estimates outside two standard deviations were discarded. This was done twice for all tracks and for all retracking methods. As seen, the MWaPP retracker improves the obtained height estimates significantly for both lakes. The MWaPP retracker also provides the lowest standard deviation for the Amazon River, however, the improvement is less distinct.

The time series derived from the two retrackers as well as the in situ data for Lake Vänern are shown in Figure 6.7, where it is seen that the results from the MWaPP retracker fits the gauge data better than the NPPR heights. The same is seen in Figure 6.8, which shows the time series obtained for Lake Okeechobee. It should be noted that the mean of each altimetry data set was aligned with the in situ data. The misfit of the NPPR data can therefore not be explained by a difference in overall water level, as this bias was removed.

Figure 6.9 shows the time series derived over the Amazon River near Óbidos, Brazil. As seen, both retrackers perform well, although not with as high precision as

in the other study areas. As seen, both retrackers struggle to retrieve the right water level during low flow season during winter 2012/2013, where the time series show a series of overestimated height. Looking at the Landsat 7 32-day NDVI composite for November-December 2012, 2013, and 2014 suggests low water levels as well as more dense vegetation i 2012, which could explain the overestimated water levels, if the altimeter sees the canopy and not the river. In general, the MWaPP method often has issues over the Amazon River due to the complex river pattern, which makes it hard to find a stable, common water level.

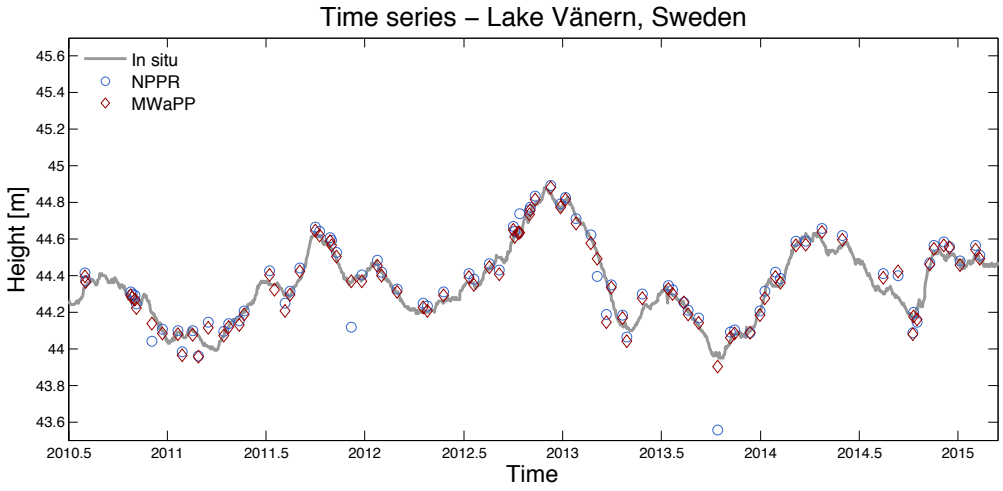

Figure 6.7: Time series obtained from the NPPR and MWaPP methods along with in situ data from Lake Vänern in Sweden.

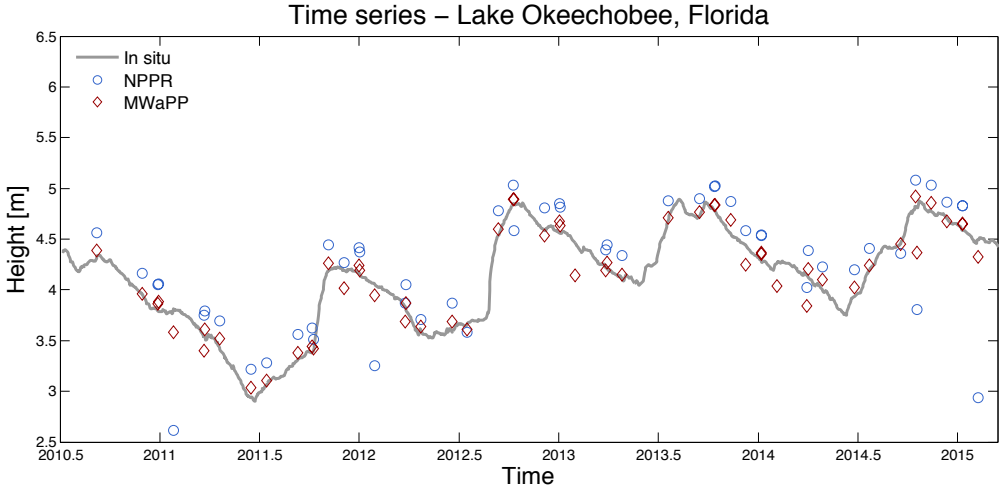

Figure 6.8: Time series obtained from the NPPR and MWaPP methods along with in situ data from Lake Okeechobee in Florida, US.

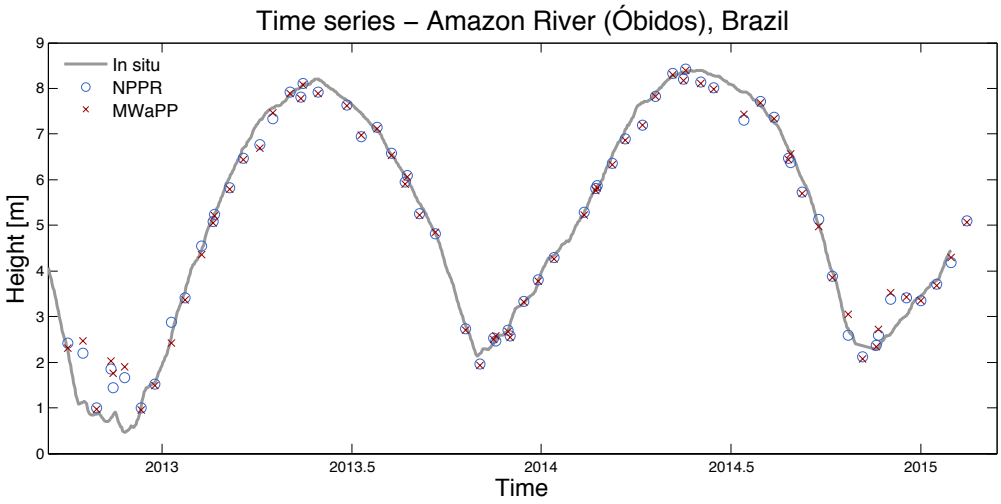

Figure 6.9: Time series obtained from the NPPR and MWaPP methods along with in situ data from a gauge station from the Amazon River near Óbidos, Brazil.

The RMS errors between in situ gauges and the retrieved lake levels are given in Table 6.2, which shows that the RMS error for Lake Vänern is 11.3 cm for the NPPR method but only 5.2 cm for the MWaPP retracker. An even bigger improvement is seen in Lake Okeechobee, where the RMS error drops from 61.8 cm to 12.6 cm, which is roughly 20% of the original RMS error. Many of the outliers causing the higher RMS error of the NPPR data set could of course have been avoided by using more sophisticated outlier detection methods, but the MWaPP method presented in this study allows for retrieval of a higher number of useful heights, which especially in data sparse regions, such as narrow rivers, seems like a better alternative. For the Amazon River the RMS errors from the NPPR and the MWaPP retrackers are very similar, with values of 14.7 cm and 15.0 cm, respectively. As mentioned above, the waveforms retrieved over the Amazon River are highly contaminated - often showing more simple waveforms over vegetated areas, and noisier waveforms over the river, making it hard to identify the correct retracking point. Still, compared to the recent study by *Schwatke et al.* (2015a), the results are very impressive. *Schwatke et al.* (2015a) compared SARAL and Envisat time series to gauge station data for nine different overpasses with river widths between 2.3 and 17.5 km. They used a Kalman filter approach (*Schwatke et al.*, 2015b) for down-weighting of bad data to estimate the time series, which is a far more sophisticated approach than the one used here. They obtained mean RMS errors for Envisat and SARAL of 32.2 cm and 17.5 cm, respectively. The RMS error of 15 cm obtained for CryoSat-2 is in the lower end of their obtained RMS errors, which is very encouraging when the relocation of CryoSat-2 observations is taken into account. In *Berry et al.* (2005), they achieved a correlation coefficient of 0.98 between Envisat data and in situ measurements for a different stretch of the Amazon River. For ERS-1 the correlation was 0.93, and for

RMS errors			
Retracking method	**Lake Vänern**	**Lake Okeechobee**	**Amazon River**
NPPR	10.9 cm	61.8 cm	14.7 cm
MWaPP	5.0 cm	12.6 cm	15.0 cm
ESA L2	47.0 cm	121.9 cm	88.8 cm

Table 6.2: RMS errors between retracked heights and in situ water levels for Lake Vänern and Lake Okeechobee.

TOPEX it was 0.91. Here, the obtained correlation between CryoSat-2 and in situ data in the Amazon River basin reaches 0.99. In *Berry et al.* (2005), the time series were obtained at virtual stations, whereas the CryoSat-2 time series presented here were derived using relocationg of observations. Despite the errors introduced by assuming a linear river profile, the correlation between CryoSat-2 data and in situ measurements is similar, and even slightly higher, than for Envisat.

6.5 Summary

For this study a new algorithm which takes adjacent waveforms into account before extracting the subwaveform to be retracked by a threshold retracker was developed. The results showed that the algorithm provides water levels that are much more stable compared to the NNPR retracker. The mean standard deviation was improved in all study areas, with a maximum reduction in standard deviation of 65% in Lake Okeechobee, where the mean standard deviation went from 39.23 cm to 13.35 cm. Comparing with in situ data the RMS errors were improved significantly, bringing them down from 10.9 to 5.0 cm for Lake Vänern and from 61.8 cm to 12.6 cm for Lake Okeechobee. The MWaPP retracker did not offer similar improvements in the Amazon River, which could be explained by the complexity of the river pattern combined with the river dynamics.

In most cases it would appear that the correct retracking position is always found at the primary peak, however, the example from Lake Harris, Florida, where the NPPR retracker places the retracking position too early in the waveform shows why it would not be enough to simply make the NPPR retracker more sensitive.

The MWaPP retracker was developed for SAR waveforms, but it is also applicable to other altimetry modes. It was found that for SARIn covered regions, it was necessary to perform the oversampling in batches instead of for an entire track, as the topographic variance in SARIn covered regions is challenging for the interpolation steps.

Height estimates similar to those from the MWaPP retracker might be obtainable simply by using a more complex outlier detection method such as presented in

Nielsen et al. (2015a) - however, the results presented here are achieved without unnecessary exclusion of data points, which is preferable over smaller water bodies where the number of observations is already limited.

Chapter 7

Study III: The best of both worlds – combining retrackers

This chapter is based on the work submitted in Villadsen et al. (2015b) and focuses on the combination of SAMOSA3 and empirical retrackers for SAR altimetry. The classification and bias minimization methods are explained and studied in more detail here compared to the paper, and more statistics have been included correspondingly to allow for a method comparison. In addition, the study area in the Amazon River was changed, since in situ data were found for another stretch of the river.

For this study, all CryoSat-2 20 Hz L1b SAR data were retracked by the author. The methods for waveform classification and bias minimization were inspired by the work done by Dr. Nurul H. Idris (Idris, 2014) and carried out under the supervision of Dr. Xiaoli Deng at the University of Newcastle, NSW, Australia. MATLAB codes for the SAMOSA3 retracking algorithms were provided by Dr. Maulik Jain, who, during his PhD studies at DTU Space, investigated the use of SAMOSA3 on CryoSat-2 SAR waveforms retrieved over the Arctic Ocean (Jain, 2015).

7.1 Introduction

Over ocean, physical models are known to give very accurate and precise height estimates as well as information about other geophysical parameters such as SWH and wind speed. It should be kept in mind, that these models were developed for ocean retrievals and are not able to describe most power echoes coming from other surface types, and as such, some waveforms obtained over inland water will be suited for physical retracking, whereas others will need an empirical approach. Combining physical and empirical retrackers would allow us to get the best of both types of retrackers – the accuracy and knowledge about geophysical parameters

from the physical models whenever these are applicable, but also the ability to retrack complex waveforms whenever physical models cannot be used. For this reason, the possibility of combining physical and empirical retrackers for CryoSat-2 data over inland water is investigated in this chapter. Combining retrackers introduces some extra challenges, which were briefly described in Section 3.4 and are treated in more detail here.

The study regions used for the evaluation of the combined method are the same as presented in Section 6.2.

7.2 Retrackers to be combined

For this study the physical SAMOSA3 retrackers (see Section 3.1.2) are combined with one of two empirical retrackers. The combined method uses the physical retrackers whenever possible and an empirical retracker everywhere else. The SAMOSA3 retrackers are either combined with the empirical NPPR method described in Section 3.2.4 or the new MWaPP retracker described in Chapter 6. The SAMOSA-O retracker is used to fit ocean-like waveforms, and SAMOSA-L retracker will be used on specular waveforms. As a reference for the combined methods data sets with purely empirically retracked heights are derived.

7.2.1 Notes on the SAMOSA3 retrackers

It was found that the SAMOSA3 retrackers only provide more precise height estimates compared to the NPPR retracker if the correlation between the fitted waveform and the observed waveform was higher than 99% in the ten bins closest to the estimated retracking point. In many cases ($\approx$40%) the SAMOSA-L model fits the same waveforms that can be fitted with the SAMOSA-O model, and sometimes the SAMOSA-L fit will even be better. Waveforms that are classified as ocean-like are therefore fitted with both the SAMOSA-O and the SAMOSA-L model. If both the SAMOSA-O and the SAMOSA-L models provides fits with correlations higher than 99%, the retracking correction belonging to the model with the lowest sum of errors in the 10 closest bins of the epoch is chosen. This approach is chosen since the correlation did not always reveal the best fit.

7.2.2 Data handling

The data handling consists of several steps as empirical and physical retrackers are combined, which requires some extra precautions. The list below briefly describes the steps of the method. Some of the steps are explained in more details in the following sections.

Step 1. The data are masked with the GLWD described in Section 4.2.2.

Step 2. Waveforms that seem appropriate to retrack using the physical retrackers are isolated by waveform classification as described in Section 7.3. The waveforms are divided into 12 classes based on the shape of the power echoes using a Naive Bayes classifier. The Naive Bayes classifier was set up using a training set of approximately 6000 waveforms over inland water. This training set consists of most waveform types and was used for all three study regions.

Step 3. All waveforms are retracked using the NPPR retracker and the MWaPP retracker. In addition, suitable waveforms are retracked using the SAMOSA-O and SAMOSA-L retrackers depending on the classification results. A result from one of the SAMOSA3 retrackers is accepted if the correlation between the observed and the modelled waveform is higher than 99%.

Step 4. The worst outliers are removed by discarding all observations more than two standard deviations from the track mean. This outlier detection is performed twice. Tracks with fewer than six observations left are excluded from the study.

Step 5. For the retracking procedure where the physical and empirical retrackers are combined, the bias between the retracked heights are minimized using either a mean method, or by using a neural network approach as done in *Idris* (2014) with a training set of 30%. To train the neural network either the NPPR retracker or the proposed MWaPP retracker is used. This leaves us with five datasets:

(a) NPPR: Heights obtained using only the NPPR retracker

(b) MWaPP: Heights obtained using only the proposed empirical retracker

(c) Combined (NPPR) + mm: Heights obtained using a combination of the SAMOSA3 and the NPPR retracker. The bias was minimized using a mean method approach with the NPPR data.

(d) Combined (NPPR) + nn: Heights obtained using a combination of the SAMOSA3 and the NPPR retracker. The bias was minimized using the NPPR heights for the training set.

(e) Combined (MWaPP) +mm: Heights obtained using a combination of the SAMOSA3 and the proposed MWaPP retracker. The bias was minimized using the MWaPP heights for the training set.

(f) Combined (MWaPP) + nn: Heights obtained using a combination of the SAMOSA3 and the proposed MWaPP retracker. The bias was minimized using the MWaPP heights for the training set.

(g) SAMOSA-O: Heights obtained using *only* the results from the traditional SAMOSA3 model for ocean-like waveforms.

In addition, the corresponding results of the ESA L2 product will be shown for comparison.

Step 6. For each track a mean is calculated, which is to be used for time series. The standard deviation of the mean is listed as a measure of method precision.

Due to the slope of the Amazon River, the track means used to derive the time series are detrended in the zonal direction similar to *Villadsen et al.* (2015a) using the retracked heights derived in this study. From the obtained CryoSat-2 heights, the slope is estimated to be around 1 m per degree longitude.

For Lake Vänern and Lake Okeechobee the track means obtained from the various retracking methods are compared with in situ data. The offsets between the retracked data and the in situ data are removed prior to creating the time series by adjusting the level of the retracked data sets so the time series have the same mean values as the in situ data. As such, the accuracy of the altimetric heights will not be discussed. Instead, the comparison is performed by looking at the RMS error.

When precision is mentioned in this study it refers to the precision of the mean (as in *Nielsen et al.* (2015a)), i.e. the mean standard deviation of all tracks crossing each study area.

7.3 Waveform classification over inland water

To have an indication of which retracker to use, all observations are classified based on the shape of the power waveform and assigned the most appropriate retracker. This is an easy way to avoid unnecessary, time-consuming model fitting of all waveforms.

Firstly, a training set consisting of a high number ($\sim$5000) of waveforms retrieved over inland water are classified using k-means clustering (*Seber*, 2008) to get a rough estimate of the number of classes that could possibly be retrieved from any kind of river or lake. In this way it will be possible to classify and compare the observed kinds of waveforms over any water body in the same manner independent of inland water type or data availability. It was found that dividing the power echoes into 12 classes using the k-means clustering was the best approach.

Using this training set, each track crossing one of the study regions is then divided into the predefined 12 classes using a supervised Naive Bayes classifier (*Manning et al.*, 2008), which consists of two steps, 1) a training step - which is where the results from the k-means classification is used, and 2) a prediction step where the data set of interest is divided into the most appropriate of the previously defined classes. Using a combination of k-means and Naive Bayes, waveforms can easily

be classified in the same manner independent of the available types of waveforms in the current track and study region.

After classification all power echoes are assigned one of three retrackers depending on the pulse peakiness and number of major peaks in the corresponding class. Per default, all waveforms are retracked using the empirical retrackers, as such there is no need to isolate these waveforms but only those to be retracked with the SAMOSA3 retrackers. Ocean-like waveforms are found by identifying the classes with a cluster centroid peakiness between 0.02 and 0.05 and with only one peak higher than 40% of the maximum power. These waveforms will be flagged for the SAMOSA-O retracker. Specular waveforms are isolated by finding the classes with a cluster centroid peakiness higher than 0.1 and only one peak higher than 40% of the maximum power. These specular waveforms are flagged for the SAMOSA-L retracker.

The cluster centroids of the 12 training classes obtained from the k-means classification as well as the retracker they are assigned are shown in Figure 7.1. Looking at the shape of the 12 classes, some of the classes containing peaky waveforms could be merged as they appear very similar, this was however not found necessary for this study. Choosing a lower number of classes, such as 9 or 10, did not remove these peaky classes.

7.4 Reducing biases between retrackers

When switching from one retracker to another a discontinuity is introduced, which has to be minimized. In this study, the bias is minimized using two different methods following the approach presented in *Idris and Deng* (2013):

1. Using a mean method by simply adding the mean bias to all SAMOSA3 height estimates.
2. Using a neural network to minimize the bias since the bias is not constant everywhere, but e.g. seems to depend on the distance to the shore of the inland water body.

7.4.0.1 Mean method approach

Here the offset between the SAMOSA3 retrackers and the empirical threshold retracker is minimized by subtracting the mean difference from the SAMOSA3 retracked heights. The mean difference for each study area, a, is determined by comparing the results from the empirical retracker, h_e, and the chosen SAMOSA3 retracker, h_p, for each observation, i, where a SAMOSA3 retracker is found suitable.

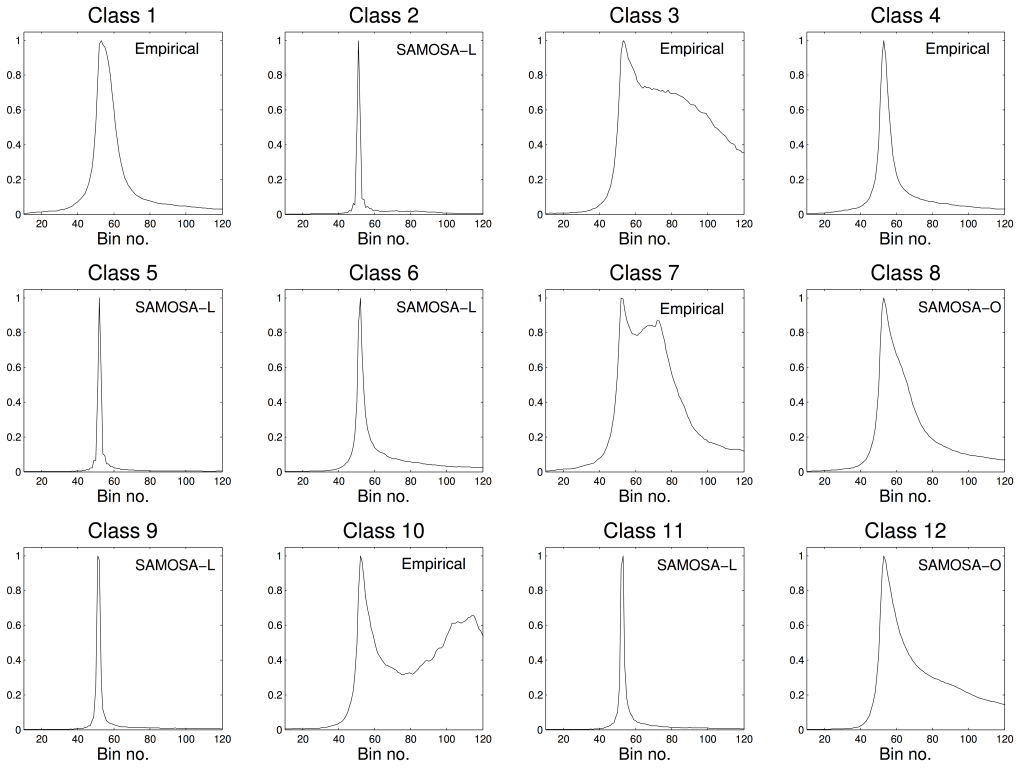

Figure 7.1: Normalized cluster centroids as determined from the k-means classification of the power waveforms as well as the retracking method suggested for the waveforms belonging to each class.

$$mm_a = \sum_{i}^{N} h_e^i - h_s^i \tag{7.1}$$

The mean method reveals mean differences of around 13 cm, 13.9 cm and 12.4 cm for Lake Vänern, Lake Okeechobee, and the Amazon River, respectively. The mean method has previously been used in studies like *Deng* (2003) and *Idris* (2014). The method is very simple and can be used no matter how many observations are available; however, a problem with this method is that it assumes that the difference is constant over the water body as it applies the same correction everywhere. Our studies showed that the offset in some cases seem to depend on the distance to the shore - probably a result of the differences in significant wave height. The reason for the variations in retracker offset are not investigated in this study; instead another and more dynamic method is tested.

7.4.0.2 Neural network approach

Using a neural network approach to estimate and minimize the bias will help alleviate the differences in the bias that exists between central and coastal parts of the water bodies. The neural network develops a model, which describes the relationship between the two retrackers - a model based on fuzzy logics that is able to describe functions that would be hidden to the human eye or too complex to describe with mathematical functions. Neural networks can simulate the behaviour of complex systems without any a priori knowledge of the internal relations within the system (*Haykin*, 1994).

Here, a multi-layer feed forward neural network is used. It is trained with a back-propagation learning algorithm, which is the most popular type of neural network. More details on the feed forward model and the back propagation learning method can be found in *Rao and Mandal* (2005) and *Haykin* (1994). Neural networks have become more common for various purposes within in civil and ocean engineering and have amongst other things been used for rainfall forecasting (*French et al.*, 1992), forecasting of runoff (*Crespo and Mora*, 1993), and forecasting of ocean wave heights (*Deo and Naidu*, 1999). The neural network approach has previously proven useful for minimizing retracker offsets in *Idris* (2014), where the 20 Hz Jason-1 and Jason-2 data were retracked using several both empirical and physical methods in the Great Barrier Reef in Australia in order to obtain useful height estimates closer to the coast.

For this study the training set is chosen to consist of 30% of all observations where the waveform could be fitted by one of the SAMOSA3 retrackers - the 30% were chosen randomly. In the training mode the weights within the model are adjusted until the input (SAMOSA3 heights) matches the target output (the threshold retracker derived heights), i.e. when the sum of the squared differences between

the computed and desired output values are minimized. When the training mode is finalized a model capable of estimating the bias is achieved. When the model has been trained it is applied to all available observations retracked with the SAMOSA3 retrackers.

7.5 Results

7.5.1 Waveform classification

The spatial distributions of the used retrackers for Lake Vänern, Lake Okeechobee, and the Amazon River are shown in Figures 7.2, 7.3, and 7.4, respectively. The results reveal that all three types of retrackers (SAMOSA-O, SAMOSA-L, and empirical) are seen in each study area. The degree to which they are used, however, depends on the characteristics of the water body.

In Lake Vänern, which is the largest lake in this study, the SAMOSA-O retracker is the most commonly used retracker in the central parts of the lake and is used for 32.9 % of all waveforms retrieved over the lake. For some of the ocean-like waveforms the SAMOSA-L retracker provides a better fit, and especially in the south borders of the western part of the lake the SAMOSA-L retracker is used to fit more specular waveforms near the shore. In 51 % of the cases the empirical retracker is chosen, especially in the vicinity of the shore where the waveforms get more complex due to contamination from land signals. It should be noted, that the apparent lack of data availability in the eastern part of Lake Vänern is due to the seasonally changing geographical mode mask of CryoSat-2, which makes the altimeter operate in LRM mode in the eastern part of the lake for most of the year.

For Lake Okeechobee the same pattern is seen with slightly more waveforms retracked with the lead adaptation of the SAMOSA3 retracker. The two tracks far to the west, that appear to cross a part of the lake that is more shallow than the rest, are not surprisingly classified as specular waveforms.

The distribution of assigned classes is slightly different in the Amazon River (see Figure 7.4 with a larger number of empirically retracked waveforms. This agrees well with our expectations, as the Amazon River is smaller in size and has a channel pattern that is more complex compared to the regular shapes of the lakes. All of these characteristics are bound to produce more waveforms that are either noisy or specular, which the SAMOSA-O model will not be able to fit. It is also seen that the specular waveforms are found in the narrow parts of the Amazon and its tributaries, whereas the SAMOSA-O model is mostly used for waveforms retrieved over the wider stretches.

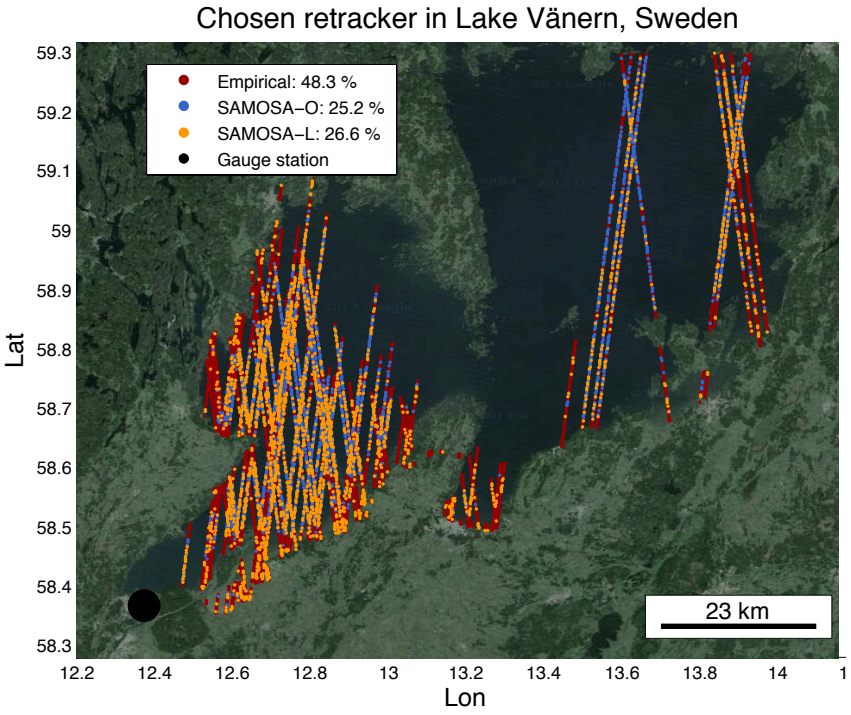

Figure 7.2: Classification results over Lake Vänern in Sweden along with the location of the field gauge station.

7.5.2 Comparison of retrackers for a couple of tracks in the Amazon and Lake Vänern

To compare the different retracking methods some examples of the results for a track crossing Lake Vänern and the Amazon River are shown in Figures 7.5 and 7.6, respectively.

Looking at the detailed plot in Figure 7.5(c), it is seen that the combined methods using the NPPR method provide results very similar to those of the NPPR method. Although not shown, the same was seen for the combined method using the MWaPP retracking method.

The example over the Amazon River in Figure 7.6 shows that the two pure empirical retrackers give similar results for most waveforms. The results from the combined methods using NPPR heights are slightly different from those obtained by the empirical retrackers. It was also observed, but not shown here, that the results from the combined method using the neural network approach varied a lot between each time the neural network model was invoked regardless of the size of the training set used for the neural network.

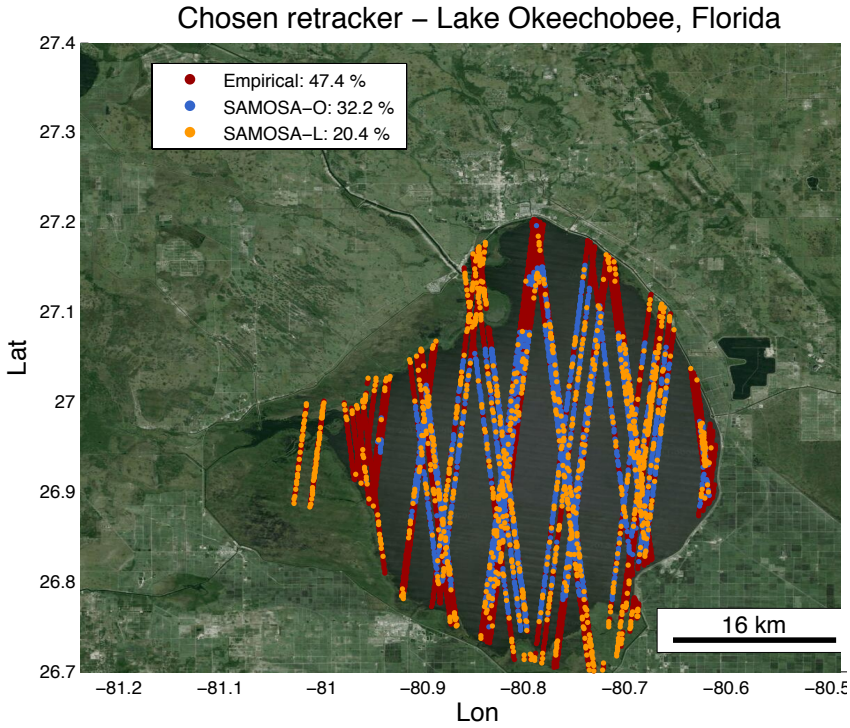

Figure 7.3: Classification results over Lake Okeechobbe in Florida, USA.

7.5.3 Standard deviations of overpasses

For each study area the standard deviation of the mean is given in Tables 7.1 and 7.2. Table 7.1 lists the standard deviation of the mean using all observations, and Table 7.2 lists the same statistics but only for the observations where both the SAMOSA-O and SAMOSA-L retrackers could have been used, respectively. The latter comparison was done to see how well the SAMOSA-O retracker performs compared to the empirical retrackers without the noise that is introduced when combining the retrackers.

From Table 7.1 it is seen that the MWaPP retracker has the lowest standard deviation of 9.11 cm over Lake Vänern, which is to be expected since this method will alleviate some snagging cases that a simple outlier removal method will not detect. The combined methods where the MWaPP retracker has been used together with one of the two bias minimization methods also perform well with a mean standard deviation of around 9.8-9.9 cm. The performance of the NPPR retracker is not as good with standard deviations around 15-16 cm for both the purely empirical and the combined data sets. The same pattern is seen for Lake Okeechobee and the Amazon River: the methods that perform the best are those using the MWaPP retracker. The combined method only offers an improvement over the Amazon River,

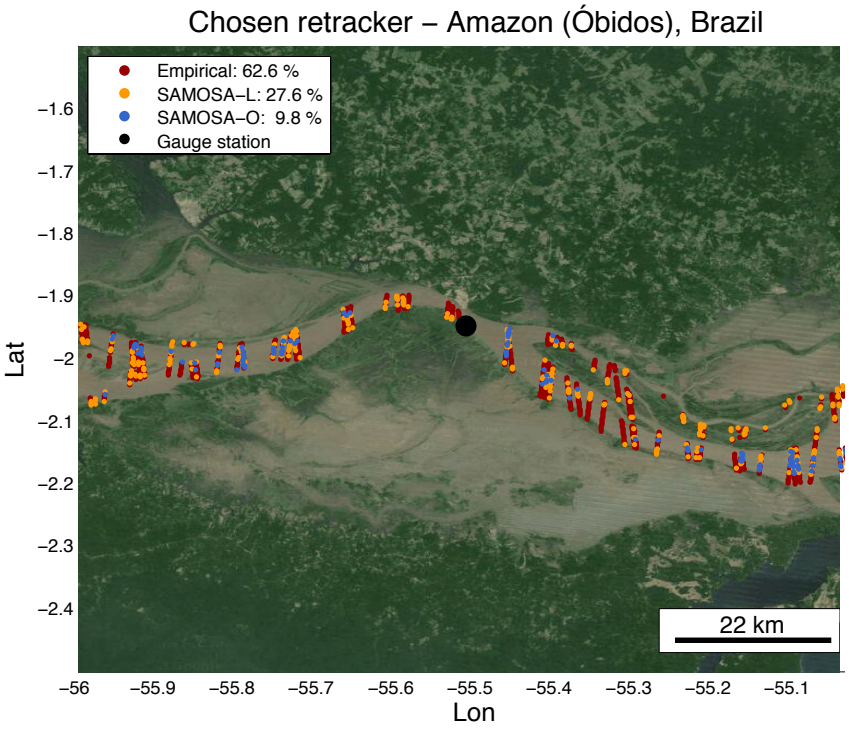

Figure 7.4: Classification results over the Amazon River in Brazil along with the location of the field gauge station.

which is surprising as this study area is the one with the least number of heights obtained with the SAMOSA-O retracker.

For comparison the results from the ESA L2 product have been included. It should be noted that the L2 product from ESA does not provide stable heights over inland water, and it is therefore preferable to use other retrackers. In general, standard deviations are expected to decrease with increasing size of the water body, which is what is seen for the methods that perform the best.

As mentioned above, Table 7.2 shows the standard deviations *only* including retracked heights obtained from waveforms that could be fitted with both SAMOSA3 retrackers, which leaves us with only the well-behaved waveforms. Looking at only these waveforms allows for a fair comparison of the various retrackers, and as expected the precision increases in general for all retracking methods. Comparing precisions between study areas becomes somewhat misleading, as the number of remaining observations for the smaller water bodies is very low (e.g. 3-4 SAMOSA fits per Amazon track). One should therefore only compare values for the same study area.

For Lake Vänern it is seen that the highest precisions are obtained when using

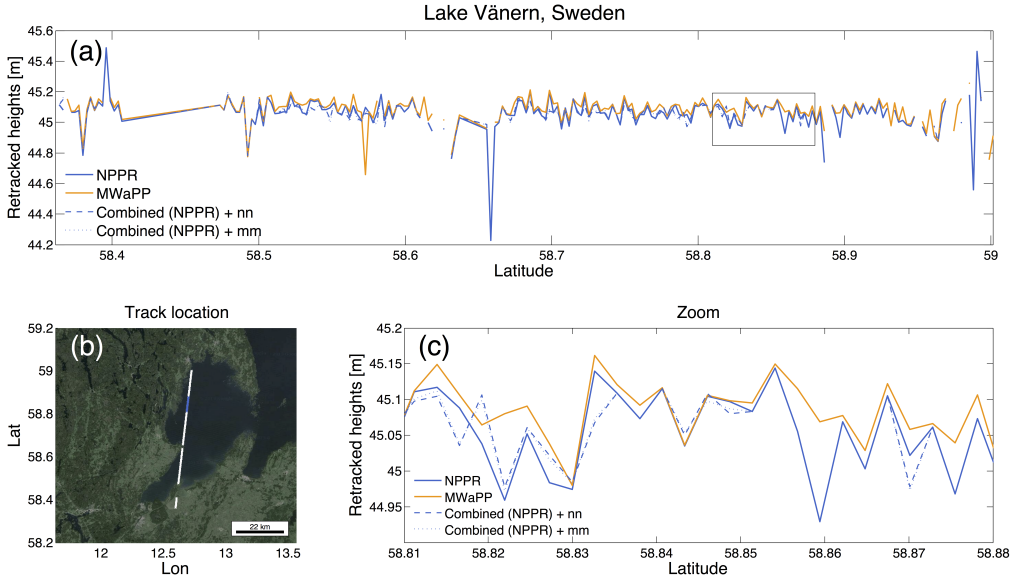

Figure 7.5: (a) Comparison of retracking methods over Lake Vänern for a track on October 31st, 2011. (b) Track location across the lake. Highlighted (blue) points mark the observations shown in the detailed plot of (a) in (c).

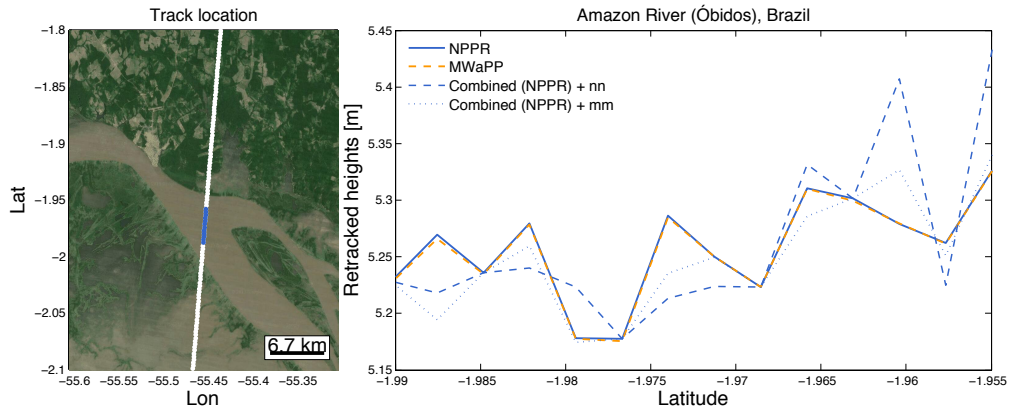

Figure 7.6: Comparison of retracking methods over the Amazon River for a track crossing the river on June 28th, 2014.

just the SAMOSA-O retracker, which is expected considering the size of the lake.

For Lake Okeechobee the lowest standard deviations are once again obtained when using only the SAMOSA-O retracker, but for the Amazon River the methods that performs best are those using the NPPR method - in particular the combined method using a neural network to minimize the bias. It should be noted that for all methods apart from the ESA L2 product, the standard deviations only vary around 1 cm (1.1 cm for Lake Vänern, 0.5 cm for Lake Okeechobee, and 0.7 cm for the

Retracking method	Lake Vänern (∼100)	Lake Okeechobee (∼98)	Amazon River (∼16)
NPPR	15.32 cm [98]	39.23 cm	29.91 cm
MWaPP	**9.11 cm** []	**13.35 cm**	**29.00 cm**
Combined (NPPR) + nn	15.94 cm	40.05 cm	29.96 cm
Combined (NPPR) + mm	15.99 cm	40.07 cm	29.90 cm
Combined (MWaPP) + nn	9.82 cm	13.80 cm	29.54 cm
Combined (MWaPP) + mm	9.94 cm	13.88 cm	29.46 cm
ESA L2	53.86 cm	78.82 cm	81.62 cm

Table 7.1: Mean track standard deviations for the different methods for *all* available observations. The name of the retracking method is written in a way so that "Combined (MWaPP) + nn" refers to the results from the combined method using the MWaPP retracker, and where the bias was minimized using a neural network trained with the results from the combined method and the MWaPP method. The average number of data points per crossover is shown in parenthesis.

Amazon River).

7.5.4 Time series

The time series obtained for the three study areas are shown in Figures 7.7, 7.8 and 7.9. For all three study areas the available in situ water levels have been included for comparison and the corresponding RMS errors are given in Table 7.3. As in the previous chapter, RMS errors are calculated after removing the offset between the altimetric and the in situ time series.

The temporal changes for Lake Vänern in Figure 7.7 are captured well with all the methods used in this study. The lowest RMS errors are obtained with the SAMOSA-O retracker, but it should be noted that the SAMOSA-O data set only include results from the well-behaved waveforms. Comparing the RMS errors obtained from the NPPR and MWaPP methods for only these observations reveal similar performances.

The time series for Lake Okeechobee reveal that the mean values from MWaPP and the combined method with MWaPP values are almost identical. In fact, the mean absolute difference is only half a centimetre. Looking at the RMS errors, the same thing as in Lake Vänern is seen, i.e. that the MWaPP retracker provides heights that follow the in situ levels much closer than the NPPR method, and that combining the physical and empirical retrackers only provide slightly lower RMS errors.

For the Amazon River, the RMS errors are significantly higher, which is not

Retracking method	Lake Vänern (∼20)	Lake Okeechobee (∼25)	Amazon River (∼2)
NPPR	5.31 cm	4.35 cm	3.16 cm
MWaPP	5.17 cm	4.32 cm	3.48 cm
Combined (NPPR) + nn	4.73 cm	4.40 cm	**2.80 cm**
Combined (NPPR) + mm	5.17 cm	4.30 cm	3.06 cm
Combined (MWaPP) + nn	4.76 cm	4.26 cm	3.28 cm
Combined (MWaPP) + mm	4.85 cm	4.18 cm	3.06 cm
SAMOSA-O	**4.23 cm**	**3.94 cm**	3.37 cm
ESA L2	9.62 cm	9.91 cm	4.75 cm

Table 7.2: Mean track standard deviations for the different methods for waveforms where *both* SAMOSA3 retrackers have correlations higher than 99%. The name of the retracking method is written in a way so that "Combined (MWaPP) + nn" refers to the results from the combined method using the MWaPP retracker, and where the bias was minimized using a neural network trained with the results from the combined method and the MWaPP method. The average number of data points per crossover is shown in parenthesis.

surprising, since the river is a much bigger challenge due to the river pattern. Still, the altimetry data still captures the seasonal pattern very well, resulting in a RMS error around ∼15 cm. The lowest RMS error is obtained with the NPPR method, which also showed the lowest standard deviation of the mean in 7.2.

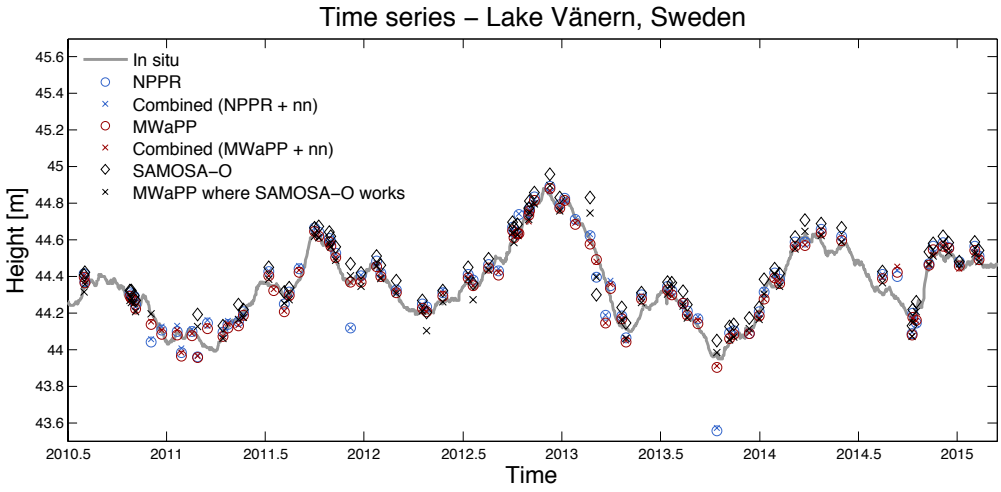

Figure 7.7: Time series for CryoSat-2 data retrieved over Lake Vänern alongside the in situ data from SMHI.

In general, results from all retrackers are quite good, but it is clear that the MWaPP retracker adds something very valuable and allows us to retrieve heights

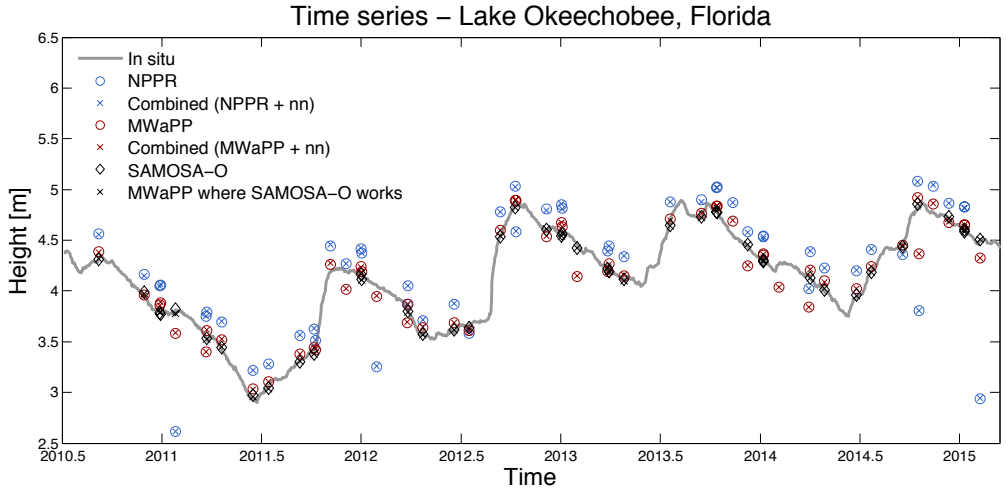

Figure 7.8: Time series for CryoSat-2 data retrieved over Lake Okeechobee alongside the in situ data from NWIS.

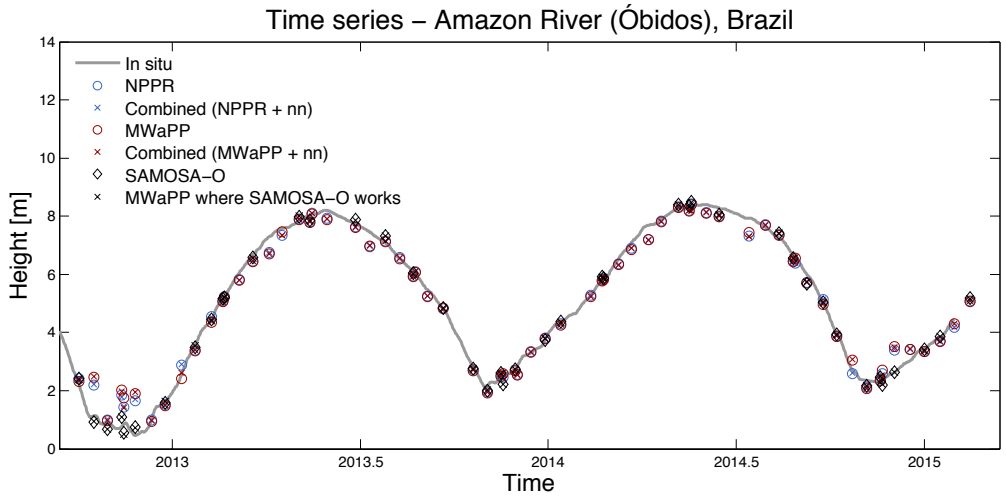

Figure 7.9: Time series for the data retrieved over the Amazon river alongside the in situ data from HYBAM.

that would otherwise be flagged as outliers and discarded. The method has a very low computational cost compared to the SAMOSA3 model, and although the results from the SAMOSA3 retracker are better, i.e. have higher precisions and lower RMS errors, it is debatable whether or not the time consuming implementation and fitting is worth the gain in precision. The results presented here also indicate that the bias issues that are introduced when combining retrackers mask the potential benefits of such a method.

It should be noted that many of the outliers causing the higher RMS errors of

Retracking method	Lake Vänern	Lake Okeechobee	Amazon River
NPPR	10.9 (5.1) cm	61.8 (2.4) cm	33.3 (14.7) cm
MWaPP	5.0 (3.8) cm	12.6 (2.4) cm	38.5 (15.0) cm
Combined (NPPR) + nn	10.9 cm	61.6 cm	33.2 cm
Combined (NPPR) + mm	10.9 cm	61.6 cm	32.9 cm
Combined (MWaPP) + nn	5.1 cm	12.3 cm	38.3 cm
Combined (MWaPP) + mm	4.9 cm	12.5 cm	37.2 cm
SAMOSA-O	3.5 cm	2.1 cm	15.3 cm
ESA L2	47.0 cm	121.9 cm	88.8 cm

Table 7.3: RMS errors between retracked heights and in situ water levels for Lake Vänern, Lake Okeechobee, and the Amazon River. The numbers in the parentheses are the same statistics but only including the observations where the SAMOSA-O retracker could be used.

the NPPR data set could have been avoided by using more sophisticated outlier detection methods, such as done in *Nielsen et al.* (2015a), but the MWaPP method presented in this study allows for retrieval of a higher number of useful heights, which is preferable especially in data sparse regions.

There is no doubt that the SAMOSA3 retracker provides very stable water levels. The benefit of using the retracker is, however, concealed in regions of inland water where complicated waveforms are repeatedly encountered and an empirical retracker is needed as well. Trying to avoid the offset by adjusting the 80% threshold level for the empirical retrackers was unsuccessful. Therefore, the offset is reduced using the neural network in this study.

After this study was completed, some issues with the SAMOSA3 implementations were realized. The current implementation follows that of *Jain* (2015), which normalizes all waveforms prior to the fitting procedure, meaning that the amplitude, P_u, is not fitted, but always set to 1. This will of course affect the estimated retracking corrections, and a new implementation of the SAMOSA3 model is currently under developtment and will be evaluated. The results from the SAMOSA3 retracker are, however, very good, and the improvements caused by the new implementation are expected to be minor.

7.6 Summary

In this study a number of novel methods for retracking SAR waveforms over inland water are presented. The MWaPP retracker provides a new way of taking adjacent waveforms into account during retracking to find the subwaveform that

is most likely to hold the echo from the water body at nadir. A combined method that uses an empirical retracker as well as the SAMOSA3 model with retracking offsets minimized using a neural network approach was also presented. The results showed that the SAMOSA3 model provides results with high precisions. However, the results were not much better than those obtained using the empirical MWaPP retracker presented in this study.

When combining the physical and empirical retrackers, the higher precision of the SAMOSA3 model is concealed by the retracking offsets even after these were minimized using a neural network. Due to these findings it is suggested using the proposed MWaPP retracker in regions where most waveforms cannot be retracked by the SAMOSA3 model. In bigger lakes with a high number of observations it could prove more beneficial to use the SAMOSA3 retrackers, especially if information on significant wave height or roughness is desirable, and simply discard waveforms where an acceptable fit is not obtainable. To further improve precisions and RMS errors, it is advised to use a more sophisticated method for outlier detection and determination of robust mean water levels such as described in *Nielsen et al.* (2015a).

Finally, it should be noted that the methods derived here are used on CryoSat-2 data, but should be easily applicable to any SAR data (such as from the upcoming Sentinel-3 mission) with only a few simple adjustments of the many parameters in the SAMOSA3 model. Sentinel-3 and its SRAL SAR altimeter will improve the possibilities for inland water monitoring even further with the repeat orbit of 27 days.

Chapter 8

Summary, conclusions, and outlook

This chapter contains a brief summary of the challenges and findings of the work presented in this thesis, as well as a short outlook on planned satellite missions that show great promise for further studies on inland water monitoring.

8.1 Summary and conclusions

The field of satellite altimetry for land hydrology has advanced significantly in recent years. Water levels from satellite altimetry have become notably better, and the hydrological community has accepted satellite data as an aid in hydrological modelling as the number of in situ gauges has decreased.

The focus of this PhD was to develop methods for SAR mode altimetry from the CryoSat-2 mission to obtain stable lake and river levels. The CryoSat-2 mission is very different compared to earlier missions used for inland water monitoring for two reasons: 1) The SIRAL altimeter has the ability to work in SAR mode, where the along-track resolution is increased to 300 m, which reduces themeasurement footprint of the altimeter significantly, resulting in less contaminated waveforms obtained over smaller lakes and rivers. 2) CryoSat-2 flies in a geodetic orbit with a repeat period of 369 days and subcycles of 30 days, which is atypical for inland water monitoring. Together, the 30-day subcycles ensure a great spatial coverage, which can be utilized.

The first study of this thesis mainly dealt with the derivation of time series in the Ganges-Brahmaputra River basin. This area is of great interest to the hydrological community, and was chosen as a study region following a request from the hydrologists within the LOTUS project group. This river basin is a perfect example of a

region, where the number of river gauges is decreasing and any existing data are confidential between countries, although the river discharge is of vital importance to the community and the basin is one of the biggest in the world.

The geographical mode mask of CryoSat-2 allowed a comparison of results from all three modes of the SIRAL altimeter against conventional altimetric time series provided by Envisat. A method was developed to create virtual stations for CryoSat-2 by relocating observations up- and downstream, as CryoSat-2 does not provide data on traditional virtual stations. Despite the relocation, the derived time series captured annual signals similar to those of Envisat. Although obtaining time series over these rivers required some additional steps, the results clearly showed that CryoSat-2 is able to contribute to river monitoring even though this was expected due to the geodetic orbit. Unfortunately, without in situ data it is hard to draw any conclusions about whether Envisat or CryoSat-2 provides the best height estimates.

Chapter 5 also showed that it is possible to detect flooding events. By looking at flood events in Bangladesh (2014) and Thailand (2011) changes were detected not only as higher surface elevations as the land became inundated, but also as increases in peakiness and backscatter of the radar echoes.

While studying the highly contaminated waveforms over Brahmaputra and Ganges, it became evident that obtaining a stable water level would either require a very strict outlier detection method, or a different retracking approach. In areas where the number of observations is low to start with, it is preferable to keep as many observations as possible. For this reason, the Multiple Waveform Persistent Peak (MWaPP) retracker was developed. The MWaPP retracker identifies the subwaveform most likely to represent the water level at nadir by looking at adjacent waveforms before choosing the subwaveform to retrack. Some results from this new method were presented in Chapter 6, and they revealed some very promising improvements, especially when comparing time series from Lake Okeechobee and Lake Vänern with in situ data. The MWaPP method brings down the RMS errors from 10.9 to 5.0 cm in Lake Vänern, and from 61.8 cm to 12.6 cm in Lake Okeechobee. The Amazon River proved to be a more difficult task for the MWaPP method, which is most likely due to the difficulty of finding a common water level in an area where a static water mask is very inadequate, and where the observations across the river are discontinuous due to a complex river pattern.

Up until now, inland water levels from altimetry have always been derived using empirical retrackers due to complex waveform shapes. However, with the introduction of SAR it becomes more plausible to use a physical model over inland water bodies as the risk of violating the assumptions for the model decreases tremendously with the smaller Doppler footprint. Unfortunately, a lot of the retrieved waveforms will still be unsuited for a physical model. Chapter 7 looked into the possible benefits of combining the physical SAMOSA3 model with an em-

pirical retracker. By doing so, it is possible to obtain the very accurate heights from SAMOSA3, while still getting height estimates with the empirical approach when the waveforms are too complex for the physical model. When comparing with in situ data, our results show that the empirical retrackers are able to obtain heights that constitute time series with RMS errors similar to those obtained only from SAMOSA3 height estimates. Of course, a physical model offers knowledge about additional parameters as well, such as significant wave height and wind speed, however, these parameters are seldom of interest for inland water altimetry and were outside the scope of this work.

8.2 Outlook

From the CryoSat-2 studies presented here the benefits of SAR and SARIn altimetry compared to LRM are undeniable. With this is mind, there are two upcoming missions that look particularly promising for the future of inland water altimetry. One of these missions is the Sentinel-3 mission, which was supposed to be the main focus of this thesis before the mission launch was delayed. The other is the Surface Water & Ocean Topography (SWOT) mission, which is planned for launch around 2020.

With the launch of Sentinel-3 in February 2016, the community got the first altimetry mission with global SAR mode coverage. This ensures that all rivers will be observed with an along-track resolution of 300 m, facilitating the measurement of narrow rivers and small lakes. The measurements obtained with the SRAL altimeter carried by Sentinel-3 will be almost identical to those from the SAR mode observations from SIRAL/CryoSat-2, and as such, the methods developed here should be directly applicable. In addition, the 27-day repeat orbit of Sentinel-3 will be much more appropriate for river monitoring, making it easier to derive traditional time series. In this work, the many crossovers of CryoSat-2 were used to derive time series by relocating the observations. With the repeat tracks of Sentinel-3 there will be fewer crossovers, but the observations will once again be located at virtual stations as known from Envisat and SARAL studies. With its geodetic orbit, CryoSat-2 offers us an opportunity to study the rivers in much higher spatial detail, while still allowing us to derive time series. Combining SAR derived heights from CryoSat-2 and Sentinel-3 could provide the hydrological community with altimetric time series of unprecedented quality for many years to come.

Unlike any other altimetric mission, the SWOT mission has been designed specifically with the purpose of monitoring surface waters. The SWOT mission is a collaboration between the communities of oceanography and hydrology, and the primary payload of the SWOT satellite is the Ka-band Radar Interferometer (KaRIN) altimeter. The SWOT mission will have a repeat period of roughly 21 days, and ascending and descending pass swath coverage implies an average revisit time

of around 11 days near the equator. With the interferometric capabilities of the altimeter, the SWOT mission is designed to observe all rivers broader than 100 m and water bodies with an area greater than 250 m$\times$250 m that lie within the swath coverage. More information about the SWOT mission and its contribution to inland water altimetry can be found in *Rodríguez* (2015) and *Biancamaria et al.* (2015), respectively.

CryoSat-2 was not believed to be usable for inland water monitoring due to its geodetic orbit, which was designed to study slow changing ice sheets. However, the studies presented here have shown that CryoSat-2 is able to provide time series with higher correlations and lower RMS errors compared to conventional altimetry missions such as Envisat and SARAL. The success of CryoSat-2 can be accredited its SAR mode, which has an unprecedented small footprint with an along-track width of just 300 m, and thereby avoids the hooking effect previously seen with conventional altimeters.

Improving some aspects of the methodology could further improve the results presented in this thesis. For one, river altimetry would benefit greatly from dynamic masks based on satellite imagery. Static masks do not reflect the dramatic seasonal changes that occur in river channels, and dynamic, or even just seasonal masks, would make it possible to extract more reliable water level estimates. Secondly, time series could be obtained using more sophisticated methods such as presented in *Nielsen et al.* (2015a) and *Schwatke et al.* (2015b), which would provide an even better agreement with in situ data. Finally, it should be mentioned that the methods developed here will need to be evaluated in many more study areas.

The investigations carried out during this PhD are important for understanding of the use of CryoSat-2 altimetry for inland water monitoring, but also for SAR altimetry for land hydrology purposes in general. In this thesis, several methods have been developed, which will be of important use for future SAR altimetry over inland water monitoring and enable researchers to keep an eye on the state of rivers and lakes worldwide as our climate changes.

Bibliography

Al-Mahmood, S. Z. (2014), Flooding in bangladesh leaves nearly half a million people homeless, `http://www.wsj.com/articles/flooding-in-bangladesh-leaves-nearly-half-a-million-people-homeless-1408969241`, [Online; accessed 2-December-2015].

Amarouche, L., P. Thibaut, O. Z. Zanife, J. P. Dumont, P. Vincent, and N. Steunou (2004), Improving the Jason-1 Ground Retracking to Better Account for Attitude Effects, *Marine Geodesy*, *27*(1-2), 171–197, doi:10.1080/01490410490465210.

Andersen, O. B., A. Abulaitijiang, P. Knudsen, and L. Stenseng (2014), Coastal Sea Level From CRYOSAT-2 SAR and SAR-In Altimetry, *AGU Fall Meeting Abstracts*.

Armitage, T. W. K., and M. W. J. Davidson (2014), Using the interferometric capabilities of the ESA CryoSat-2 mission to improve the accuracy of sea ice freeboard retrievals, *IEEE Transactions on Geoscience and Remote Sensing*, *52*(1), 529–536, doi:10.1109/TGRS.2013.2242082.

Babel, M. S., and S. M. Wahid (2011), Hydrology, management and rising water vulnerability in the Ganges-Brahmaputra-Meghna River basin, *Water International*, *36*(3), 340–356, doi:10.1080/02508060.2011.584152.

Bao, L., Y. Lu, and Y. Wang (2009), Improved retracking algorithm for oceanic altimeter waveforms, *Progress in Natural Science*, *19*, 195 – 203, doi:10.1016/j.pnsc.2008.06.017.

Berry, P. (2006), Two Decades of Inland Water Monitoring Using Satellite Radar Altimetry, *Proceedings of the Symposium on 15 Years of Progress in Radar Altimetry, ESA Special Publication*, *614*, 8.

Berry, P. A. M., J. D. Garlick, J. A. Freeman, and E. L. Mathers (2005), Global inland water monitoring from multi-mission altimetry, *Geophysical Research Letters*, *32*(16), doi:10.1029/2005GL022814.

Biancamaria, S., F. Hossain, and D. P. Lettenmaier (2011), Forecasting transboundary river water elevations from space, *Geophysical Research Letters*, *38*(11), doi:10.1029/2011GL047290.

Biancamaria, S., D. P. Lettenmaier, and T. M. Pavelsky (2015), The SWOT Mission and Its Capabilities for Land Hydrology, *Surveys in Geophysics*, doi:10.1007/s10712-015-9346-y.

Birkett, C. (1995), The contribution of TOPEX/POSEIDON to the global monitoring of climatically sensitive lakes, *Journal of Geophysical Research - Oceans*, *100*(C12), 25,179–25,204.

Birkett, C., C. Reynolds, B. Beckley, and B. Doorn (2011), From Research to Operations: The USDA Global Reservoir and Lake Monitor, in *Coastal Altimetry*, edited by S. Vignudelli, A. G. Kostianoy, P. Cipollini, and J. Benveniste, pp. 19–50, Springer Berlin Heidelberg, doi:10.1007/978-3-642-12796-0_2.

Birkett, C. M. (1994), Radar altimetry: A new concept in monitoring lake level changes, *Eos, Transactions American Geophysical Union*, *75*(24), 273, doi:10.1029/94eo00944.

Birkett, C. M. (1998), Contribution of the TOPEX NASA Radar Altimeter to the global monitoring of large rivers and wetlands, *Water Resources Research*, *34*(5), 1223–1239, doi:10.1029/98WR00124.

Birkinshaw, S. J., G. M. O'Donnell, P. Moore, C. G. Kilsby, H. J. Fowler, and P. A. M. Berry (2010), Using satellite altimetry data to augment flow estimation techniques on the Mekong River, *Hydrological Processes*, *24*(26), 3811–3825, doi:10.1002/hyp.7811.

Bouzinac, C. (2013), CryoSat Product Handbook, *Tech. rep.*, ESA, [Online; accessed 14-December-2015].

Brakenridge, G. R., S. Cohen, A. J. Kettner, T. De Groeve, S. V. Nghiem, J. P. M. Syvitski, and B. M. Fekete (2012), Calibration of satellite measurements of river discharge using a global hydrology model, *Journal of Hydrology*, *475*, 123–136, doi:10.1016/j.jhydrol.2012.09.035.

Brown, G. (1977), The average impulse response of a rough surface and its applications, *Antennas and Propagation, IEEE Transactions on*, *25*(1), 67–74, doi:10.1109/TAP.1977.1141536.

Chelton, D. B., J. C. Ries, B. J. Haines, L.-L. Fu, and P. S. Callahan (2001), Chapter 1 - Satellite Altimetry, in *Satellite Altimetry and Earth Sciences- A Handbook of Techniques and Applications*, *International Geophysics*, vol. 69, edited by L.-L. Fu and A. Cazenave, pp. 1 – ii, Academic Press, doi:http://dx.doi.org/10.1016/S0074-6142(01)80146-7.

Cheng, K.-C., S. Calmant, C.-Y. Kuo, H.-Z. Tseng, C. K. Shum, F. Seyler, and J. S. D. Silva (2009), Branco River Stage Gradient Determination and Amazon Hydrologic Studies Using GPS Water Level Measurements, *Marine Geodesy*, *32*(3), 267–283, doi:10.1080/01490410903094460.

Cochonneau, G., et al. (2006), The environmental observation and research project, ORE HYBAM, and the rivers of the Amazon basin, L'Observatoire de recherche en environnement, ORE HYBAM sur les grands fleuves amazoniens.

Crespo, J., and E. Mora (1993), Drought Estimation with Neural Networks, *Advances in Engineering Software*, *18*(3), 167–170, doi:10.1016/0965-9978(93)90064-Z.

Cretaux, J.-F., and C. Birkett (2006), Lake studies from satellite radar altimetry, *Comptes Rendus Geoscience*, *338*(1-2), 1098–1112, doi:10.1016/j.crte.2006.08.002.

Crétaux, J.-F., et al. (2011), SOLS: A lake database to monitor in the Near Real Time water level and storage variations from remote sensing data, *Advances in Space Research*, *47*(9), 1497 – 1507, doi:http://dx.doi.org/10.1016/j.asr.2011.01.004.

da Silva, J. S., S. Calmant, F. Seyler, O. C. Rotunno Filho, G. Cochonneau, and W. J. Mansur (2010), Water levels in the Amazon basin derived from the ERS 2 and ENVISAT radar altimetry missions, *Remote Sensing of Environment*, *114*(10), 2160–2181, doi:10.1016/j.rse.2010.04.020.

Davis, C. (1995), Growth of the Greenland ice sheet: A performance assessment of altimeter retracking algorithms, *Ieee Transactions on Geoscience and Remote Sensing*, *33*(5), 1108–1116, doi:10.1109/36.469474.

Davis, C. H. (1997), A robust threshold retracking algorithm for measuring ice-sheet surface elevation change from satellite radar altimeters, *IEEE T. Geoscience and Remote Sensing*, *35*(4), 974–979.

Defense Video & Imagery Distribution System - Navy Visual News Service (2011), USS Mustin provides post-flood relief in Thailand, `https://www.dvidshub.net/image/478066/uss-mustin-provides-post-flood-relief-thailand`, [Online; accessed 16-November-2015].

Deng, X. (2003), *Improvement of Geodetic Parameter Estimation in Coastal Regions from Satellite Radar Altimetry*, Curtin University of Technology, Dept. of Spatial Sciences.

Deo, M., and C. Naidu (1999), Real time wave forecasting using neural networks, *Ocean Engineering*, *26*(3), 191–203.

Desportes, C., E. Obligis, and L. Eymard (2007), On the Wet Tropospheric Correction for Altimetry in Coastal Regions, *Geoscience and Remote Sensing, IEEE Transactions on*, *45*(7), 2139–2149, doi:10.1109/TGRS.2006.888967.

Dinardo, S., B. Lucas, C. Gommenginger, C. Martin-Puig, M. Srokosz, M. Caparrini, and J. Benveniste (2013), Detailed Processing Model of the Sentinel-3 SRAL SAR altimeter ocean waveform retracker – v2.3.0.

Dinardo, S. (2013), Guidelines for the SAR (Delay-Doppler) L1b Processing.

eoPortal (2015), eoPortal — SWOT, https://directory.eoportal.org/web/eoportal/satellite-missions/s/swot, [Online; accessed 16-January-2016].

Farr, T. G., et al. (2007), The Shuttle Radar Topography Mission, *Reviews of Geophysics*, *45*(2), doi:10.1029/2005RG000183.

Fernandes, M. J., C. Lazaro, A. L. Nunes, and R. Scharroo (2014), Atmospheric Corrections for Altimetry Studies over Inland Water, *Remote Sensing*, *6*(6), 4952–4997.

Fetterer, F. M., M. R. Drinkwater, K. C. Jezek, S. W. C. Laxon, R. G. Onstott, and L. M. H. Ulander (2013), *Sea Ice Altimetry*, pp. 111–135, American Geophysical Union, doi:10.1029/GM068p0111.

Frappart, F., S. Calmant, M. Cauhopé, F. Seyler, and A. Cazenave (2006), Preliminary results of ENVISAT RA-2-derived water levels validation over the Amazon basin, *Remote Sensing of Environment*, *100*(2), 252–264.

Frappart, F., C. Fatras, E. Mougin, V. Marieu, A. Diepkilé, F. Blarel, and P. Borderies (2015), Radar altimetry backscattering signatures at Ka, Ku, C, and S bands over West Africa, *Physics and Chemistry of the Earth, Parts A/B/C*, pp. –, doi:http://dx.doi.org/10.1016/j.pce.2015.05.001.

French, M., W. Krajewski, and R. Cuykendall (1992), Rainfall forecasting in space and time using a neural network, *Journal of Hydrology*, *137*(1-4), 1–31.

GISTDA (2015), Thailand Flood Monitoring System, http://flood.gistda.or.th/indexEN.html, [Online; accessed 7-December-2015].

Gomez-Enri, J., S. Vignudelli, G. D. Quartly, C. P. Gommenginger, P. Cipollini, P. G. Challenor, and J. Benveniste (2010), Modeling Envisat RA-2 Waveforms in the Coastal Zone: Case Study of Calm Water Contamination, *Ieee Geoscience and Remote Sensing Letters*, *7*(3), 474–478, doi:10.1109/lgrs.2009.2039193.

Gommenginger, C., P. Thibaut, L. Fenoglio-Marc, G. Quartly, X. Deng, J. Gómez-Enri, P. Challenor, and Y. Gao (2011), *Coastal Altimetry*, chap. Retracking Altimeter Waveforms Near the Coasts, pp. 61–101, Springer Berlin Heidelberg, Berlin, Heidelberg, doi:10.1007/978-3-642-12796-0_4.

Gommenginger, C., C. Martin-Puig, L. Amarouche, and R. K. Raney (2013), Review of state of knowledge for SAR altimetry over ocean. Report of the EUMETSAT JASON-CS SAR mode error budget study, *Tech. rep.*, National Oceanography Centre, Southampton.

Haykin, S. (1994), *Neural Networks: A Comprehensive Foundation*, Macmillan.

Hayne, G. (1980), Radar altimeter mean return waveforms from near-normal-incidence ocean surface scattering, *Antennas and Propagation, IEEE Transactions on*, *28*(5), 687–692, doi:10.1109/TAP.1980.1142398.

Idris, N. H. (2014), Development of New Retracking Methods for Mapping Sea Levels over the Shelf Areas from Satellite Altimetry Data, Ph.D. thesis, The University of Newcastle Australia.

Idris, N. H., and X. Deng (2013), An iterative coastal altimetry retracking strategy based on fuzzy expert system for improving sea surface height estimates, *International Geoscience and Remote Sensing Symposium (IGARSS)*, pp. 2954–2957, doi:10.1109/igarss.2013.6723445.

Jain, M. (2015), Improved sea level determination in the Artic regions through development of tolerant altimetry retracking, Ph.D. thesis, DTU Space - National Space Institute, Technical University of Denmark.

Jain, M., C. Martin-Puig, O. Baltazar Andersen, J. Dall, and L. Stenseng (2014), Determination of sea surface heights in the Arctic using SAMOSA3 Adapted retracker on Cryosat-2 SAR data, in *EGU General Assembly Conference Abstracts*, *EGU General Assembly Conference Abstracts*, vol. 16.

Jain, M., O. B. Andersen, J. Dall, and L. Stenseng (2015), Sea surface height determination in the Arctic using Cryosat-2 SAR data from primary peak empirical retrackers, *Advances in Space Research*, *55*(1), 40–50, doi:10.1016/j.asr.2014.09.006.

Jarihani, A. A., J. N. Callow, K. Johansen, and B. Gouweleeuw (2013), Evaluation of multiple satellite altimetry data for studying inland water bodies and river floods, *Journal of Hydrology*, *505*, 78–90, doi:10.1016/j.jhydrol.2013.09.010.

Kleinherenbrink, M., R. Lindenbergh, and P. Ditmar (2015), Monitoring of lake level changes on the Tibetan Plateau and Tian Shan by retracking Cryosat SARIn waveforms, *Journal of Hydrology*, *521*, 119 – 131, doi:http://dx.doi.org/10.1016/j.jhydrol.2014.11.063.

Koblinsky, C. J., R. T. Clarke, A. C. Brenner, and H. Frey (1993), Measurement of river level variations with satellite altimetry, *Water Resources Research*, *29*(6), 1839–1848, doi:10.1029/93WR00542.

Kurtz, N. T., N. Galin, and M. Studinger (2014), An improved CryoSat-2 sea ice freeboard retrieval algorithm through the use of waveform fitting, *Cryosphere*, *8*(4), 1217–1237, doi:10.5194/tc-8-1217-2014.

Laxon, S. (1994), Sea ice extent mapping using the ERS-1 radar altimeter, *EARSeL Advances in Remote Sensing*, *3*, 112–116.

Lee, H., C. Shum, Y. Yi, A. Braun, and C.-Y. Kuo (2008), Laurentia crustal motion observed using TOPEX/POSEIDON radar altimetry over land, *Journal of Geodynamics*, *46*(3–5), 182 – 193, doi:http://dx.doi.org/10.1016/j.jog.2008.05.001.

Lehner, B., and P. Doll (2004), Development and validation of a global database of lakes, reservoirs and wetlands, *Journal of Hydrology*, *296*(1-4), 1–22, doi:10.1016/j.jhydrol.2004.03.028.

Maillard, P., N. Bercher, and S. Calmant (2015), New processing approaches on the retrieval of water levels in envisat and saral radar altimetry over rivers: A case study of the sao francisco river, brazil, *Remote Sensing of Environment*, *156*, 226–241, doi:10.1016/j.rse.2014.09.027.

Manning, C. D., P. Raghavan, and H. Schütze (2008), *Introduction to Information Retrieval*, Cambridge University Press, New York, NY, USA.

Martin-Puig, C., G. Ruffini, and J. Marquez (2008a), Theoretical Model for SAR altimeter mode processed echoes over ocean surfaces.

Martin-Puig, C., G. Ruffini, J. Marquez, D. Cotton, M. Srokosz, P. Challenor, K. Raney, and J. Benveniste (2008b), Theoretical model of SAR altimeter over water surfaces, *International Geoscience and Remote Sensing Symposium (IGARSS)*, *3*(1), 4779,328, III242–III245, doi:10.1109/igarss.2008.4779328.

Maus, S., C. Green, and J. Fairhead (1998), Improved ocean-geoid resolution from retracked ERS-1 satellite altimeter waveforms, *Geophysical Journal International*, *134*(1), 243–253.

Michailovsky, C., S. McEnnis, P. A. M. Berry, R. Smith, and P. Bauer-Gottwein (2012), River monitoring from satellite radar altimetry in the Zambezi River basin, *Hydrology and Earth System Sciences*, *16*(7), 2181–2192, doi:10.5194/hess-16-2181-2012.

Michailovsky, C. I., C. Milzow, and P. Bauer-Gottwein (2013), Assimilation of radar altimetry to a routing model of the Brahmaputra River, *Water Resources Research*, *49*(8), 4807–4816, doi:10.1002/wrcr.20345.

MODIS Rapid Response Team (2011), 2011 Thailand floods - MODIS 2011-10-19, `https://en.wikipedia.org/wiki/File:2011_Thailand_floods-MODIS_2011-10-19.jpg`, [Online; accessed 17-November-2015].

Neal, J., G. Schumann, P. Bates, W. Buytaert, P. Matgen, and F. Pappenberger (2009), A data assimilation approach to discharge estimation from space, *Hydrological Processes*, *23*(25), 3641–3649, doi:10.1002/hyp.7518.

Nielsen, K., L. Stenseng, O. Andersen, H. Villadsen, and P. Knudsen (2015a), Validation of CryoSat-2 SAR mode based lakes levels, *Remote Sensing of Environment*, *Accepted for publication*.

Nielsen, K., L. Stenseng, O. Andersen, H. Villadsen, and P. Knudsen (2015b), Validation of Lake Levels Based on CryoSat-2 SAR Mode Data, in *Validation of Lake Levels Based on CryoSat-2 SAR Mode Data*, Presented at the Sentinel-3 for Science Workshop, Venice, Italy (June 2015).

Nikolakopoulos, K. G., E. K. Kamaratakis, and N. Chrysoulakis (2006), SRTM vs ASTER elevation products. Comparison for two regions in Crete, Greece, *International Journal of Remote Sensing*, *27*(21), 4819–4838, doi:10.1080/01431160600835853.

Papa, F., F. Durand, W. B. Rossow, A. Rahman, and S. K. Bala (2010), Satellite altimeter-derived monthly discharge of the Ganga-Brahmaputra River and its seasonal to interannual variations from 1993 to 2008, *Journal of Geophysical Research: Oceans*, *115*(C12), n/a–n/a, doi:10.1029/2009JC006075.

Passaro, M., P. Cipollini, S. Vignudelli, G. D. Quartly, and H. M. Snaith (2014), ALES: A multi-mission adaptive subwaveform retracker for coastal and open ocean altimetry, *Remote Sensing of Environment*, *140*, 173–189, doi:10.1016/j.rse.2014.02.008.

Powell, R., A. Birks, W. Bradford, C. Wrench, and J. Biddiscombe (1993), Using transponders with the ERS-1 and TOPEX altimeters to measure orbit altitude to $\pm$3 cm, *Advances in Space Research*, *13*(5), 61 – 67, doi:http://dx.doi.org/10.1016/0273-1177(93)90528-J.

Promchote, P., S.-Y. S. Wang, and P. G. Johnson (2015), The 2011 Great Flood in Thailand: Climate Diagnostics and Implications from Climate Change, *Journal of Climate*, p. 151023111532004, doi:10.1175/jcli-d-15-0310.1.

Quartly, G. (1998), Determination of oceanic rain rate and rain cell structure from altimeter waveform data. Part I: Theory, *Journal of Atmospheric and Oceanic Technology*, *15*(6), 1361–1378.

Quartly, G. (2010), Hyperbolic Retracker: Removing Bright Target Artefacts from Altimetric Waveform Data, *ESA Living Planet Symposium, Bergen, 28th Jun-2nd July 2010.*

Quartly, G., T. Guymer, and M. Srokosz (1996), The effects of rain on TOPEX radar altimeter data, *Journal of Atmospheric and Oceanic Technology*, *13*(6), 1209–1229.

Raney, R. (2012), CryoSat SAR-Mode Looks Revisited, *Geoscience and Remote Sensing Letters, IEEE*, *9*(3), 393–397, doi:10.1109/LGRS.2011.2170052.

Raney, R. K. (1998), The delay/Doppler radar altimeter, *IEEE Transactions on Geoscience and Remote Sensing*, *36*(5), 1578–1588, doi:10.1109/36.718861.

Raney, R. K., and L. Phalippou (2011), *Coastal Altimetry*, chap. The Future of Coastal Altimetry, pp. 535–560, Springer Berlin Heidelberg, Berlin, Heidelberg, doi:10.1007/978-3-642-12796-0_20.

Rao, S., and S. Mandal (2005), Hindcasting of storm waves using neural networks, *Ocean Engineering*, *32*(5-6), 667–684, doi:10.1016/j.oceaneng.2004.09.003.

Ray, C., C. Martin-Puig, M. P. Clarizia, G. Ruffini, S. Dinardo, C. Gommenginger, and J. Benveniste (2015), SAR Altimeter Backscattered Waveform Model, *IEEE Transactions on Geoscience and Remote Sensing*, *53*(2), 911–919, doi:10.1109/TGRS.2014.2330423.

Rodríguez, E. (2015), Surface Water and Ocean Topography mission (SWOT), Science Requirements Document, `https://swot.jpl.nasa.gov/files/swot/SRD_021215.pdf`, accessed November 2015.

Salomon, J., et al. (2004), Global land-water mask derived from MODIS Nadir BRDF-adjusted reflectances (NBAR) and the MODIS land cover algorithm, in *Geoscience and Remote Sensing Symposium, 2004. IGARSS '04. Proceedings. 2004 IEEE International*, vol. 1, pp. –241, doi:10.1109/IGARSS.2004.1369005.

Sandwell, D., and W. Smith (2005), Retracking ERS-1 altimeter waveforms for optimal gravity field recovery, *Geophysical Journal International*, *163*(1), 79–89, doi:10.1111/j.1365-246x.2005.02724.x.

Sarkar, A. (2012), RS-GIS Based Assessment of River Dynamics of Brahmaputra River in India, *Journal of Water Resource and Protection*, *04*(02), 63–72, doi:10.4236/jwarp.2012.42008.

Schwatke, C., D. Dettmering, E. Boergens, and W. Bosch (2015a), Potential of SARAL/AltiKa for Inland Water Applications, *Marine Geodesy*, *38*(sup1), 626–643, doi:10.1080/01490419.2015.1008710.

Schwatke, C., D. Dettmering, W. Bosch, and F. Seitz (2015b), Kalman filter approach for estimating water level time series over inland water using multi-mission satellite altimetry, *Hydrology and Earth System Sciences Discussions*, *12*(5), 4813–4855, doi:10.5194/hessd-12-4813-2015.

Schwatke, C., D. Dettmering, W. Bosch, and F. Seitz (2015c), Kalman filter approach for estimating water level time series over inland water using multi-mission satellite altimetry, *Hydrology and Earth System Sciences Discussions*, *12*(5), 4813–4855, doi:10.5194/hessd-12-4813-2015.

Seber, G. A. F. (2008), *Frontmatter*, John Wiley & Sons, Inc., doi:10.1002/9780470316641.fmatter.

Seppälä, M. (2005), *The physical geography of Fennoscandia*, The Oxford regional environments series, Oxford University Press.

Song, C., B. Huang, and L. Ke (2014), Inter-annual changes of alpine inland lake water storage on the Tibetan Plateau: Detection and analysis by integrating satellite altimetry and optical imagery, *Hydrological Processes*, *28*(4), 2411–2418, doi:10.1002/hyp.9798.

Stenseng, L. (2011), Polar Remote Sensing by CryoSat-type Radar Altimetry, Ph.D. thesis, DTU Space - National Space Institute, Technical University of Denmark.

Taylor, J. (1997), *An Introduction to Error Analysis: The Study of Uncertainties in Physical Measurements*, A series of books in physics, University Science Books.

Thibaut, J., P.and Aublanc, T. Moreau, F. Boy, and N. Picot (2014), Delay/Doppler Waveform Processing in Coastal Zones, 8th Coastal Altimetry Workshop - Konstanz, Germany.

Thibaut, P., J. C. Poisson, E. Bronner, and N. Picot (2010), Relative Performance of the MLE3 and MLE4 Retracking Algorithms on Jason-2 Altimeter Waveforms, *Marine Geodesy*, *33*(sup1), 317–335, doi:10.1080/01490419.2010.491033.

Thibaut, P., T. Moreau, F. Boy, and N. Picot (2012), Coastal Altimetry: Evolution of measurement and retracking problems when switching from conventional (Ku, Ka) to SAR altimetry, `http://www.coastalt.eu/files/gardaworkshop12/pres/13_Coastal_Issues_FromKutoSAR_Thibaut.pdf`, [Presented at the 6th Coastal Altimetry Workshop - Lake Garda 2012. Online; accessed 12-December-2015].

Tourian, M., O. Elmi, Q. Chen, B. Devaraju, S. Roohi, and N. Sneeuw (2015), A spaceborne multisensor approach to monitor the desiccation of Lake Urmia in Iran, *Remote Sensing of Environment*, *156*, 349 – 360, doi:http://dx.doi.org/10.1016/j.rse.2014.10.006.

Tourian, M. J. (2013), Application of spaceborne geodetic sensors for hydrology, Ph.D. thesis, Geodätisches Institut der Universität Stuttgart.

Tournadre, J., K. Whitmer, and F. Girard-Ardhuin (2008), Iceberg detection in open water by altimeter waveform analysis, *Journal of Geophysical Research - Part F - Solid Earth*, *113*(C8), C08,040.

Villadsen, H., O. B. Andersen, L. Stenseng, K. Nielsen, and P. Knudsen (2015a), CryoSat-2 altimetry for river level monitoring — Evaluation in the Ganges–Brahmaputra River basin, *Remote Sensing of Environment*, *168*, 80–89, doi:10.1016/j.rse.2015.05.025.

Villadsen, H., X. Deng, B. Andersen, L. Stenseng, K. Nielsen, and P. Knudsen (2015b), Improved inland water levels from SAR altimetry using novel empirical and physical retrackers, *Journal of Hydrology*, *under revision*.

Wingham, D., et al. (2006), CryoSat: A mission to determine the fluctuations in Earth's land and marine ice fields, *Advances in Space Research*, *37*(4), 841 – 871, doi:http://dx.doi.org/10.1016/j.asr.2005.07.027.

Wingham, D. J., C. G. Rapley, and H. Griffiths (1986), New techniques in satellite altimeter tracking systems, in *ESA Proceedings of the 1986 International Geoscience and Remote Sensing Symposium (IGARSS'86) on Remote Sensing: Today's Solutions for Tomorrow's Information Needs*, vol. 3.

Wongsa, S. (2014), Simulation of Thailand Flood 2011, *International Journal of Engineering and Technology*, *6*(6), 452–458, doi:10.7763/ijet.2014.v6.740.

Yi, Y., A. V. Kouraev, C. K. Shum, V. S. Vuglinsky, J.-F. Cretaux, and S. Calmant (2013), The performance of altimeter waveform retrackers at Lake Baikal, *Terrestrial Atmospheric and Oceanic Sciences*, *24*(4), 513–519, doi:10.3319/tao.2012.10.09.01(tibxs).

Zakharova, E. A., A. V. Kouraev, F. Rémy, V. A. Zemtsov, and S. N. Kirpotin (2014), Seasonal variability of the Western Siberia wetlands from satellite radar altimetry, *Journal of Hydrology*, *512*(39), 366–378, doi:10.1016/j.jhydrol.2014.03.002.

Appendix A

Publications

A.1 CryoSat-2 altimetry for river level monitoring – Evaluation in the Ganges–Brahmaputra River basin

Paper published in Remote Sensing of Environment July, 2015.

Remote Sensing of Environment 168 (2015) 80–89

Contents lists available at ScienceDirect

Remote Sensing of Environment

journal homepage: www.elsevier.com/locate/rse

CryoSat-2 altimetry for river level monitoring — Evaluation in the Ganges–Brahmaputra River basin

Heidi Villadsen *, Ole B. Andersen, Lars Stenseng, Karina Nielsen, Per Knudsen

National Space Institute, Technical University of Denmark, Elektrovej 327, 2800 Kgs. Lyngby, Denmark

ARTICLE INFO

Article history:
Received 8 April 2014
Received in revised form 5 December 2014
Accepted 27 May 2015
Available online 8 July 2015

Keywords:
CryoSat-2
Envisat
Satellite altimetry
Inland water
Hydrology

ABSTRACT

The performance of CryoSat-2/SIRAL altimetry for river level monitoring is investigated by using river levels retrieved from Ganges and Brahmaputra. A key concern for the CryoSat-2 orbit has been its long repeat period of 369 days, which is usually undesirable for river and lake monitoring. However, the results from the method developed in this study involving virtual stations show that the CryoSat-2 data can indeed be used for such monitoring by utilizing the high spatial coverage and the sub-cycle period of 30 days. The results show that it is possible to capture the peak flow occurring during late summer due to monsoonal precipitation and the melting of snow in the Himalayas. The evaluation of CryoSat-2 river levels is performed by comparing with Envisat data in terms of annual signals and amplitudes. The obtained annual amplitudes agree well with the Envisat data, although CryoSat-2 exhibit larger differences. For five virtual stations in the Brahmaputra River, the mean difference between the obtained amplitudes is ~10 cm, whereas the mean phase difference is less than 2.7 days. A virtual station in the Ganges River shows a phase difference of around 5 days and a difference in amplitude of 2 cm.

1. Introduction

Satellite radar altimetry was mainly developed with the purpose of monitoring the oceans, but is now also used for monitoring other surfaces such as inland water. Fresh water is a very valuable resource, and a lot of effort is going into monitoring of lakes and rivers to get accurate estimates of the available water resources. Obtaining in-situ data can be difficult due to lack of infrastructure, inaccessibility of remote rivers and lakes, and undisclosed data, especially in a transboundary context. Satellite altimetry can be used to improve hydrological models by either complementing existing in-situ data or by offering elevation estimates in un-gauged rivers and lakes while staying within the same height reference system.

In one of the first studies on the potential of radar altimetry over rivers (Koblinsky, Clarke, Brenner, & Frey, 1993), the study focused on the Amazon Basin using Geosat-derived elevation estimates, which were found to have a root-mean-square error (RMSE) of 70 cm relative to in-situ measurements. Birkett (1998) showed that the NASA radar altimeter carried by the TOPEX/Poseidon satellite was able to track rivers and wetlands with widths >1 km with a RMSE sometimes as low as ~11 cm. A more recent study by Berry, Garlick, Freeman, and Mathers (2005) demonstrated the value of satellite radar altimetry in the field of measuring and monitoring land hydrology using multi-mission altimetry data over the Amazon Basin. In general, satellite altimetry has been accepted as an important provider of global inland water heights with a unique monitoring capability (Berry, 2006).

The usefulness of satellite radar altimetry data both in near real-time and long-term applications has been demonstrated in several studies, with purposes such as discharge modelling and flood warning (Biancamaria, Hossain, & Lettenmaier, 2011; Michailovsky, Milzow, & Bauer-Gottwein, 2013; Neal et al., 2009). In addition to the scientific and practical advantages, satellite altimetry also provides a way of overcoming the difficulty of transboundary river management, which is often hindered by local governments considering their hydrological measurements as sensitive.

Several projects already provide historical inland water levels from altimetry through web databases, such as the ESA River&Lake project (http://earth.esa.int/riverandlake, Berry et al., 2005), the Global Reservoir and Lake Monitor (http://www.pecad.fas.usda.gov/cropexplorer/global_reservoir/, Birkett, Reynolds, Beckley, & Doorn, 2011) and the HYDROWEB database (http://www.LEGOS.obs-mip.fr/soa/hydrologie/HYDROWEB, Crétaux et al., 2011). However, none of these data archives have included CryoSat-2 data.

In this study the potential of CryoSat-2 for river level monitoring is evaluated by comparing the annual signals obtained from CryoSat-2 and Envisat. CryoSat-2 offers altimetry in three modes, particularly the SAR mode reducing the along track resolution to 300 m is very interesting for hydrology, but it has a very special orbit. Envisat has a repeat orbit period of 35 days, whereas the repeat orbit of CryoSat-2 is 369 days with sub-cycles of 30 days. Usually, a shorter repeat period, such as that for Envisat, is preferred by hydrologists in order to

* Corresponding author.
E-mail address: hvil@space.dtu.dk (H. Villadsen).

http://dx.doi.org/10.1016/j.rse.2015.05.025
0034-4257/

obtain time series that are easily comparable to river gauge data and readily applicable to river modelling. However, with this study we want to show that CryoSat-2 river retrievals can be just as valuable for hydrologist, even if not sampled from a repeat orbit, by applying only few adjustments.

2. The Ganges–Brahmaputra River basin

For this study the Ganges and Brahmaputra Rivers were chosen due to their decent sizes, which act as a good base for conducting an initial validation of CryoSat-2 altimetry data. Choosing this river basin also has the benefit that the area is covered by all three CryoSat-2 SIRAL modes (LRM, SAR and SARIn; see Section 3.1) making an intercomparison possible. The Ganges and Brahmaputra Rivers constitute one of the largest river basins in the world, and is home to around 600 million people across five Asian countries: India, Bangladesh, Nepal, China and Bhutan, which makes exchange of river gauge information complicated. The drainage basin includes some of the highest mountains in the world, the Himalayas, and is plagued by floods and droughts as well as sedimentation in the rivers and flood plains due to erosion of the steep topography surrounding the river (Babel & Wahid, 2011). The high rate of erosion and subsequent deposition of sediments in the river basin leads to constant changes in channel pattern and shifting of bank lines (Sarkar, 2012). The Ganges–Brahmaputra delta is one of the most densely populated areas in the world, and the people living here depend heavily on the state of the rivers and their tributaries. 89% of the extracted water is used for agricultural purposes, corresponding to an annual demand of around 230 billion m^3 (Babel & Wahid, 2011). The strong seasonal signal caused by the summer monsoon and the melting of glaciers in the Himalayas gives rise to flooding from June to October, which is followed by a much drier period in the winter months.

3. Data sets

3.1. CryoSat-2

CryoSat-2 was launched by the European Space Agency (ESA) on the 8th of April 2010 to monitor variations in the cryosphere, i.e. the marine ice cover and continental ice sheets. The primary payload on-board CryoSat-2 is the altimeter, SIRAL (SAR Interferometric Radar Altimeter), which is a state of the art altimeter working in three different measurement modes depending on a geographical mode mask (Wingham et al., 2006). Besides the conventional low resolution mode CryoSat-2 operates in high resolution modes which are very valuable for hydrology. The three modes are:

LRM: Over the oceans and ice sheet interiors, CryoSat-2 operates like a conventional radar altimeter in Low Resolution Mode (LRM).

SAR: Designed for observing sea ice with an increased resolution and precision, coherently transmitted echoes are focused via Synthetic Aperture Radar (SAR) processing (also known as Delay–Doppler processing), to reduce the along-track surface footprint to 300 m. It can also be used more successfully over difficult surfaces such as coastal zone and inland water.

SARIn: The most advanced mode of SIRAL is used in areas with high surface slopes, and is as such used mostly over mountainous regions and the margins of the ice sheets. Here, the altimeter performs synthetic aperture processing along-track, has an extended range sampling window, and uses a second antenna as an interferometer to determine the across-track angle to the earliest radar returns with the interferometry technique.

Since the launch of CryoSat-2 the mode mask have changed several times over the river basins. The previous as well as the current mode masks can be seen in Fig. 1. The current mode mask was implemented in October 2012 and introduced a region where the altimeter operates in SAR mode instead of LRM mode along the coast of Bangladesh.

All data were taken from the ESA baseline-b L1b 20 Hz data product. The waveforms retrieved from CryoSat-2 since July 2010 over the chosen region were retracked using a primary peak threshold retracker (Bao, Lu, & Wang, 2009; Fenoglio-Marc et al., 2010; Jain, Andersen, Dall, & Stenseng, 2015; Vignudelli, Kostianoy, Cipollini, & Benveniste, 2011), which was found to give the most stable results over land and inland water. The retracker first identifies the leading and trailing edge of the primary peak, and then uses the OCOG method (Wingham, Rapley, & Griffiths, 1986) around the start and end gates to compute the amplitude of the extracted sub-waveform. For the retracking a threshold of 80% for SAR and SARIn waveforms and 31% for LRM waveforms was used. These threshold levels were chosen in order to obtain continuity in the retracked heights above inland water when the altimeter switches from one mode to another.

For SARIn data the range error due to off-nadir ranging was determined according to Armitage and Davidson (2014). Furthermore, the phase difference waveforms were used to determine the off-nadir coordinates corresponding to the retracked waveform bins.

Hence, since no available in-situ measurements were found to coincide with the CryoSat-2 mission, Envisat data were chosen as the basis for our evaluation.

3.2. Envisat

Previous studies using Envisat data over large rivers have shown that the altimetric data is a powerful tool for obtaining river levels for hydrological purposes (da Silva et al., 2010; Frappart, Calmant, Cauhopé, Seyler, & Cazenave, 2006; Michailovsky, McEnnis, Berry, Smith, & Bauer-Gottwein, 2012; Papa, Durand, Rossow, Rahman, & Bala, 2010).

Envisat was launched in 2002 by ESA with a conventional LRM radar altimeter, RA-2, which delivered altimetry data until April 8th 2012 when all contact with the satellite was lost. Envisat had a 35-day repeat period from 82.48°N to 82.48°S until October 2010. In November 2010 the so-called "Envisat extension orbit" was implemented, which introduced a minor drift in the orbit and a new repeat cycle of 30 days. The Envisat data used for this study was processed using the ICE-1 retracker. The ICE-1 retracker has previously been found to be the Envisat retracker that compares best to in situ measurements over inland water (Cheng et al., 2009; da Silva et al., 2010; Frappart et al., 2006).

3.3. Water mask

The MODIS (or Moderate Resolution Imaging Spectroradiometer) land-water mask was used to identify water. MOD44W is an improvement of the previous MODIS Nadir Bidirectional Reflectance Distribution Function (BRDF)-Adjusted Reflectance (NBAR) and MODIS land cover-based global land-water mask (Salomon et al., 2004). The binary

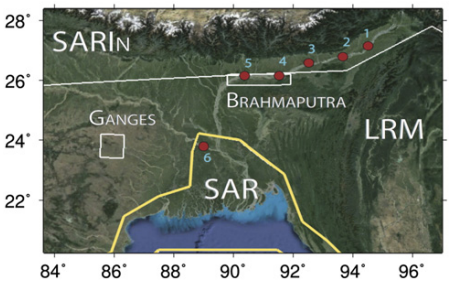

Fig. 1. Original CryoSat-2 mode mask (white polygons) and the SAR mask which was implemented in October 2012 (yellow). The red markers indicate the locations of the virtual stations (VS1–VS6).

grid mask has a resolution of 250 m, which is sufficient for our study, since the parts of the Ganges and Brahmaputra rivers on which we are focusing always are wider than a couple of kilometres. The mask was interpolated onto the locations of the observations from Envisat and CryoSat-2 resulting in a fraction between 0 and 100%. In this study we will only include observations which are classified as ≥99% inland water by the MODIS mask to exclude retrievals that are close to the river shores and thus more prone to pollution by topography.

The complexity and dynamics of the highly alluvial rivers chosen for this study impose a great challenge regarding masking out signals retrieved over land, as droughts and floods occur frequently and change the course and channel pattern of the river. In this study we have settled on a static mask, but a more dynamic mask could and should be developed, e.g. with the use of multispectral satellite images.

4. Editing of altimeter data

After the surface elevations were estimated, Envisat and CryoSat-2 data retrieved over the Brahmaputra and Ganges Rivers were extracted using the MOD44W mask as described in the previous section. The extracted height estimations for CryoSat-2 retrievals from the launch of the satellite in April 2010 to August 2014 are shown in Fig. 2 relative to the geoid (EGM08). As seen, the mask captures the Ganges and Brahmaputra River basins very well south of the Himalayas. On the Tibetan plateau, no-data regions in the digital elevation model (DEM) derived from the Shuttle Radar Topography Mission (SRTM, Farr et al., 2007) in the mountainous regions cause discontinuities in the MODIS mask, but river heights can still be retrieved. The discontinuities in the northern part of the Brahmaputra River can be ignored as we are focusing on the parts of the rivers south of the mountain range. A similar map of the Envisat data is shown in Fig. 3.

For each river crossing height observations beyond three standard deviations of all observations were excluded. If less than a certain number of observations remained (six for Brahmaputra, three for Ganges) within the river crossing the track was discarded. The height estimates within each track displayed high variation, which most likely was caused by the inability of MOD44w to accurately mask the highly dynamic and complex river channel pattern. Therefore, only the lowest height observations were used to estimate the mean of each river crossing. Doing this we assume that the lowest estimates will be those with the highest chance of being non-contaminated river retrievals.

5. Deriving time series

The special orbit of CryoSat-2 does not allow for a traditional comparison of time series due to the long repeat period. However, by taking advantage of the spatial coverage of the sub-cycle ground track and spatially relocating the observations to a series of virtual stations (VS) we can obtain time series with temporal resolutions comparable to those of Envisat. The locations of these stations were chosen arbitrarily at 90.5, 91.5, 92.5, 93.5 and 94.5°E (VS5-VS1) for the Brahmaputra River and 89.3°E (VS6) for the Ganges River. In this way river observations between 90 and 91°E will be relocated to 90.5°E, points from 91 to 92°E to 91.5°E, and so forth. To get as many observations from a satellite as possible it is preferred that the river flows in a zonal direction although this is not necessary.

The short mission overlap between Envisat and CryoSat-2 introduces another challenge. As the overlapping period between the two missions is too short for a thorough analysis and has a bias towards winter data, which are more prone inaccurate height estimates caused by contaminated waveforms during low water stages, consequently, our study compares mean annual signals estimated for all available data and not only the overlapping period. The temporal and spatial distribution of CryoSat-2 data retrieved over the Brahmaputra River is seen in Figs. 4 and 5.

The time series derivation in this study consists of several steps, once the retracked heights are obtained and the positions of the virtual stations are chosen:

1. The retracked heights are used to determine along-river height profiles for the Ganges and Brahmaputra Rivers (see Section 5.1).
2. Using the height differences between the point of observation and the virtual station according to the height profile we can spatially relocate the observation (see Section 5.2).
3. Once all observations have been relocated to their respective virtual

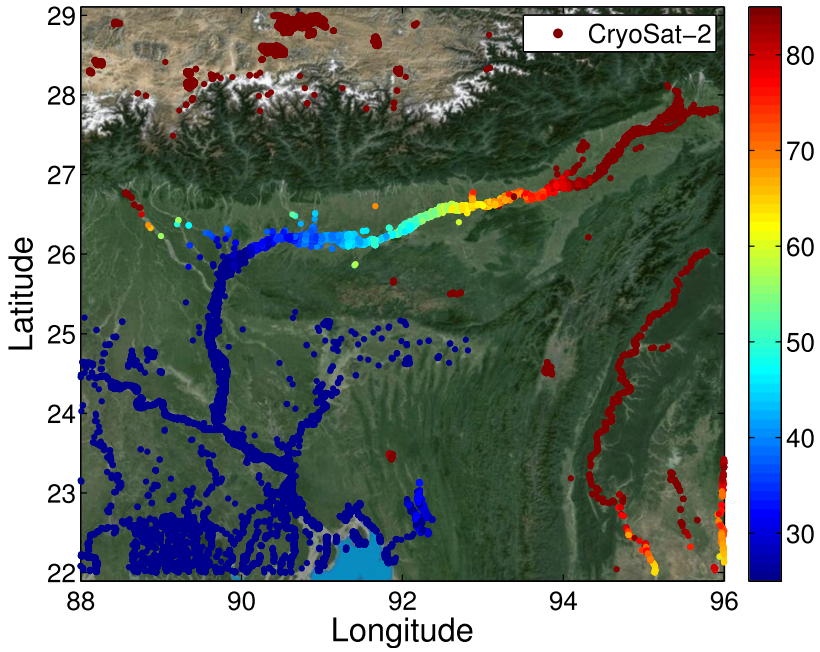

Fig. 2. Retracked CryoSat-2 heights from July 2010 to August 2014 for all modes. Masked with MOD44W.

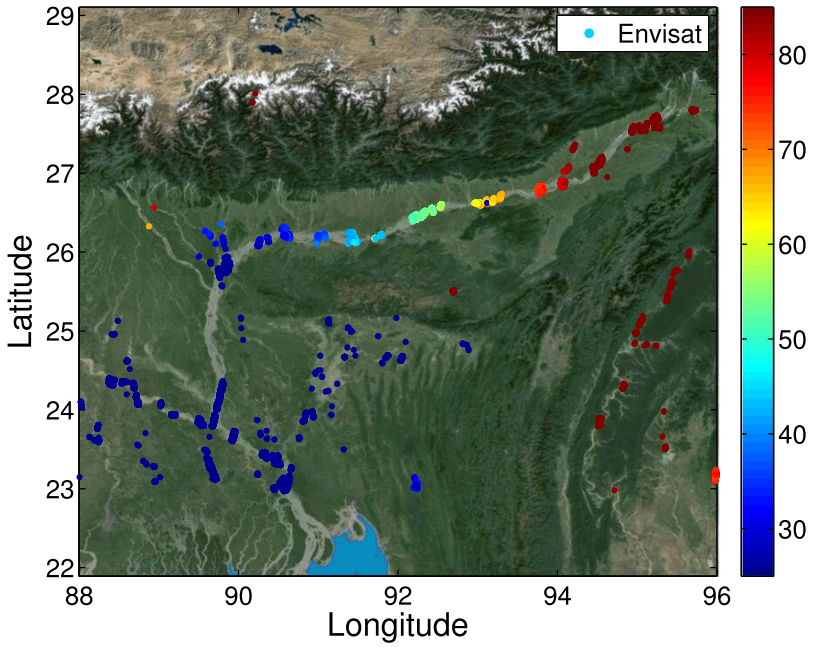

Fig. 3. Retracked Envisat heights from January 2003 to March 2012. Masked with MOD44W.

stations the annual signals are determined by fitting a simple model to the obtained time series (see Section 5.3).

5.1. Height profiles of the rivers

In order to apply the slope correction described in Section 5.2 a mean height profile along the river is necessary. By fitting simple functions to the retrieved CryoSat-2 heights over the rivers we ensure uneven temporal distribution of the observations do not affect the height model used for the slope correction. Unfortunately, these functions will not be able to describe local topography, which introduces some errors in the relocation.

Similarly, the mean height profiles used here do not account for varying river slopes caused by portions of the river reacting differently to high flow and low flow seasons.

5.1.1. Ganges River

The heights retrieved over the Ganges River are shown in Fig. 6 as a function of along river distance starting from 89.1°E going downriver. Fitting the retracked heights in this river segment with a linear function

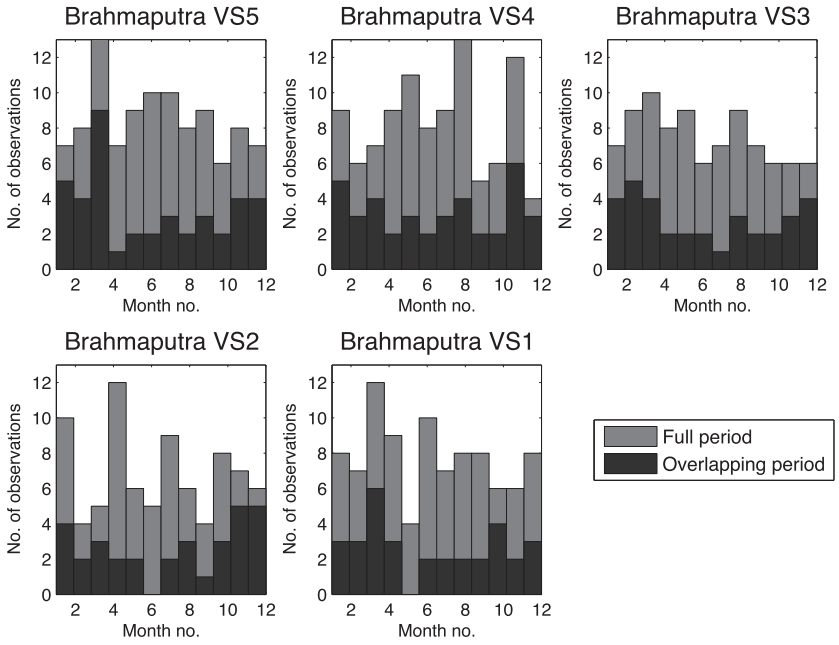

Fig. 4. Histograms showing the temporal distribution of observations at the virtual stations in the Brahmaputra River basin.

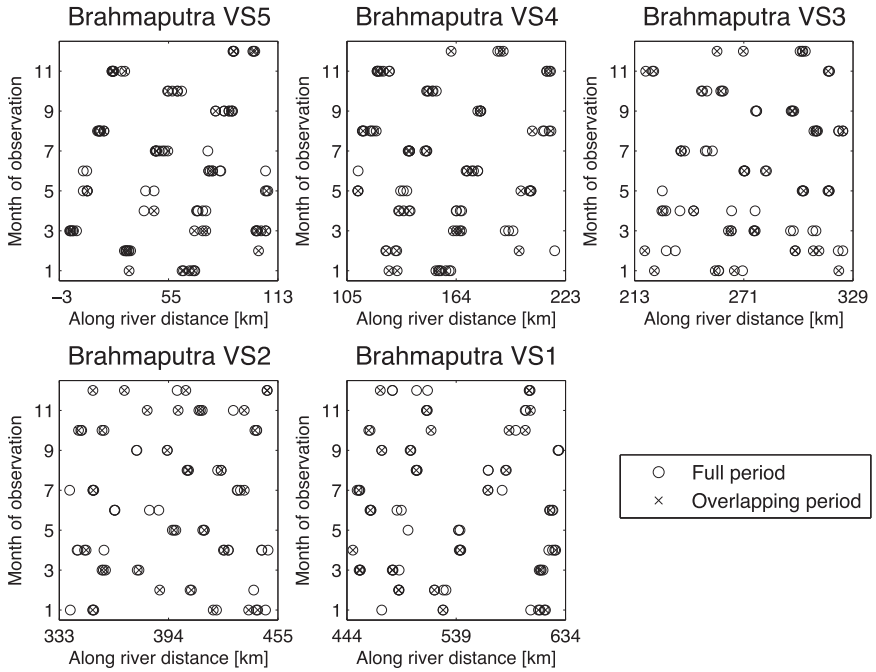

Fig. 5. Scatter plots showing the temporal and spatial distribution of observations at the virtual stations in the Brahmaputra River basin.

the following model was obtained:

$$H = -0.024 \cdot x + 7.1\,\text{m} \quad (1)$$

where x is the along river distance in km.

5.1.2. Brahmaputra River

The heights retrieved over the Brahmaputra River are shown in Fig. 7 as a function of along river distance starting from 90°E going eastward. Fitting the CryoSat-2 data with a cubic function we get the height model:

$$H = -3.121 \cdot 10^{-8} \cdot x^3 + 7.242 \cdot 10^{-5} \cdot x^2 + 0.08999 * x + 26.08\,\text{m} \quad (2)$$

where x is the along river distance in km.

We attempted using the digital elevation model from the Shuttle Radar Topography Mission (Farr et al., 2007) and the Altimetry Corrected Elevations (Berry, Smith, & Benveniste, 2010) to relocate the observations to the chosen virtual stations. However, this introduced much more noise, and so this approach was abandoned.

5.2. Relocation of observations

The observations were subsequently relocated segment-wise to their corresponding virtual stations using slope correction based on the height profiles above. Using a river centerline the mean height along the river was estimated from CryoSat-2 data and observations were moved by taking the height difference between the point of observation and the location of the virtual station into account. In this way we were able to estimate time series at chosen virtual stations for both CryoSat-2 and Envisat. Naturally, the relocation is larger for CryoSat-2 than for Envisat, as seen in Figs. 7 and 6.

A sketch of the slope correction is given in Fig. 8 and the corresponding equations are as follows in Eq. (3).

$$\begin{aligned} h_{new} &= h_{obs} + H_D \\ &= h_{obs} + (H_{VS} - H_{OBS}) \end{aligned} \quad (3)$$

In the equation above h_{obs} is the instantaneous measurement from the altimeter, H_D is the difference between the mean heights at the point of observation (H_{OBS}) and the corresponding virtual station (H_{VS}). After the height difference has been calculated, the absolute

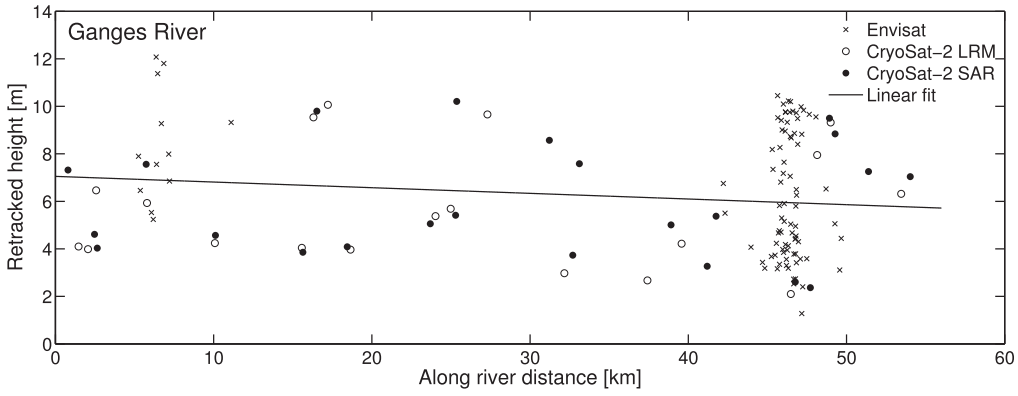

Fig. 6. Retracked heights for CryoSat-2 and Envisat as a function of along river distance and the corresponding linear fit used for the slope correction for VS6 (see location in Fig. 1).

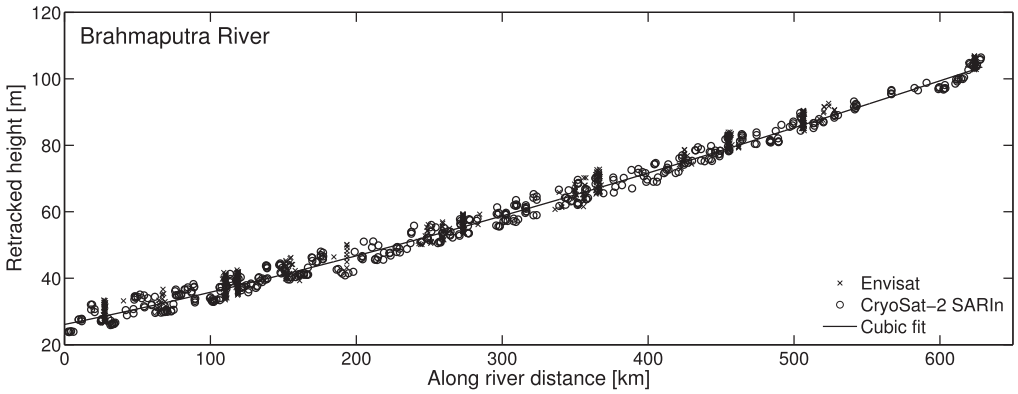

Fig. 7. Retracked heights for CryoSat-2 SARIn and Envisat as a function of along river distance and the corresponding linear fit used for the slope correction for VS1–VS5 (see locations in Fig. 1).

height, h_{new}, at the virtual station is calculated by simply adding the difference to the original retracked height, h_{obs}.

5.3. Estimation of annual phase and amplitude

A model was fitted to the obtained time series in order to derive their annual phases and amplitudes. The model includes an offset, A, a trend, B, and a linear combination of a cosine and sine wave with amplitudes C and D, respectively.

$$f(t) = A + Bt + C\cos(t') + D\sin(t') \tag{4}$$

where t is the time in decimal years relative to January 1st 2012 and $t' = 2\pi t$. E.g. January 1st 2011 would correspond to $t = -1$ and July 1st 2012 would correspond to $t = 0.5$. The model was fitted to the data using multiple linear regression, where it is assumed that the retracked heights, $Y = (h_1, h_2, \ldots, h_n)^T$, can be described as a function of time:

$$Y(t) = X(t) \cdot \beta + \epsilon \tag{5}$$

where X is the design matrix describing the model:

$$X = \begin{pmatrix} 1 & t_1 & cos(t'_1) & sin(t'_1) \\ 1 & t_2 & cos(t'_2) & sin(t'_2) \\ \vdots & \vdots & \vdots & \vdots \\ 1 & t_n & cos(t'_n) & sin(t'_n) \end{pmatrix} \tag{6}$$

and β is a vector holding the coefficients A, B, C and D: $\beta = (A, B, C, D)^T$.

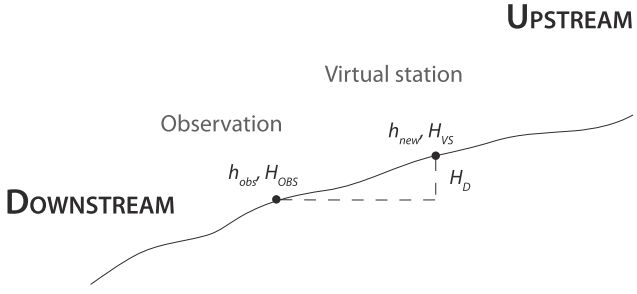

Fig. 8. Sketch of slope correction.

Here, the phases will be given in decimal months, where all months have been assumed to be equally long.

The amplitude, a, is derived from the amplitudes of the cosine and sine waves:

$$a = \sqrt{C^2 + D^2}. \tag{7}$$

The resulting phase of the cosine and sine waves can be found by using the atan2 function and converting from degrees to months

$$p_d = \frac{180}{\pi}\,\mathrm{arctan2}(D, C) \tag{8}$$

$$p_m = \frac{12}{360}p_d + 1. \tag{9}$$

The amplitude, a, in Eq. (7) is given in metres and the phase, p_m, in Eq. (9) is given in decimal months. If the phase in Eq. (8) is negative, 360° must be added before converting the phase to decimal months.

5.3.1. Error estimation

Once the coefficients in Eq. (4) were determined, their corresponding standard errors could be computed according to Eq. (10), which gives the standard error matrix, S, in which the standard errors of the estimated coefficients (S_A, S_B, S_C and S_D) are found in the diagonal entries.

$$S = \sqrt{\frac{\sum_i^n (r_i^2)}{n-m-1}\left(X^T X\right)^{-1}} \tag{10}$$

where n, is the number of data points in the time series, r_i is the residual for the ith data point, m is the number of estimated coefficients (i.e. four in this case) and X is the design matrix introduced earlier. The standard

Table 1
Comparison of amplitude and phase of annual cycles for CryoSat-2 and Envisat data in the Ganges River. Phases are given in decimal months and amplitudes in metres.

Data set	Period	Phase, p_m	Amplitude, a	n
CryoSat LRM	07/2010–10/2012	8.83 ± 0.16	3.50 ± 0.29	19
CryoSat SAR	10/2012–08/2014	9.10 ± 0.13	3.36 ± 0.22	23
LRM + SAR	07/2010–08/2014	9.06 ± 0.08	3.56 ± 0.15	42
Envisat	01/2003–03/2012	8.83 ± 0.06	3.63 ± 0.11	92

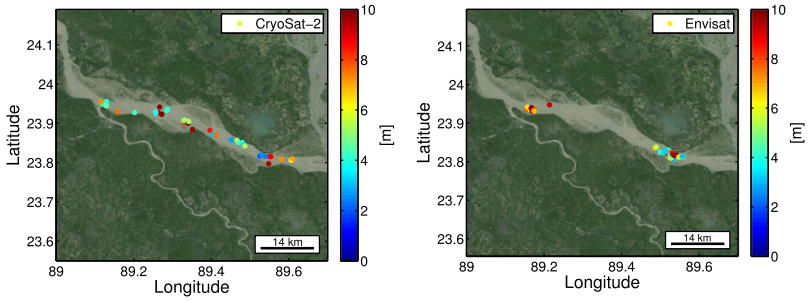

Fig. 9. Retracked heights for CryoSat-2 LRM (left) and Envisat (right) from April 2010 to March 2012 in a portion of the Ganges River. Masked with MOD44W.

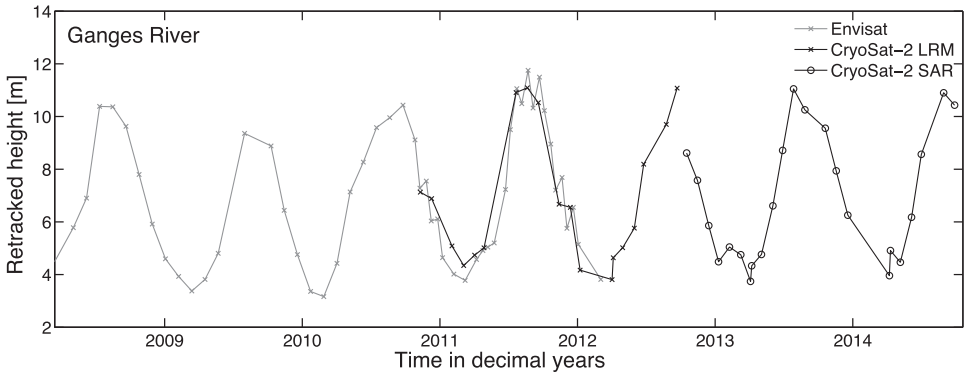

Fig. 10. Ganges River time series showing estimated river levels for Envisat, and CryoSat-2 LRM, and SAR for VS6 (see location in Fig. 1).

errors on phase, δp_m, and amplitude, δa, were then determined from standard error propagation as given by Eq. (3.47) in Taylor (1997).

$$\delta p_m = \frac{6}{\pi}\frac{\sqrt{C^2 s_C^2 + D^2 s_D^2}}{C^2 + D^2} \tag{11}$$

$$\delta a = \sqrt{\frac{C^2 s_C^2 + D^2 s_D^2}{C^2 + D^2}} \tag{12}$$

6. Evaluation of CryoSat-2 river height retrievals

The observations obtained from the CryoSat-2 and Envisat missions over the Ganges and Brahmaputra are compared in this section to see how well they agree on annual time scale. Time series as well as estimated phases and amplitudes obtained according to the method described in Section 5 are compared.

6.1. CryoSat-2 LRM and SAR over the Ganges River

The observations used for constructing the time series at virtual station no. 6, i.e. VS6 (see Fig. 1), from Envisat and CryoSat-2 can be seen in Fig. 9. The figure shows how the observations from CryoSat-2 are more spread out in the zonal direction compared to the repeat orbit observations from Envisat and that the river level decreases towards the east as the river approaches the Bay of Bengal.

Correcting for the slope and referencing all the observations to VS6 at 89.3°E time series obtained for both missions are shown in Fig. 10. There is a small offset (~1 m) between the Envisat and CryoSat-2 data, which is most likely caused by the different retracking methods and the method used for relocation of the observations. The offset has been removed in all time series presented in this study.

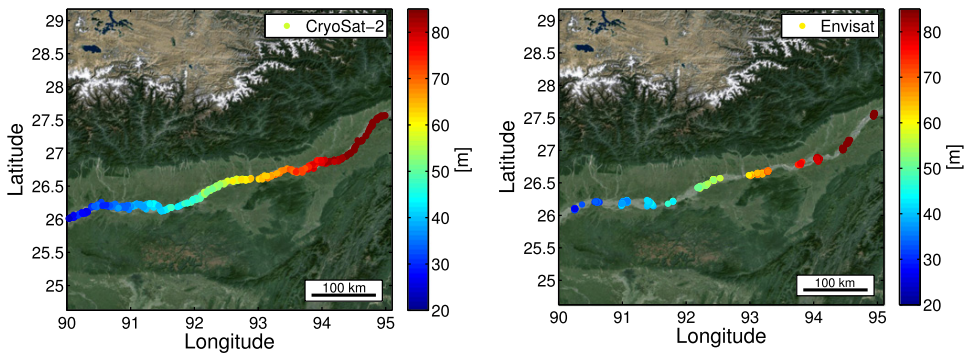

Fig. 11. Retracked heights for CryoSat-2 SARIn (left) and Envisat (right) from April 2010 to August 2014 in the Brahmaputra River. Masked with MOD44W.

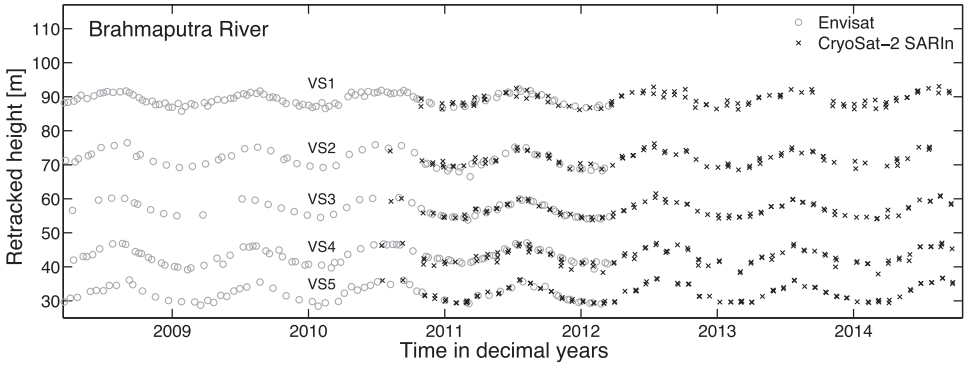

Fig. 12. Brahmaputra River time series showing estimated river levels for Envisat and CryoSat-2 SARIn data.

From the estimated river level time series it is evident that both satellites capture the annual signal nicely. Estimated phases for the time series (see Table 1) were found to be 9.06 ± 0.08 and 8.83 ± 0.06 for CryoSat-2 and Envisat, respectively, which corresponds to a peak flow in the river around the end of August to early September. The annual phases agree reasonably well. Any discrepancies could be due to the crude assumptions made throughout the post processing, i.e. the static water mask, the assumed linearity of the river slope, and the fit of the simple time series model. Differences in the temporal sampling of the two altimeters could also contribute to the difference between the

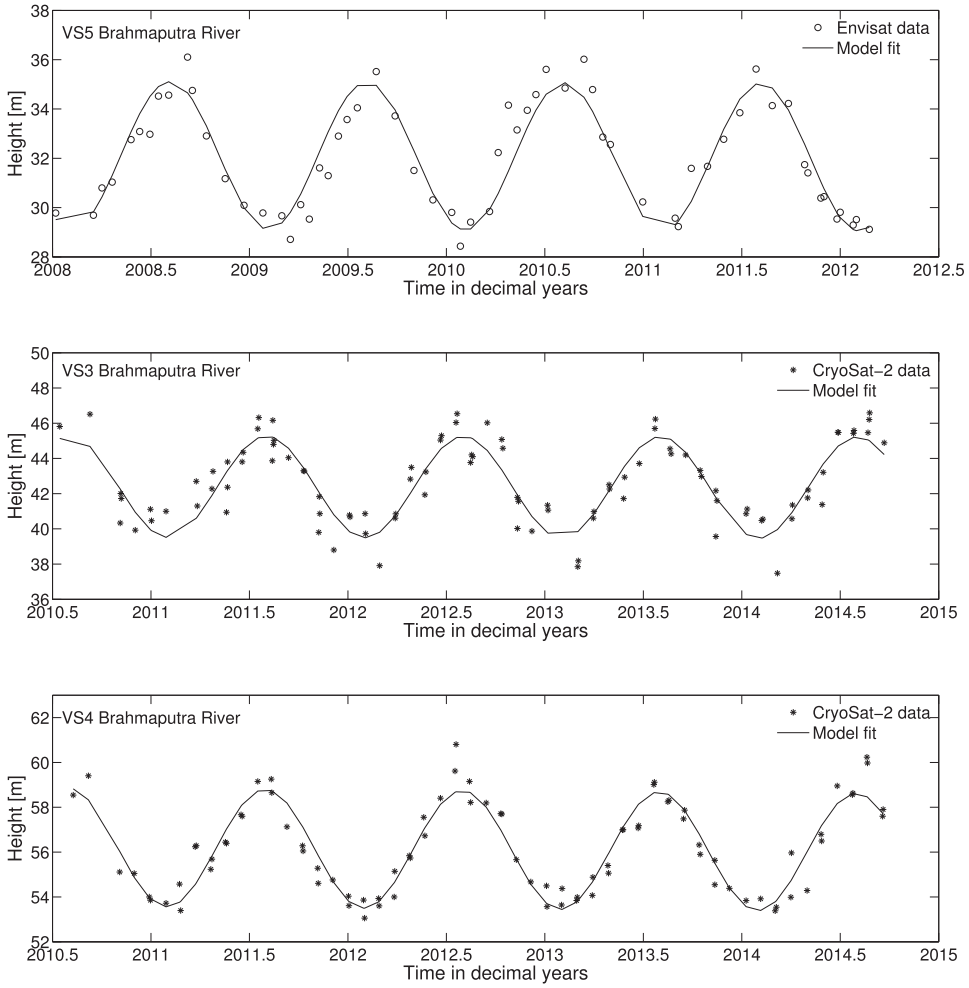

Fig. 13. Examples of the estimated model fits compared to the data in the Brahmaputra River. (Top) Model fit for Envisat data at VS5 (middle) model fit for CryoSat-2 data at VS3, and (bottom) model fit for CryoSat-2 data at VS4.

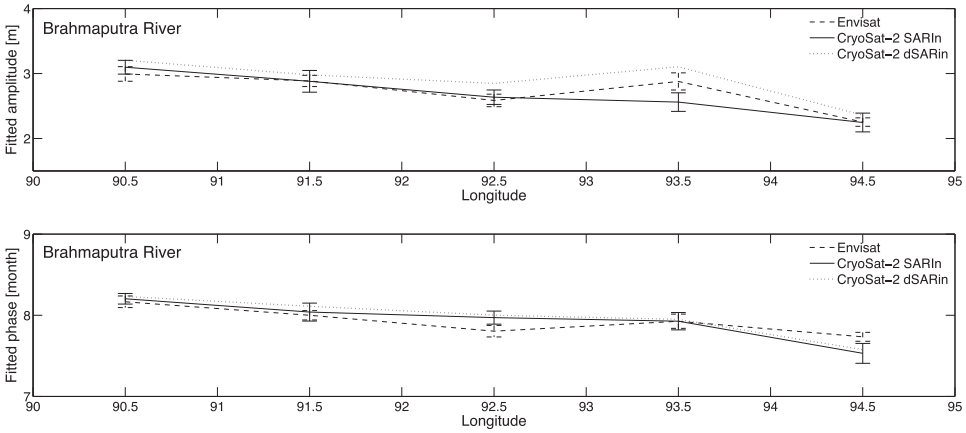

Fig. 14. Fitted phases and amplitudes for time series obtained from Envisat and CryoSat-2 SARIn and degraded SARIn (dSARIn) data in the Brahmaputra River.

captured phases. The amplitude of the CryoSat-2 data was found to be 3.56 ± 0.15 m, which is in good agreement with the estimated phase for the Envisat data of 3.63 ± 0.11 m.

6.2. CryoSat-2 SARIn over the Brahmaputra River

Another stretch of river in the river basin which is used for the comparison is the Brahmaputra River from 90°E to 95°E. In this portion of the river time series were constructed for VS1–5. The retracked heights included in the time series can be seen in Fig. 11.

The time series obtained for VS1–5 within the SARIn mask of CryoSat-2 (see Fig. 1) of Brahmaputra are shown in Fig. 12. From the time series it is obvious that the late Envisat orbit provides time series that are less smooth compared to the previous exact repeat orbit of Envisat. This is most likely due to 1) the assumption that the elevation along the river can be described by a cubic function and 2) variations in the riverbanks, which determines how different parts of the river react to a higher or lower inflow of water. This effect is not included here as it would require a high number of rating curves, which are unavailable, and at last 3) local tributaries can affect the local river level, which would also introduce errors when the observations are relocated from one location to another. However, the time series still appear with the same seasonal patterns despite these fluctuations.

Fig. 13 shows three examples of how well the time series model fit the time series obtained in the Brahmaputra River. All Envisat time series show almost equally good time series, as seen in the top curve for VS5. The middle curve for VS3 shows the most noisy of the CryoSat-2 data in the Brahmaputra, and the bottom curve shows one of the better fits for CryoSat-2, here for VS4. In general, all time series follow the time series model very well.

Fig. 14 shows the detailed estimated fitted amplitudes and phases for CryoSat-2 SARIn (solid), and Envisat (dashed). The largest difference in amplitude is ~30 cm and the mean difference of all five stations is ~10 cm. The phase of the annual variation captured by CryoSat-2 and Envisat in each segment of the river has a mean difference of 2.7 days, which is surprisingly good considering the nature of the orbits. The fitting has its limitations, as the temporal distribution of the points affects the fit of the model. All phases and amplitudes with their corresponding uncertainties can be seen in Tables 2 and 3. It should be noted, that the standard errors estimated from Eq. (10) mainly depend on the number of observations.

As an additional experiment the analysis in the Brahmaputra River was done using pseudo-SAR data, also known as degraded SARIn. Here, no off-nadir correction was applied for the SARIn data, instead the nadir location as given in the CryoSat L1b product was used. Annual phases and amplitudes for the pseudo-SAR time series are shown in Fig. 14 as dotted lines. Although the phase for degraded SARIn looks more similar to the Envisat phase at VS2 at 93.5°E, the overall mean difference is 3.34 days, which is higher than for the range-corrected SARIn data. The mean difference of the amplitudes is 18 cm, which is also higher than for the SARIn data.

7. Conclusions

Annual signals were determined for both CryoSat-2 and Envisat data. The annual signals were studied by relocating the observations to a series of virtual stations in the Ganges–Brahmaputra River basin due to the orbital pattern of CryoSat-2. The results showed that the two satellites captured comparable annual signals even though CryoSat-2 is in a drifting orbit with a repeat period of more than a year and Envisat is in a near-repeat orbit. Fitting a set of harmonic functions to the river level time series revealed a peak flow in late July and late August for Brahmaputra and Ganges, respectively, with differences between Envisat and CryoSat-2 of just a couple of days. The amplitudes of the flow in the rivers also showed encouraging results, with a difference of 10 cm or less for all virtual stations in both Ganges and Brahmaputra except for the virtual station at 93.5°E in the Brahmaputra River.

The method presented in this study makes it possible to perform river level monitoring using not only CryoSat-2, but also Sentinel-3 data, when these become available in the future, due to the similarities of the altimeters. With this it is possible to continue the river level time series retrieved from satellite radar altimetry and to keep providing hydrologists with valuable information needed for fresh water monitoring which is important for millions of people.

Table 2
Comparison of phases, p_m, for CryoSat-2 (CS-2) SARIn from launch to August 2014 and Envisat data from launch to March 2012. Phases are given in decimal months.

VS no.	Longitude	Mode	p_m, CS-2	p_m, Envisat	n, CS2/Envisat
1	94.5°E	SARIn	7.53 ± 0.12	7.73 ± 0.06	91/183
2	93.5°E	SARIn	7.93 ± 0.11	7.93 ± 0.09	82/97
3	92.5°E	SARIn	7.97 ± 0.08	7.80 ± 0.07	89/90
4	91.5°E	SARIn	8.04 ± 0.11	8.00 ± 0.06	96/145
5	90.5°E	SARIn	8.20 ± 0.07	8.17 ± 0.07	102/94

Table 3
Comparison of amplitudes, a, for CryoSat-2 (CS-2) SARIn from launch to August 2014 and Envisat data from launch to March 2012. Amplitudes are given in metres.

VS no.	Longitude	Mode	a, CS-2	a, Envisat	n, CS2/Envisat
1	94.5°E	SARIn	2.25 ± 0.14	2.25 ± 0.07	91/183
2	93.5°E	SARIn	2.56 ± 0.14	2.89 ± 0.13	82/97
3	92.5°E	SARIn	2.63 ± 0.11	2.59 ± 0.10	89/90
4	91.5°E	SARIn	2.88 ± 0.17	2.89 ± 0.09	96/145
5	90.5°E	SARIn	3.10 ± 0.11	2.99 ± 0.11	102/94

Future work to improve the presented method should include a better mask for extracting the observations retrieved over rivers or perhaps a way of classifying the waveforms for the different surface types. A dynamic, or at least a high-resolution mask, could be obtained with the use of satellite imagery, which would allow for less data editing.

Furthermore, the mean along-river heights used for relocating the observations in this study are simplified due to lack of a satisfactory digital elevation model and/or rating curves along the river. More information about the nature of the rivers would be very beneficial — e.g. in the form of rating curves, which links the discharge and water level, since it is assumed in this study that an elevation change at one location of the river would have been the same at another location at the same time.

Another error source in this study involves the time lag of flow in the river, which could cause errors spanning from minutes to days depending on the distance between the observation and the chosen virtual station. Accounting for this is not trivial, and in this study it is assumed that the corresponding error is negligible since we look at segments that are no longer than ~100 km.

However, one of the most crucial parts of constructing these time series lies within the way the waveforms are being retracked. Retracking waveforms from inland water is challenging due to the highly varying topography within the radar footprint. More effort should be put into developing a retracker specifically for retracking inland water waveforms in order to ensure that the height estimations are, in fact, from the desired lake or river surface and not from the surrounding topography.

Acknowledgements

CryoSat-2 and Envisat data were provided by the European Space Agency (ESA). This research has been supported by the EU FP7 LOTUS project (Preparing Land and Ocean Take Up From Sentinel-3) (313238). All map data were provided by Google Earth (SIO, NOAA, U.S. Navy, NGA, GEBCO and Landsat).

References

Armitage, T. W. K., & Davidson, M. W. J. (2014). Using the interferometric capabilities of the ESA CryoSat-2 mission to improve the accuracy of sea ice freeboard retrievals. *IEEE Transactions on Geoscience and Remote Sensing, 52*, 529–536. http://dx.doi.org/10.1109/TGRS.2013.2242082.

Babel, M. S., & Wahid, S. M. (2011). Hydrology, management and rising water vulnerability in the Ganges–Brahmaputra–Meghna River basin. *Water International, 36*, 340–356. http://dx.doi.org/10.1080/02508060.2011.584152.

Bao, L., Lu, Y., & Wang, Y. (2009). Improved retracking algorithm for oceanic altimeter waveforms. *Progress in Natural Science, 19*, 195–203. http://dx.doi.org/10.1016/j.pnsc.2008.06.017.

Berry, P. (2006). Two decades of inland water monitoring using satellite radar altimetry. *Proceedings of the symposium on 15 years of progress in radar altimetry. ESA Special, Publication, 614.* (pp. 8).

Berry, P. A. M., Garlick, J. D., Freeman, J. A., & Mathers, E. L. (2005). Global inland water monitoring from multi-mission altimetry. *Geophysical Research Letters, 32*. http://dx.doi.org/10.1029/2005GL022814.

Berry, P., Smith, R., & Benveniste, J. (2010). Ace2: The new global digital elevation model. In S. P. Mertikas (Ed.), *Gravity, geoid and earth observation. International Association of Geodesy Symposia, volume 135.* (pp. 231–237). Berlin Heidelberg: Springer. http://dx.doi.org/10.1007/978-3-642-10634-7_30.

Biancamaria, S., Hossain, F., & Lettenmaier, D. P. (2011). Forecasting transboundary river water elevations from space. *Geophysical Research Letters, 38*. http://dx.doi.org/10.1029/2011GL047290 (n/a–n/a).

Birkett, C. M. (1998). Contribution of the TOPEX NASA Radar Altimeter to the global monitoring of large rivers and wetlands. *Water Resources Research, 34*, 1223–1239. http://dx.doi.org/10.1029/98WR00124.

Birkett, C., Reynolds, C., Beckley, B., & Doorn, B. (2011). From research to operations: The USDA global reservoir and lake monitor. In S. Vignudelli, A. G. Kostianoy, P. Cipollini, & J. Benveniste (Eds.), *Coastal altimetry* (pp. 19–50). Berlin Heidelberg: Springer. http://dx.doi.org/10.1007/978-3-642-12796-0_2.

Cheng, K. -C., Calmant, S., Kuo, C. -Y., Tseng, H. -Z., Shum, C. K., Seyler, F., et al. (2009). Branco river stage gradient determination and amazon hydrologic studies using GPS water level measurements. *Marine Geodesy, 32*, 267–283. http://dx.doi.org/10.1080/01490410903094460.

Crétaux, J. -F., Jelinski, W., Calmant, S., Kouraev, A., Vuglinski, V., Bergé-Nguyen, M., et al. (2011). SOLS: A lake database to monitor in the near real time water level and storage variations from remote sensing data. *Advances in Space Research, 47*, 1497–1507. http://dx.doi.org/10.1016/j.asr.2011.01.004 (URL: http://www.sciencedirect.com/science/article/pii/S0273117711000287).

da Silva, J. S., Calmant, S., Seyler, F., Rotunno Filho, O. C., Cochonneau, G., & Mansur, W. J. (2010). Water levels in the Amazon basin derived from the ERS 2 and ENVISAT radar altimetry missions. *Remote Sensing of Environment, 114*, 2160–2181. http://dx.doi.org/10.1016/j.rse.2010.04.020.

Farr, T. G., Rosen, P. A., Caro, E., Crippen, R., Duren, R., Hensley, S., et al. (2007). The shuttle radar topography mission. *Reviews of Geophysics, 45*. http://dx.doi.org/10.1029/2005RG000183.

Fenoglio-Marc, L., Fehlau, M., Ferri, L., Becker, M., Gao, Y., & Vignudelli, S. (2010). Coastal sea surface heights from improved altimeter data in the Mediterranean Sea. In S. P. Mertikas (Ed.), *Gravity, geoid and earth observation. International Association of Geodesy Symposia, volume 135.* (pp. 253–261). Berlin Heidelberg: Springer. http://dx.doi.org/10.1007/978-3-642-10634-7_33.

Frappart, F., Calmant, S., Cauhopé, M., Seyler, F., & Cazenave, A. (2006). Preliminary results of ENVISAT RA-2-derived water levels validation over the Amazon basin. *Remote Sensing of Environment, 100*, 252–264.

Jain, M., Andersen, O. B.., Dall, J., & Stenseng, L. (2015). Sea surface height determination in the arctic using CryoSat-2 SAR data from primary peak empirical retrackers. *Advances in Space Research, 55*(1), 40–50. http://dx.doi.org/10.1016/j.asr.2014.09.006 (ISSN: 0273-1177).

Koblinsky, C. J., Clarke, R. T., Brenner, A. C., & Frey, H. (1993). Measurement of river level variations with satellite altimetry. *Water Resources Research, 29*, 1839–1848. http://dx.doi.org/10.1029/93WR00542.

Michailovsky, C., McEnnis, S., Berry, P. A. M., Smith, R., & Bauer-Gottwein, P. (2012). River monitoring from satellite radar altimetry in the Zambezi River basin. *Hydrology and Earth System Sciences, 16*, 2181–2192. http://dx.doi.org/10.5194/hess-16-2181-2012.

Michailovsky, C. I., Milzow, C., & Bauer-Gottwein, P. (2013). Assimilation of radar altimetry to a routing model of the Brahmaputra River. *Water Resources Research, 49*, 4807–4816. http://dx.doi.org/10.1002/wrcr.20345.

Neal, J., Schumann, G., Bates, P., Buytaert, W., Matgen, P., & Pappenberger, F. (2009). A data assimilation approach to discharge estimation from space. *Hydrological Processes, 23*, 3641–3649. http://dx.doi.org/10.1002/hyp.7518.

Papa, F., Durand, F., Rossow, W. B., Rahman, A., & Bala, S. K. (2010). Satellite altimeter-derived monthly discharge of the Ganga–Brahmaputra River and its seasonal to inter-annual variations from 1993 to 2008. *Journal of Geophysical Research, Oceans, 115*. http://dx.doi.org/10.1029/2009JC006075 (n/a–n/a).

Salomon, J., Hodges, J. C. F., Friedl, M., Schaaf, C., Strahler, A., Gao, F., et al. (2004). Global land-water mask derived from MODIS nadir BRDF-adjusted reflectances (NBAR) and the MODIS land cover algorithm. *Geoscience and Remote Sensing Symposium, 2004. IGARSS '04. Proceedings. 2004 IEEE International, volume 1.* (pp. 241). http://dx.doi.org/10.1109/IGARSS.2004.1369005.

Sarkar, A. (2012). RS-GIS based assessment of river dynamics of Brahmaputra River in India. *Journal of Water Resource and Protection, 04*, 63–72. http://dx.doi.org/10.4236/jwarp.2012.42008.

Taylor, J. (1997). *An introduction to error analysis: The study of uncertainties in physical measurements.* A series of books in physics. University Science Books (URL: http://books.google.dk/books?id=giFQcZub80oC).

Vignudelli, S., Kostianoy, A. G., Cipollini, P., & Benveniste, J. (Eds.). (2011). *Coastal altimetry*. Berlin: Springer.

Wingham, D., Francis, C., Baker, S., Bouzinac, C., Brockley, D., Cullen, R., et al. (2006). CryoSat: A mission to determine the fluctuations in Earths land and marine ice fields. *Advances in Space Research, 37*, 841–871. http://dx.doi.org/10.1016/j.asr.2005.07.027.

Wingham, D. J., Rapley, C. G., & Griffiths, H. (1986). New techniques in satellite altimeter tracking systems. *ESA Proceedings of the 1986 International Geoscience and Remote Sensing Symposium (IGARSS'86) on Remote Sensing: Today's Solutions for Tomorrow's Information Needs, volume 3*.

A.2 Improved inland water levels from SAR altimetry using novel empirical and physical retrackers

Paper under revision for publication in *Journal of Hydrology*. Submitted in September 2015. The work is based on research carried out at the University of Newcastle in NSW, Australia, in the winter 2014/2015.

Improved inland water levels from SAR altimetry using novel empirical and physical retrackers

Heidi Villadsen[a], Xiaoli Deng[b], Ole B. Andersen[a], Lars Stenseng[a], Karina Nielsen[a], Per Knudsen[a]

[a] *National Space Institute, Technical University of Denmark, Elektrovej 327, 2800 Kgs. Lyngby, Denmark*
[b] *School of Engineering, University of Newcaste, Australia*

Abstract

Satellite altimetry has proven a valuable resource of information on river and lake levels where in-situ data are sparse or non-existent. In this study we present and evaluate several new methods for obtaining stable inland water levels from SAR altimetry. In addition we investigate the possible benefits from combining physical and empirical retrackers.

The retracking methods evaluated in this paper include the physical SAMOSA3 model, a traditional threshold retracker, the proposed MWaPP retracker, and a method combining the physical and empirical retrackers. Using a physical SAR waveform retracker over inland water has not been attempted before but shows great promise in this study.

The evaluation is performed for medium-sized lakes (Lake Vänern in Sweden and Lake Okeechobee in Florida), and in the Amazon River in Brazil. Comparing with in-situ data shows that using the SAMOSA3 retracker provides the lowest root-mean-squared-errors (RMSE), but with the MWaPP retracker giving similar RMSEs. The RMSE values obtained when comparing with in-situ data in Lake Vänern and Lake Okeechobee are in the order of 2-5 cm for well-behaved waveforms, and around 11-13 cm when including more noisy waveforms using empirical retrackers. Combining the physical and empirical retrackers did not offer significantly improved mean track standard deviations or RMSEs. Based on our results we suggest that future SAR derived water levels, such as from the upcoming Sentinel-3 mission, are obtained using either the SAMOSA3 re-

tracker whenever possible, such as in medium-sized and large lakes and rivers, if other parameters such as the significant waveheight or roughness is desirable. For small or braided rivers where the physical retrackers cannot be used we suggest using the empirical retracker described in this paper, which is both easy to implement, computationally efficient, and gives a height estimate for even the most contaminated waveforms.

Keywords: CryoSat-2, satellite altimetry, retracking, SAR, inland water, SAMOSA.

1. Introduction

In recent years the availability of in-situ lake and river levels has declined, which is very unfortunate in a time with increasing focus on climate change and concern about freshwater resources. Satellite altimetry offers continuous and global information about river and lake levels independent of infrastructure and governmental politics, which can greatly benefit the fields of hydrology, climate change detection, and flood/drought forecasting.

Satellite altimetry has been used for monitoring purposes of inland waters for more than 20 years. Some studies has focused on lakes (Birkett, 1994; Cretaux & Birkett, 2006; Song et al., 2014), while others have focused on rivers (Koblinsky et al., 1993; Birkett, 1998; Berry et al., 2005), or wetlands (Zakharova et al., 2014).

Previous studies using CryoSat-2 data over inland water are scarce but include Tourian et al. (2015), where they used several remote sensing methods to monitor the desiccation of Lake Urmia in Iran - here amongst low-resolution-mode (LRM) data from the CryoSat-2 mission. Another study from Kleinherenbrink et al. (2015) used SARIn data to monitor lake level changes on the Tibetan Plateau and Tian Shan. In Nielsen et al. (2015a) lake levels were estimated for several lakes in Denmark using CryoSat-2 synthetic aperture radar (SAR) mode data finding an along-track precision of only a couple of centimetres. In general, satellite altimetry has been accepted as an important source of

global inland water heights with a unique monitoring capability (Berry, 2006).

The usefulness of satellite radar altimetry data both in near real-time and long-term applications has been demonstrated in several studies, with purposes such as discharge modelling and flood warning (Neal et al., 2009; Biancamaria et al., 2011; Michailovsky et al., 2013). In addition to the scientific and practical advantages, satellite altimetry also provides a way of overcoming the difficulty of transboundary river management, which is often hindered by local governments considering their hydrological measurements as sensitive.

Several projects already provide historical inland water levels from altimetry through web databases, such as the ESA River&Lake project (`http://earth.esa.int/riverandlake`, Berry et al. (2005)), the Global Reservoir and Lake Monitor (`http://www.pecad.fas.usda.gov/cropexplorer/global_reservoir/`, Birkett et al. (2011)), the HYDROWEB database (`http://www.legos.obs-mip.fr/soa/hydrologie/hydroweb/`, Crétaux et al. (2011)), and the DAHITI database (Schwatke et al. (2015), `http://dahiti.dgfi.tum.de/en`). Of these four databases, DAHITI is the only one that provides heights from CryoSat-2 data. At DTU Space at the Technical University of Denmark a new data product is currently being developed that provides water level time series from CryoSat-2 for a high number of lakes around the world (Nielsen et al., 2015b). A challenge with CryoSat-2 is the highly discussed atypical orbit, which makes monitoring of land hydrology difficult. However, due to the 30-day sub-cycles, capturing annual signals in a time series is still possible if the water body is of a sufficient size. The ability to retrieve annual signals from CryoSat-2 data comparable to those from Envisat has previously been shown in the Ganges-Brahmaputra basin (Villadsen et al., 2015).

In this study the aim is to investigate the possibility of obtaining better heights by using a physical retracker or a combination of physical and empirical retrackers. Up until now, SAR waveforms over inland water have been retracked using empirical retrackers only, apart from the study by Kleinherenbrink et al. (2014), where the cross-correlation between the observed waveforms and a simulated waveform was used to estimate the retracking correction. In this study

we show that it is possible to retrack a large part of the waveforms with the SAMOSA3 (SAR Altimetry MOde Studies and Applications) retracker, which accommodates both ocean-like and specular waveforms. In addition, we develop a new empirical retracker, which takes adjacent waveforms into account before choosing the location of the subwaveform to be retracked.

2. Data

2.1. CryoSat-2 20 Hz SAR waveforms

CryoSat-2 was launched by the European Space Agency (ESA) on the 8th of April 2010 to monitor variations in the cryosphere, i.e. the marine ice cover and continental ice sheets. The primary payload on-board CryoSat-2 is the SIRAL altimeter, which is a state-of-the-art altimeter working in three different measurement modes depending on a geographical mode mask (Wingham et al., 2006). In this study our focus has been on the SAR mode, which is also the mode that the SRAL altimeter on the upcoming Sentinel-3 mission will operate in. The basis for our data processing is the 20 Hz L1b and the L2 data sets provided by ESA. More information on SAR altimetry can be found in Raney (1998), where SAR altimetry was first proposed and described as Delay/Doppler altimetry.

2.2. Water mask - GLWD

Waveforms retrieved over the study areas presented in Section 2.3 are extracted using the water masks GLWD-1 and GLWD-2, which are products from the Global Lakes and Wetlands Database (Lehner & Doll, 2004). The masks were derived from a variety of existing maps, data and information by the World Wildlife Fund (WWF) and the Center for Environmental Systems Research, University of Kassel, Germany. The product is available on global scale (1:1 to 1:3 million resolution), and can be downloaded as a shapefile from the WWF website (`https://www.worldwildlife.org/pages/global-lakes-and-wetlands-database`). The Level 1 product consists of the

3067 largest lakes and the 654 largest reservoirs worldwide. Level 2 comprises permanent water bodies with surfaces areas down to 0.1 km^2, excluding the water bodies contained in GLWD-1.

2.3. Study areas

This section briefly describes the chosen study areas and the availability of in-situ data. The choice of study regions was limited by the availability of SAR data from CryoSat-2, the size of the water body, and the availability of in-situ data.

2.3.1. Lake Okeechobee

Lake Okeechobee is the largest freshwater lake in Florida with an area of 1900 km^2 and has an average depth of around 3 m. In-situ data from Okeechobee were obtained from the National Water Information System (`http://waterdata.usgs.gov/nwis`), and are relative to National Geodetic Vertical Datum of 1929 (NGVD 29).

2.3.2. Lake Vänern

Lake Vänern is the largest lake in Sweden and in the European Union with an area of 5,650 km^2 (Seppl, 2005). The average depth of the lake is 27 m with a maximum depth of 106 m. Gauge data for Lake Vänern are available from the Swedish Meteorological and Hydrological Institute (SMHI) and are referenced to the Swedish height system Riket höjdsystem 1900 (RH 00).

2.3.3. Amazon River near Almeirim

Although it was not possible to find any in-situ data for rivers of a sufficient size for physical retracking and with SAR coverage we have included the results for a stretch of the Amazon River in the vicinity of Prainha and Almeirim in Brazil. The Amazon River is the largest river in the world with respect to discharge and has a dry season width of several kilometres – sometimes as much as 48 km in the wet season. The properties and width of the Amazon River

facilitates a good testing ground for the method developed in this study, since most types of waveforms will be present here.

3. Retracking CryoSat-2 SAR waveforms

This section briefly describes the basic theory of satellite altimetry, the used retracking methods, the steps of the algorithm developed in this study for combining physical and empirical retrackers, and the general data handling, such as the initial classification of waveforms and the minimization of the bias that is observed when combining retrackers.

It all begins with the satellite radar altimeter emitting a microwave pulse towards the surface of the Earth. At the surface the pulse is reflected back into space where it is received by the altimeter. The returned power echo is called a waveform and the shape of the retrieved waveform is related to the complexity of the entire illuminated surface within the altimeter footprint. From the waveform the exact time of the arrival of the reflection from nadir can be determined; this is done by retracking the waveform. The height of the surface (H) above the geoid can be determined as given in Eq. 1.

$$H = H_{alt} - H_{range} - N_{geoid} \tag{1}$$

H depends on the altitude of the satellite above the reference ellipsoid (H_{alt}) and the range (H_{range}). N_{geoid} is the geoid height above the reference ellipsoid, which is subtracted in order to reference the water level to the geoid, since this is a more appropriate reference for inland water bodies. For this study we use the EGM2008 geoid model (Pavlis et al., 2012).

The range to the retracked bin in the waveform is calculated as follows,

$$H_{range} = \frac{c}{2} WD - H_{retrack} - H_{geo}, \tag{2}$$

where c is the speed of light, WD is the window delay in seconds, $H_{retrack}$ is the retracking correction, and H_{geo} is the sum of the applied geophysical

corrections.

Precise estimation of the retracking correction is especially important over topographic surfaces, where the on-board tracking system struggles with maintaining the reflection from nadir in the nominal range bin, since this is predicted from the position of the previous waveforms (Gommenginger et al., 2011). More on the retrackers chosen for this study can be found in the following subsections.

3.1. Empirical retrackers

The two empirical retrackers presented here use a simple threshold approach on a subwaveform to estimate the epoch. The two methods differ in the way that the subwaveform is extracted; the Narrow Primary Peak Retracker (NPPR) focuses only on the current waveform, whereas the Multiple Waveform Persistent Peak (MWaPP) retracker developed for this study takes adjacent waveforms into account.

When using the NPPR method the subwaveform is extracted by identifying the bins where the primary peak begins and ends. This is done by looking at the evolution of the power in the reflected waveform as described in Jain et al. (2015); Vignudelli et al. (2010); Bao et al. (2009). Here we used a threshold of 80% to determine the retracking point as previously done in Nielsen et al. (2015a) and Villadsen et al. (2015).

3.1.1. The MWaPP retracker

For this study we developed the new MWaPP retracker, which looks at adjacent waveforms in order to determine the best subwaveform for retracking. In this way we can identify persistent peaks, which are expected to represent the underlying water body of interest. Looking at neighbouring waveforms can help alleviate snagging issues, where a waveform is dominated by reflections from points off-nadir. The method presented here does not average waveforms, but simply tries to determine the bins in the waveform where the reflection from the water surface at nadir is most likely found. Since the range to the water

body at nadir should be the same in all waveforms, the averaged waveform is not dominated by off-nadir echoes. The proposed retracking method consists of the following:

1. For each waveform the heights corresponding to all 128 bins are determined according to Eq. 1.
2. The surface height span of all waveforms within each track is determined and the waveforms are oversampled to 1 cm height intervals using linear interpolation. This allows us to align the waveforms with respect to obtained surface height instead of bin number.
3. For each oversampled waveform an average of the current and the four nearest waveforms is calculated.
4. For each oversampled and averaged waveform the first peak that exceeds 20% of the maximum power is flagged. This is assumed to represent the water level common to all five waveforms.
5. For each original waveform the peak closest to the flagged peak from the previous step is found, and a subwaveform consisting of the three previous and following bins around this peak is extracted.
6. The OCOG amplitude (Vignudelli et al., 2010) is then calculated for the extracted subwaveform, which consists of 128 bins of which all but 7 are zero. The point where the subwaveform exceeds 80% of the amplitude is marked as the retracking point.

To illustrate the benefits of the MWaPP retracker, some intermediate results for an ascending track crossing Lake Okeechobee in Florida September 7th 2010 are shown in Fig. 1. The map in Fig. 1(a) shows the location of a specific waveform and highlights the adjacent waveforms. As seen from the retracked heights in Fig. 1(b) the standard NPPR retracker fails to determine the leading edge of the nadir reflection and instead retracks the echo coming from an off-nadir bright target located near the coast. As seen, the MWaPP retracker is able to determine a much more stable water level. Fig. 1(c) shows how the

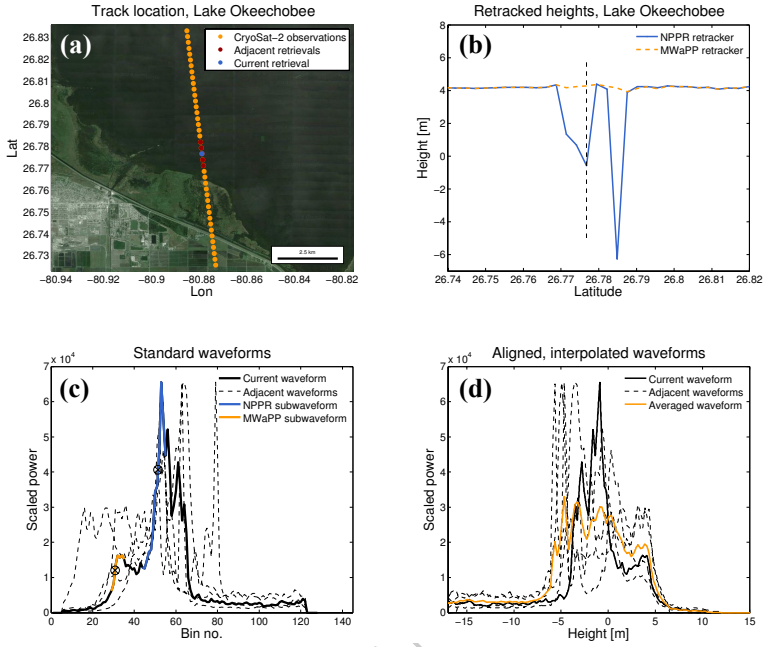

Figure 1: An ascending track over Lake Okeechobee in Florida, September 7th 2010. **(a)** Part of the track with the current observation (blue) and its adjacent points (red) highlighted, **(b)** the retracked heights obtained from both the NPPR retracker (blue) and the proposed MWaPP retracker (yellow), **(c)** the current (solid) and the four adjacent (dashed) waveforms along with the subwaveforms and retracking points obtained with the NPPR retracker (blue) and the proposed MWaPP retracker (yellow), and **(d)** the aligned and oversampled current (solid), adjacent (dashed), and averaged waveforms (yellow).

leading edges of the lake surface reflection are not aligned when the waveforms are referenced to bin number. However, when we oversample the waveforms and reference them to a height, a persistent leading edge appears around a height of 4-5 m and we are able to extract the correct subwaveform.

3.2. The physical SAMOSA3 retracker

SAR altimeter waveforms are different from waveforms from conventional altimetry in the way that the power waveform is much more focused with a steeper leading edge and a faster decaying trailing edge. The SAMOSA

(SAR Altimetry MOde Studies and Applications) project has developed new theoretical models necessary to retrack SAR mode waveforms in order to build on the theoretical knowledge and practical experience needed for the CryoSat-2 and Sentinel-3 missions (Jain, 2015; Dinardo et al., 2013). Information on the details of the development of the SAMOSA processing model can be found in Ray et al. (2015); Dinardo et al. (2013).

The SAMOSA3 model used for this study exists in two modes (Jain et al., 2014); the standard mode for ocean waveforms (hereafter called SAMOSA-O), and a mode adapted for lead type waveforms where the trailing edge is a lot steeper due to a more specular surface reflection (hereafter called SAMOSA-L). Since inland water, like leads, can cause very specular waveforms, SAMOSA-L is included in this study. The retracking correction is estimated in both modes. In ocean mode the significant wave height can be estimated and for the lead mode the roughness can be estimated. For this study we are only interested in the ability of the SAMOSA3 retracker to fit the epoch, or height, but it is worth noting the ability of the retracker to fit other parameters as well, as these might be useful for other studies.

It was found that the SAMOSA3 retrackers only provide more precise height estimates if the correlation between the fitted waveform and the observed waveform was higher than 0.99 in the ten bins closest to the estimated epoch. In many cases (≈40%) the SAMOSA-L model fits the same waveforms that can be fitted with the SAMOSA-O model, and sometimes the SAMOSA-L fit will even be better. Waveforms that were classified as ocean-like were therefore fitted with both the SAMOSA-O and the SAMOSA-L model. If both the SAMOSA-O and the SAMOSA-L models provided fits with correlations higher than 99%, the retracking correction belonging to the model with the lowest sum of errors in the 10 closest bins of the epoch was chosen. This approach was chosen since the correlation did not always reveal the best fit.

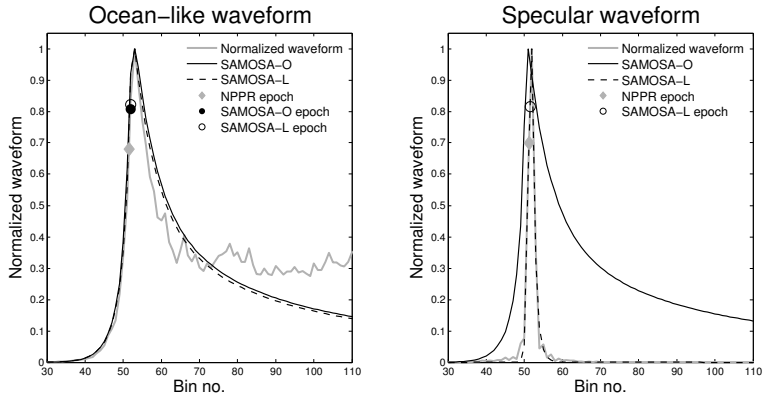

Figure 2: The fits of SAMOSA-O and SAMOSA-L for an ocean-like (left) and a specular (right) waveform retrieved over Lake Okeechobee, Florida. The estimated epochs for each retracking method are also shown for comparison.

Some examples of the ability of the two SAMOSA3 models to fit the CryoSat-2 waveforms are shown in Fig. 2. The results from an ocean-like waveform are shown in the graph to the left and the corresponding results are shown for a specular waveform to the right. Both SAMOSA3 models fit the ocean-like waveform, with correlations of 99.6% and 99.8% for the SAMOSA-O and the SAMOSA-L, respectively. The two fits for the specular example in Fig. 2 had correlations of 72.7% and 99.6% for SAMOSA-O and SAMOSA-L, respectively.

3.3. Data handling

The data handling consisted of several steps, since we will be using multiple retrackers for the retracking procedure where the physical and empirical retrackers are combined, which requires some extra precautions.

1. The data are masked with the GLWD described in Section 2.2.
2. Waveforms that seem appropriate to retrack using the physical retrackers are isolated by waveform classification. The waveforms are divided into 12 classes based on the shape of the power echoes using a Naive Bayes classifier. The Naive Bayes classifier was set up using a training set of

approximately 6000 waveforms over inland water. This training set consist of most waveform types and was used for all study regions.

3. All waveforms are retracked using the NPPR retracker and the proposed MWaPP retracker. Suitable waveforms are retracked using the SAMOSA3 retrackers depending on the classification results, and heights for which the correlation between the observed and the modelled waveform is higher than 99% are accepted.
4. The worst outliers are removed by discarding all observations more than two standard deviations from the track mean - the outlier detection was performed twice. Tracks with fewer than six observations left were excluded from the study.
5. For the retracking procedure where the physical and empirical retrackers are combined, the bias between them are minimized using a neural network approach as done in Idris (2014) using a training set of 30%. To train the neural network either the NPPR retracker or the proposed MWaPP retracker is used. This leaves us with five datasets:
   (a) NPPR: Heights obtained using only the NPPR retracker
   (b) MWaPP: Heights obtained using only the proposed empirical retracker
   (c) Combined (NPPR): Heights obtained using a combination of the SAMOSA3 and the NPPR retracker. The bias was minimized using the NPPR heights for the training set.
   (d) Combined (MWaPP): Heights obtained using a combination of the SAMOSA3 and the proposed MWaPP retracker. The bias was minimized using the MWaPP heights for the training set.
   (e) SAMOSA-O: Heights obtained using *only* the results from the traditional SAMOSA3 model for ocean-like waveforms.
6. For each track a mean is calculated, which is to be used for time series.

Due to the slope of the Amazon River, the track means used to derive the time series were detrended in the zonal direction similar to Villadsen et al. (2015)

using the retracked heights derived in this study. The slope was estimated to be around 1 m per degree longitude.

For Lake Vänern and Lake Okeechobee the track means obtained from the various retracking methods were compared with in-situ data. The offsets between the retracked data and the in-situ data were removed prior to creating the time series by adjusting the level of the retracked data sets so the time series had the same mean values as the in-situ data. As such, we will not be discussing the accuracy of the altimetric heights. Instead, the comparison was done by looking at the root-mean-squared-error (RMSE).

When precision is mentioned in this study we are referring to the precision of the mean (as in Nielsen et al. (2015a)), i.e. the mean standard deviation of each track crossing the study area in question.

4. Results

4.1. Classification

The spatial distributions of the used retrackers for Lake Vänern, Lake Okeechobee, and the Amazon River are shown in Fig. 3. The results reveal that all three types of retrackers (SAMOSA-O, SAMOSA-L, and empirical) are seen in each study area. The degree to which they are used, however, depend on the characteristics of the water body.

In Lake Vänern, which is the largest lake in this study, the SAMOSA-O retracker is the most commonly used retracker in the central parts of the lake and is used for 32.9 % of all waveforms retrieved over the lake. For some of the ocean-like waveforms the SAMOSA-L retracker provides a better fit, and especially in the south borders of the western part of the lake the SAMOSA-L retracker is used to fit more specular waveforms near the shore. In 51 % of the cases the empirical retracker is chosen, especially in the vicinity of the shore where the waveforms get more complex due to contamination from land signals. For Lake Okeechobee the same pattern is seen with slightly more waveforms retracked with the lead adaptation of the SAMOSA3 retracker.

The distribution of assigned classes is slightly different in the Amazon River (see Fig. 3(c) with a larger number of empirically retracked waveforms. This agrees well with our expectations, as the Amazon River is smaller in size and has a channel pattern that is more complex compared to the regular shapes of the lakes. All of these characteristics are bound to produce more waveforms that are either noisy or specular, which the SAMOSA-O model will not be able to fit. It is also seen that the specular waveforms are found in the narrow parts of the Amazon and its tributaries, whereas the SAMOSA-O model is mostly used for waveforms retrieved over the wider stretches.

4.2. Comparison of retracking methods

To compare the different retracking methods some examples of the results for a couple of tracks crossing Lake Vänern and the Amazon River are shown in Figs. 4 and 5, respectively. Looking at the detailed plot in Fig. 4(c) we clearly see that the results from the MWaPP retracker are less noisy, such as the heights retrieved around 58.86°N. There are of course exceptions to this, and the sudden decrease in surface height around 58.58°N looks unnatural and must be a retracking error. However, in general the MWaPP approach appears to provide the best results.

The example over the Amazon River in Fig. 5 shows that the two pure empirical retrackers give similar results for most waveforms. It was observed that the results from the combined method varies a lot regardless of the size of the training set used for the neural network.

4.3. Standard deviations of overpasses

The mean standard deviations, for all tracks for each study area are given in Tables 1 and 2 for all observations and observations where both SAMOSA-O and SAMOSA-L could have been used, respectively. The latter comparison was done to see how well the SAMOSA-O retracker performs compared to the empirical retrackers. From Table 1 it is seen that the MWaPP retracker has the lowest standard deviation of 9.11 cm over Lake Vänern, which is to be expected

Retracking method	Lake Vänern	Lake Okeechobee	Amazon River
NPPR	15.32 cm	39.23 cm	15.66 cm
MWaPP	**9.11 cm**	**13.35 cm**	**14.91 cm**
Combined (SAMOSA3 + NPPR)	15.91 cm	40.07 cm	16.41 cm
Combined (SAMOSA3 + MWaPP)	9.78 cm	13.78 cm	15.88 cm
ESA L2	53.86 cm	78.82 cm	47.29 cm

Table 1: Mean track standard deviations for the different methods for *all* available observations.

since this method will alleviate some snagging cases that a simple outlier removal method will not detect. The combined method where the MWaPP retracker has been used also performs well with a mean standard deviation of 9.78 cm. The performance of the NPPR retracker is not as good with standard deviations around 15-16 cm for both the purely empirical and the combined data sets. For comparison the results from the ESA L2 product have been included. It should be noted that the L2 product from ESA does not provide stable heights over inland water and other retrackers should be used. In general we expect the standard deviations to decrease with increasing size of the water body, which is what we see for the methods that perform the best.

Table 2 shows the track standard deviations *only* including retracked heights obtained from waveforms that could be fitted with both SAMOSA3 retrackers, which leaves us with only the well-behaved waveforms. Looking at only these waveforms allows for a fair comparison of the various retrackers, and as expected the precision increases in general for all retracking methods. Comparing precisions between study areas becomes somewhat misleading, as the number of remaining observations for the smaller water bodies is very low (e.g. 3-4 SAMOSA fits per Amazon track). One should therefore only compare values for the same study area.

For Lake Vänern we see that the highest precisions are obtained when using just the SAMOSA-O retracker, which is what we would expect considering the size of the lake.

Retracking method	Lake Vänern	Lake Okeechobee	Amazon River
NPPR	5.31 cm	4.35 cm	4.12 cm
MWaPP	5.17 cm	4.32 cm	4.19 cm
Combined (SAMOSA3 + NPPR)	4.73 cm	4.36 cm	4.44 cm
Combined (SAMOSA3 + MWaPP)	4.70 cm	4.18 cm	4.54 cm
SAMOSA-O	**4.23 cm**	**4.04 cm**	**3.42 cm**
ESA L2	9.62 cm	9.91 cm	5.56 cm

Table 2: Mean track standard deviations for the different methods for waveforms where *both* SAMOSA3 retrackers have correlations higher than 99%.

For Lake Okeechobee and the Amazon River we also get the lowest standard deviations when using only the SAMOSA-O retracker. It should be noted that for all methods apart from the ESA L2 product, the precision only varies within a few centimetres (1.1 cm for Lake Vänern, 0.3 cm for Lake Okeechobee, and 0.7 cm for the Amazon River). Although the biases between the physical and empirical retrackers were minimized using a neural network there still appears to be some excess noise in these data sets compared to those that are obtained purely from empirical retrackers.

4.4. Time series

The time series obtained for the three study areas are shown in Figs. 6(a), 6(b) and 6(c). For Lake Vänern and Okeechobee the available in-situ water levels have been included for comparison and the corresponding RMSEs are given in Table 3.

The time series for Lake Vänern in Fig. 6(a) shows a complicated pattern, which is captured well with satellite altimetry. The lowest RMSEs are obtained with the SAMOSA-O retracker, but it should be noted that the SAMOSA-O data set only include results from the well-behaved waveforms. Comparing the RMSEs obtained from the NPPR and MWaPP methods for only these observations reveal similar performances.

When using all observations to derive time series data the RMSEs are slightly

Retracking method	Lake Vänern	Lake Okeechobee
NPPR	11.3 (5.2) cm	60.6 (2.4) cm
MWaPP	5.2 (3.8) cm	12.8 (2.4) cm
Combined (SAMOSA3 + NPPR)	11.2 cm	60.5 cm
Combined (SAMOSA3 + MWaPP)	5.2 cm	12.7 cm
SAMOSA-O	3.5 cm	2.1 cm
ESA L2	46.7 cm	103.5 cm

Table 3: Root-mean-square-errors (RMSE) between retracked heights and in-situ water levels for Lake Vänern and Lake Okeechobee. The numbers in the parentheses are the same statistics but only including the observations where the SAMOSA-O retracker could be used.

higher. The results from the MWaPP retracker give an RMSE around 5 cm, whereas the NPPR method has an RMSE around 11 cm. The RMSE values show that combining the physical and empirical retrackers do not offer better time series data.

The time series over Okeechobee reveals that the mean values from MWaPP and the combined method with MWaPP values are almost identical. In fact, the mean absolute difference is only half a centimetre. Looking at the RMSE values we see the same thing as in Lake Vänern, i.e. that the MWaPP retracker provides heights that follow the in-situ levels much closer than the NPPR method.

5. Discussion

In general we see great results from all retrackers, but it is clear that the MWaPP retracker adds something very valuable and allows us to retrieve heights that would otherwise be flagged as outliers and discarded. The method has a very low computational cost compared to the SAMOSA3 model, and although the results from the SAMOSA3 retracker are better, i.e. have higher precisions and lower RMSEs, it is debatable whether or not the time consuming implementation and fitting is worth the gained precision. The results presented here also indicate that the bias issues that are introduced when combining retrackers mask the potential benefits of such a method. Many of the outliers causing the

higher RMSE of the NPPR data set could of course haven been avoided by using more sophisticated outlier detection methods, such as done in Nielsen et al. (2015a), but the MWaPP method presented in this study allows for retrieval of a higher number of useful heights, which especially in data sparse regions, such as narrow rivers, is preferable.

There is no doubt that the SAMOSA3 retracker provides very stable water levels, the benefit of using the SAMOSA retracker is however concealed in regions like inland water where complicated waveforms are repeatedly encountered and an empirical retracker is needed as well. Trying to avoid the offset by adjusting the 80% threshold level for the empirical retrackers was unsuccessful. Therefore, the offset is reduced using the neural network in this study.

6. Conclusions and outlook

In this study we presented a number of novel methods for retracking SAR waveforms over inland water, especially the new way of taking adjacent waveforms into account during retracking to find the subwaveform that is most likely to hold the echo from the water body at nadir. We also presented a combined method that uses an empirical retracker as well as the SAMOSA3 model with retracking offsets minimized using a neural network approach.

The results showed that the SAMOSA3 model provides results with high precisions. However, the results were not much better than those obtained using the empirical MWaPP retracker presented in this study. When combining the physical and empirical retrackers, the higher precision of the SAMOSA3 model is concealed by the retracking offsets even after these were minimized using a neural network. Due to these findings we suggest using the proposed MWaPP developed for this study in regions where most waveforms cannot be retracked by the SAMOSA3 model. In bigger lakes with a high number of observations it could prove more beneficial to use the SAMOSA3 retrackers, especially if information on significant wave height or roughness is desirable, and simply discard waveforms where an acceptable fit is not obtainable.

To further improve precisions and RMS errors, we also suggest using more sophisticated methods for outlier detection and determination of robust mean water levels such as described in Nielsen et al. (2015a). Finally, it should be noted that the methods derived here are used on CryoSat-2 data, but should be easily applicable to any SAR data (such as from the upcoming Sentinel-3 mission) with only a few simple adjustments of the many parameters in the SAMOSA3 model. Sentinel-3 and its SRAL SAR altimeter will improve the possibilities for inland water monitoring even further with the repeat orbit of 27 days.

Acknowledgements

We would like to thank the European Space Agency (ESA) for providing CryoSat-2 data. This research was conducted with support from the EU FP7 LOTUS project (Preparing Land and Ocean Take Up From Sentinel-3) - Grant no. 313238. A special thank you to the SAMOSA team for providing the MATLAB codes necessary for the implementation of their model. All map data were provided by Google Earth (SIO, NOAA, U.S. Navy, NGA, GEBCO and Landsat).

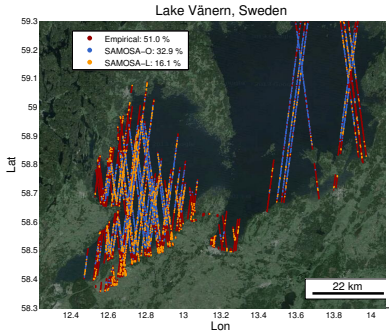

(a)

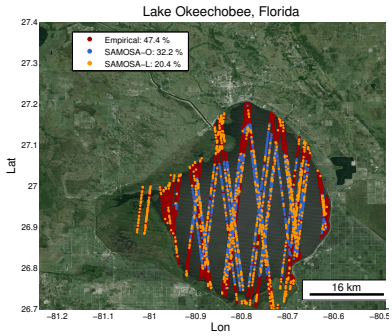

(b)

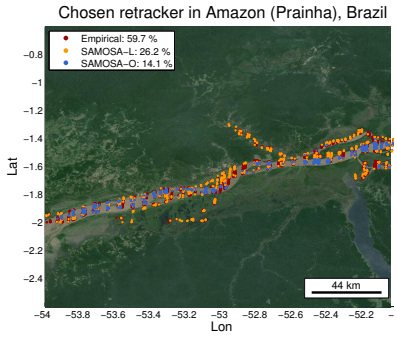

(c)

Figure 3: Classification results over the three different study areas. Distributions as well as percentages showing where and how frequently the different retrackers were used.

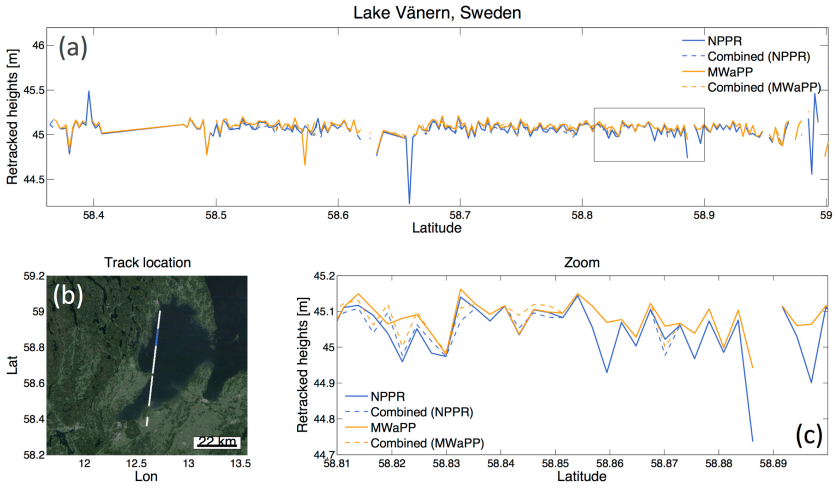

Figure 4: (a) Comparison of retracking methods over Lake Vänern for a track on October 31st, 2011. (b) Track location across the lake. Highlighted (red) points mark the observations shown in the detailed plot of (a) in (c).

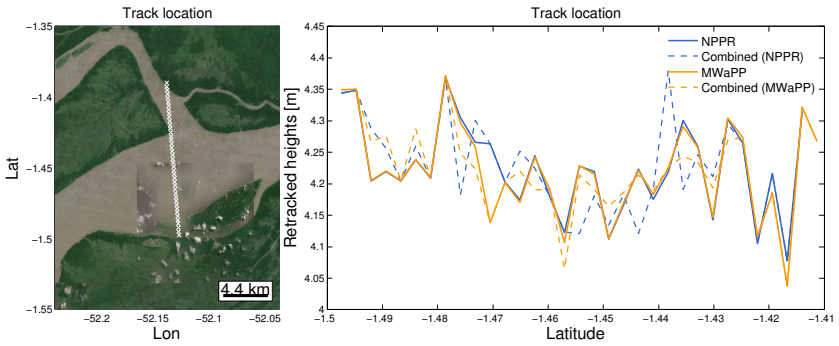

Figure 5: Comparison of retracking methods over the Amazon River for a track crossing the river on June 28th, 2014.

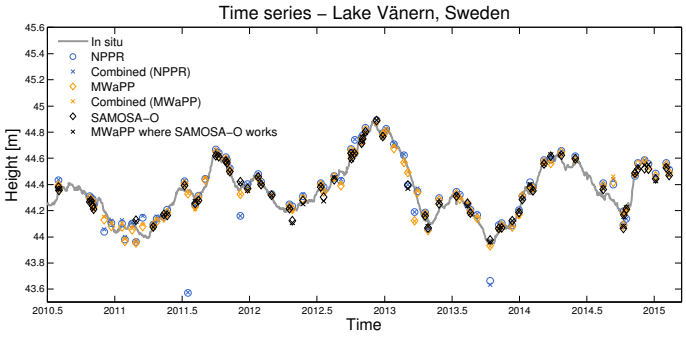

(a)

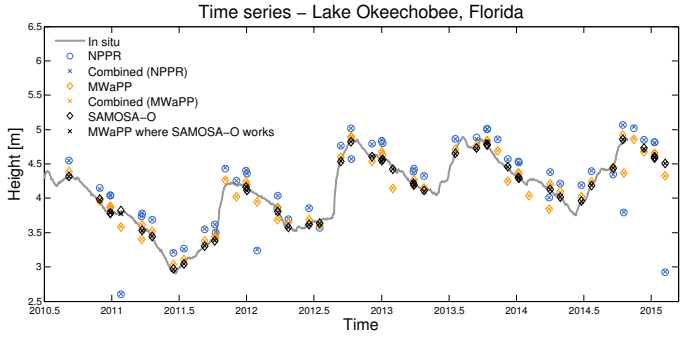

(b)

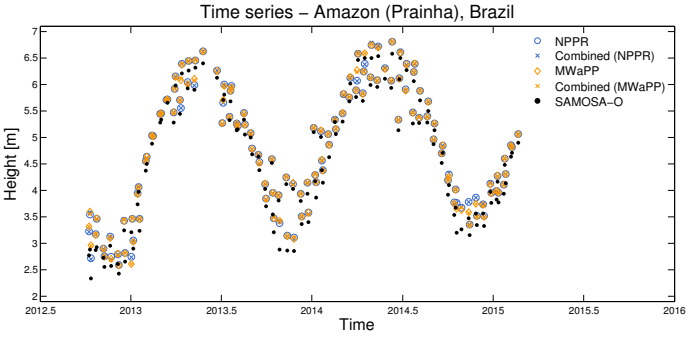

(c)

Figure 6: Time series for the three different study areas derived from retracked heights and compared with in-situ data where possible.

References

Bao, L., Lu, Y., & Wang, Y. (2009). Improved retracking algorithm for oceanic altimeter waveforms. *Progress in Natural Science*, *19*, 195 – 203. doi:10.1016/j.pnsc.2008.06.017.

Berry, P. (2006). Two Decades of Inland Water Monitoring Using Satellite Radar Altimetry. *Proceedings of the Symposium on 15 Years of Progress in Radar Altimetry, ESA Special Publication*, *614*, 8.

Berry, P. A. M., Garlick, J. D., Freeman, J. A., & Mathers, E. L. (2005). Global inland water monitoring from multi-mission altimetry. *Geophysical Research Letters*, *32*. doi:10.1029/2005GL022814.

Biancamaria, S., Hossain, F., & Lettenmaier, D. P. (2011). Forecasting transboundary river water elevations from space. *Geophysical Research Letters*, *38*, n/a–n/a. doi:10.1029/2011GL047290.

Birkett, C., Reynolds, C., Beckley, B., & Doorn, B. (2011). From Research to Operations: The USDA Global Reservoir and Lake Monitor. In S. Vignudelli, A. G. Kostianoy, P. Cipollini, & J. Benveniste (Eds.), *Coastal Altimetry* (pp. 19–50). Springer Berlin Heidelberg. URL: http://dx.doi.org/10.1007/978-3-642-12796-0_2. doi:10.1007/978-3-642-12796-0_2.

Birkett, C. M. (1994). Radar altimetry: A new concept in monitoring lake level changes. *Eos, Transactions American Geophysical Union, Eos: Earth and Space Science News, Eos Trans. Agu, Eos Transactions, Eos (washington Dc), Eos*, *75*, 273. doi:10.1029/94eo00944.

Birkett, C. M. (1998). Contribution of the TOPEX NASA Radar Altimeter to the global monitoring of large rivers and wetlands. *Water Resources Research*, *34*, 1223–1239. doi:10.1029/98WR00124.

Cretaux, J.-F., & Birkett, C. (2006). Lake studies from satellite radar altimetry. *Comptes Rendus Geoscience, Comptes Rendus. Goscience, C. R. Geosci, C*

R Geosci, Cr Geosci, Comptes Rendus Geosciences, C R Geoscience, C.r. Geosci, *338*, 1098–1112. doi:10.1016/j.crte.2006.08.002.

Crétaux, J.-F., Jelinski, W., Calmant, S., Kouraev, A., Vuglinski, V., Bergé-Nguyen, M., Gennero, M.-C., Nino, F., Rio, R. A. D., Cazenave, A., & Maisongrande, P. (2011). SOLS: A lake database to monitor in the Near Real Time water level and storage variations from remote sensing data. *Advances in Space Research*, *47*, 1497 – 1507. URL: http://www.sciencedirect.com/science/article/pii/S0273117711000287. doi:http://dx.doi.org/10.1016/j.asr.2011.01.004.

Dinardo, S., Lucas, B., Gommenginger, C., Martin-Puig, C., & et al. (2013). Detailed processing model of the sentinel-3 sral sar altimeter sea waveform retracker v2.3.0.

Gommenginger, C., Thibaut, P., Fenoglio-Marc, L., Quartly, G., Deng, X., Gomez-Enri, J., Challenor, P., & Gao, Y. (2011). Retracking altimeter waveforms near the coasts a review of retracking methods and some applications to coastal waveforms. *Coastal Altimetry, Coast. Altimetry*, (pp. 61–101). doi:10.1007/978-3-642-12796-0_4.

Idris, N. H. (2014). *Development of New Retracking Methods for Mapping Sea Levels over the Shelf Areas from Satellite Altimetry Data*. Ph.D. thesis PhD Thesis, The University of Newcastle Australia.

Jain, M. (2015). *Improved sea level determination in the Artic regions through development of tolerant altimetry retracking*. Ph.D. thesis DTU Space, Technical University of Denmark.

Jain, M., Andersen, O. B., Dall, J., & Stenseng, L. (2015). Sea surface height determination in the arctic using cryosat-2 {SAR} data from primary peak empirical retrackers. *Advances in Space Research*, *55*, 40 – 50. URL: http://www.sciencedirect.com/science/article/pii/S0273117714005705. doi:http://dx.doi.org/10.1016/j.asr.2014.09.006.

Jain, M., Martin-Puig, C., Andersen, O. B., Stenseng, L., & Dall, J. (2014). Evaluation of samosa3 adapted retracker using cryosat-2 sar altimetry data over the arctic ocean, . (pp. 5115–5118). doi:10.1109/IGARSS.2014.6947648.

Kleinherenbrink, M., Ditmar, P., & Lindenbergh, R. (2014). Retracking cryosat data in the sarin mode and robust lake level extraction. *Remote Sensing of Environment*, *152*, 38.

Kleinherenbrink, M., Lindenbergh, R., & Ditmar, P. (2015). Monitoring of lake level changes on the tibetan plateau and tian shan by retracking cryosat {SARIn} waveforms. *Journal of Hydrology*, *521*, 119 – 131. URL: http://www.sciencedirect.com/science/article/pii/S0022169414009858. doi:http://dx.doi.org/10.1016/j.jhydrol.2014.11.063.

Koblinsky, C. J., Clarke, R. T., Brenner, A. C., & Frey, H. (1993). Measurement of river level variations with satellite altimetry. *Water Resources Research*, *29*, 1839–1848. doi:10.1029/93WR00542.

Lehner, B., & Doll, P. (2004). Development and validation of a global database of lakes, reservoirs and wetlands. *Journal of Hydrology*, *296*, 1–22. doi:10.1016/j.jhydrol.2004.03.028.

Michailovsky, C. I., Milzow, C., & Bauer-Gottwein, P. (2013). Assimilation of radar altimetry to a routing model of the Brahmaputra River. *Water Resources Research*, *49*, 4807–4816. doi:10.1002/wrcr.20345.

Neal, J., Schumann, G., Bates, P., Buytaert, W., Matgen, P., & Pappenberger, F. (2009). A data assimilation approach to discharge estimation from space. *Hydrological Processes*, *23*, 3641–3649. doi:10.1002/hyp.7518.

Nielsen, K., Stenseng, L., Andersen, O., Villadsen, H., & Knudsen, P. (2015a). Validation of cryosat-2 sar mode based lakes levels. *Remote Sensing of Environment*, *under revision*.

Nielsen, K., Stenseng, L., Andersen, O., Villadsen, H., & Knudsen, P. (2015b). Validation of lake levels based on cryosat-2 sar mode data. Presented at the Sentinel-3 for Science Workshop, Venice, Italy (June 2015).

Pavlis, N. K., Holmes, S. A., Kenyon, S. C., & Factor, J. K. (2012). The development and evaluation of the earth gravitational model 2008 (egm2008). *Journal of Geophysical Research - Solid Earth*, *117*, –. doi:10.1029/2011JB008916.

Raney, R. K. (1998). The delay/doppler radar altimeter. *IEEE Transactions on Geoscience and Remote Sensing*, *36*, 1578–1588. doi:10.1109/36.718861.

Ray, C., Martin-Puig, C., Clarizia, M. P., Ruffini, G., Dinardo, S., Gommenginger, C., & Benveniste, J. (2015). Sar altimeter backscattered waveform model. *IEEE TRANSACTIONS ON GEOSCIENCE AND REMOTE SENSING*, *53*, 911–919. doi:10.1109/TGRS.2014.2330423.

Schwatke, C., Dettmering, D., Bosch, W., & Seitz, F. (2015). Kalman filter approach for estimating water level time series over inland water using multi-mission satellite altimetry. *Hydrology and Earth System Sciences Discussions*, *12*, 4813–4855. URL: http://www.hydrol-earth-syst-sci-discuss.net/12/4813/2015/. doi:10.5194/hessd-12-4813-2015.

Seppl, M. (2005). *The physical geography of Fennoscandia*. The Oxford regional environments series. Oxford University Press. URL: http://ci.nii.ac.jp/ncid/BA80490866.

Song, C., Huang, B., & Ke, L. (2014). Inter-annual changes of alpine inland lake water storage on the tibetan plateau: Detection and analysis by integrating satellite altimetry and optical imagery. *Hydrological Processes, Hydrol. Process, Hydrol Proc, Hydrol Process, Hydrological Processes an International Journal, Hydrol. Processes*, *28*, 2411–2418. doi:10.1002/hyp.9798.

Tourian, M., Elmi, O., Chen, Q., Devaraju, B., Roohi, S., & Sneeuw, N. (2015). A spaceborne multisensor approach to monitor the desiccation of lake urmia in iran. *Remote Sensing of*

Environment, *156*, 349 – 360. URL: http://www.sciencedirect.com/science/article/pii/S0034425714004027. doi:http://dx.doi.org/10.1016/j.rse.2014.10.006.

Vignudelli, S., Kostianoy, A., Cipollini, P., & Benveniste, J. (2010). *Coastal Altimetry*. Springer Berlin Heidelberg. URL: https://books.google.com/books?id=M_2ljwEACAAJ.

Villadsen, H., Andersen, O., Stenseng, L., Nielsen, K., & Knudsen, P. (2015). Cryosat-2 altimetry for river level monitoring - evaluation in the ganges-brahmaputra river basin. *Remote Sensing of Environment*, *in print*.

Wingham, D., Francis, C., Baker, S., Bouzinac, C., Brockley, D., Cullen, R., de Chateau-Thierry, P., Laxon, S., Mallow, U., Mavrocordatos, C., Phalippou, L., Ratier, G., Rey, L., Rostan, F., Viau, P., & Wallis, D. (2006). CryoSat: A mission to determine the fluctuations in Earths land and marine ice fields. *Advances in Space Research*, *37*, 841 – 871. doi:http://dx.doi.org/10.1016/j.asr.2005.07.027.

Zakharova, E. A., Kouraev, A. V., Rmy, F., Zemtsov, V. A., & Kirpotin, S. N. (2014). Seasonal variability of the western siberia wetlands from satellite radar altimetry. *Journal of Hydrology, J. Hydrol*, *512*, 366–378. doi:10.1016/j.jhydrol.2014.03.002.

A.3 A new SAR waveform retracking system for inland water height determination

Conference proceedings for the Sentinel-3 for Science Workshop held in Venice, Italy, June 2015.

A NEW SAR WAVEFORM RETRACKING SYSTEM FOR INLAND WATER HEIGHT DETERMINATION

Heidi Villadsen[1], Ole B. Andersen[1], Lars Stenseng[1], Karina Nielsen[1], Per Knudsen[1], and Xiaoli Deng[2]

[1]*National Space Institute, Technical University of Denmark, Elektrovej 327, 2800 Kgs. Lyngby, Denmark*
[2]*School of Engineering, University of Newcastle, University Drive, Callaghan NSW 2308, Australia*

ABSTRACT

Here we investigate the benefits of using a retracking method that combines the accuracy and precision of the physical SAMOSA3 retracker with the stability of an empirical primary peak threshold retracker by classifying the waveforms prior to retracking and minimizing the bias that is introduced by combining the retrackers along track. The results show that SAR altimetry offers a great supplement to traditional gauge data independent of the complexity of the retracking method. This is believed to be caused by the unavoidable bias between empirical and physical retrackers, which clouds the benefit of using physical retrackers.

Key words: Altimetry; CryoSat-2; Inland water; SAMOSA; Retracking; Classification.

1. INTRODUCTION

Concern about climate change and fresh water availability has increased the need for accurate water levels of rivers and lakes. Unfortunately, at the same time there has been a decrease in available in-situ data from monitoring stations. Satellite altimetry can provide water levels globally independently of infrastructure. However, the best methods for obtaining accurate water levels from observations retrieved over smaller water bodies are still not fully explored. Altimeters such as the SIRAL altimeter on-board CryoSat-2 and the upcoming SRAL altimeter on Sentinel-3 have the great benefit of operating in Synthetic Aperture Radar (SAR) mode, which gives an along-track resolution of just 300 m a resolution that will improve the ability to obtain inland water heights. Here we present a new method for retracking of SAR waveforms over rivers and lakes. Satellite altimetry offers frequent and global sampling across borders, which can be used to validate and calibrate hydrological models in remote areas where in situ measurements are scarce.

The retracking system was developed using CryoSat-2 20 Hz SAR data, but due to the similarities between the Sentinel-3 SRAL altimeter and the SIRAL altimeter on-board CryoSat-2 an adaption of the method will be straightforward.

The SAMOSA retracker has previously demonstrated to perform better than other existing SAR retrackers over water surfaces and has therefore been chosen as the primary retracker whenever applicable. To find the waveforms for which the SAMOSA3 retracker is appropriate, a classification is performed and the waveforms are retracked accordingly.

When all waveforms are retracked, biases introduced by using different retrackers are minimized in order to assure continuity, which would otherwise be obscured by offsets between the empirical and physical retrackers.

2. STUDY REGIONS

The retracking method developed in this study was tested in Lake Okeechobee (with an area of 1.900 m^2) in Florida and in a stretch of the Amazon River near Prainha (with widths from 5 to 10 km) in Brazil. Lake Okeechobee is of a decent size, which should be ideal for the SAMOSA3 retracker using the standard model. In Okeechobee it is possible to compare our results with in-situ data obtained from the National Water Information System, http://waterdata.usgs.gov/nwis, and are relative to NGVD 1929.

3. METHODS

This study was completed in three steps:

- Classify the waveforms and assign each waveform to one of three retrackers.
- Retrack each waveform using the assigned retracker.

- Minimize the bias between the physical and the empirical retrackers using a mean method or a neural network.

3.1. Classification

To have an indication of which retracker to use, all observations are classified from the shape of the power waveform and assigned the most appropriate retracker. Classifying waveforms prior to retracking is an easy way of avoiding unnecessary, time-consuming fitting of all waveforms. A training set consisting of 12 classes made from a k-means classification is used as input for a Naive Bayes classifier. Depending on the pulse peakiness and number of major peaks in the corresponding class a waveform is flagged for later fitting with the SAMOSA3 model.

3.2. Retracking

Using the previous classification the waveforms that are found suitable for the SAMOSA3 retracker are isolated; these are the ocean-like and the highly specular waveforms. If the SAMOSA3 retracker is found unsuitable, or if the obtained result from this retracker is unsatisfactory, the waveform is retracked using an empirical sub-waveform threshold retracker. When using the empirical retracker the sub-waveform most likely to represent the echo from nadir is identified by studying adjacent waveforms.

3.2.1. Narrow primary peak retracker

This retracker uses a simple threshold approach on a sub-waveform around the primary peak to estimate the epoch [1]. The narrow primary peak retracker (NPPR) provides a very stable height estimate. For this study we used a threshold of 80 %. In addition, an extended method (NPPRM) where five consecutive waveforms are used to find the strongest common primary peak was derived. Looking at multiple waveforms to decide which sub-waveform to extract alleviates most cases of snagging, where an off-nadir reflector obscures the signal of interest from nadir.

3.2.2. SAMOSA3

The SAMOSA3 retracker is based on a physical model of power returns from a homogenous ocean surface [2, 3]. Given that the model fits the waveform perfectly, the retracker will give a highly accurate estimate of the range to nadir. In addition to the standard SAMOSA3 model used for ocean-like waveforms (SAMOSA-O), we also use a modification adapted for specular waveforms over leads (SAMOSA-L). Since inland water, like leads, causes very specular waveforms this modification had to be included.

3.3. Bias reduction

Combining empirical and physical retrackers inferred a bias of around 13 cm. In this study we tried to minimize the bias using two different methods:

1. Using a mean method by simply adding the mean bias to all SAMOSA3 height estimates.
2. Using a neural network to remove the bias since the bias is not constant everywhere, but e.g. seems to depend on the distance to the shore of the inland water body.

4. RESULTS

An example of how the SAMOSA-O and SAMOSA-L models fit an ocean-like waveform along with their corresponding leading edge points (LEP) is shown in Figures 1 and 2. As seen, the SAMOSA-L model has the ability to adjust the trailing edge of the fit to accommodate very peaky waveforms.

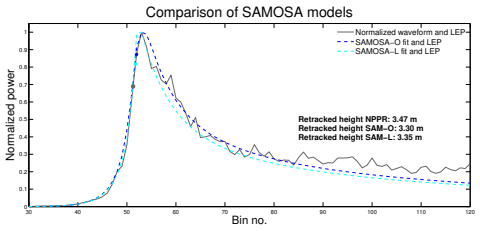

Figure 1. Example of SAMOSA3 model fits for an ocean-like waveform and the obtained epochs.

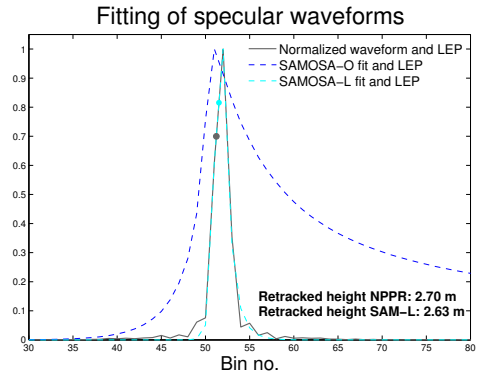

Figure 2. Example of SAMOSA3 model fits for a specular waveform and the obtained epochs.

Maps showing the distribution of assigned retrackers in Lake Okeechobee and a stretch of the Amazon River are shown in Figures 3 and 4. The SAMOSA-O retracker is usually chosen in the central parts of the water body, the empirical retrackers are chosen for the observations in non-central parts, whereas the SAMOSA-L retracker is often used very close the shore, where calm and shallow waters give very specular waveforms.

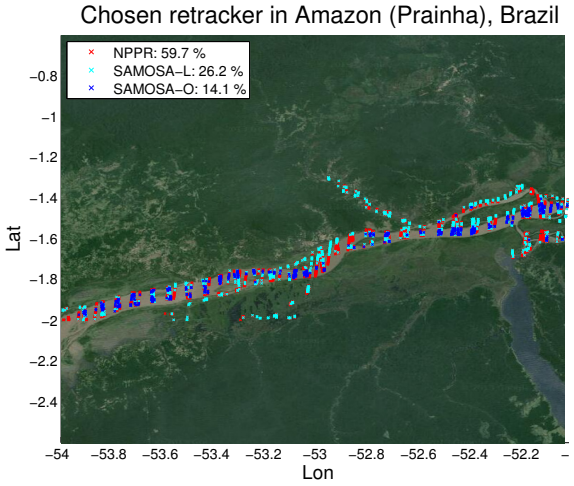

Figure 3. Assigned retracker in the Amazon River.

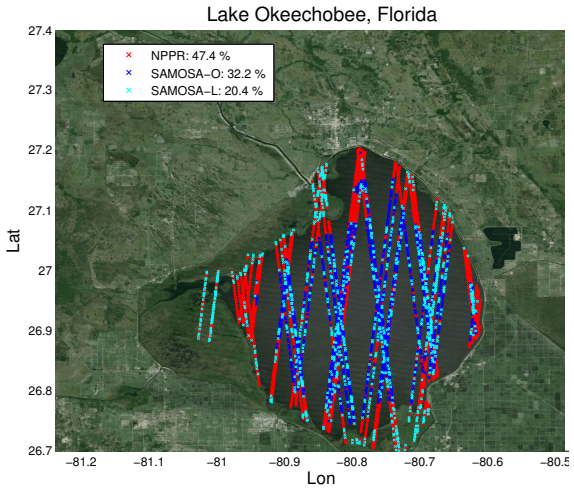

Figure 4. Assigned retracker in Lake Okeechobee.

Examples of the retracked heights for a track in the Amazon and Lake Okeechobee are shown in Figures 5 and 6. The results show that the difference between using the neural network and the mean method is minimal. It is also seen that the combined method gives results very similar to those of the empirical retracker once the biases are reduced.

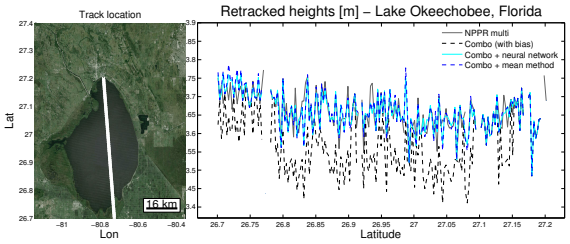

Figure 5. Comparison of obtained heights from different retracking methods for an ascending track crossing Lake Okeechobee in Florida.

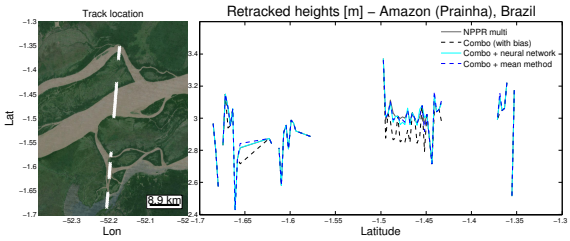

Figure 6. Comparison of obtained heights from different retracking methods for a descending track crossing the Amazon River.

Time series of the two study regions are shown in Figures 7 and 8. In Lake Okeechobee where there are in-situ data, the retracked heights and the in-situ heights, in arbitrary local height systems, are in good agreement. There appears to be no major difference between the time series obtained from the different retracking methods.

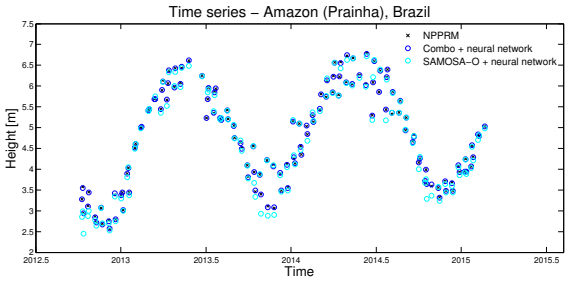

Figure 7. Comparison of the obtained time series in the Amazon River for different retracking methods.

5. CONCLUSIONS

We investigated the benefits of using a combined retracking method that uses the physical SAMOSA3 retracker whenever possible and an empirical threshold retracker elsewhere. For points where the SAMOSA3 model fits, the results generally have a higher precision

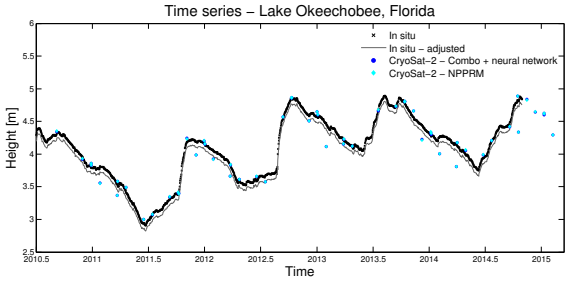

Figure 8. Comparison of the obtained time series in Lake Okeechobee with in-situ data.

than any other retracker. When combining the retrackers the induced bias masks the benefits of the SAMOSA3 retracker, and using a threshold retracker everywhere is deemed more suitable. Our results show that Sentinel-3 SAR altimetry will provide great results for inland water monitoring – even when using a simple empirical retracker.

ACKNOWLEDGEMENTS

For masking out the observations over land we used the Global Lakes and Water Database [4].

All map data was provided by Google Earth (SIO, NOAA, U.S. Navy, NGA, GEBCO and Landsat).

This research has been supported by the EU FP7 LOTUS project (Preparing Land and Ocean Take Up From Sentinel-3).

REFERENCES

[1] Jain, M., Andersen, O.B., Dall, J, Stenseng, L. (2015), Sea Surface height determination in the Arctic using Cryosat-2 SAR data from primary peak empirical retrackers, *Advances in Space Research* **55**(1), 40-50.

[2] Jain, M. (2015), Improved sea level determination in the Artic regions through development of tolerant altimetry retracking, PhD thesis. Contact: jain@space.dtu.dk

[3] Dinardo, S., Lucas, B., Gommenginger, C., Martin-Puig, C., et al. (2013), Detailed Processing Model of the Sentinel-3 SRAL SAR Altimeter sea waveform retracker v2.3.0, *European Space Agency Contract 20698/07/I-LG*.

[4] Lehner, B., Döll, P. (2004), "Development and validation of a global database of lakes, reservoirs and wetlands", *Journal of Hydrology* **296**(1), 1-22.

A.4 Annual cycle in lakes and rivers from CryoSat-2 altimetry – The Brahmaputra River

Conference proceedings for IEEE Geosciences and Remote Sensing Symposium (IGARSS) held in Québec, Canada, in July 2014.

ANNUAL CYCLE IN LAKES AND RIVERS FROM CRYOSAT-2 ALTIMETRY - THE BRAHMAPUTRA RIVER

H. Villladsen, O. B. Andersen and L. Stenseng

DTU Space, Elektrovej bldg. 328, 2800 Kgs Lyngby, Denmark (oa@space.dtu.dk)

ABSTRACT

A key concern of the CryoSat-2 orbit has been its long repeat period of 369 days, which is usually undesirable for river and lake monitoring. However, the results of this study show that CryoSat-2 data can indeed be used for such monitoring by utilizing the high spatial coverage and the sub-cycle period of 30 days. The performance of CryoSat-2/SIRAL altimetry for river level monitoring is investigated by studying river levels retrieved from Ganges and Brahmaputra. An evaluation of CryoSat-2 river levels from LRM, SAR and SARIn data is performed by comparing with Envisat data from the period in which the two missions overlapped (2010-2012). Time series constructed using simple linear interpolation are fitted with a model to compare the captured annual signals and amplitudes. The annual cycles seen in CryoSat-2 and Envisat altimetry data agree very well and provide confidence in using CryoSat-2 data to continue river level archives from satellite radar altimetry.

Index Terms— CryoSat, Envisat, satellite altimetry, inland waters, Brahmaputra, hydrology

1. INTRODUCTION

With the release of the new ESA Cryosat-2 satellite mission data are becoming available for studies of lake and river levels. The Cryosat-2 mission opens up for an entire new suite of applications as it provides data with a 369-days near repeat orbit since 2010 but with a ground track distance of just 8 km [3]. This is significantly different from any other altimetric satellite, which typically has repeat sampling of less than one month but at ground track separated by 100 km or more. Here we have investigated the use of Cryosat-2 for river level retrieval focusing on the ability to extract heights and also temporal height variations in large rivers particularly the Brahmaputra and Ganges Rivers. We present the first evaluation of the data in which we consider data measured by all the three available modes in Cryosat-2 derived from retracking the low level waveform data provided by ESA. Several projects already provide historical inland water levels from altimetry through web data bases, such as the ESA River&Lake project (`http://tethys.eaprs.cse.dmu.ac.uk/RiverLake/shared/main`), the Global Reservoir and Lake Monitor (GRLM) (`http://www.pecad.fas.usda.gov/cropexplorer/global_reservoir` [1]), and the HYDROWEB data base (`http://www.LEGOS.obs-mip.fr/soa/hydrologie/HYDROWEB`, [2]). However, none of these data archives have included CryoSat-2 data.

Thanks to XYZ agency for funding.

2. DATA

2.1. CryoSat-2

The SIRAL altimeter onboard Cryosat-2 is capable of operating in both conventional mode (LRM or low resolution mode), in Synthetic Aperture Radar mode (SAR) where the along track resolution is increased from 7 km to around 300 meters and in SAR-Interferometric mode (SARIn), where two antennas operate simultaneously [3]. The satellite operates under a geographical mode mask defined by ESA, which is modified from time to time depending on user needs. Here we use the ESA Level 1B waveform data which we retrack using a primary peak retracker [4]. Subsequently, the lake range observations were processed with the standard set of range and geophysical corrections for inland water where only solid and pole tides, dry and wet troposphere and ionosphere corrections were applied [5]. We have interpolated and evaluated all the corrections at 20 Hz or 300 meters along track in order to use the full resolution of the observations as these are needed for investigation of rivers and lakes.

2.2. Envisat

Previous studies using Envisat data over large rivers have shown that the altimetric data is a powerful tool for obtaining river levels and using them for hydrological purposes [6, 7, 8]. Hence, since no available in-situ measurements were found to coincide with the CryoSat-2 mission, Envisat data was chosen as the basis for our evaluation.
The Envisat data used for this study was processed using the ICE-1 retracker, which is an empirical OCOG retracker. The ICE-1 retracker has previously been found to be the Envisat retracker that compares best to in situ measurements over inland waters [6, 8].

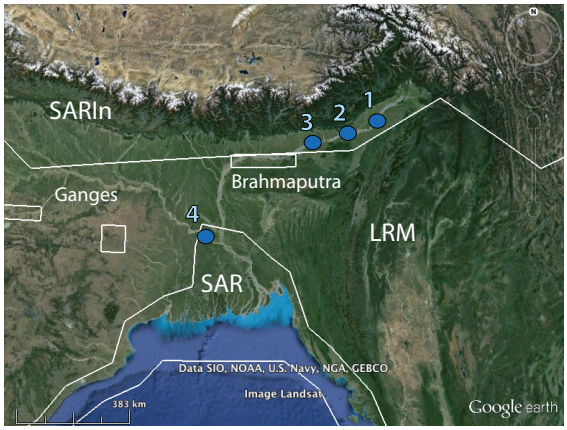

Fig. 1. Geographical mode mask of the CryoSat-2 altimeter and the locations of the different virtual stations. The SAR region was implemented in October 2012.

2.3. The MOD44w land-water mask

The satellite observations are masked using the MOD44w land-water mask, which is an improvement of the previous MODIS Nadir Bidirectional Reflectance Distribution Function (BRDF)-Adjusted Reflectance (NBAR) and MODIS land cover-based global land-water mask[9]. The binary grid mask has a resolution of 250 m. The mask was interpolated onto the locations of the observations from Envisat and CryoSat-2 resulting in a fraction between 0 and 100%.

2.4. The SRTM and ACE2 digital elevations models

The retracked heights obtained with CryoSat-2 and Envisat data are compared with the elevations given in the Shuttle Radar Topography Mission (SRTM) and the Altimetry Corrected Elevation 2 (ACE2) digital elevation models (DEMs). The SRTM data set has a resolution of 90 m and is near-global covering all land surfaces between +-60 degrees latitude. Using additional satellite data the SRTM was merged with available multimission satellite altimetry data, mainly data from the ERS-1 mission to create the ACE2 data set (`http://tethys.eaprs.cse.dmu.ac.uk/ACE2/shared/overview`). As SRTM, ACE2 also has a resolution of 90 m.

3. INVESTIGATED AREA

For this study the Ganges and Brahmaputra Rivers were chosen due to their decent sizes, which act as a good base for conducting an initial validation of CryoSat-2 altimetry data. Choosing this river basin also has the benefit that the area is covered by all three SIRAL modes making an intercomparison possible. The Ganges and Brahmaputra Rivers constitute one of the largest river basins in the world. The drainage basin includes some of the highest mountains present on the planet, the Himalayas. The Ganges-Brahmaputra delta is also one of the most densely populated areas in the world, and the people living here depends heavily on the state of the rivers and their tributaries. The strong seasonal signal caused by the summer monsoon and the melting of glaciers in the Himalayas gives rise to flooding during June to October, which is followed by a much drier period in the winter months.

4. DATA PROCESSING

For this study, CryoSat-2 and Envisat data are processed in the same manner, except for the retracking, which is described in sections 2.1 and 2.2. All observations are masked using the MOD44w land-water mask with the requirement that the observation is classified as >99% water. Outliers from each track are then removed by only including observations within three standard deviations from the mean. Tracks are used for the analysis if they contain at least six points after the outlier removal and if there is less than 0.5 degrees longitude to the closest virtual stations shown in figure reffig:map. A mean for each satellite crossing is calculated and assigned to the closest virtual station. All heights presented in this study are referenced to the WGS84 ellipsoid.

4.1. Slope correction

Usually, a time series will consist of a series of observations from the same location on the river. However, due to its orbit, CryoSat-2 does not offer this possibility. In stead, the observations in the vicinity of the defined virtual stations are corrected for the slope of the river by assuming it to be linear. After the observations are corrected a time series for each virtual station is constructed.

4.2. Estimating annual signals

In order to obtain information about the annual cycles of our time series a model is fitted to the water level time series. This model is defined as $f(t) = A + Bt + C\cos(t') + D\sin(t')$, where t is the time in decimal years relative to January 1st 2012 and $t' = 2\pi t$. From this fit the annual phases and amplitudes are estimated and compared.

5. RESULTS

Figure 2 shows the estimated heights in the Brahmaputra River as given by satellite altimetry from CryoSat-2 and Envisat, and the height estimates from the digital elevation models SRTM and ACE2 at the locations of the CryoSat-2 observations. Evidently, the CryoSat-2 heights exhibit much less noise compared to the other data sets, which is most likely due to the reduced satellite footprint.

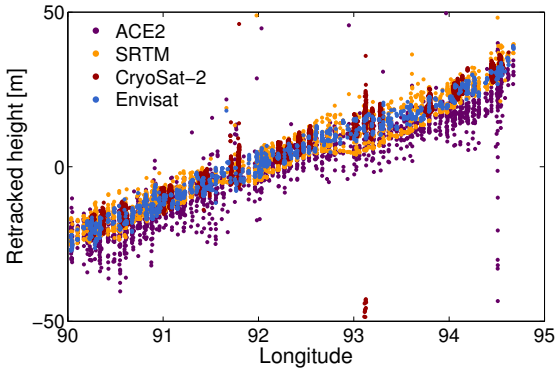

Fig. 2. Comparison of CryoSat-2 data with heights from Envisat and the digital elevation models SRTM and ACE2. Outliers have not been removed for this comparison.

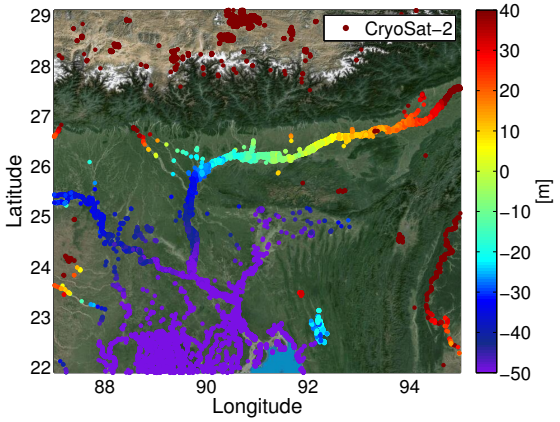

Fig. 3. Map of CryoSat-2 heights within the Brahmaputra River.

A map showing the raw but masked CryoSat-2 heights is seen in figure 3. It is evident that CryoSat-2 offers a data set with a high spatial resolution compared to previous altimetry missions with a shorter repeat period.

The time series obtained by applying the linear slope correction are shown in figures 4 and 5 for the different modes of the SIRAL altimeter. Although CryoSat-2 doesn't operate with a usual repeat orbit the annual signals are clearly visible. The time series from CryoSat-2 do, however, show more noise than the Envisat data, which could be caused by problems with the land-water mask, or by the assumption that the river will have a linear slope.

The annual signals of the Envisat and CryoSat-2 time series are shown in figure 6. The amplitudes of the time series are of the same order and mainly follow the same pattern downriver.

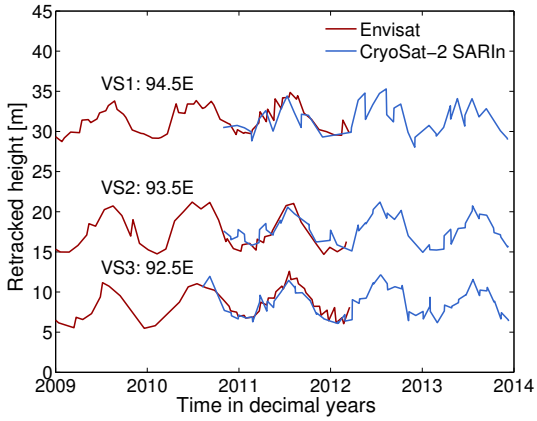

Fig. 4. Extended Brahmaputra river times series showing estimated river levels for Envisat (red) and CryoSat-2 SARIn (blue).

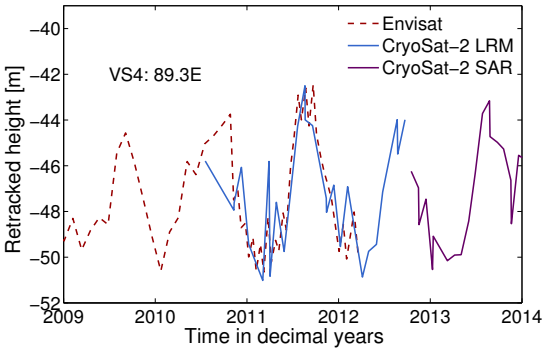

Fig. 5. Extended Ganges river times series showing estimated river levels for Envisat (red), CryoSat-2 LRM (blue) and SAR (purple), the latter from October 2012 onwards.

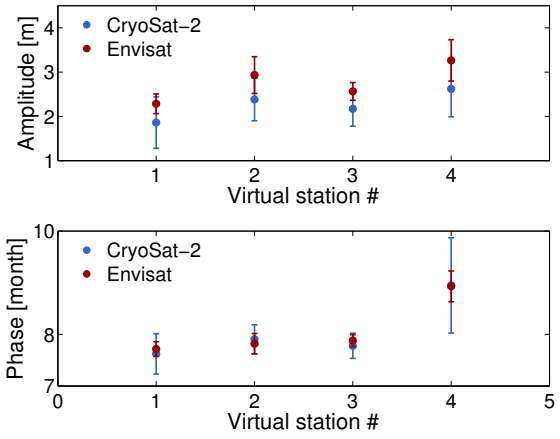

Fig. 6. Fitted phases and amplitudes for time series obtained from CryoSat-2 SARIn and Envisat data from July 2010 to March 2012.

6. CONCLUSIONS

Annual cycles were studied for both CryoSat-2 and Envisat data in the period spanning from the launch of CryoSat-2 in July 2010 to the end of the Envisat mission in March 2012.The results showed that the two satellites captured comparable annual signals and that CryoSat-2 has great potential in the field of inland water monitoring.

Future work to improve the presented method could include an improvement of or an alternative to existing land-water masks. However, the most crucial improvement lies within the development of a retracker specifically designed to retrack heights over inland waters.

7. ACKNOWLEDGEMENTS

CryoSat-2 and Envisat data were provided by the European Space Agency (ESA). This research has been supported by the EU FP7 LOTUS project (Preparing Land and Ocean Take Up From Sentinel-3). All map data was provided by Google Earth (SIO, NOAA, U.S. Navy, NGA, GEBCO and Landsat).

8. REFERENCES

[1] C. Birkett, C. Reynolds, B. Beckley, and B. Doorn, "From Research to Operations: The USDA Global Reservoir and Lake Monitor," in *Coastal Altimetry*, S. Vignudelli, A. G. Kostianoy, P. Cipollini, and J. Benveniste, Eds., pp. 19–50. Springer Berlin Heidelberg, 2011.

[2] J.-F. Crétaux, W. Jelinski, S. Calmant, A. Kouraev, V. Vuglinski, M. Bergé-Nguyen, M.-C. Gennero, F. Nino, R. A. D. Rio, A. Cazenave, and P. Maisongrande, "SOLS: A lake database to monitor in the Near Real Time water level and storage variations from remote sensing data," *Advances in Space Research*, vol. 47, no. 9, pp. 1497 – 1507, 2011.

[3] D. Wingham, C. Francis, S. Baker, C. Bouzinac, D. Brockley, R. Cullen, P. de Chateau-Thierry, S. Laxon, U. Mallow, C. Mavrocordatos, L. Phalippou, G. Ratier, L. Rey, F. Rostan, P. Viau, and D. Wallis, "CryoSat: A mission to determine the fluctuations in Earths land and marine ice fields," *Advances in Space Research*, vol. 37, no. 4, pp. 841 – 871, 2006.

[4] M. Jain, O. B. Andersen, J. Dall, and L. Stenseng, "Sea Surface Height Determination In The Arctic Using CryoSat-2 SAR Data From Primary Peak Empirical Retrackers," Submitted for publication, march 2014.

[5] O. Andersen and R. Scharroo, *Range and geophysical corrections in coastal regions: and implications for mean sea surface determination*, pp. 103–146, Springer, 2011.

[6] F. Frappart, S. Calmant, M. Cauhopé, F. Seyler, and A. Cazenave, "Preliminary results of ENVISAT RA-2-derived water levels validation over the Amazon basin," *Remote Sensing of Environment*, vol. 100, no. 2, pp. 252–264, 2006.

[7] F. Papa, F. Durand, W. B. Rossow, A. Rahman, and S. K. Bala, "Satellite altimeter-derived monthly discharge of the Ganga-Brahmaputra River and its seasonal to interannual variations from 1993 to 2008," *Journal of Geophysical Research: Oceans*, vol. 115, no. C12, pp. n/a–n/a, 2010.

[8] J. S. da Silva, S. Calmant, F. Seyler, O. C. Rotunno Filho, G. Cochonneau, and W. J. Mansur, "Water levels in the Amazon basin derived from the ERS 2 and ENVISAT radar altimetry missions," *Remote Sensing of Environment*, vol. 114, no. 10, pp. 2160–2181, 2010.

[9] J. Salomon, J. C. F. Hodges, M. Friedl, C. Schaaf, A. Strahler, F. Gao, A. Schneider, X. Zhang, N. El Saleous, and R. Wolfe, "Global land-water mask derived from MODIS Nadir BRDF-adjusted reflectances (NBAR) and the MODIS land cover algorithm," in *Geoscience and Remote Sensing Symposium, 2004. IGARSS '04. Proceedings. 2004 IEEE International*, Sept 2004, vol. 1, pp. –241.

A.5 Estimation of river and lake heights using CryoSat-2 altimetry

Conference proceedings for ESA Living Planet Symposium held in Edinburgh, Scotland, in September 2013.

ESTIMATION OF RIVER AND LAKE HEIGHTS USING CRYOSAT-2 ALTIMETRY

Heidi Villadsen, Ole B. Andersen, and Lars Stenseng

DTU Space – National Space Institute, Technical University of Denmark, Elektrovej, Building 327, 2800 Lyngby, Denmark. E-mail: hvil@space.dtu.dk

ABSTRACT

Using a simple threshold retracker on SAR and LRM data from CryoSat-2 it is seen that the SIRAL radar altimeter shows great potential for height estimation over land and inland waters. Differences between heights from the SRTM DEM and the retracked heights were less than 1 m for Lake Vättern in Sweden, which is well within the error range of 16 m for SRTM. However, some difficulties where encountered, such as snagging due to bright targets off-nadir, as well as an occasional inability of the altimeter to adjust the window delay to the underlying terrain. It was also found, that classification of waveforms over land and inland waters is challenging. Therefore, using a well resolved river and lake mask and focusing on small test regions is recommended until radar altimetry over land and inland waters is fully understood.

Key words: Radar altimetry, SAR, river and lake levels, land hydrology, retracking.

1. INTRODUCTION

As a result of global climate change floods and droughts are expected to become more frequent and more severe. It is therefore crucial to be able to monitor the changing water levels in rivers and lakes accurately; both purely for monitoring purposes but also in order to increase our ability to model future changes in land hydrology. So far, these reservoirs have been too small to resolve using satellite radar altimetry but with the introduction of the new high-resolution SRAL SAR altimeters, as carried onboard CryoSat-2 and soon Sentinel-3, it is expected to improve significantly.

Supported by the recently funded EU 7th Framework LOTUS project, which focuses on the development of applications of Sentinel-3 for land and ocean monitoring for GMES, a customized retracker specifically for inland water purposes will be developed using the SAR altimeter data from CryoSat-2 until Sentinel-3 data are available.

In this study height estimations of land and inland waters using a threshold retracker are presented to evaluate the potential of CryoSat-2 (and Sentinel-3) data for retrieval of heights over inland water bodies.

2. METHODS

2.1. Data

For this study SAR and LRM data from CryoSat-2 for the year 2012 were used. The radar altimeters onboard the CryoSat-2 and the upcoming Sentinel-3 missions are very similar, making it possible to develop methods for the Sentinel-3 SRAL SAR altimeter data retracking before the actual launch of the satellite.
CryoSat-2 has an almost annual repeat cycle of 369 days, with a subcycle of around 29 days, which gives great spatial coverage. The altimeter data used here are the 20 Hz data sets, corresponding to a ground spacing of approximately 250-300 m along track [1]. Since the mask that is provided in the CryoSat-2 product has a poor accuracy it was decided to retrack both land and inland water waveforms.
In addition to CryoSat-2 data the *Shuttle Radar Topography Mission Digital Elevation Model* [2] (SRTM DEM) was also utilized to investigate the general performance of the retracker over land and inland waters in a region covering Denmark and southern Sweden. The coverage of the entire SRTM dataset is near global extending from 56°S to 60°N in latitude with a resolution of 90 m×90 m. The error on the SRTM data has been found to be around $\pm$16 m [3].

2.2. Retracking

Waveforms obtained over land and inland waters are often more complex than waveforms retrieved from homogenous surfaces, such as oceans or an ice sheets, since in this case the satellite footprint covers an area with a high variety of surface types and elevations, which affects the reflection of the pulse. SAR waveforms are well understood when it comes to oceans and ice sheets, however, retracking waveforms retrieved from land and inland waters is still considered challenging.

Before the decision on which retracker to use was taken, the general appearance of waveforms over land and inland waters was studied. The analysis indicated multiple peaks in the waveforms, and that the overall appearance vary beyond the possibility of simple waveform classification. Therefore, only empirical retrackers were chosen to be included in the retracking analysis, since the varying topography on land does not allow for the use of a physical retracker, such as the Brown model, which was designed for ocean retrievals. Here, the results from using a standard threshold retracker [4] are shown. The thresholds were chosen to be 80/,% and 31.3 % for SAR and LRM waveforms, respectively. These thresholds were chosen in order to achieve a minimal difference in estimated lake heights in lakes where the altimeter changes between altimeter modes.

3. RESULTS

Fig. 1 shows the result of retracking all LRM and SAR waveforms over land and inland waters for CryoSat-2 tracks from the year 2012. Areas of SARIn mode and continental ice and ocean where not included and show up as grey areas. From this global map it is seen that using a simple threshold retracker provides us with a recognizable topography map. Focusing in on a smaller area, as done in Fig. 2 reveals the high density of tracks due to the near-repeat track feature of the satellites orbit.
When looking at the difference between SRTM heights and the obtained retracked heights in Fig. 3, a strong negative bias is observed, meaning that our estimated heights are smaller than the SRTM heights. This bias is caused by the "snagging" effect, where bright targets off nadir give the illusion of a longer distance between the satellite and the ground surface. Closing in on the obtained heights over the Swedish lakes Vänern and Vättern, it is seen that the estimated heights are generally in very good agreement with SRTM with differences under 1 m. However, continuous errors are observed around the southeastern shores at Lake Vttern for the ascending tracks.
A plausible explanation for this is, that the window delay does not adjust quickly enough in order to catch the return signal from the lake after the track leaves the mountainous area to the southeast part of the lake. The satellite only has a window corresponding to around 30 m to catch the return signal, so if the altimeter looks for the return signal in the wrong time period, because it overestimates the altitude of the lake due to the previous altitudes over the mountains, it will not be able to receive the return signal from the time of nadir reflection. The difficulties of the altimeters adjustment of window delay is shown in Fig. 4 together with some other parameters.
In this study the development of a discrimination method was also pursued. The ability to distinguish between signals from land and signals from inland waters would provide a way of identifying changing water levels, e.g. floods or lakes and rivers which are changing due to changes in the hydrological cycle. A way of discriminating between land and inland waters could include criteria on backscatter and peakiness for each waveform, however, no set of criteria was found to capture inland waters satisfactory. Allowing for only very specular waveforms we will end up with returns from inland waters and nothing else, but most of the water bodies are also excluded in the process.

4. DISCUSSION

From the results it is clear that although CryoSat-2 was not intended for studying topography or inland waters it shows great potential. The standard threshold retracker performs very well in general over inland waters, and even over land. Difficulties are particularly seen when the satellite footprint covers a wide variety of different surfaces, especially when very bright targets are located slightly off nadir, giving rise to off-ranging; an overestimation of the travel time between the satellite and the underlying surface. Therefore, a general underestimation of the surface heights compared to SRTM is seen. Unfortunately, the altimeter also seems to struggle with severe terrain, which makes it hard for the window delay to adjust automatically. However, tracks with this problem are easily identified and can be discarded totally or partially. Retracking CryoSat-2 data over large lakes is already now seen to give promising results as shown for lakes Vänern and Vättern in Sweden, where the difference between retracked heights and SRTM was well below 1 m for points without obvious problems such as unadjusted window delay and off-ranging. Issues like these make the possibility of an automatic retracking system unlikely, since the retracked heights from each track must be individually analyzed.
Before a global approach is possible, a thourough investigation of test regions is necessary. Comparison with coinciding in situ measurements would provide a useful way of determining the accuracy of CryoSat-2 altimetry over lakes. Furthermore, since it is hard to distinguish between retrievals from land and inland waters using a mask is recommendable. However, masks with higher resolution than the one provided in the CryoSat-2 product do exist and should therefore be used.

REFERENCES

[1] *CryoSat Product Handbook*, April 2012.

[2] Jarvis A., Reuter H.I, Nelson A., Guevara E. (2008), Hole-filled SRTM for the globe Version 4, available from the CGIAR-CSI SRTM 90m Database (http://srtm.csi.cgiar.org).

[3] Berry, P.A.M et al. (2007), Near-global validation of the SRTM DEM using satellite radar altimetry, *Remote Sens. Environ.* 106, 17-27.

[4] Wingham, D.J. et al. (1986), New techniques in satellite altimeter tracking systems, In: P*roceeding of IGARSS 88 Symposium*. September, Zurich, Switzerland pp. 1339-1344.

[5] Farr, T. G., et al. (2007), The Shuttle Radar Topography Mission, *Rev. Geophys.*, vol 45, RG2004.

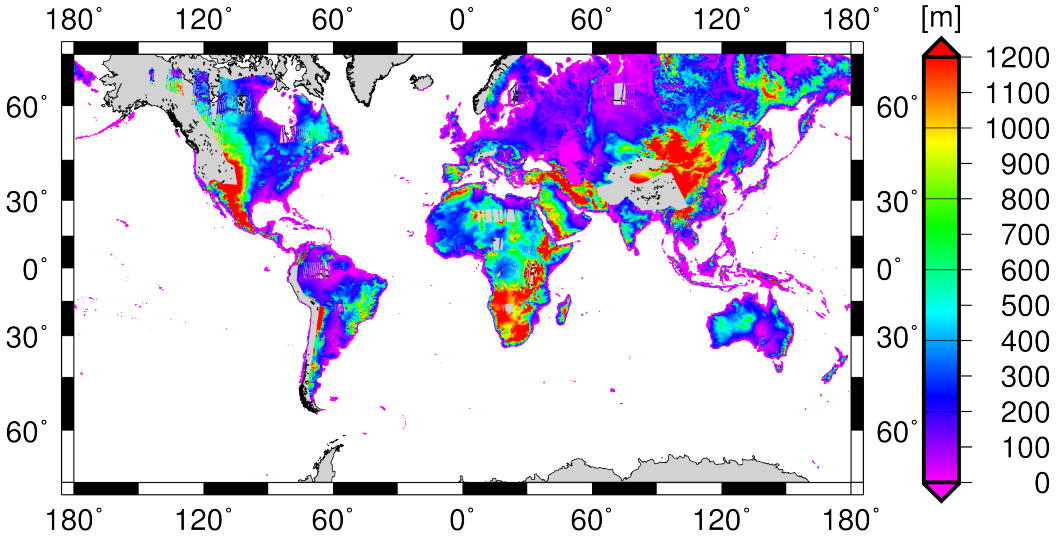

Figure 1: Retracked heights for SAR and LRM data using threshold retracker. Heights are relative to the EGM96 geoid and grey areas correspond to SARIn regions or regions marked as continental ice.

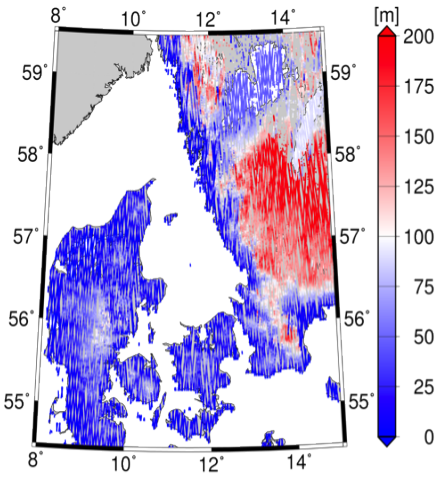

Figure 2: Estimated retracked heights referenced to EGM96.

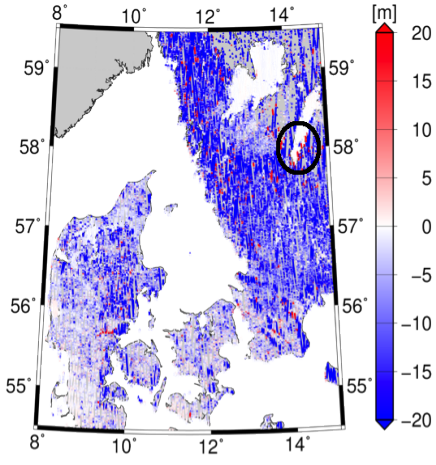

Figure 3: Difference between SRTM DEM heights and retracked heights.

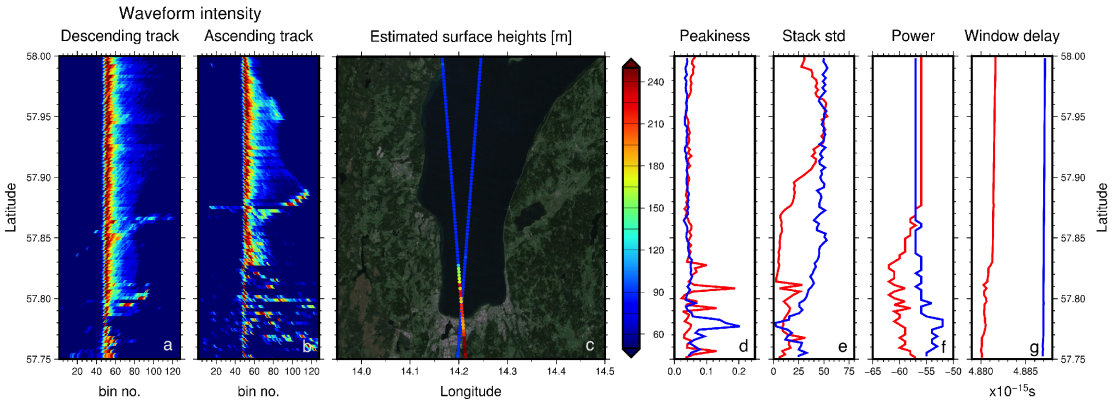

Figure 4: Two tracks crossing Lake Vättern in Sweden; one ascending (left track) and one descending (right track). a-b) Waveforms as a function of bin no. and latitude, c) map showing the location of the two tracks and the retracked heights, d-g) parameters as stated for ascending track (red) ad descending track (blue).

DTU Space
National Space Institute
Technical University of Denmark

Elektrovej 328
DK-2800 Kgs. Lyngby

Tel +45 4525 9500
Fax +45 4525 9575

http://www.space.dtu.dk